

497

"The Numerical Synthesis and Inversion of
Acoustic Fields Using the Hankel Transform
with Application to the Estimation of the
Plane Wave Reflection Coefficient of the
Ocean Bottom"

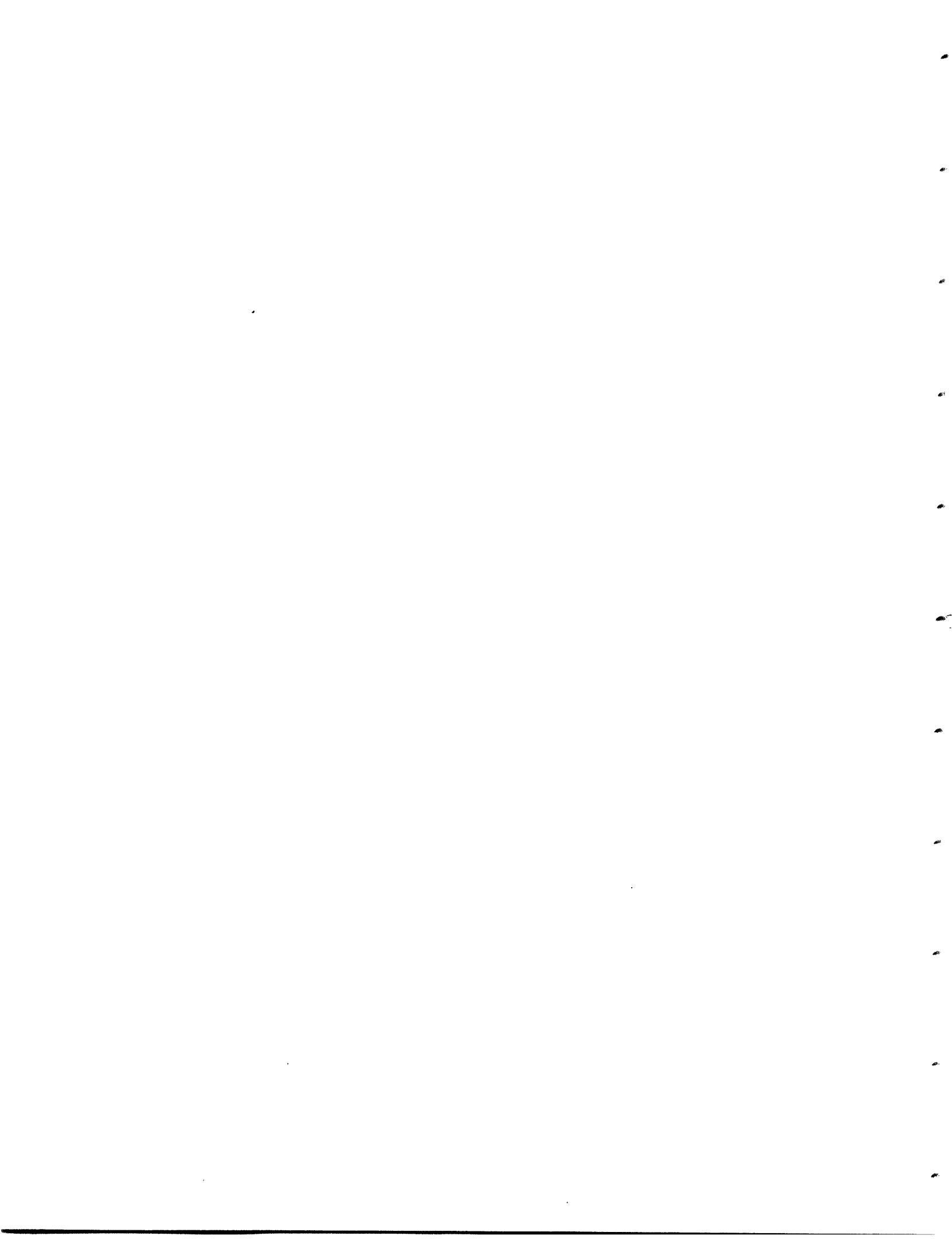
Douglas R. Mook

Technical Report 497 - January 1983

M.I.T., R.L.E.

Loan Copy Only

This work has been supported in part by the Advanced Research Projects Agency monitored by ONR under Contract N00014-81-K-0742 NR-049-506 and in part by the National Science Foundation under Grant ECS80-07102.



REPORT DOCUMENTATION PAGE		READ INSTRUCTIONS BEFORE COMPLETING FORM
1. REPORT NUMBER 497	2. GOVT ACCESSION NO.	3. RECIPIENT'S CATALOG NUMBER
4. TITLE (and Subtitle) The Numerical Synthesis and Inversion of Acoustic Fields Using the Hankel Transform with Application to the Estimation of the Plane Wave Reflection Coefficient of the Ocean Bottom		5. TYPE OF REPORT & PERIOD COVERED Technical Report
		6. PERFORMING ORG. REPORT NUMBER Ocean Bottom
7. AUTHOR(s) Douglas R. Mook		8. CONTRACT OR GRANT NUMBER(s) N00014-81-K-0742
9. PERFORMING ORGANIZATION NAME AND ADDRESS Research Laboratory of Electronics Massachusetts Institute of Technology Cambridge, MA 02139		10. PROGRAM ELEMENT, PROJECT, TASK AREA & WORK UNIT NUMBERS NR-049-506
11. CONTROLLING OFFICE NAME AND ADDRESS Advanced Research Projects Agency 1400 Wilson Boulevard Arlington, VA 22217		12. REPORT DATE January 1983
		13. NUMBER OF PAGES 226
14. MONITORING AGENCY NAME & ADDRESS (if different from Controlling Office) Office of Naval Research Mathematical and Information Sciences Division, 800 North Quincy Street Arlington, VA 22217		15. SECURITY CLASS. (of this report) Unclassified
		15a. DECLASSIFICATION/DOWNGRADING SCHEDULE
16. DISTRIBUTION STATEMENT (of this Report) approved for public release; distribution unlimited		
17. DISTRIBUTION STATEMENT (of the abstract entered in Block 20, if different from Report)		
18. SUPPLEMENTARY NOTES		
19. KEY WORDS (Continue on reverse side if necessary and identify by block number) Hankel transform plane wave reflection coefficient Sommerfeld integral depth-dependent Green's function trapped waves acoustic CW point source		
20. ABSTRACT (Continue on reverse side if necessary and identify by block number) see other side		

ABSTRACT

The plane wave reflection coefficient is an important geometry independent means of specifying the acoustic response of a horizontally stratified ocean bottom. It is an integral step in the inversion of acoustic field measurements to obtain parameters of the bottom and it is used to characterize an environment for purposes of acoustic imaging. This thesis studies both the generation of synthetic pressure fields through the plane wave reflection coefficient and the inversion of measured pressure fields to estimate the plane wave reflection coefficient. These are related through the Sommerfeld integral which is in the form of a Hankel transform. The Hankel transform is extensively studied in this thesis and both theoretical properties and numerical implementations are considered. These results have broad applications. When we apply them to the generation of synthetic data, we obtain hybrid numerical-analytical algorithms which provide extremely accurate synthetic fields without sacrificing computational speed. These algorithms can accurately incorporate the effects of trapped modes guided by slow speed layers in the bottom. We also apply these tools to study the inversion of measured pressure field data for the plane wave reflection coefficient. We address practical issues associated with the inversion procedure including removal of the source field, sampling, field measurements over a finite range, and uncontrolled variations in source-height. A phase unwrapping and associated interpolation scheme is developed to handle improperly spaced data.

A preliminary inversion of real pressure field data is performed. In parallel, an inversion of a synthetically generated field for similar bottom parameters is also performed and the results of processing the real and synthetic data are compared. The estimate for the depth dependent Green's function obtained from the real data shares many features with the depth dependent Green's function estimated from the synthetic data, suggesting that the total inversion to obtain the plane wave reflection coefficient will soon be possible. Errors in the present estimate of the plane wave reflection coefficient are associated with uncontrolled source-height variations during the acquisition of data.

**The Numerical Synthesis and Inversion of Acoustic Fields
Using the Hankel Transform with Application to the
Estimation of the Plane Wave Reflection Coefficient of the
Ocean Bottom**

Douglas R. Mook

Submitted in partial fulfillment
of the requirements for the degree of
Doctor of Science

at the

MASSACHUSETTS INSTITUTE OF TECHNOLOGY
and the
WOODS HOLE OCEANOGRAPHIC INSTITUTION

January, 1983

ABSTRACT

The plane wave reflection coefficient is an important geometry independent means of specifying the acoustic response of a horizontally stratified ocean bottom. It is an integral step in the inversion of acoustic field measurements to obtain parameters of the bottom and it is used to characterize an environment for purposes of acoustic imaging. This thesis studies both the generation of synthetic pressure fields through the plane wave reflection coefficient and the inversion of measured pressure fields to estimate the plane wave reflection coefficient. These are related through the Sommerfeld integral which is in the form of a Hankel transform. The Hankel transform is extensively studied in this thesis and both theoretical properties and numerical implementations are considered. These results have broad applications. When we apply them to the generation of synthetic data, we obtain hybrid numerical-analytical algorithms which provide extremely accurate synthetic fields without sacrificing computational speed. These algorithms can accurately incorporate the effects of trapped modes guided by slow speed layers in the bottom. We also apply these tools to study the inversion of measured pressure field data for the plane wave reflection coefficient. We address practical issues associated with the inversion procedure including removal of the source field, sampling, field measurements over a finite range, and uncontrolled variations in source-height. A phase unwrapping and associated interpolation scheme is developed to handle improperly spaced data.

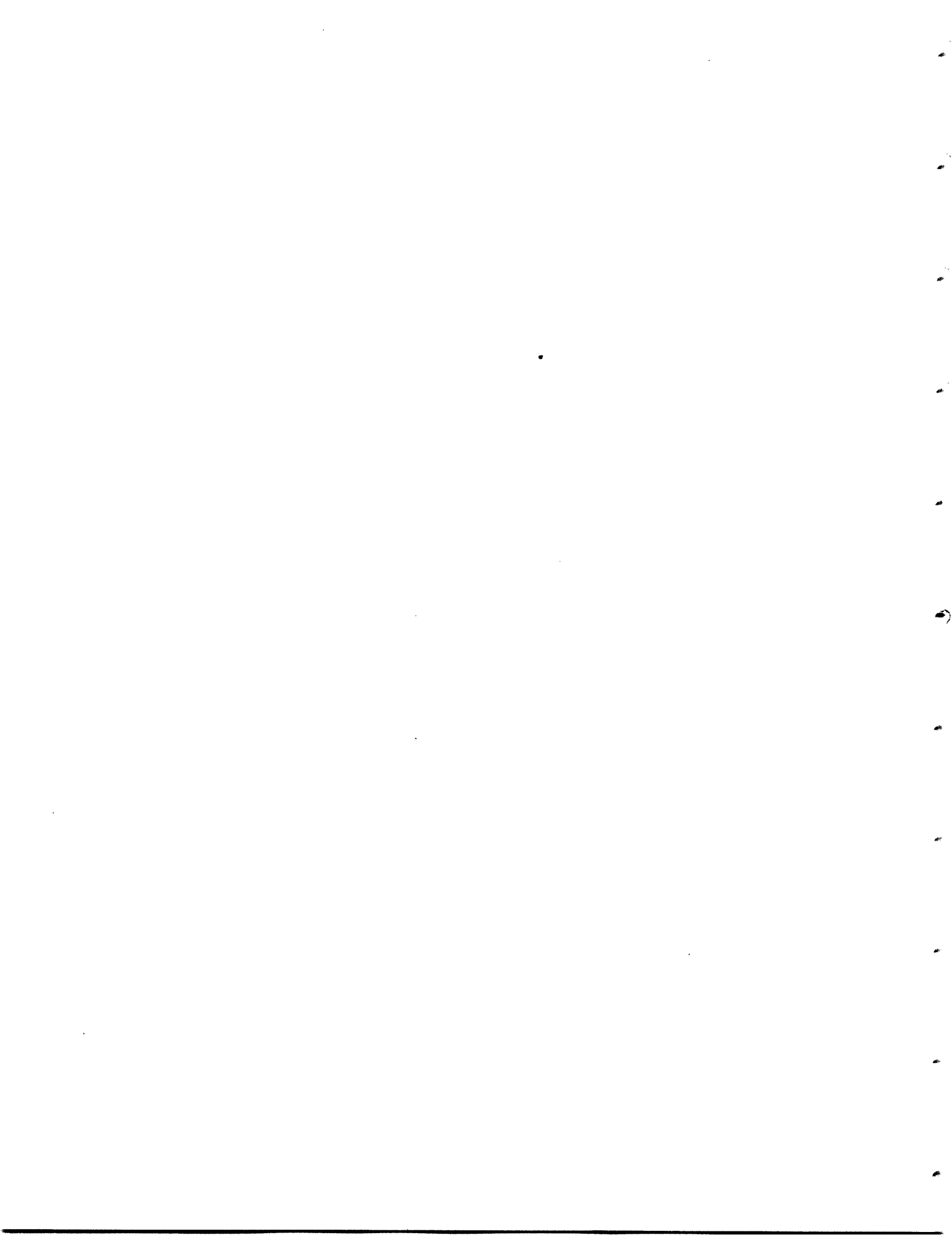
A preliminary inversion of real pressure field data is performed. In parallel, an inversion of a synthetically generated field for similar bottom parameters is also performed and the results of processing the real and synthetic data are compared. The estimate for the depth dependent Green's function obtained from the real data shares many features with the depth dependent Green's function estimated from the synthetic data, suggesting that the total inversion to obtain the plane wave reflection coefficient will soon be possible. Errors in the present estimate of the plane wave reflection coefficient are associated with uncontrolled source-height variations during the acquisition of data.

Thesis supervisors:

George V. Frisk, Associate Scientist, Woods Hole Oceanographic Institution

Alan V. Oppenheim, Professor of Electrical Engineering, Massachusetts Institute of Technology

To
Algonda M. Mook
and
Adolf J. Mook
with love



Acknowledgements

Many people have made this thesis possible and it gives me great pleasure to thank those I can, in this small space. First and foremost I would like to thank my parents, whose love and unfailing support gave me the emotional foundation to start and finish this work. I would like also to thank Julie Hanson for the sunshine I might otherwise have forgotten. To my advisors, Al Oppenheim and George Frisk, my debt goes beyond words. The technical content of this thesis represents only a small part of what I have gained from these two men. It is my hope that our friendship as well as technical collaboration, will continue throughout our lives.

A particular thanks goes to those who made this document possible- to Betsey Pratt for the figures and to Bruce Musicus and Mike McIlrath who tricked the computer into finally printing out the document. To my readers, Art Baggeroer and Bob Porter, and to Earl Hays go my thanks as well, for reading this thesis and for their comments and advice.

Through the joint program I have had the privilege of being part of two thriving intellectual environments. I wish it were possible to thank all my friends and colleagues who have made this such a positive experience. I would particularly like to thank Andy Kurjian, now at Schlumberger, Dave Stickler, of the Courant Institute, and Mike Wengrovitz at MIT for many stimulating discussions. I would also like to thank Mike for implementing my Hankel transform program on the VAX.

Two people deserve special thanks- Jim Doutt at WHOI and Webster Dove at MIT. Jim not only made it possible for me to use the computer at WHOI but helped me study some of the effects covered in this thesis. To Webster Dove, whose total communion with our computer at MIT is legendary, goes my deepest thanks for mediating the many disputes between organic and inorganic intelligence.

Finally I would like to thank those whom I know and the many I do not, for the MIT/WHOI joint program. The rich interface between technical worlds made possible by this program was one of life's rare opportunities.

Al, thanks for introducing me to windsurfing.

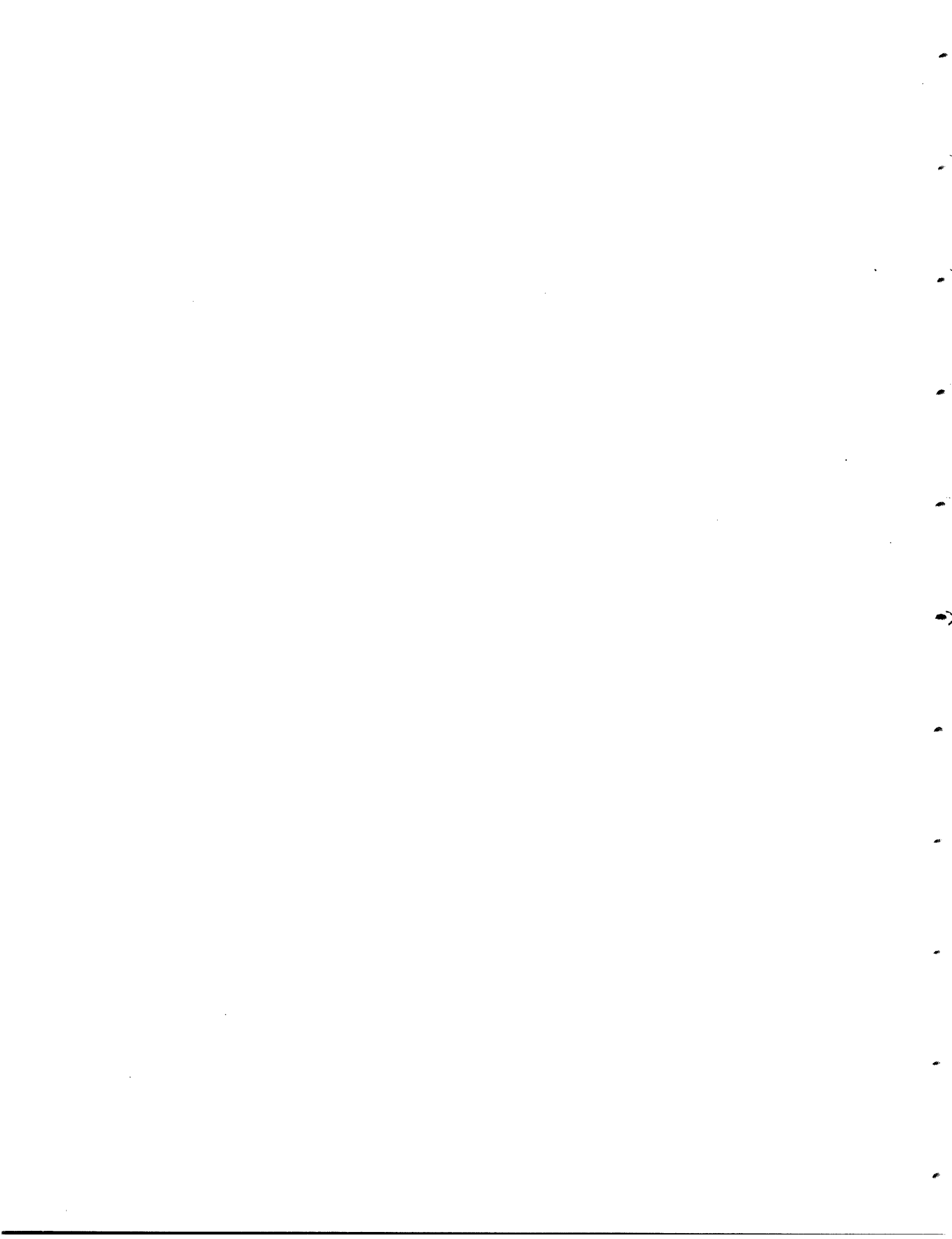


Table of Contents

ABSTRACT	2
ACKNOWLEDGEMENTS	5
TABLE OF CONTENTS	6
CHAPTER I: INTRODUCTION	
1: Overview	10
2: Plane Waves and a Horizontally Stratified Environment	12
3: The Weyl Integral	14
4: The Sommerfeld Integral	16
5: Obtaining the Reflection Coefficient	18
6: The Experimental Model	19
7: Summary	21
CHAPTER II: THE HANKEL TRANSFORM	
1: Overview	25
2: Definitions	26
3: The Hankel Transform as a Two Dimensional Fourier Transform	27
4: Asymptotics	29
5: General Properties	31
6: Windowing and the Hankel Transform	
a: An Exact Windowing Expression	31
b: Approximation as a Convolution	33
c: Resolution and Leakage	34
d: Examples	35
7: Sampling and Aliasing	43
8: The Effect of Additive White Gaussian Noise on the Hankel Transform	
a: Statement of the Effect	50

b: Proof that if $f(\sqrt{r})$ is Stationary White Gaussian Noise 55
then $F(\sqrt{\rho})$ will also be Stationary White Gaussian Noise
where $F(\rho)$ is the Hankel Transform of $f(r)$

i: Proof that $F_2(\rho)$ is Stationary White Gaussian Noise .. 55
if and only if $f(r)$ is Stationary White Gaussian Noise,
Where $F_2(\rho)$ is the Hankel transform of $f(r)$
as defined by Bateman

ii: Proof that $\sqrt{\rho}F(\rho)$ is Stationary White Gaussian .. 56
Noise if and only if $\sqrt{r}f(r)$ is Stationary White
Gaussian Noise, where $F_2(\rho)$ is the Hankel
Transform of $f(r)$

iii: Proof that $\sqrt{r}f(r)$ is Stationary White Gaussian noise .. 57
if and only if $f(\sqrt{r})$ is Stationary White Gaussian
noise

iv: Conclusion 58

9: Summary 58

CHAPTER III: COMPUTING THE HANKEL TRANSFORM

1: Overview 60

2: The Fourier-Bessel Series 60

3: The Backsmear Method 62

4: The Asymptotic Transform 64

5: A Combined Transform Method 68

6: A Convolutional Method 70

7: The Projection-Slice Method

a: Overview 71

b: The Abel Transform 72

c: The Hankel Transform 78

d: Discussion 81
e: Summary 85
f: Conclusion 86
8: Summary 86

CHAPTER IV: SYNTHETIC DATA GENERATION

1: Overview 89
2: The Propagator Matrix Approach to Generating the Plane 90
 Wave Reflection Coefficient
 a: The Method in Principle
 i: Overview 91
 ii: The Propagator Matrix 93
 b: Numerical Implementation
 i: The Modified Propagation Matrix 94
 ii: Relation of the Modified Propagation Matrix to the Incident 95
 and Reflected Waves
 c: Selected Properties of the Reflection Coefficient 96
3: Evaluating the Sommerfeld Integral 100
 a: The Source Singularity 101
 i: Hard Bottom 106
 ii: Slow Bottom 106
 iii: Fast Bottom 106
 b: Poles Due to Slow Speed Layers 106

CHAPTER V: THE INVERSION PROCEDURE

1: Overview 125
2: Source-Field Subtraction 128
3: Sampling
 a: Overview 131

b: Sampling Rate	131
c: Sampling Grid	133
d: Unwrapping the Phase	137
e: Interpolating the Magnitude and Unwrapped Phase	140
f: Phase Unwrapping Errors	155
4: Windowing	165
5: Source-Height Variation	
a: General Expression	167
b: Particular Variations	
i: No Source-Height Variation	168
ii: Linear Source-Height Variation	168
iii: Sinusoidal Source-Height Variation	169
5: Summary	176
CHAPTER VI: INVERTING REAL AND REALISTIC DATA	179
CHAPTER VII: CONTRIBUTIONS AND FUTURE WORK	
1: Contributions	208
2: Future Work	
a: Cylindrical to Cartesian Systems	210
b: Analytical-Numerical Algorithms	211
c: Waveguides	213
APPENDIX 1: Determining the Limits for the Aliasing Results of Section (II.7) ..	218
APPENDIX 2: The Value of the Kernel for the Numerical Portion of the	223
Hybrid Algorithm at the Water Wave Number	
APPENDIX 3: The Evaluation of the Pole Contribution to the field for	225
Section (IV.3b)	

CHAPTER I:

INTRODUCTION

1.1) Overview

The plane wave reflection coefficient is an important geometry independent means of specifying the acoustic response of a horizontally stratified ocean bottom. It is used both to calculate fields in propagations models and as an input to a variety of inverse techniques which seek to determine bottom parameters [1, 2, 3]. In this thesis we will study both the generation of synthetic pressure fields through the plane wave reflection coefficient and the inversion of measured pressure fields to estimate the plane wave reflection coefficient. We will consider only the fields associated with a CW point source in the deep ocean over a horizontally stratified bottom and will not allow the bottom to support shear waves. The results of this thesis, however, are applicable to a wide class of wave problems and can be generalized to permit the source to be within any isovelocity layer and the introduction of shear. Further, it is our hope that the tools developed in the course of this work will find applications in many areas.

The foundation for our studies of the forward and inverse problems is the Hankel transform, [4, 5, 6] which arises in these contexts because the Sommerfeld integral which relates the plane wave reflection coefficient to the reflected field is in that form. We will derive general properties of the Hankel transform to guide the work in these areas. We will also study and develop numerical implementations to permit computer processing. A fast, accurate numerical Hankel transform algorithm is developed and illustrated.

The Hankel transform results allow us to isolate significant sources of degradation in numerically generated synthetic fields. To remove these sources we develop a hybrid analytical-numerical procedure which is significantly more accurate without sacrificing computational speed. This hybrid algorithm performs some of the calculations analytically while keeping the numerical computation in the form of a Hankel transform.

Through another hybrid technique we incorporate the effects of trapped modes that may be

guided by low speed layers in the bottom. The results are accurate both in the near and far fields, in contrast with modal methods. The method developed for handling these modes can also be used to control other complications associated with poles in the plane wave reflection coefficient such as those that would be introduced by allowing for shear wave propagation.

In Chapter V we begin to study the inversion of pressure field data to obtain an estimate for the plane wave reflection coefficient. We draw upon our previous results to consider a recently proposed method for performing this inversion by Frisk, Oppenheim and Martinez [7]. Frisk, Oppenheim and Martinez have proposed that the Sommerfeld integral be inverted directly, without recourse to the specular approximation used by previous methods. [7] With such a direct inversion, estimates would no longer be confined to real angles of incidence and regions where the specular approximation is valid. [8, 9] Such a direct inversion has been made possible recently by coherent measurements of the reflected pressure field resulting from a point source over a horizontally stratified bottom. [10] In this chapter we study several practical issues associated with this proposed direct inversion. We consider directly the issues of source field subtraction, sampling, windowing of the pressure field, and uncontrolled variations in source height. The issue of source-field subtraction arises because the plane wave reflection coefficient is directly related to the reflected field and not the total field, which is measured. Under the issue of sampling we study both the sampling rate required to obtain a valid inversion and the effects of improperly spaced data. To handle improperly spaced data, an interpolation procedure is developed which is based on a new phase unwrapping procedure. In the discussion of windowing we determine the range to which field measurements must be taken in order to obtain a valid inversion. In the section on source-height variation we characterize the degradation that results from variation in the source-height and study canonical variations.

Having considered many of the issues affecting the direct inversion of pressure field data to obtain the plane wave reflection coefficient we now actually perform a preliminary inversion of real data. In parallel we invert synthetic data that we have generated using bottom parameters

comparable to those we believe associated with the real data. We draw upon the previous developments to interpret the results.

In the remaining portion of this chapter we briefly develop the acoustic framework upon which this thesis rests. We also describe the experimental paradigm by which the real data was gathered.

I.2) Plane Waves and a Horizontally Stratified Environment

A horizontally stratified environment is one for which the material parameters vary only vertically. Such a simple environment makes possible an in depth study without the complications that a more varied environment would introduce. The insights gained from studying this simple environment can provide an understanding of more complicated environments. Also, for many conditions, such as are found in the region of an abyssal plane in the deep ocean, the model is itself sufficient.

Figure I.2.1 shows an isovelocity water layer over a horizontally stratified bottom. Within the water a single plane wave has the form ¹:

$$e^{i(k_x x + k_y y + k_z z)} e^{-i\omega t} \quad (1)$$

For this wave to be a solution to the wave equation within the water (which has sound speed c):

$$\left[\nabla^2 - \frac{1}{c^2} \frac{\partial^2}{\partial t^2} \right] \Phi(x, t) = 0 \quad (2)$$

the wave numbers (k_x , k_y , and k_z) must satisfy:

$$k_x^2 + k_y^2 + k_z^2 - \frac{\omega^2}{c^2} = 0 \quad (3)$$

We define the vector $\mathbf{k} \equiv k_x \hat{i}_x + k_y \hat{i}_y + k_z \hat{i}_z$ and the scalar, $k \equiv \frac{\omega}{c}$. \mathbf{k} will point in the direc-

tion that the plane wave propagates. In terms of this vector, the requirement (3) can be written

$$\|\mathbf{k}\| \equiv \sqrt{k_x^2 + k_y^2 + k_z^2} = k \quad (4)$$

1) Throughout this thesis we will suppress the $e^{-i\omega t}$ time dependence because it separates out from all the field expressions.

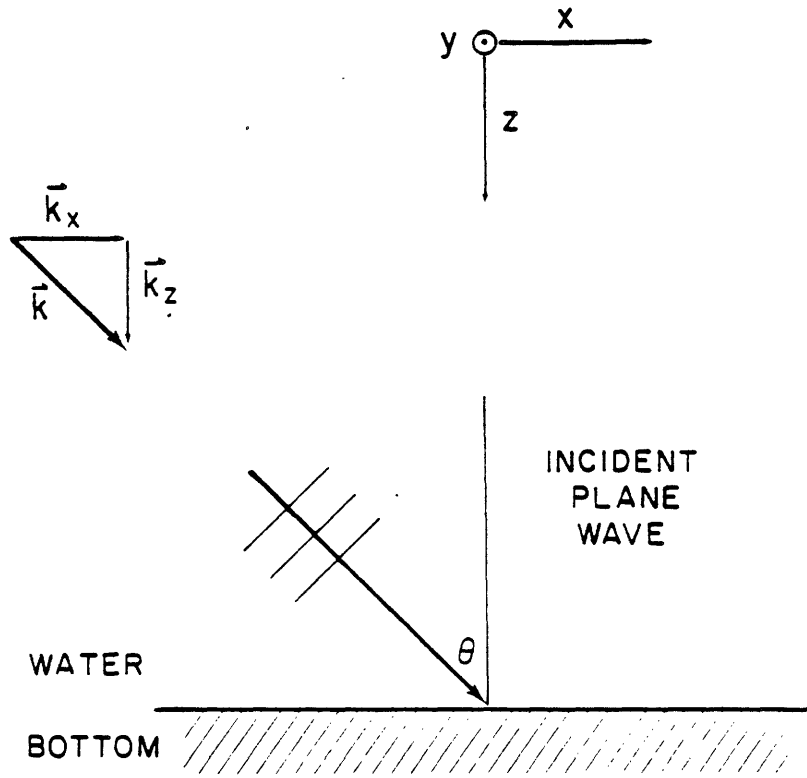


Figure I.2.1 Incident plane wave geometry

If (4) is satisfied then (1) is formally a solution to the wave equation even if \mathbf{k} is complex. When one or more of the components of \mathbf{k} are imaginary the plane wave is called evanescent and will vary exponentially in the direction of the imaginary component(s).

Considerations of symmetry guarantee that when a plane wave strikes a horizontally stratified bottom the resulting wave will also be planar. For the purposes of field calculations, plane waves are eigenfunctions of horizontally stratified systems. An incident plane wave given by :

$$P_I e^{i(k_x x + k_y y + k_z z)} \quad (5)$$

will generate the reflected wave

$$P_R e^{i(k_x x + k_y y - k_z z)} \quad (6)$$

The change in sign indicates that the reflected wave is returning in the z direction. The amplitude change defines the plane wave reflection coefficient, which may be a function of \mathbf{k} . Since for fixed ω only two of the three components of \mathbf{k} can be specified independently we write the plane wave reflection coefficient explicitly as a function of only two:

$$\Gamma_C(k_x, k_y) \equiv \frac{P_R}{P_I} \quad (7)$$

Our plane wave reflection coefficient is defined for a single frequency only. This implies that the incident signal has been present for all time. The returning wave, $P_R e^{i(k_x x + k_y y - k_z z)}$, is influenced by the bottom at all depths. This is in contrast to the occasional usage of the term for which only the surface contribution to a pulsed input is considered.

I.3) The Weyl Integral

Because the wave propagation we consider is linear we can determine the response to a more complicated incident field by considering that field as a superposition of plane waves. [9]

To calculate the reflected responses to a point source shown in Figure I.3.1 we first express the field of the point source at $z = z_0$ as a superposition of plane waves. We write:¹

¹) We will use k_0 to denote the wave number in the water.

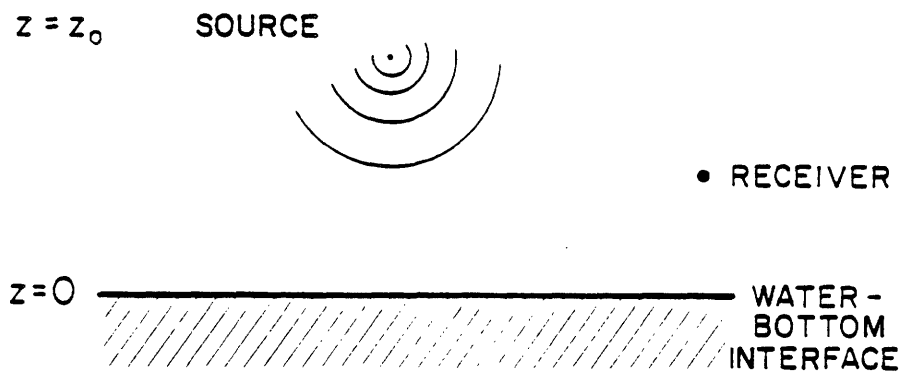


Figure I.3.1 Point source geometry

$$P_I(x, y, z_0) = \frac{e^{ik_0\sqrt{x^2+y^2}}}{\sqrt{x^2+y^2}} = \frac{1}{2\pi} \int_{-\infty}^{\infty} \int_{-\infty}^{\infty} A(k_x, k_y) e^{i(k_x x + k_y y)} dk_x dk_y \quad (1)$$

Equation (1) is a two dimensional Fourier transform and can be inverted to determine $A(k_x, k_y)$:

$$A(k_x, k_y) = \frac{1}{2\pi} \int_{-\infty}^{\infty} \int_{-\infty}^{\infty} \frac{e^{ik_0\sqrt{x^2+y^2}}}{\sqrt{x^2+y^2}} e^{-i(k_x x + k_y y)} dx dy = \frac{i}{\sqrt{k_0^2 - k_x^2 - k_y^2}} \quad (2)$$

Each plane wave in the superposition (1) propagates in the z direction as $e^{i\sqrt{k_0^2 - k_x^2 - k_y^2}z}$ or $e^{-i\sqrt{k_0^2 - k_x^2 - k_y^2}z}$ depending on its direction. Because the incident waves are those which carry energy from the source to the bottom we know that all the waves have $Re(k_z) > 0$.¹ This allows us to write the field at $z > z_0$ as

$$z > z_0 \quad P_I(x, y, z) = \frac{1}{2\pi} \int_{-\infty}^{\infty} \int_{-\infty}^{\infty} \frac{i}{\sqrt{k_0^2 - k_x^2 - k_y^2}} e^{i\sqrt{k_0^2 - k_x^2 - k_y^2}(z-z_0)} e^{i(k_x x + k_y y)} dk_x dk_y \quad (3)$$

When these waves strike the bottom at $z=0$ each is turned around ($+k_z \rightarrow -k_z$) and is scaled by the plane wave reflection coefficient. The reflected field at $z=0$ is given by:

$$P_R(x, y, 0) = \frac{1}{2\pi} \int_{-\infty}^{\infty} \int_{-\infty}^{\infty} \frac{i\Gamma_C(k_x, k_y)}{\sqrt{k_0^2 - k_x^2 - k_y^2}} e^{i\sqrt{k_0^2 - k_x^2 - k_y^2}z_0} e^{i(k_x x + k_y y)} dk_x dk_y \quad (4)$$

The reflected field at any height $z > 0$ is determined by propagating this reflected field up just as we propagated the incident field down.

$$z + z_0 > 0 \quad P_R(x, y, z) = \frac{1}{2\pi} \int_{-\infty}^{\infty} \int_{-\infty}^{\infty} \frac{i\Gamma_C(k_x, k_y)}{\sqrt{k_0^2 - k_x^2 - k_y^2}} e^{i\sqrt{k_0^2 - k_x^2 - k_y^2}(z+z_0)} e^{i(k_x x + k_y y)} dk_x dk_y \quad (5)$$

Equation (5) is often called the Weyl integral. [13]

I.4) The Sommerfeld Integral

1) The complex Poynting vector [11] associated with a plane wave is given by $S(x, y, z) = \frac{1}{2} P U^* = \frac{\sqrt{k_0^2 - k_x^2 - k_y^2}}{2\omega\rho} |P|^2$. [12] The power of the wave flows in the direction of the real part of the Poynting vector. A wave with positive real part of $\sqrt{k_0^2 - k_x^2 - k_y^2}$ carries energy in the positive z direction.

The field associated with a point source over a horizontally stratified bottom is symmetric about the z axis of Figure I.3.1. We can exploit this symmetry to reduce the two dimensional Weyl integral (I.3.5) to a one dimensional integral.

The symmetry of the problem guarantees that all the field variables in space show a cylindrical symmetry. Because the two dimensional Fourier transform of a circularly symmetric function will also be circularly symmetric, the Fourier domain will also display a cylindrical symmetry.

We define

$$\begin{aligned} r^2 &\equiv x^2 + y^2 \\ k_r^2 &\equiv k_x^2 + k_y^2 \end{aligned} \quad (1)$$

With these definitions we write (I.3.5) in cylindrical coordinates as:

$$P_R(r, z) = \frac{1}{2\pi} \int_0^{\infty} \int_0^{2\pi} \frac{i}{\sqrt{k_0^2 - k_r^2}} \Gamma(k_r) e^{i\sqrt{k_0^2 - k_r^2}(z_0 + z)} e^{ik_r \cos\theta} k_r dk_r d\theta \quad (2)$$

With $\Gamma(\sqrt{k_x^2 + k_y^2}) \equiv \Gamma_C(k_x, k_y)$. Performing the θ integration and using [14]

$$J_0(x) \equiv \frac{1}{2\pi} \int_0^{2\pi} e^{ix \cos\theta} d\theta \quad (3)$$

Equation (2) becomes

$$P_R(r, z) = \int_0^{\infty} \frac{i}{\sqrt{k_0^2 - k_r^2}} \Gamma(k_r) e^{i\sqrt{k_0^2 - k_r^2}(z_0 + z)} J_0(k_r r) k_r dk_r \quad (4)$$

This is the Sommerfeld integral. [13]

The Sommerfeld integral has the form

$$P_R(r, z) = \int_0^{\infty} G(k_r, z, z_0) J_0(rk_r) k_r dk_r \quad (5)$$

where

$$G(k_r, z, z_0) \equiv \frac{i}{\sqrt{k_0^2 - k_r^2}} \Gamma(k_r) e^{i\sqrt{k_0^2 - k_r^2}(z_0 + z)} \quad (6)$$

We will refer to $G(k_r, z, z_0)$ as the depth dependent Green's function or the Green's function.

The integral transform (5) is the Hankel transform. [4, 5, 6]

Equation (4) represents the reflected field as a superposition of cylindrical waves of the form $J_0(k_r r) e^{i\sqrt{k_0^2 - k_r^2} z}$, each of which can be considered to be a superposition of plane waves all striking the surface with the same horizontal wave number, k_r . Because $\Gamma(k_r)$ is related so directly to the plane wave reflection coefficient, $\Gamma(\sqrt{k_x^2 + k_y^2}) = \Gamma_C(k_x, k_y)$, we will refer to it as the plane wave reflection coefficient.

I.5) Obtaining the Reflection Coefficient

Presently most techniques for determining the plane wave reflection coefficient as a function of horizontal wave number, $\Gamma(k_r)$, from the reflected pressure field, $P_R(r)$, do not concentrate on inverting Equation (I.4.4). Instead they consider the stationary phase approximation to that Equation given by:¹ [9]

$$P_R(r) \approx \frac{\Gamma\left(\frac{rk_0}{R}\right) e^{ik_0 R}}{R} \quad (1)$$

where k_0 is defined to be the water wave number, $\frac{\omega}{c}$, and $R^2 \equiv r^2 + (z_0 + z)^2$

Equation (I.4.4) is inverted to provide

$$\Gamma\left(\frac{rk_0}{R}\right) \approx \left[\frac{R}{e^{ik_0 R}} \right] P_R(r) \quad (2)$$

If Equation (2) is used to estimate $\Gamma\left(\frac{rk_0}{R}\right)$ then $|\Gamma\left(\frac{rk_0}{R}\right)|$ can be estimated from the magnitude of $P_r(r)$ alone through:

$$\left| \Gamma\left(\frac{rk_0}{R}\right) \right| \approx |R| |p(r)| \quad (4)$$

This fact together with the simplicity of Equation (2) account for its widespread use.

1) More frequently the plane wave reflection coefficient as a function of angle is related through the specular approximation to reflected pressure field. We present it as a function of horizontal wave number to be consistent with the rest of the text. If we denote $\Gamma_\theta(\theta)$ as the plane wave reflection coefficient as a function of angle, the two formulations are related through $\Gamma_\theta(\theta) = \Gamma(k_0 \sin(\theta))$. $k_0 \frac{r}{R}$ is the horizontal wave number corresponding to the specular angle.

Unfortunately the stationary phase approximation upon which (4) is based is appropriate only for distances, R , large compared to a wavelength and only for specular angles less than critical. [8,9] It completely ignores near field effects associated with $\Gamma(k_r)$ for $k_r > k_0$. For applications that consider near field effects or the character of the pressure field close to or greater than the critical angle, a more exact inversion of Equation (I.4.4) is required.

For such applications Frisk, Oppenheim, and Martinez [7] have proposed that both the magnitude and phase of the reflected pressure field be measured and that the Sommerfeld integral of Equation (I.4.4) be inverted directly, without recourse to the stationary phase approximation. The Sommerfeld integral is in the form of a Hankel transform. Since the Hankel transform is its own inverse [5], Equation (I.4.4) can be inverted and solved for the plane wave reflection coefficient in terms of $P_R(r)$, the reflected response to a point source. This gives:

$$\Gamma(k_r) = -i \sqrt{k_0^2 - k_r^2} e^{-i \sqrt{k_0^2 - k_r^2} |z+z_0|} \int_0^{\infty} P_R(r) J_0(k_r r) r dr \quad (5)$$

I.6) *Experimental Model*

In this thesis we will perform a preliminary inversion of measured pressure field data according to Equation (I.5.5), as suggested by Frisk, Oppenheim, and Martinez. [7] The data we analyze was taken by G. Frisk, J. Doust, and E. Hays in 1981. In this section we present the details of the experimental configuration they used. A similar experimental configuration has been described in the literature. [10]

Figure I.6.1 shows the experimental configuration used by Frisk, Doust, and Hays. As shown, two receivers were moored 1.17 and 54.55 meters from the bottom of the ocean on an abyssal plain under 1900 meters of ocean. The source was attached by cable to a ship on the surface, and drifted slowly away at a height off the bottom of approximately 135 meters. Every 12 seconds the source emitted a 4 second 220 Hertz tone which the receivers recorded after quadra-

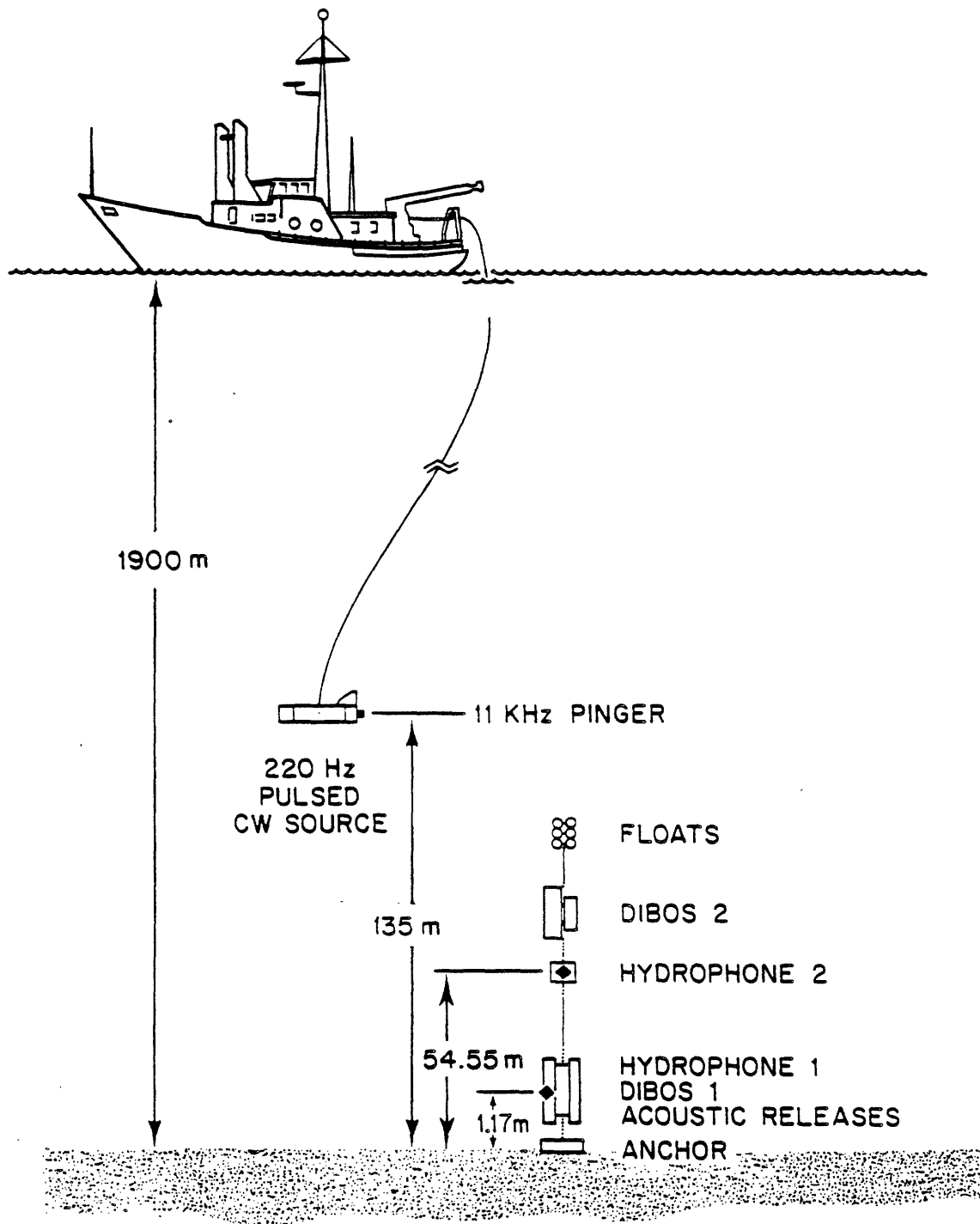


Figure I.6.1 Experimental configuration used by Frisk, Doult and Hays to obtain real data

ture demodulation and low pass filtering. In this way the complex amplitude of the field as a function of range was recorded. The source strength was 177 dB re 1 μ Pa at 1 meter.

Recording by the receivers was initiated every 12 seconds upon recognition of an 11 kHz trigger pulse sent from a pinger mounted on the source, and continued for 6 seconds. During this time the output of the receivers was quadrature demodulated, low pass filtered to 2 Hz, digitized by a 12 bit A/D converter at a 5 Hz rate and recorded on cassette tape. A schematic of the preliminary data processing in the receiver system is shown in Figure I.6.2.

The ship drifted at a speed of about 1/2 kn allowing one sample of the field every half wavelength. The clocks in the source and receiver were synchronized and had a stability of about one part in 10^9 per day. The 11 kHz emission times at the source and the arrival time at the receivers were used to determine the slant range between the source and the receivers. As part of the processing it was necessary to estimate the source height and convert from slant ranged to horizontal range.

Frisk, Doust and Hays determined that the signal was in a steady state condition by the 4th data sample.

I.7) Summary

In this thesis we consider the generation of synthetic pressure fields through the evaluation of the Sommerfeld integral. This integral is in the form of the Hankel transform of the depth-dependent Green's function. We also consider the inversion of a measured pressure field to estimate the depth-dependent Green's function and from that the plane wave reflection coefficient. The foundation of both these procedures is the Hankel transform. In the next chapter we will both catalogue and develop the properties of the Hankel transform that will provide the foundation for the work of this thesis.

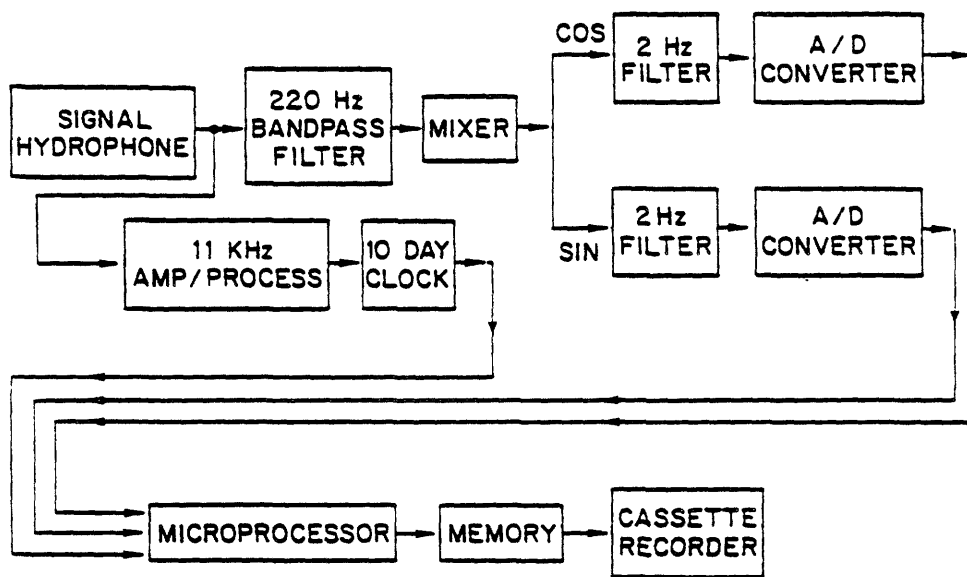
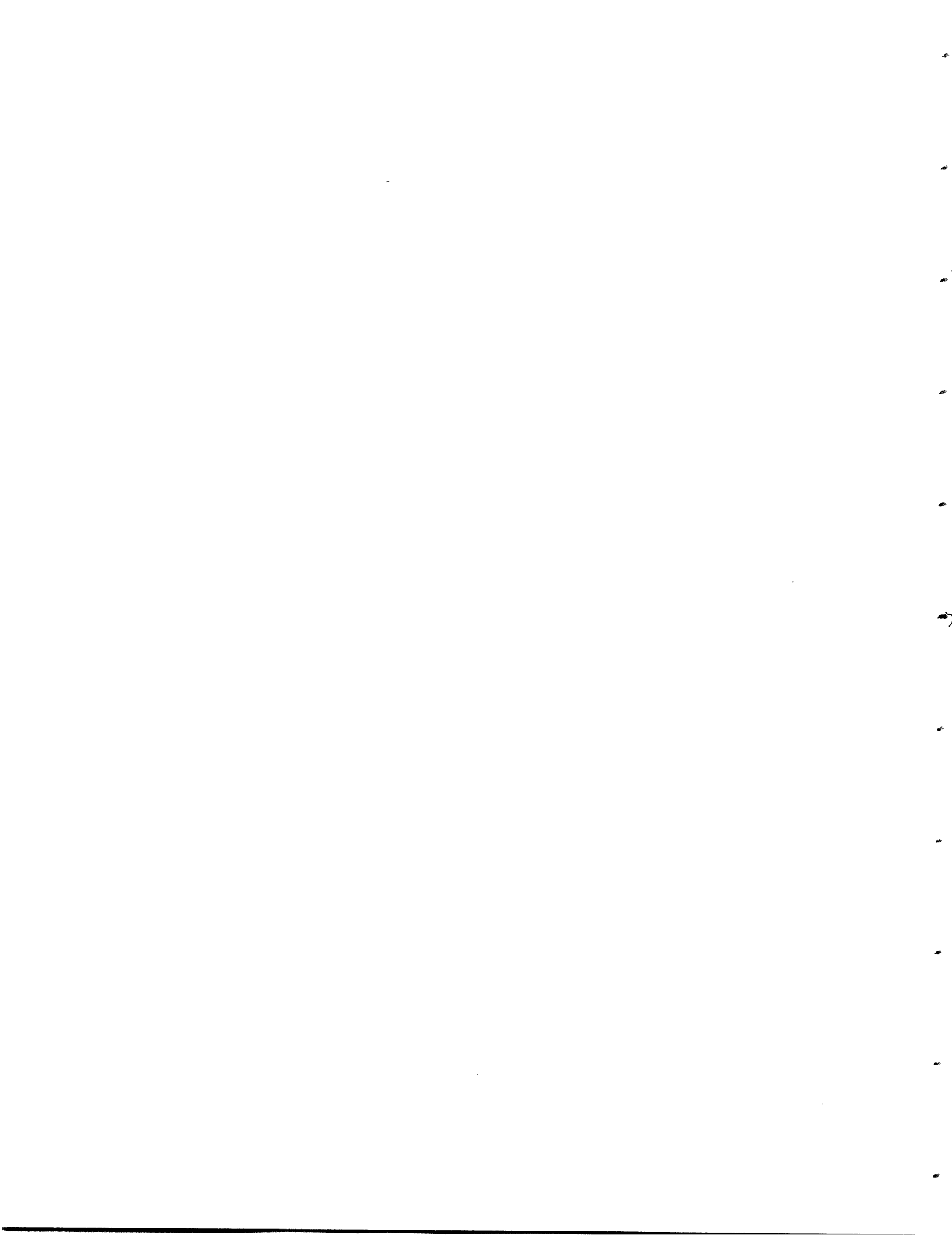


Figure I.6.2 Schematic of preliminary processing by data acquisition system

References

1. D.C. Stickler and P.A. Deift, "Inverse Problem for a Stratified Ocean and Bottom," *J. Acoust. Soc. Am.* 70, pp.1723-1727 (1981).
2. D.C. Stickler, Personal communication.
3. H.E. Moses and C.M. deRidder, *Properties of Dielectrics from Reflection Coefficients in One Dimension*, Lincoln Laboratory Technical Report no. 322, Lincoln, Massachusetts (July 11 1963).
4. G. N. Watson, *Theory of Bessel Functions 2nd Ed.*, Cambridge at the University Press, New York (1966).
5. R. Bracewell, *The Fourier Transform and Its Applications*, McGraw-Hill, New York (1965).
6. Papoulis, *Systems and Transforms with Applications in Optics*, McGraw-Hill, New York (1968).
7. G.V. Frisk, A.V. Oppenheim, and D. Martinez, "A Technique for Measuring the Plane-Wave Reflection Coefficient of the Ocean Bottom," *J. Acoustical Soc. Amer.* 68 (2), pp.602-612 (1980).
8. D.C. Stickler, "Negative Bottom Loss, Critical-Angle Shift, and the Interpretation of the Bottom Reflection Coefficient," *J. Acoust. Soc. Am.* 61, pp.707-710 (March 1977).
9. Brekhovskikh, *Waves in Layered Media*, Academic Press, New York (1960).
10. G.V. Frisk, J. Douth, and E. Hays, "Bottom Interaction of Low-Frequency Acoustic Signals at Small Grazing Angles in the Deep Ocean," *J. Acoustical Soc. Amer.* 69 (1) (1981).
11. R.B. Adler, L.J. Chu, and R.M. Fano, *Electromagnetic Energy Transmission and Radiation*, M.I.T. Press, Cambridge, Massachusetts (1973).
12. L.L. Beranek, *Acoustics*, McGraw-Hill Book Co., New York (1954).

13. K. Aki and P.G. Richards, *Quantitative Seismology Theory and Methods*, W.H. Freeman and Co., San Francisco (1980).
14. Sommerfeld, *Partial Differential Equations in Physics*, Academic Press, New York (1964).



CHAPTER II: THE HANKEL TRANSFORM

II.1) *Overview*

The relation of the Hankel transform to the two dimensional Fourier transform of a circularly symmetric function makes it as important a tool for problems cast in cylindrical coordinate systems as the Fourier transform for problems in cartesian systems. Applications can be found in such diverse fields as astronomy, electrodynamics, electrostatics, oceanography, physics, and seismology. Because it relates the pressure field associated with a point source in a horizontally stratified medium to the plane wave reflection coefficient, it forms the foundation of this thesis. In this chapter we explore the properties of the Hankel transform.

We begin by presenting the most common definitions of the Hankel transform in Section II.2. We show how the Hankel transform arises from the two dimensional Fourier transform of a circularly symmetric function in Section II.3. To relate the Hankel transform to the more familiar one dimensional Fourier transform, in Section II.4 we present its asymptotic form. In Section II.5 we complete our presentation of available properties with a summary of important results available in the literature.

The remainder of this chapter is devoted to results previously unavailable. We derive these results to provide the foundation for our work later in this thesis. Section II.6 examines windowing and the Hankel transform. We will later use the results derived in this section to determine the range over which pressure field data must be known in order to successfully estimate the plane wave reflection coefficient. We will also later use the approximate results presented in this section to determine the effect of varying source-height during data acquisition on the estimate of the plane wave reflection coefficient. Section II.7 studies the effect of sampling on the Hankel transform. Sampling issues arise both when data to be transformed is available only on a discrete set of points and when the Hankel transform is computed numerically. The results from this section will be used extensively in Chapter IV.

The addition of white Gaussian noise is often a reasonable model for the accumulated effect of many sources of corruption acting on a measured signal. Section II.8 discusses the degradation introduced into the Hankel transform of a signal by the addition of white Gaussian noise. It also shows that sampling such a function on a square root grid can improve the noise behavior of the associated Hankel transform.

We begin now by presenting common definitions of the Hankel transform.

II.2) Definition of the Hankel Transform

In the literature a number of different integral transforms are referred to as the Hankel transform.¹ Three of these are presented below:

$$1) HT_1 \left\{ f(r) \right\} \equiv \int_0^{\infty} f(r) J_0(\rho r) r dr \equiv F_1(\rho) \text{ Watson [1966]}$$

$$2) HT_2 \left\{ f(r) \right\} \equiv 2\pi \int_0^{\infty} f(r) J_0(2\pi \rho r) r dr \equiv F_2(\rho) \text{ Bracewell [1965]}$$

$$3) HT_3 \left\{ f(r) \right\} \equiv \int_0^{\infty} f(r) J_0(\rho r) \sqrt{\rho r} dr \equiv F_3(\rho) \text{ Bateman [1953]}$$

Definitions (1) and (2) are only superficially different since $F_2(\rho) = 2\pi F_1(2\pi\rho)$. Definition (3) is substantially different with

$$\frac{F_3(\rho)}{\sqrt{\rho}} = HT_1 \left\{ \frac{f(r)}{\sqrt{r}} \right\} \quad (4)$$

As we will see, under definition (3) the Hankel transform has properties very similar to the Fourier transform. We will use definition (1), never-the-less, because of its relationship to the two dimensional Fourier transform.

1) Sometimes these transforms are also referred to as the zero-order Hankel transform. We will not make that distinction in this thesis.

II.3) The Hankel Transform as a Two Dimensional Fourier Transform

If we use the definition of Watson

$$HT \left\{ f(r) \right\} \equiv \int_0^{\infty} f(r) J_0(\rho r) r dr \equiv F(\rho) \quad (1)$$

then the Hankel transform is simply related to the 2 dimensional Fourier transform of a circularly symmetric function. [1,2] To show this we write the 2 dimensional Fourier transform in cartesian coordinates:

$$F_C(k_x, k_y) \equiv \frac{1}{2\pi} \int_{-\infty}^{\infty} \int_{-\infty}^{\infty} f_C(x, y) e^{i(k_x x + k_y y)} dx dy \quad (2)$$

If $f_C(x, y)$ is circularly symmetric we can unambiguously define

$$f(r) \equiv f_C(x, y) \quad \text{where} \quad r \equiv \sqrt{x^2 + y^2} \quad (3)$$

Writing (2) in polar coordinates we have:

$$F_P(\rho, \phi) = \frac{1}{2\pi} \int_0^{\infty} \int_0^{2\pi} f(r) e^{i\rho r \cos(\theta - \phi)} r dr d\theta \quad (4)$$

A change of variables $\xi \equiv \theta - \phi$ shows that:

$$F_P(\rho, \phi) = \frac{1}{2\pi} \int_0^{\infty} \int_0^{2\pi} f(r) e^{i\rho r \cos \xi} r dr d\xi \quad (5)$$

so $F_P(\rho, \phi)$ is not a function of ϕ . We suppress ϕ , drop the subscript, P , and perform the ξ integration using

$$\frac{1}{2\pi} \int_0^{2\pi} e^{ix \cos \xi} d\xi \equiv J_0(x) \quad (6)$$

to see that any radial slice of the two dimension Fourier transform of the circularly symmetric function $f_C(x, y)$ is given by:

$$F(\rho) = \int_0^{\infty} f(r) J_0(\rho r) r dr \quad (7)$$

which is the Hankel transform.

By considering the Hankel transform as the two dimensional Fourier transform of a circularly symmetric function we can also relate the Hankel transform to the Abel transform. The

Abel transform frequently arises in optics, seismology and other fields. In this formulation it will appear as the projection of a two dimensional circularly symmetric function onto its axis.

We begin by noting that the slice of the two dimensional Fourier transform in polar form, $F_P(\rho, 0)$, equals the slice of the two dimensional Fourier transform in cartesian form, $F_C(\rho, 0)$, since both functions represent the same slice of the two dimensional Fourier transform. When $f_C(x, y)$ is circularly symmetric then its transform in polar form, $F_P(\rho, \phi)$, is circularly symmetric and equal to $F(\rho)$, its Hankel transform, as we have shown. For this case we can therefore write:

$$F(\rho) = F_P(\rho, 0) = F_C(\rho, 0) = \frac{1}{2\pi} \int_{-\infty}^{\infty} \int_{-\infty}^{\infty} f_C(x, y) e^{i\rho x} dx dy \quad (8)$$

If we perform the y integration first we have

$$F(\rho) = \frac{1}{2\pi} \int_{-\infty}^{\infty} \left[\int_{-\infty}^{\infty} f_C(x, y) dy \right] e^{i\rho x} dx \quad (9)$$

The integral in y generates the projection of $f_C(x, y)$ onto the x axis. We define this projection to be $p(x)$. If we use the circular symmetry of $f_C(x, y)$ we can rewrite this projection as:

$$p(x) = \int_{-\infty}^{\infty} f_C(x, y) dy = \int_{-\infty}^{\infty} f_C(\sqrt{x^2+y^2}, 0) dy = 2 \int_0^{\infty} f_C(\sqrt{x^2+y^2}, 0) dy \quad (10)$$

Or in the cylindrical coordinate system

$$p(x) = 2 \int_{|x|}^{\infty} \frac{f(r) r dr}{\sqrt{r^2-x^2}} \quad (11)$$

Equation (11) is the Abel transform of $f(r)$. The Abel transform can therefore be considered as the projection of a circularly symmetric $f_C(x, y)$ onto the x axis. Since the Hankel transform was shown to be the Fourier transform of the projection we see that

$$F(\rho) \equiv HT \left\{ f(r) \right\} = FT \left\{ A \left\{ f(r) \right\} \right\} \quad (12)$$

This relationship was presented by Bracewell. [3] Implementation of the Hankel transform through Equation (12) is equivalent to the projection-slice method proposed by Oppenheim,

Frisk, and Martinez. [4]

Equation (12) relates the Hankel transform and the one dimensional Fourier transform through the Abel transform. When we consider only large values of ρ , the transform variable, an approximate relationship between the Hankel transform and the one dimensional Fourier transform can be developed that does not involve the Abel transform. This can be done through the asymptotic form of the Hankel transform, which we present in the next section.

II.4) The Asymptotic Form

If the Hankel transform is not dominated for all values of ρ by the behavior of the kernel near the origin (as would be the case for $\delta(r)/r$ for example) then the asymptotic behavior of the transform can be studied by substituting in the asymptotic form for the Bessel function. If we use the asymptotic form for the Bessel function presented by Lipschitz [5, 6] ¹

$$\frac{\sqrt{\pi x}}{\sqrt{2}} J_0(x) = \cos(x - \frac{\pi}{4}) + \frac{1}{8x} \sin(x - \frac{\pi}{4}) - \frac{9}{128x^2} \left[\cos(x - \frac{\pi}{4}) - \theta \frac{2}{3x} \right] \quad x > 0 \quad (1)$$

where $|\theta| \leq 1$ and we keep only the leading terms in x , the Hankel transform becomes:

$$\sqrt{|\rho|} F(\rho) \approx \frac{\sqrt{2}}{\sqrt{\pi}} \int_0^{\infty} f(r) \cos(|\rho r| - \frac{\pi}{4}) \sqrt{r} dr \quad (2)$$

If we expand the cosine term Equation (2) becomes:

$$\sqrt{|\rho|} F(\rho) \approx \frac{1}{\sqrt{\pi}} \left[\int_0^{\infty} f(r) \cos(\rho r) \sqrt{r} dr + \operatorname{sgn}(\rho) \int_0^{\infty} f(r) \sin(\rho r) \sqrt{r} dr \right] \quad (3)$$

The integrals in Equation (3) are the Fourier cosine transform and the Fourier sine transform [8]. In some cases this form allows us to extend results available for these Fourier transforms to the Hankel transform. When the $\operatorname{sgn}(\rho)$ term can be ignored, for example, Equation (3) suggests that asymptotically $\sqrt{|\rho|} F(\rho)$ behaves much like the Fourier transform of $\sqrt{|r|} f(r)$. The $\operatorname{sgn}(\rho)$ term can not be ignored without further approximation when the values of the sine

1) A more recent reference in the form of an asymptotic series with the same leading term is [7]

and cosine transforms for negative ρ effect the positive part of the spectrum. Such is the case when these transforms are degraded by sampling or integration to a finite limit, for example. [9]

Had we used the definition of Bateman for the Hankel transform, Equation (3) would have appeared even more like a Fourier transform:

$$F_3(\rho) \approx \frac{1}{\sqrt{\pi}} \left[\int_0^{\infty} f(r) \cos(\rho r) dr + \text{sgn}(\rho) \int_0^{\infty} f(r) \sin(\rho r) dr \right] \quad (4)$$

Bateman's definition (Equation II.2.3) is more directly related to the Fourier transform than the definition of Watson (Equation II.2.2). Despite this, we use the definition of Watson because we wish to preserve the relationship between the Hankel transform and the 2-dimensional Fourier transform presented in Section II.3.

II.5) General Properties of the Hankel Transform

A number of properties for the Hankel transform are readily available in the literature. [10, 1, 6, 7] We present some of the more important of these here for completeness.¹

PROPERTY	$f(r)$	$F(\rho) = \int_0^{\infty} f(r) J_0(\rho r) r dr$
<i>self-inverse</i>	$F(\rho)$	$f(r)$
<i>linearity</i>	$a f_1(r) + f_2(r)$	$a F_1(\rho) + F_2(\rho)$
<i>scaling</i>	$f(ar)$	$\frac{1}{a^2} F\left(\frac{\rho}{a}\right)$
<i>derivative</i>	$\nabla^2 f(r)$	$-\rho^2 F(\rho)$
<i>power</i>	$\int_0^{\infty} f(r) g^*(r) r dr = \int_0^{\infty} F(\rho) G^*(\rho) \rho d\rho$	
<i>moment</i>	$F(\rho) = \sum_{n=0}^{\infty} \frac{(-1)^n m_{2n+1}}{(n!)^2 2^{2n}} \rho^{2n}$ with $m_n \equiv \int_0^{\infty} r^n f(r) dr$	

In the remainder of this chapter we develop properties of the Hankel transform not available in the literature but of considerable importance to the later developments in this thesis. We begin by determining the effect of on the Hankel transform of a function when it is multiplied by a range limited window.

II.6) Windowing and the Hankel Transform

a) An exact windowing expression

The definition of the Hankel transform has infinity as the upper limit of integration. In practice it is often impossible to carry out the integration to infinity. This may be because the function to be transformed is only known out to a finite range or because the integration must be

¹We will consider two functions to be equal if the result of convolving their difference with a band-limited function is always zero. This is equality in the sense of generalized functions.

performed numerically and only a finite number of calculations can be made. Following the convention used with the Fourier transform we will write the upper limit of integration as infinity but will make the function to be transformed zero beyond some finite upper limit by multiplying by a window of finite extent. [9] In this section we will explore the degradation introduced into the Hankel transform of a function by such windowing. The results of this section will also find application to the approximate evaluation of integrals of the form

$$\int_0^{\infty} f(r) J_0(\rho r) J_0(\xi r) r dr \quad (1)$$

which arise in this thesis in connection with source-height effects.

An exact but cumbersome expression for the effect of windowing can be derived from a result presented by Bracewell. [10] If we define:

$$\begin{aligned} P(\rho) &\equiv \int_0^{\infty} p(r) J_0(\rho r) r dr \\ W(\rho) &\equiv \int_0^{\infty} w(r) J_0(\rho r) r dr \end{aligned} \quad (2)$$

Then $P_w(\rho)$, the Hankel transform of the product of $p(r)$ and $w(r)$ is given by:

$$P_w(\rho) \equiv \int_0^{\infty} p(r) w(r) J_0(\rho r) r dr = \int_0^{\infty} \int_0^{2\pi} P(\xi) W(\sqrt{\rho^2 + \xi^2 - 2\rho\xi\cos\theta}) \xi d\theta d\xi \quad (3)$$

We can relate the Hankel transform of the windowed function, $P_w(\rho)$ to the Hankel transform of the unwindowed function, $P(\rho)$, by carrying out the theta integration in Equation (3) to obtain:

$$P_w(\rho) = \int_0^{\infty} P(\xi) H(\rho, \xi) d\xi \quad \text{with} \quad H(\rho, \xi) \equiv \xi \int_0^{2\pi} W(\sqrt{\rho^2 + \xi^2 - 2\rho\xi\cos\theta}) d\theta \quad (4)$$

If $H(\rho, \xi)$ had the form $\hat{H}(\rho - \xi)$, then Equation (4) would be a convolution, reminiscent of the windowing result for the Fourier transform. [9] By placing some restrictions of $w(r)$ we can derive an approximate expression for the effect of windowing that has the form of a convolution.

b) Approximation as a convolution

A simpler approximate expression describing the effect of windowing can be derived by using the asymptotic expression for the Hankel transform:

$$\begin{aligned} \sqrt{|\rho|}F(\rho) &\approx \frac{1}{\pi} \left[\int_0^{\infty} f(r) \cos(\rho r) \sqrt{r} dr + \operatorname{sgn}(\rho) \int_0^{\infty} f(r) \sin(\rho r) \sqrt{r} dr \right] \\ &\equiv \frac{1}{\pi} \left[G_e(\rho) + \operatorname{sgn}(\rho) G_o(\rho) \right] \end{aligned} \quad (1)$$

$G_e(\rho)$ and $G_o(\rho)$ are a Fourier cosine transform and Fourier sine transform respectively. [8] The cosine transform and the sin transform each have the property that the transform of a product is the convolution of the transforms. Using this, the effect of windowing in the asymptotic formulation of Equation (1):

$$\sqrt{|\rho|}F_w(\rho) \approx \frac{1}{\pi} \left[\int_0^{\infty} f(r)w(r) \cos(\rho r) \sqrt{r} dr + \operatorname{sgn}(\rho) \int_0^{\infty} f(r)w(r) \sin(\rho r) \sqrt{r} dr \right] \quad (2)$$

can be written as:

$$\sqrt{|\rho|}F_w(\rho) \approx G_e(\rho) * W_F(\rho) + \operatorname{sgn}(\rho) \left[G_o(\rho) * W_F(\rho) \right] \quad (3)$$

where we have defined:

$$W_F(\rho) \equiv \int_{-\infty}^{\infty} w(r) e^{i\rho r} dr \quad (4)$$

In general Equation (3) can not be rewritten as the convolution of $F(\rho)$ with a window term because of the $\operatorname{sgn}(\rho)$ term. However, if the Fourier transform of the window, $W_F(\rho)$, is effectively confined to a narrow band around $\rho = 0$, then for ρ larger than this band (B_w):

$$\rho > B_w \quad G_e(\rho) * W_F(\rho) + \operatorname{sgn}(\rho) \left[G_o(\rho) * W_F(\rho) \right] \approx G_e(\rho) * W_F(\rho) + \left[\operatorname{sgn}(\rho) G_o(\rho) \right] * W_F(\rho) \quad (5)$$

Combining Equations (2), (3), and (5) we have:

$$\sqrt{|\rho|}F_w(\rho) \approx \left[\sqrt{|\rho|}F(\rho) \right] * W_F(\rho) \quad (6)$$

which is our asymptotic result.

If $W_F(\rho)$ is not negligible beyond some band, B_w , then the effect of windowing on the

Hankel transform can not be put in this simple form. For such cases the exact result of Equation (II.6a.4) must be used.

c) *Resolution and leakage*

Given Equation (II.6b.6) we can address the practical issues associated with windowing. As is frequently done for the Fourier transform, we divide the issues associated with windowing into two general classes. The first we call resolution and refers to the local smearing affected by the main lobe of the window. The second we call leakage and refers to the contribution of the side lobes. [9, 11]

We begin by expanding Equation (I.6b.6) to write:

$$\rho > 0 \quad \sqrt{\rho} F_w(\rho) \approx \int_0^{\infty} \sqrt{\xi} F(\xi) W_F(\rho - \xi) d\xi \quad \text{with} \quad W_F(\rho) \equiv \int_{-\infty}^{\infty} w(r) e^{i\rho r} dr \quad (1)$$

When ρ is sufficiently large (ρ greater than some ρ_0) then $\sqrt{\xi}$ can be considered constant over the main lobe of $W_F(\rho - \xi)$. For these ρ , Equation (1) can be written approximately as

$$\rho > \rho_0 \quad \sqrt{\rho} F_w(\rho) \approx \sqrt{\rho} \int_0^{\infty} F(\xi) W_F(\rho - \xi) d\xi \quad (2)$$

so that

$$F_w(\rho) \approx \int_0^{\infty} F(\xi) W_F(\rho - \xi) d\xi \quad (3)$$

Under this condition the issues of resolution for the Hankel transform are the same as those for the Fourier transform. If we desire to resolve events in the Hankel transform on the order of δ then the lobe of our window must be less than δ . Discussions about a variety of windows are available in the literature. [9, 11] For the Hanning class of windows, the main lobe width is $\frac{1}{B}$, where B is the length of the window. Our requirement for resolution of events on the order δ becomes:

$$B > \frac{1}{\delta} \quad (4)$$

Leakage is the phenomena we associate with the side lobes. For the purpose of this analysis

we consider the lobe width to be sufficiently small that it can be approximated by an impulse so that we ignore the smearing effects that we have assigned to resolution. We approximate $W_F(\rho)$ as a weighted superposition of impulses:

$$W_F(\rho) \approx \sum_i a_i \delta(\rho - T_i) \quad (5)$$

The a_i indicate the rate at which the side lobes approach zero. The convolution of Equation (2) becomes:

$$\begin{aligned} \sqrt{\rho} F(\rho) &\approx \int_{-\infty}^{\infty} \sqrt{\xi} F(\xi) \sum_i a_i \delta(\rho - \xi - T_i) d\xi \\ &\sum_i a_i \sqrt{\rho - T_i} F(\rho - T_i) \end{aligned} \quad (6)$$

When we are concerned about the leakage due to a singularity, we must consider the weighting $a_i \sqrt{\rho - T_i}$ which indicates the amount of leakage of an event at T_i of strength 1 would have at ρ . Here the Hankel transform differs from the Fourier transform because of the $\sqrt{\rho - T_i}$ term which slows the decay rate. Consequently for equivalent leakage, the lobes of the window must fall by a factor of $\frac{1}{\sqrt{\rho}}$ faster than that required for equivalent performance in the Fourier transform. For this reason we have concentrated on the Hanning window rather than the Hamming in many of our examples.

By weighting the side lobe heights by a factor of $\sqrt{\rho}$, optimal windows could be designed for Hankel transforms in a manner analogous to the Fourier transform.

d) Examples

In this section we present two examples of windowing and the Hankel transform. To each we apply a rectangular window:

$$w(r) = \begin{cases} 1 & 0 < r < 4000 \\ 0 & 4000 < r \end{cases} \quad (1)$$

which has a length similar to the range over which data is available in the experiment described in Section (I.6). The first function we transform is $\frac{e^{ik\sqrt{r^2+2^2}}}{\sqrt{r^2+2^2}}$ for which the true Hankel

transform is given by $\frac{i}{\sqrt{k^2-\rho^2}}e^{i\sqrt{k^2-\rho^2}(2)}$. Figure II.6d.1 presents the log-magnitude of

$\frac{e^{ik\sqrt{r^2+(2)^2}}}{\sqrt{r^2+(2)^2}}$ $0 < r < 4000$. As can be seen in the figure, this function decays almost four

orders of magnitude over the window length. Figures II.6d.2a and II.6d.2b present the magnitude and phase of its computed transform. Essentially no degradation due to aliasing is apparent

in the computed transform. Figure II.6.3 presents the magnitude of $\frac{e^{ik\sqrt{r^2+(133)^2}}}{\sqrt{r^2+(133)^2}}$. Over the

window length this function has decayed roughly two orders of magnitude. Figures II.6d.4a and II.6d.4b present the magnitude and phase of its Hankel transform. The correct transform is

given by: $\frac{i}{\sqrt{k^2-\rho^2}}e^{i\sqrt{k^2-\rho^2}(133)}$. The magnitude of the correct transform should look like

$\left| \frac{e^{ik\sqrt{r^2+(2)^2}}}{\sqrt{k^2-\rho^2}} \right|$ for $0 \leq \rho \leq k$. Instead the magnitude of the transform shown in Figure II.6d.4a

shows considerably more degradation than that of Figure II.6d.2a. This is due to the fact that this is the transform of a function which has proportionally more energy outside the window.

One is tempted to assume the ripples apparent in Figure II.6d.4a are due to leakage of the

$\frac{1}{\sqrt{k^2-\rho^2}}$ singularity. This is not the source of degradation, however as may be seen by noting

that this same singularity is present in the first transform of Figure II.6d.2a for which no such rippling is apparent. The rippling is due to the smearing of the transform in Figure II.6d.3a over

its rapidly oscillating phase term $e^{i\sqrt{k^2-\rho^2}(133)}$ which is not apparent in the magnitude plot.

When the true phase varies rapidly over the width of the main lobe of the window the effect of smoothing can actually be to introduce rippling into the computed magnitude.

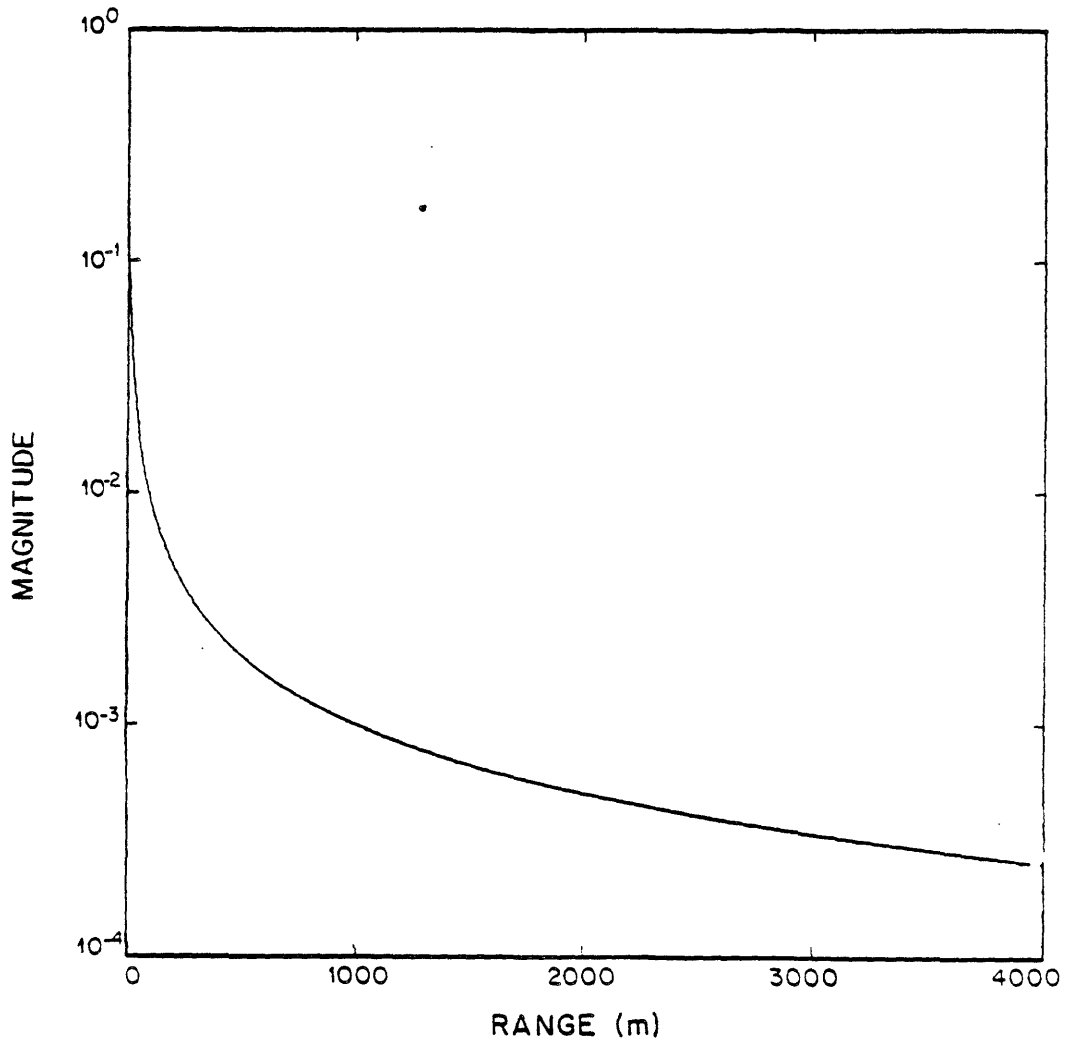


Figure II.6d.1 Magnitude of $\frac{e^{ik\sqrt{r^2+(2)^2}}}{\sqrt{r^2+(2)^2}}$

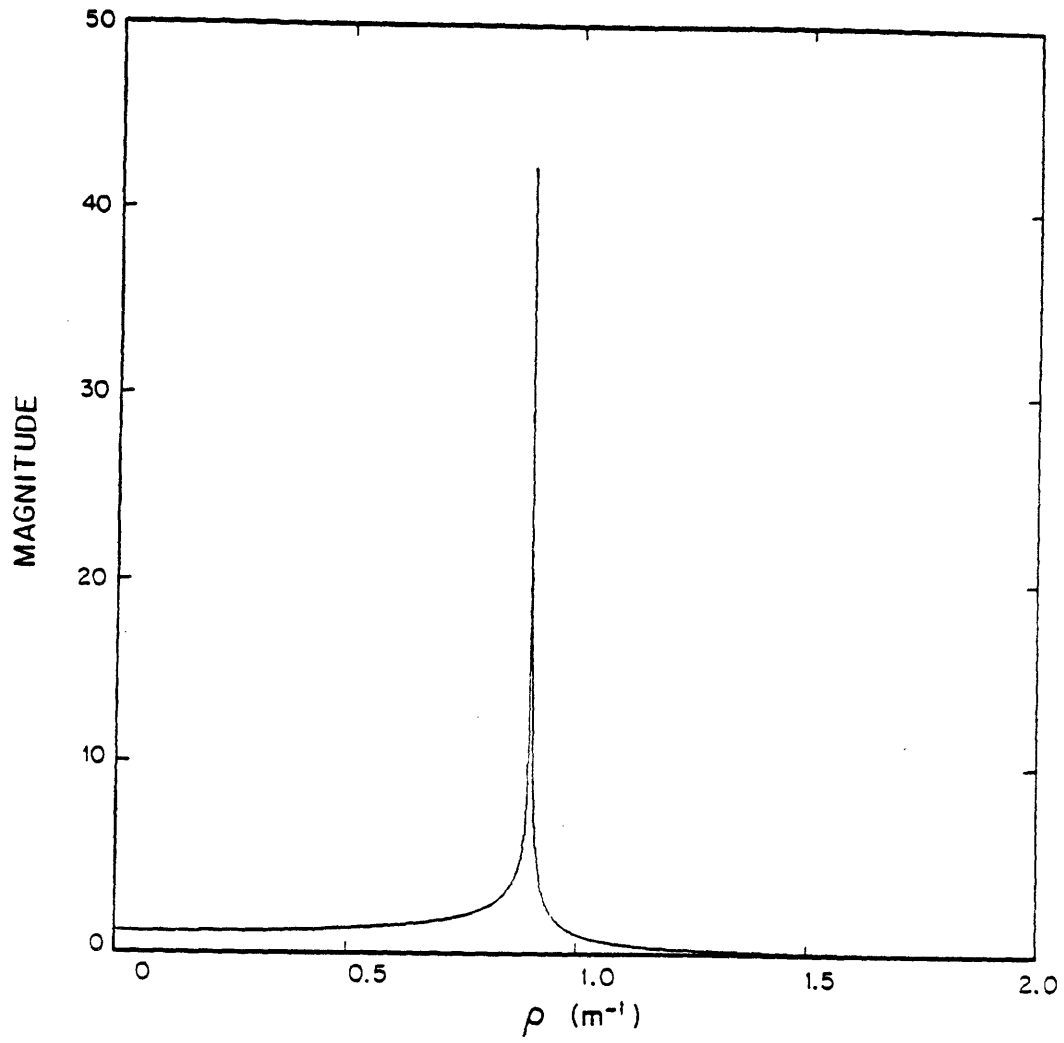


Figure II.6d.2a Magnitude of numerically generated Hankel transform of function shown in Figure II.6d.1

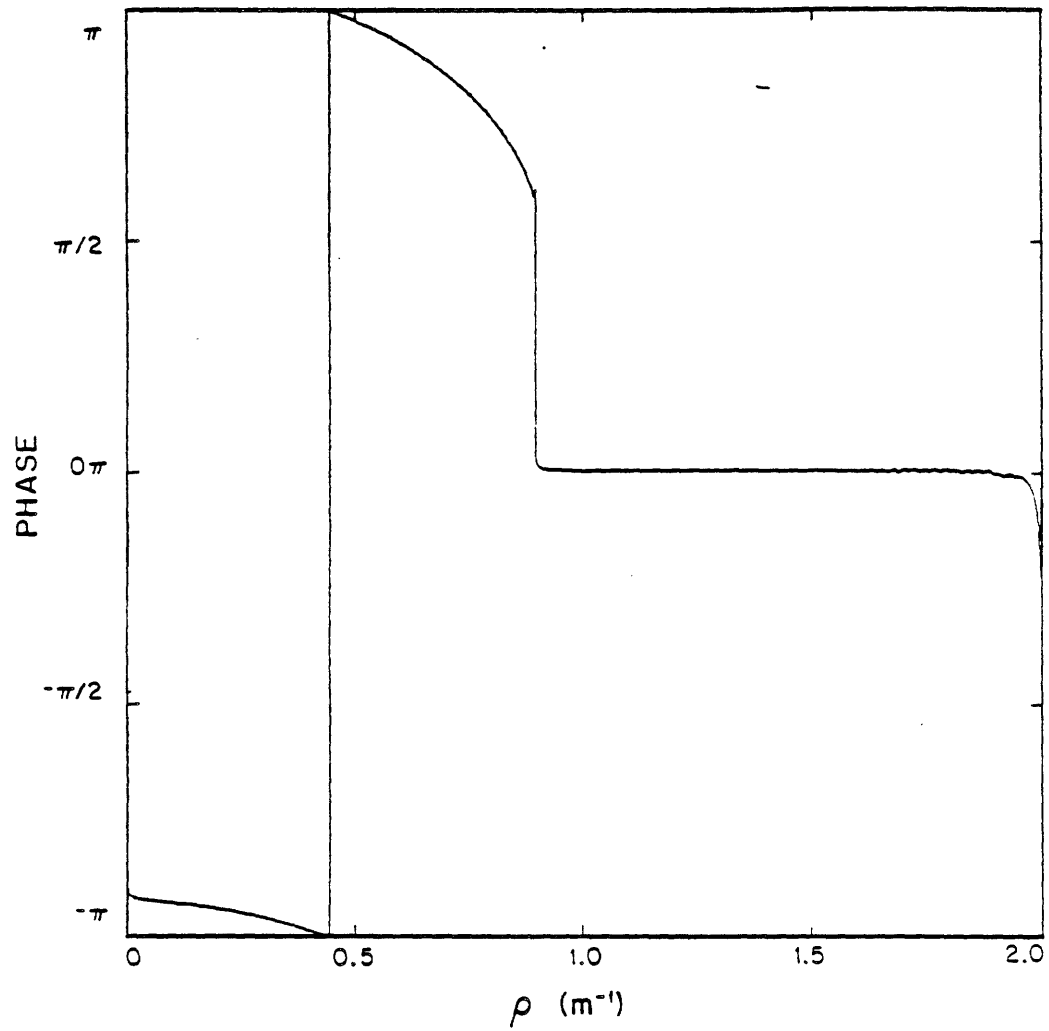


Figure II.6d.2b Phase of numerically generated Hankel transform of function shown in Figure II.6d.1

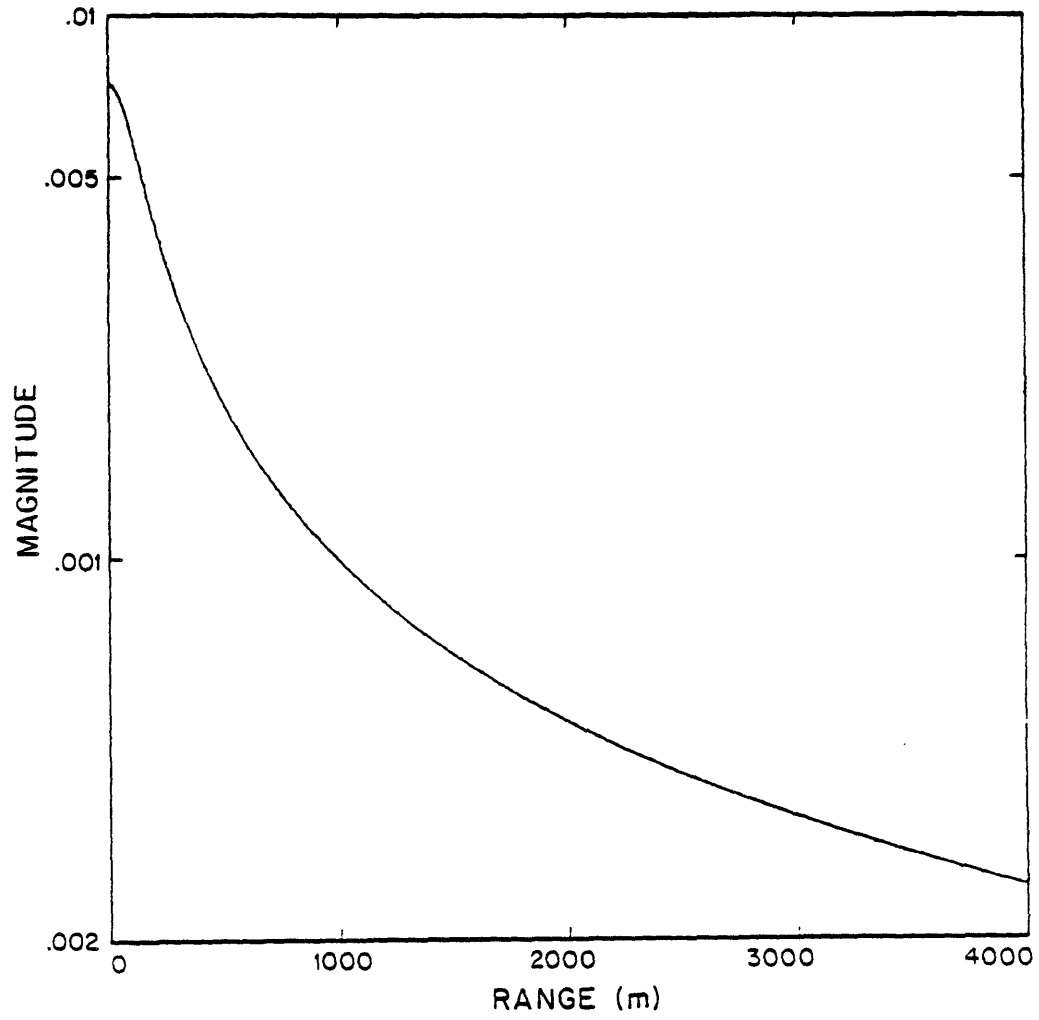


Figure II.6.3 Magnitude of $\frac{e^{ik\sqrt{r^2+(133)^2}}}{\sqrt{r^2+(133)^2}}$

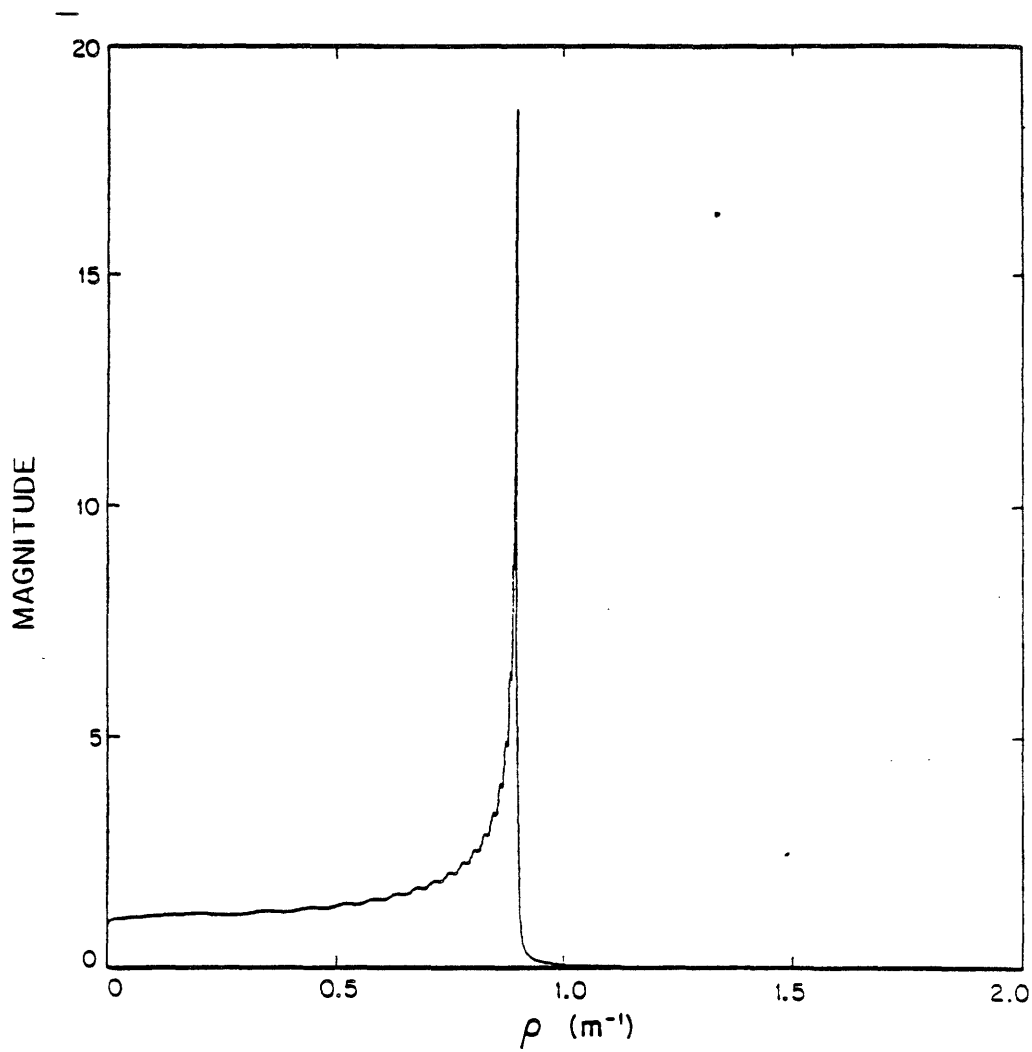


Figure II.6.4a Magnitude of numerically generated Hankel transform of function shown in Figure II.6.3

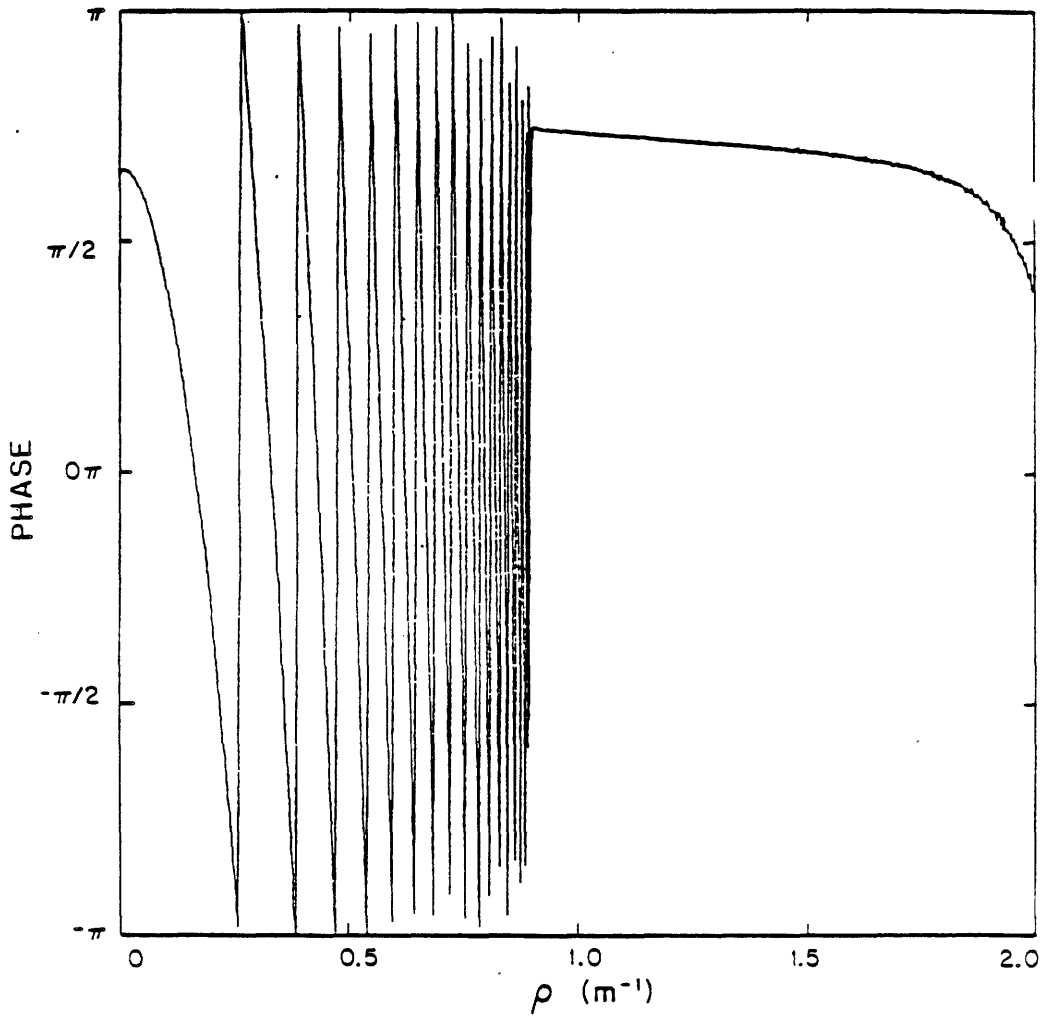


Figure II.6.4b Phase of numerically generated Hankel transform of function shown in Figure II.6.3

II.7) Sampling and Aliasing

It is often necessary to approximate the integral in the Hankel transform by a sum. This approximation may be necessary because the function to be transformed is known only on a discrete set of points or because the integral must be evaluated numerically. The resulting sum will be a degraded version of the true Hankel transform. We will adopt the terminology of Fourier transforms and refer to the replacement of the integral by a sum as sampling and the resulting degradation as aliasing. In this section we examine the form that aliasing takes for the Hankel transform.

The discrete sum approximation that we will concentrate on is the Fourier-Bessel series. We will derive an expression that relates the output of the Fourier-Bessel series to the true Hankel transform. Because the Fourier-Bessel series uses samples on a set of points that is approximately evenly spaced, the results we derive will be approximately correct for any evenly spaced sampling scheme.

We begin with the formulation of the Fourier-Bessel series [7, 6] which states:¹

$$0 < \rho < 1 \quad F(\rho) = 2 \sum_{n=1}^{\infty} \int_0^1 \frac{F(\xi) J_0(\lambda_n \xi) \xi d\xi}{J_1^2(\lambda_n)} J_0(\lambda_n \rho) \quad (1)$$

Where λ_n $n=1,2,3, \dots$ are the ordered zeros of $J_0(x)$.

If $F(\rho) = 0$ for $\rho > 1$ then the integral in the expression above is just the Hankel transform of $F(\rho)$ evaluated at λ_n , $f(\lambda_n)$ so that the Hankel transform, $F(\rho)$, can be expressed exactly as a sum:

$$0 < \rho < 1 \quad F(\rho) = 2 \sum_{n=1}^{\infty} \frac{f(\lambda_n)}{J_1^2(\lambda_n)} J_0(\lambda_n \rho) \quad \text{when } F(\rho) = 0 \text{ for } \rho > 1 \quad (2)$$

When $F(\rho)$ is not truly bandlimited to $\rho < 1$ and/or the sum is not carried out to infinity, Equation (2) is only an approximation to the Hankel transform. The study of the effect of finite N on

1) We will call two functions equal if the Fourier transform of their difference has no energy at any finite frequency. For this reason we need not single out the values of $F(\rho)$ in Equation (1) at points of discontinuity.

the approximation is the study of windowing, covered in the previous section. Here we consider only the degradation that occurs because the infinite series is used in place of the integral. Finally, we note that it is because the zeros of $J_0(x)$, λ_n , rapidly approach $n\pi + \frac{1}{4}$ that the sampling above is approximately evenly spaced.

To determine the effect of approximating the Hankel transform:

$$F(\rho) = \int_0^{\infty} f(r) J_0(\rho r) r dr \quad (3)$$

by the Fourier-Bessel series:

$$0 < \rho < 1 \quad \hat{F}(\rho) = \sum_{n=1}^N \frac{2}{J_1^2(\lambda_n)} f(\lambda_n) J_0(\lambda_n \rho) \quad (4)$$

we express $\hat{F}(\rho)$ in terms of the correct transform, $F(\rho)$, by inverting (3) to write $f(r)$ in terms of $F(\rho)$. We substitute this into Equation (4) to yield:

$$0 < \rho < 1 \quad \hat{F}(\rho) = \sum_{n=1}^N \frac{2}{J_1^2(\lambda_n)} \left[\int_0^{\infty} F(\xi) J_0(\lambda_n \xi) \xi d\xi \right] J_0(\lambda_n \rho) \quad (5)$$

Interchanging the order of integration and summation we have

$$\hat{F}(\rho) = \int_0^{\infty} F(\xi) T_N(\rho, \xi) \xi d\xi \quad (6)$$

Where, following the notation of Watson (page 582) [7] we define:

$$T_N(\rho, \xi) \equiv 2 \sum_{n=1}^N \left[\frac{J_0(\lambda_n \xi) J_0(\lambda_n \rho)}{J_1^2(\lambda_n)} \right] \quad (7)$$

The study of aliasing for the Fourier-Bessel series is the study of $T_N(\rho, \xi)$. We can obtain an expression for $T_N(\rho, \xi)$ by using an asymptotic result presented by Schlafli:^{1,2} [12]

$$T_N(\rho, \xi) \sim \frac{1}{2\sqrt{\rho\xi}} \left[\frac{\sin A_N(\rho-\xi)}{\sin \frac{\pi}{2}(\rho-\xi)} - \frac{\sin A_N(2-\rho-\xi)}{\sin \frac{\pi}{2}(2-\rho-\xi)} \right] \text{ where } A_N = (N + \frac{1}{4})\pi \quad (8)$$

1) This differs from Watson's presentation of Schlafli's result.

2) Schlafli does not restrict the region of validity of his result. Watson, however, states that Schlafli's result proceeds from a formula which is strictly valid only for $0 < \rho + \xi < 2$ and $\rho \neq \xi$. We will later plot $T_{128}(\rho, \xi)$ to show that the results of this analysis appear valid inside the region $0 < \rho - \xi \leq 2$ and approximately valid outside that region.

As $N \rightarrow \infty$ $T_N(\rho, \xi)$ approaches a weighted sequence of impulses. We determine that sequence here.

We begin our analysis of Equation (8) by first considering the expression:

$$\frac{\sin A_N x}{\sin \frac{\pi x}{2}} = \frac{\sin \left[N \pi x + \frac{\pi x}{4} \right]}{\sin \frac{\pi x}{2}} \quad (9)$$

Which equals

$$\frac{\sin N \pi x}{\sin \frac{\pi x}{2}} \cos \frac{\pi x}{4} + \frac{\cos N \pi x}{\sin \frac{\pi x}{2}} \sin \frac{\pi x}{4} \quad (10)$$

In Appendix I we show that as $N \rightarrow \infty$ the first term in (10) approaches the limit:

$$\sum_k (-1)^k \delta\left(\frac{x}{2} - 2k\right) \quad (11)$$

In Appendix I we also show that the second term in Equation (10) approaches 0. The limit of Equation (9) is therefore given by:

$$\lim_{N \rightarrow \infty} \frac{\sin A_N x}{\sin \frac{\pi x}{2}} = \sum_k (-1)^k \delta\left(\frac{x}{2} - 2k\right) \quad (12)$$

Using Equation (12) the first term in Equation (8) can now be seen to approach the limit:

$$\lim_{N \rightarrow \infty} \frac{\sin A_N (\rho - \xi)}{\sin \frac{\pi(\rho - \xi)}{2}} = 2 \sum_k (-1)^k \delta(\rho - \xi - 4k) \quad (13)$$

The second term in Equation (8) can be put in the form of Equation (9) by defining $y \equiv 2 - \rho - \xi$:

$$\frac{\sin A_N (2 - \rho - \xi)}{\sin \frac{\pi(2 - \rho - \xi)}{2}} = \frac{\sin A_N y}{\sin \frac{\pi y}{2}} \quad (14)$$

Combining Equations (13) and (14) we have:

$$\lim_{N \rightarrow \infty} \frac{\sin A_N (2 - \rho - \xi)}{\sin \frac{\pi(2 - \rho - \xi)}{2}} = 2 \sum_k (-1)^k \delta(2 - \rho - \xi - 4k) \quad (15)$$

We can determine $T_{\infty}(\rho, \xi)$ by combining (13) and (15):¹

$$\lim_{N \rightarrow \infty} T_N(\rho, \xi) = \frac{1}{\sqrt{\rho\xi}} \sum_k (-1)^k \left[\delta(\rho - \xi - 4k) - \delta(2 - \rho - \xi - 4k) \right] \quad (16)$$

If our transform is not severely aliased so that $F(\rho)$ is negligible for $\rho > 2$ then substituting Equation (16) into Equation (6) shows that:

$$0 < \rho < 1 \quad \hat{F}(\rho) \approx \int_0^2 F(\xi) \frac{1}{\sqrt{\rho\xi}} \left[\delta(\rho - \xi) - \delta(2 - \rho - \xi) \right] \xi d\xi \quad (17)$$

which equals for $0 < \rho < 1$:²

$$\hat{F}(\rho) = F(\rho) - \frac{\sqrt{2-\rho}}{\sqrt{\rho}} F(2-\rho) \quad (18)$$

We observe that the aliasing result most directly relates $\sqrt{\rho}\hat{F}(\rho)$ to $\sqrt{\rho}F(\rho)$.

An example of aliasing is presented in Figure II.7.1 where we see $4\sqrt{\rho}$ times the Hankel transform of e^{-8r^2} generated with the Fourier-Bessel series. The figure displays the aliasing terms generated by the impulses in Equation (16). In the region $0 < \rho < 2$ the figure matches the result indicated in Equation (17) very well. In the region $0 < \rho < 4$ the figure does not correspond exactly to what would be determined by substitution Equation (16) into Equation (6) indicating the limited validity of Schlafli's result.

Figure II.7.2 shows a plot of $2\sqrt{\rho\xi}T_{128}(\rho, \xi)$ $0 < \rho < 10$ $0 < \xi < 10$. This picture supports the accuracy of Equation (16) for $T_{\infty}(\rho, \xi)$ for $0 < \rho + \xi \leq 2$ and suggests that Equation (16) is at least approximately correct over the range of ρ and ξ shown in the figure.

We conclude this section with a final example of aliasing for the Hankel transform that will play an important role in the generation of synthetic data. Figure II.7.3 shows the function

$$f(r) = \frac{1}{r^2 - r_0^2} \quad \text{Im}(r_0) > 0 \quad (19)$$

corresponding to two poles, one at $r = r_0$ and the other at $r = -r_0$. This function has the known Hankel transform: [8]

1) Over the region of validity for Schlafli's result.

2) We have included the point $\rho + \xi = 2$, which is not strictly within the interval specified by Watson.

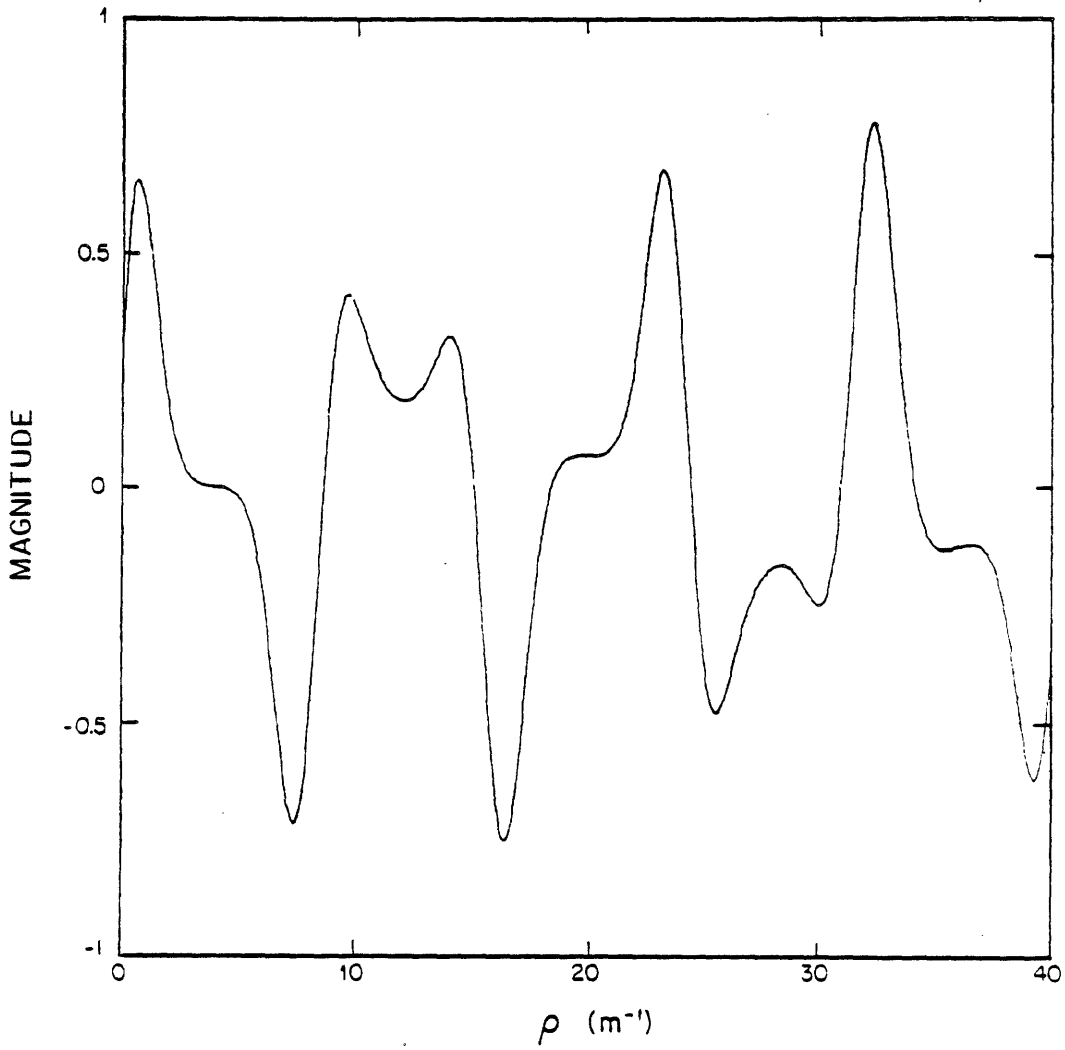


Figure II.7.1 $4\sqrt{\rho}HT\{e^{-3r^2}\}$ generated numerically

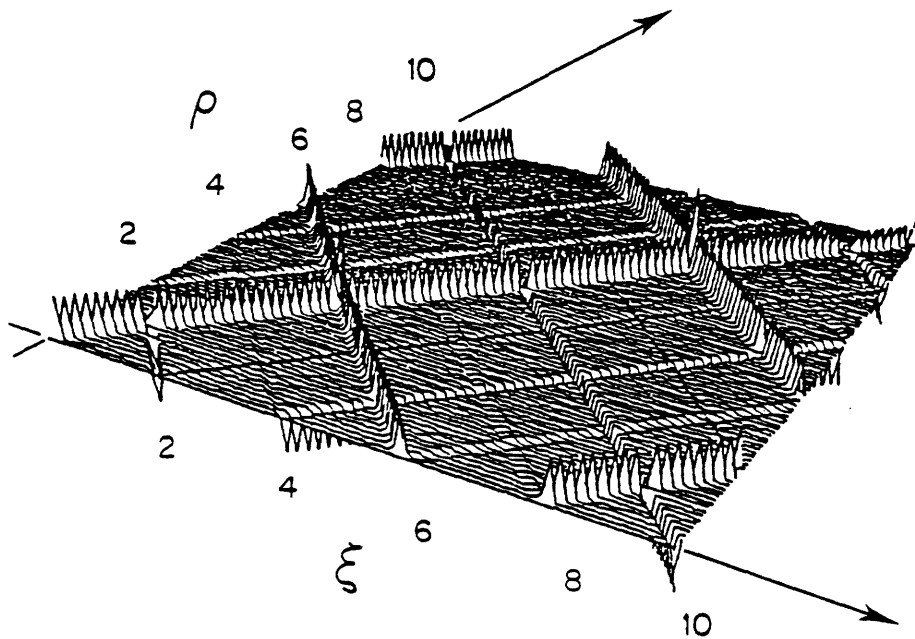


Figure H.7.2 $2\sqrt{\rho\xi}T_{128}(\rho,\xi)$

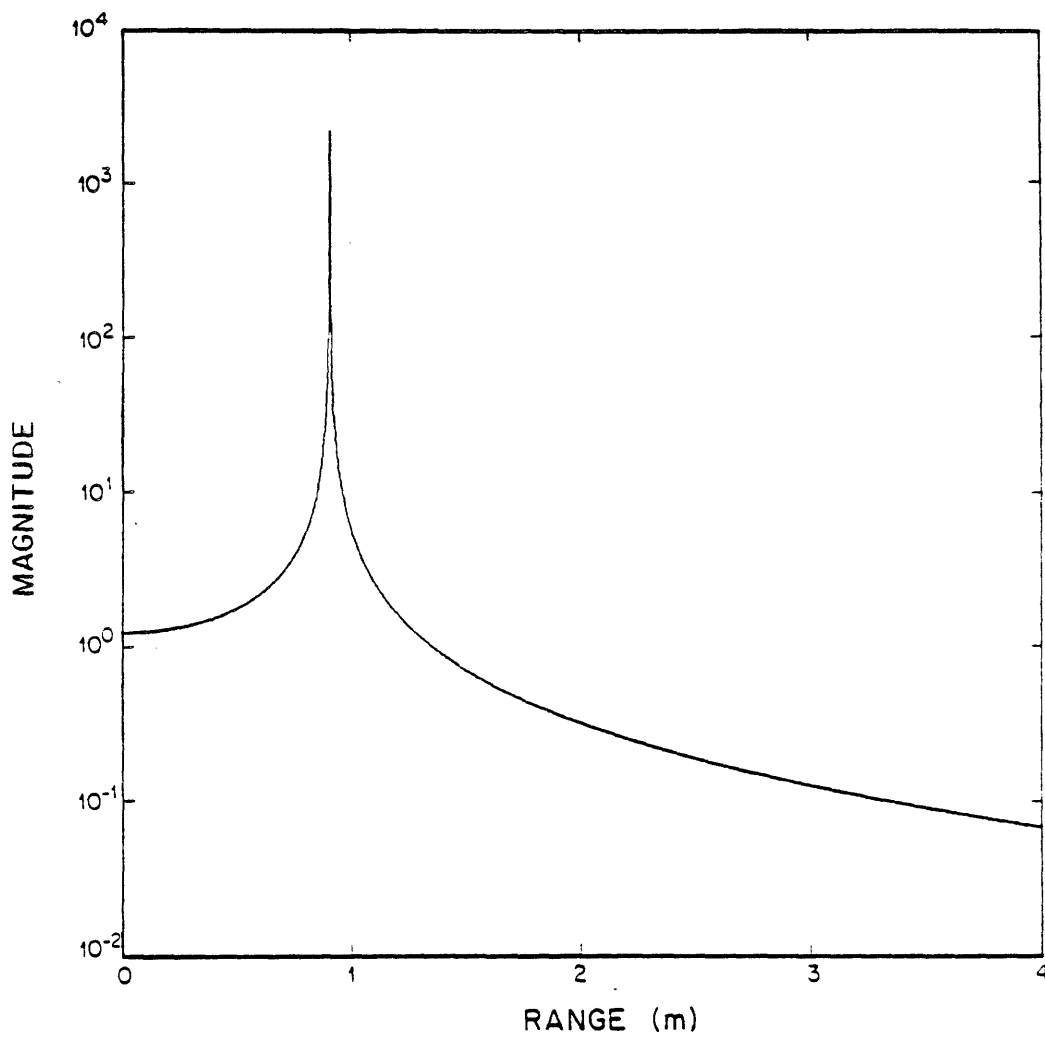


Figure II.7.3 The log magnitude of the function $\frac{1}{r^2 - r_0^2}$

$$F(\rho) = -\frac{\pi i}{2} H_0^{(1)}(r_0 \rho) \quad (20)$$

Asymptotically $H_0^{(1)}(r_0 \rho) \approx \frac{\sqrt{2}}{\sqrt{\pi r_0 \rho}} e^{-\frac{\pi i}{4}} e^{ir_0 \rho}$ so that its magnitude should appear $\approx \frac{\sqrt{2}}{\sqrt{\pi r_0 \rho}}$. Consequently the magnitude of $F(\rho)$ should appear smooth and decay as $\frac{1}{\sqrt{\rho}}$. In

Figure II.7.4 we see the numerically computed transform using the samples $f \left[\frac{\lambda_n}{2048} \right]$. Rapid oscillations are apparent which are not present in the magnitude of the correct transform. The source of these oscillations is aliasing, which can be seen by using Equation (18) to approximate the numerically computed transform:

$$\hat{F}(\rho) \approx \frac{\sqrt{2}}{\sqrt{\pi r_0 \rho}} e^{-\frac{i\pi}{4}} e^{ir_0 \rho} - \frac{\sqrt{4096-\rho}}{\sqrt{\rho}} \frac{\sqrt{2}}{\sqrt{\pi r_0 (4096-\rho)}} e^{-\frac{i\pi}{4}} e^{ir_0 (4096-\rho)} \quad (21)$$

which equals

$$\hat{F}(\rho) \approx \frac{1}{\sqrt{\rho}} \frac{\sqrt{2}}{\sqrt{\pi r_0}} e^{-\frac{i\pi}{4}} \left[e^{ir_0 \rho} - A e^{-ir_0 \rho} \right] \quad (22)$$

with $A \equiv e^{(4096)ir_0}$. This can be rewritten as:

$$\hat{F}(\rho) \approx \frac{1}{\sqrt{\rho}} \frac{\sqrt{2}}{\sqrt{\pi r_0}} e^{-\frac{i\pi}{4}} \left[(1-A) e^{ir_0 \rho} + 2iA \sin(r_0 \rho) \right] \quad (23)$$

where the beating caused by the aliasing is apparent in the $\sin(r_0 \rho)$ term. The aliased output displays the form of the $\frac{1}{\sqrt{\rho}}$ decay term times an extremely degraded estimate of $\sqrt{\rho} F(\rho)$.

When the transform decays only at a rate of $\frac{1}{\sqrt{\rho}}$, this example shows that severe degradation due to aliasing can be expected.

II.8) The Effect of Additive White Gaussian Noise on the Hankel Transform

a) Statement of the Effect of Additive White Gaussian Noise on the Hankel Transform

In practice it is seldom possible to know exactly the function whose transform we desire. Frequently it is possible to model the uncertainty about the input function by assuming that the

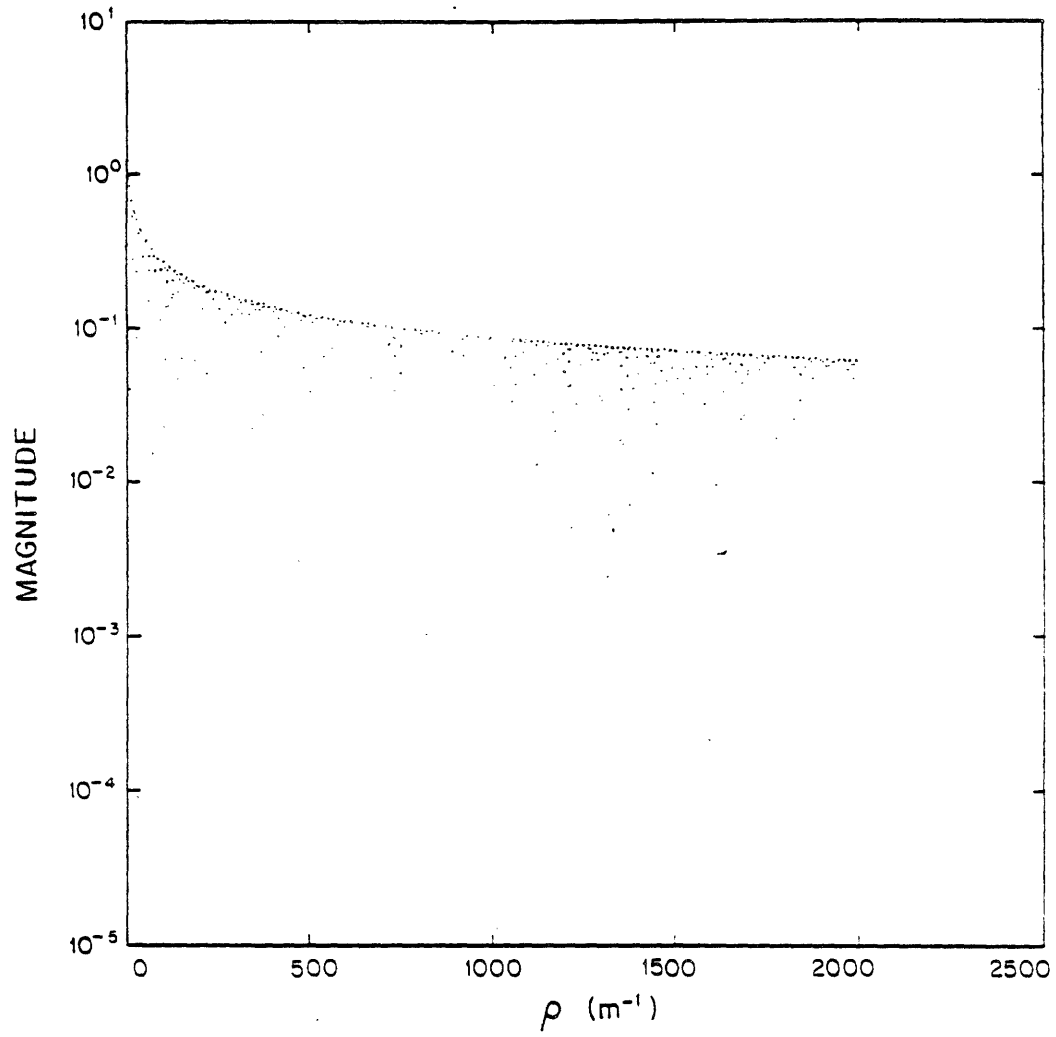


Figure II.7.4 The log magnitude of the numerically computed Hankel transform of the function shown in Figure II.7.3

errors associated with each sample are random and uncorrelated from point to point. Since the combined effect of many random factors can often be modeled with a Gaussian distribution (by invoking the central limit theorem [13]) the assumption is often added that the distribution of error around each point is Gaussian. This model of the uncertainty corresponds to additive white (the uncorrelated assumption) Gaussian noise. We assume the mean of the noise process is zero so that the expectation of the noisy input signal is the true input. If we further assume that the variance of the noise process is not a function of the input sample number then this Gaussian noise process is stationary.

In this section we explore the effect of such uncertainty on the Hankel transform of the input function. Since the Hankel transform is a linear operator and the noise process has zero mean, the effect of the noise will be to introduce a variance in the output of the Hankel transform proportional to the noise power but the expected output will not be corrupted. [14] In this section we first show that unlike the Fourier transform the variance of the Hankel transform of stationary white Gaussian noise is not stationary, but instead concentrates power near the origin. This result is important because frequently the Hankel transform is used in place of the two dimensional Fourier transform in problems with an underlying circular symmetry. Because of this property, a slice of the the two dimensional Fourier transform of noisy measurements made over a two dimensional grid of a circularly symmetric field will differ from the Hankel transform of a slice of that field.

In Section (b) we will show that if $f(\sqrt{r})$ is a stationary white Gaussian noise process then $F(\sqrt{\rho})$ will also be stationary white Gaussian noise. This result implies that if the input function is sampled on a \sqrt{r} grid and each sample is independently corrupted by (zero mean) Gaussian noise that does not depend on the sample number, then samples of the Hankel transform on a $\sqrt{\rho}$ grid will be independently corrupted by Gaussian noise and the amount of corruption will not depend on the value of ρ . On these grids each sample represents the same area of the underlying two dimensional circularly symmetric function and the noise properties of the Hankel

transform are equivalent to the noise properties of the underlying two dimensional Fourier transform.

To show that the Hankel transform concentrates noise power near the origin we first write:

$$\hat{F}_B(\rho) = \int_0^B [f(r) + n(r)] J_0(\rho r) r dr \quad (1)$$

Where we have introduced the limit of integration, B , to insure convergence. $n(r)$ is stationary white Gaussian noise with variance N_0 . The variance of \hat{F}_B is given by

$$\begin{aligned} \text{var} [\hat{F}_B(\rho)] &= \\ &= E [|\hat{F}_B(\rho) - E(\hat{F}_B(\rho))|^2] \\ &= E \left[\left| \int_0^B n(r) J_0(\rho r) r dr \right|^2 \right] \\ &= \int_0^B \int_0^B E [n(\alpha) n(\beta)] J_0(\rho \alpha) J_0(\rho \beta) \alpha \beta d\alpha d\beta \\ &= \int_0^B \int_0^B N_0 \delta(\alpha - \beta) J_0(\rho \alpha) J_0(\rho \beta) \alpha \beta d\alpha d\beta \\ &= N_0 \int_0^B J_0^2(\rho \alpha) \alpha^2 d\alpha \end{aligned} \quad (2)$$

For $\rho = 0$ Equation (2) above shows that

$$\text{VAR} [\hat{F}_B(0)] = N_0 \int_0^B \alpha^2 d\alpha = \frac{N_0 B^3}{3} \quad (3)$$

When $\rho \neq 0$

$$\text{VAR} [\hat{F}_B(\rho)] = N_0 \int_0^B J_0^2(\rho \alpha) \alpha^2 d\alpha = \frac{N_0}{\rho^3} \int_0^{\rho B} \xi^2 J_0^2(\xi) d\xi \quad (4)$$

In units of normalized frequency $\nu = \rho/B$

$$\text{VAR} [\hat{F}_B(\rho)] = N_0 \int_0^B J_0^2(\rho \alpha) \alpha^2 d\alpha = \frac{N_0}{\nu B^3} \int_0^\nu \xi^2 J_0^2(\xi) d\xi \quad (5)$$

which is plotted in Figure II.8a.1. As can be seen this function decays rapidly with ν so that the Hankel transform concentrates noise power near the origin. We can explain why this noise property of the Hankel transform differs from that for the Fourier transform by considering the underlying two dimensional circularly symmetric Fourier transform represented by the Hankel transform.

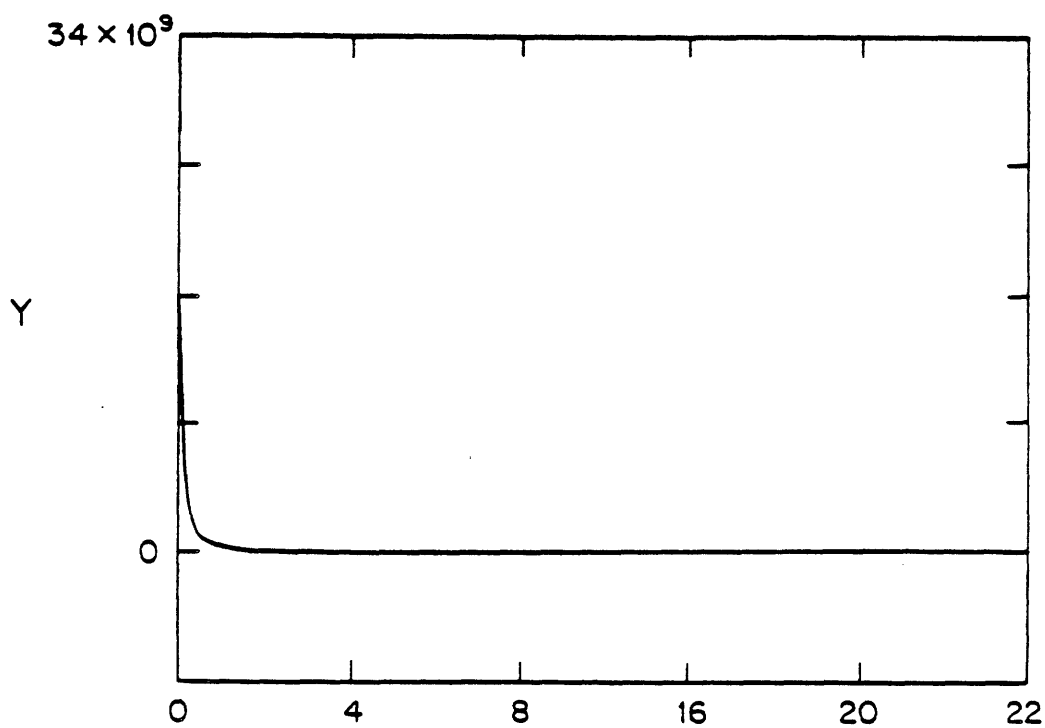


Figure II.3a.1 Noise variance of the output of the Hankel transform for an input of stationary white Gaussian Noise

We recall from Section (II.3) that the Hankel transform of a function, $f(r)$, corresponds to a slice of the two dimensional Fourier transform of the function $\tilde{f}(r, \theta)$ made by sweeping $f(r)$ around the origin in two dimensions (so that $\tilde{f}(r, \theta) = f(r)$ for all θ). When we generate the Hankel transform of the noisy input, $f(r) + n(r)$, we obtain a slice of the two dimensional Fourier transform of $f(r) + n(r)$ swept around the origin. The result is very different from sweeping $f(r)$ around the origin and then adding SWGN (stationary white Gaussian noise) in two dimensions. In the first case the noise field is circularly symmetric, in the second case it is not. It is the symmetry in the underlying noise field implied by the Hankel transform that causes the concentration of noise power near the origin.

We will now show that this behavior of the Hankel transform with respect to noise can be averted by changing to a \sqrt{r} coordinate system for the input and a $\sqrt{\rho}$ coordinate system for the output. Samples evenly spaced in these square root coordinate systems have the property that the distance between any two samples always represents the same area of the underlying two dimensional (circularly symmetric) function. Each noisy sample of the function and its Hankel transform represents the same amount of area in the underlying two dimensional spaces. Consequently the noise properties are equivalent to those associated with samples evenly space on a cartesian grid (associated with the two dimensional Fourier transform).

b) *Proof that if $f(\sqrt{r})$ is stationary white Gaussian noise then $F(\sqrt{\rho})$ will also be stationary white Gaussian noise, where $F(\rho)$ is the Hankel transform of $f(r)$*

The proof that if $f(\sqrt{r})$ is stationary white Gaussian noise (SWGN) then $F(\sqrt{\rho})$ is also SWGN, consists of three parts and a conclusion. First we will show that for the integral transform defined as $F_2(\rho) = \int_0^{\infty} f(r) J_0(\rho r) \sqrt{\rho r} dr$ that $f(r)$ is SWGN if and only if $F_2(\rho)$ is SWGN. Second we will use this to show that $\sqrt{r}f(r)$ is SWGN if and only if $\sqrt{\rho}F(\rho)$ is SWGN. Finally we show that if $\sqrt{r}f(r)$ is SWGN then $f(\sqrt{r})$ must be SWGN.

i) *Proof that $F_2(\rho)$ is stationary white Gaussian noise if and only if $f(r)$ is stationary white Gaus-*

sian noise, where $F_2(\rho)$ is the Hankel transform of $f(r)$ as defined by Bateman.

We begin by recalling that the Hankel transform defined by Bateman [8] and presented in Section (II.2) is given by $F_2(\rho) = \int_0^{\infty} f(r) J_0(\rho r) \sqrt{\rho r} dr$. Because this operator is linear, $F_2(\rho)$ is Gaussian. For the same reason if the mean of $f(r) = 0$ then the mean of $F_2(\rho)$ is also 0. We need only show, then, that

$$E [F_2(\rho_1) F_2(\rho_2)] = C \delta(\rho_1 - \rho_2) \quad (1)$$

Now

$$\begin{aligned} E [F_2(\rho_1) F_2(\rho_2)] &= \\ E \left[\int_0^{\infty} f(r) J_0(\rho_1 r) \sqrt{\rho_1 r} dr \int_0^{\infty} f(\xi) J_0(\rho_2 \xi) \sqrt{\rho_2 \xi} d\xi \right] &= \\ = \int_0^{\infty} \int_0^{\infty} N_0 \delta(r - \xi) J_0(\rho_1 r) J_0(\rho_2 \xi) \sqrt{\rho_1 \rho_2 r \xi} dr d\xi &= \\ = N_0 \sqrt{\rho_1 \rho_2} \int_0^{\infty} J_0(\rho_1 \xi) J_0(\rho_2 \xi) \xi d\xi &= \\ = N_0 \sqrt{\rho_1 \rho_2} \frac{\delta(\rho_1 - \rho_2)}{\rho_1} &= \\ = N_0 \delta(\rho_1 - \rho_2) \end{aligned} \quad (2)$$

This proves that $f(r)$ SWGN implies that $F_2(\rho)$ is SWGN. The converse is proven by noting that the above integral transform is its own inverse so that the same argument applies, replacing $f(r)$ with $F_2(\rho)$.

ii) *Proof that $\sqrt{\rho} F(\rho)$ is stationary white Gaussian noise if and only if $\sqrt{r} f(r)$ is stationary white Gaussian noise, where $F(\rho)$ is the Hankel transform of $f(r)$*

From (i) we know that if $\sqrt{r} f(r)$ is SWGN then

$$\int_0^{\infty} (\sqrt{r} f(r)) J_0(\rho r) \sqrt{\rho r} dr = \sqrt{\rho} \int_0^{\infty} f(r) J_0(\rho r) r dr = \sqrt{\rho} F(\rho) \quad (3)$$

is SWGN. Since the Hankel transform, $\int_0^{\infty} f(r) J_0(\rho r) r dr$ is its own inverse the converse follows by starting with $\sqrt{r} f(r)$.

iii) *Proof that $\sqrt{r}f(r)$ is stationary white Gaussian noise if and only if $f(\sqrt{r})$ is stationary white Gaussian noise*

First we show that if $E [f(r_1)f(r_2)] = \delta(r_1-r_2)$ then $E [f(l[r_1])f(l[r_2])] = \frac{\delta(r_1-r_2)}{l(r_1)}$

This assumes that $l(r)$ and $l^{-1}(r)$ exist in the region of interest.

Proof:

$$\begin{aligned} f(l[r]) &= \\ &= \int_{-\infty}^{\infty} f(l[\xi])\delta(r-\xi)d\xi \\ &= \int_{-\infty}^{\infty} f(\alpha)\delta(r-l^{-1}(\alpha))\frac{d\alpha}{l[l^{-1}(\alpha)]} \end{aligned} \tag{4}$$

Using Equation (4) we can write $E [f(l[r_1])f(l[r_2])]$ as:

$$\begin{aligned} E [f(l[r_1])f(l[r_2])] &= \\ &= \int_{-\infty}^{\infty} \int_{-\infty}^{\infty} E [f(\alpha_1)f(\alpha_2)] \frac{\delta[r_1-l^{-1}(\alpha_1)]\delta[r_2-l^{-1}(\alpha_2)]d\alpha_1d\alpha_2}{l[l^{-1}(\alpha_1)]l[l^{-1}(\alpha_2)]} \\ &= \int_{-\infty}^{\infty} \int_{-\infty}^{\infty} \delta(\alpha_1-\alpha_2) \frac{\delta[r_1-l^{-1}(\alpha_1)]\delta[r_2-l^{-1}(\alpha_2)]d\alpha_1d\alpha_2}{l[l^{-1}(\alpha_1)]l[l^{-1}(\alpha_2)]} \\ &= \int_{-\infty}^{\infty} \frac{\delta[r_1-l^{-1}(\alpha)]\delta[r_2-l^{-1}(\alpha)]}{l^2[l^{-1}(\alpha)]} \end{aligned} \tag{5}$$

If we define $\xi = l^{-1}(\alpha)$ so that $\alpha = l(\xi)$ and $d\alpha = l'(\xi)d\xi$ then

$$\begin{aligned} E [f(l[r_1])f(l[r_2])] &= \int_{-\infty}^{\infty} \delta(r_1-\xi)\delta(r_2-\xi)\frac{d\xi}{l'(\xi)} \\ &= \frac{\delta(r_1-r_2)}{l'(r_1)} \end{aligned} \tag{6}$$

We now show that $f(\sqrt{r})$ SWGN iff $E [f(r_1)f(r_2)] = \frac{\delta(r_1-r_2)}{r_1}$

We apply the result of the first part of this section to our special case by defining $l(r) = r^2$ so that $l'(r) = 2r$. With this definition we see that if some $p(r)$ is SWGN then $p(r^2)$ will have a variance proportional to $\frac{\delta(r_1-r_2)}{r_1}$. This implies that if $f(\sqrt{r})$ is SWGN then $f(r)$ has a variance proportional to $\frac{\delta(r_1-r_2)}{r_1}$. Finally we note that if $E [f(r_1)f(r_2)] = \frac{\delta(r_1-r_2)}{r_1}$ then

$E \left[\sqrt{r_1} f(r_1) \sqrt{r_2} f(r_2) \right] = \delta(r_1 - r_2)$ therefor if $f(\sqrt{r})$ is SWGN then $\sqrt{r} f(r)$ is SWGN. The converse follows from the same steps in reverse.

iv) *Conclusion*

In (i) and (ii) we showed that if $\sqrt{r} f(r)$ is SWGN then $\sqrt{\rho} F(\rho)$ will also be SWGN. In (iii) we showed that $\sqrt{r} f(r)$ is SWGN if and only if $f(\sqrt{r})$ is SWGN. The argument of (iii) and (iv) also showed that $\sqrt{\rho} F(\rho)$ is SWGN if and only if $F(\sqrt{\rho})$ is SWGN. Thus we have shown that if $f(\sqrt{r})$ is SWGN then $F(\sqrt{\rho})$ must also be SWGN.

II.9) *Summary*

In this chapter we have developed the properties of the Hankel transform in general. By themselves these properties might be simply interesting but together with the ability to numerically perform the Hankel transform, they become tools for scientific research. In the next chapter we will discuss methods for numerically performing the Hankel transform.

References

1. Papoulis, *Systems and Transforms with Applications in Optics*, McGraw-Hill, New York (1968).
2. G.V. Frisk, A.V. Oppenheim, and D. Martinez, "A Technique for Measuring the Plane-Wave Reflection Coefficient of the Ocean Bottom," *J. Acoustical Soc. Amer.* 68 (2), pp.602-612 (1980).
3. R. Bracewell,, "Strip Integration in Radio Astronomy," *Aust. J. Phys.* 9, pp.198-217 (1956).
4. A.V. Oppenheim, G.V.Frisk, and D.R. Martinez, "An Algorithm for the Numerical Evaluation of the Hankel Transform," *Proc. IEEE* 66, pp.264-265 (1978).

5. Lipschitz, *Journal fur Math.* 56, pp.189-196 (1859).
6. W.H. Young, "On Series of Bessel Functions," *Proc. London Math. Soc* 2 XVIII, pp.163-200 (1920).
7. G. N. Watson, *Theory of Bessel Functions 2nd Ed.*, Cambridge at the University Press, New York (1966).
8. Bateman, *Tables of Integral Transforms*, McGraw-Hill, New York (1954).
9. A.V. Oppenheim and R. Schaffer, *Digital Signal Processing*, Prentice-Hall, Englewood Cliffs, New Jersey (1975).
10. R. Bracewell, *The Fourier Transform and Its Applications*, McGraw-Hill, New York (1965).
11. McClellan, J., Parks, T., and Rabiner, L., "A Computer Program for Designing Optimum FIR Linear Phase Digital Filters," *IEEE Trans. on Audio and Electroacoustics* AU-21(6), pp.506-526 (1973).
12. L. Schlafli, "Ueber die Convergenz der Entwicklung einer Arbitraren Function $f(x)$ nach den Bessel'schen Functionen $J_a(\beta_1 x)$, . . .," *Math. Ann.* X, pp.137-142 (1876).
13. W. Feller, *An Introduction to Probability Theory and Its Applications*, John Wiley & Sons, Inc., New York (1971).
14. W.B. Davenport, Jr and W.L. Root, *An Introduction to the Theory of Random Signals and Noise*, McGraw-Hill Book Co., New York (1958).



Chapter III:

Computing the Hankel Transform

III.1) Overview

Because of the importance of the Hankel transform there presently exist many algorithms for its evaluation. As yet, however, there is no generally accepted algorithm analogous to the FFT for the Fourier transform. This chapter presents a survey of numerical Hankel transform techniques. It does not include all the published algorithms but does represent the major classes. We begin in section III.2 by discussing perhaps the oldest and best understood algorithm, the Fourier-Bessel series, that we used to derive our aliasing result of Chapter II. Section III.3 presents the backsmear method and an example of an efficient class of realizations. Section III.4 discusses the asymptotic transform method as it has been proposed in the literature and presents new results that can be used to improve this method or to assess the error in the standard realization from the output transform alone. Section III.5 discusses a common combined transform method and presents a caution about its use. Section III.6 presents a convolutional method frequently used for electromagnetic problems which require the transform of smooth functions of limited extent. Section III.7 discusses the projection-slice method. In that section we develop a fast algorithm for generating the projections (shown to be an Abel transform), which itself has wide applications. [1] When it is followed by an FFT the result is an efficient Hankel transform. Both the Abel and Hankel transform algorithms are illustrated with examples.

III.2) The Fourier-Bessel Series

Probably the first proposed method for evaluating the Hankel transform is the Fourier-Bessel series, which was discussed in the aliasing section. The Fourier-Bessel series is summarized by the identity: [2, 3]

$$0 < \rho < 1 \quad F(\rho) = 2 \sum_{n=10}^{\infty} \int_0^1 \frac{F(\xi) J_0(\lambda_n \xi) \xi d\xi}{J_1^2(\lambda_n)} J_0(\lambda_n \rho) \quad (1)$$

Where λ_n $n=1,2,3, \dots$ are the ordered zeros of $J_0(x)$.

This relation can be used to obtain the Hankel transform of a band limited function, $f(r)$, defined by

$$F(\rho) \equiv \int_0^{\infty} f(r) J_0(\rho r) r dr \quad (2)$$

where $F(\rho) = 0$ for $\rho > 1$ by noting that when $F(\rho) = 0$ $\rho > 1$:

$$f(\lambda_n) = \int_0^{\infty} F(\rho) J_0(\rho \lambda_n) \rho d\rho = \int_0^1 F(\rho) J_0(\rho \lambda_n) \rho d\rho \quad (3)$$

Substituting into Equation (1) we have:

$$0 < \rho < 1 \quad F(\rho) = 2 \sum_{n=1}^{\infty} \frac{f(\lambda_n)}{J_1^2(\lambda_n)} J_0(\lambda_n \rho) \quad (4)$$

which is in the form of a sum as we desired. If $F(\rho)$ is bandlimited to $\rho < B$, instead of $\rho < 1$, Equation (4) can be modified by a change of variables. The resulting general form states that when $F(\rho) = 0$ for $\rho > B$ then

$$0 < \rho < B \quad F(\rho) = \frac{2}{B^2} \sum_{n=1}^{\infty} \frac{f\left(\frac{\lambda_n}{B}\right)}{J_1^2(\lambda_n)} J_0\left(\frac{\lambda_n}{B} \rho\right) \quad (5)$$

The properties of the Fourier-Bessel series have been extensively studied. [2, 3] As a numerical algorithm for implementing the Hankel transform it is usually appropriate only when a few values of $F(\rho)$ are required or when computation cost is less important than careful control over the errors. This is because the Fourier-Bessel series requires that a new sum be computed for every value of ρ . Further, it requires that the function to be transformed be available on the nonuniform grid, $\frac{\lambda_n}{B}$.

Another algorithm that is appropriate when only a few values of $F(\rho)$ are required, but which accepts input values on an even grid, is the backsmeared method. We present the backsmeared method in the next section.

III.3) The Backsmear Method

The backsmear method exploits the efficiency of the FFT to provide an efficient algorithm when only a few output values of the transform are desired. This algorithm can be derived by replacing the Bessel function with its integral representation the Hankel transform can be written as the two dimensional integral:

$$F(\rho) \equiv \int_0^{\infty} f(r) J_0(\rho r) r dr = \frac{1}{2\pi} \int_0^{2\pi} \left[\int_0^{\infty} f(r) e^{i\rho r \cos\theta} r dr \right] d\theta \quad (1)$$

If we define $G(x) \equiv \int_0^{\infty} f(r) r e^{ix} dr$ and note that $\cos\theta$ is even, the transform becomes:

$$F(\rho) = \frac{1}{\pi} \int_0^{\pi} G(\rho \cos\theta) d\theta = \frac{1}{\pi} \int_0^{\frac{\pi}{2}} \left[G(\rho \cos\theta) - G(-\rho \cos\theta) \right] d\theta \quad (2)$$

$G(x)$ can be evaluated efficiently on an even grid using an FFT. [4] The integration called for in Equation (2), however, must be performed for every desired value of ρ . Further, since the integration of Equation (2) is in θ , some interpolation scheme must be used to generate $G(\rho \cos\theta)$ on the quadrature points required by the numerical integrator.

The backsmear method is appropriate when the transform is required at only a few values of ρ . When this is the case and when $G(x)$ is slowly varying so that the numerical integration which must be carried out upon it can be done efficiently, then the backsmear method is efficient. This is particularly true if the interpolation scheme used permits a quadrature formula to be developed for the numerical integration.

One such development is presented below for the case of linear interpolation between the points of $L(x) \equiv G(x) + G(-x)$.

We seek

$$F(\rho) = \frac{1}{\pi} \int_0^{\frac{\pi}{2}} L(\rho \cos\theta) d\theta \quad (3)$$

and have available only $L\left(\frac{k}{NT}\right)$ from the output of the FFT. We approximate $L(x)$ by linearly

interpolating $L\left(\frac{k}{NT}\right)$ so that

$$0 \leq \frac{1}{2T} \quad \hat{L}(x) = \sum_{j=0}^{\frac{N}{2}-1} L_j(x) \quad (4)$$

where

$$L_j(x) \equiv \begin{cases} L\left(\frac{j}{NT}\right) + (x - \frac{j}{NT})(NT) \left[L\left(\frac{j+1}{NT}\right) - L\left(\frac{j}{NT}\right) \right] & \frac{j}{NT} < x < \frac{j+1}{NT} \\ 0 & \text{otherwise} \end{cases} \quad (5)$$

We can integrate $\hat{L}(\rho \cos \theta)$ as follows

$$\int_0^{\frac{\pi}{2}} \hat{L}(\rho \cos \theta) d\theta = \int_0^{\frac{\pi}{2}} \sum_{j=1}^{\frac{N}{2}-1} L_j(\rho \cos \theta) d\theta = \sum_{j=1}^{\frac{N}{2}-1} \int_0^{\frac{\pi}{2}} L_j(\rho \cos \theta) d\theta \quad (6)$$

The L_j terms can be integrated term by term:

$$\int_0^{\frac{\pi}{2}} L_j(\rho \cos \theta) d\theta = \int_{\cos^{-1} \frac{j+1}{\rho NT}}^{\cos^{-1} \frac{j}{\rho NT}} \left[L\left(\frac{j}{NT}\right) - j \left\{ L\left(\frac{j+1}{NT}\right) - L\left(\frac{j}{NT}\right) \right\} + \rho NT \left\{ L\left(\frac{j+1}{NT}\right) - L\left(\frac{j}{NT}\right) \right\} \cos \theta \right] d\theta \quad (7)$$

where

$$\cos^{-1} x \equiv \begin{cases} \cos^{-1} x & |x| \leq 1 \\ 0 & |x| \geq 1 \end{cases} \quad (8)$$

Evaluating this integral and substituting into Equation (6) we have

$$\begin{aligned} \hat{F}\left(\frac{k}{NT}\right) &= \\ &= \sum_{j=0}^{k-1} \left[\cos^{-1}\left(\frac{j}{k}\right) - \cos^{-1}\left(\frac{j+1}{k}\right) \right] \left[L\left(\frac{j}{NT}\right) - j \left\{ L\left(\frac{j+1}{NT}\right) - L\left(\frac{j}{NT}\right) \right\} \right] \\ &+ \sum_{j=0}^{k-1} \left[\sqrt{k^2 - j^2} - \sqrt{k^2 - (j+1)^2} \right] \left[L\left(\frac{j+1}{NT}\right) - L\left(\frac{j}{NT}\right) \right] \end{aligned} \quad (9)$$

When k is small or $\hat{F}\left(\frac{k}{NT}\right)$ is desired for only a few values of k , this is an efficient procedure. When k is large and $\hat{F}\left(\frac{k}{NT}\right)$ is required for many values this is a slow method, however. In the next section we present a fast algorithm for the evaluation of the Hankel transform at large values of the transform variable, ρ .

III.4) The Asymptotic transform

In the seismic community the Hankel transform is commonly evaluated approximately by replacing the Bessel function with its asymptotic form so that the resulting integral looks like a Fourier transform. [5, 6] The result will usually asymptotically approach the Hankel transform, though pathological functions can be found for which this is not the case ($\frac{\delta(r)}{r}$ for example). The main disadvantages of this method are that it is almost never suitable for small values of ρ and that the error induced by the substitution is determined in part by the function being transformed. The main advantage is that the resulting integral looks very much like a Fourier transform and can be evaluated efficiently with an FFT.

An expression for the Bessel function, suitable for an asymptotic expansion is provided by Lipschitz:¹ [7]

$$\text{for } x > 0 \quad J_0(x) = \frac{\sqrt{2}}{\sqrt{\pi x}} \left[\cos\left(x - \frac{\pi}{4}\right) + \frac{1}{8x} \sin\left(x - \frac{\pi}{4}\right) - \frac{9}{128} \frac{1}{x} \cos\left(x - \frac{\pi}{4}\right) + \frac{3\theta(x)}{64 x^3} \right] \quad \text{where } |\theta| < 1 \quad (1)$$

In the literature describing this technique [5] only the leading term is retained, providing:

$$F(\rho) \approx \frac{\sqrt{2}}{\sqrt{\rho\pi}} \int_0^{\infty} f(r) \cos(\rho r - \frac{\pi}{4}) \sqrt{r} dr \quad \text{when } \rho > 0 \quad (2)$$

This is written as a Fourier transform by noting that

$$\cos(\rho r - \frac{\pi}{4}) = \frac{1}{\sqrt{2}} (\cos(\rho r) + \sin(\rho r)) \quad (3)$$

hence

$$F(\rho) \approx \frac{1}{\sqrt{\rho\pi}} \left[\int_0^{\infty} f(r) \sqrt{r} \cos(\rho r) dr + \int_0^{\infty} f(r) \sqrt{r} \sin(\rho r) dr \right] \quad \text{when } \rho > 0 \quad (4)$$

This expression can be evaluated with an FFT.

We can write the error associated with the transform technique as

$$\begin{aligned} \epsilon(\rho) &= \int_0^{\infty} f(r) r \left[J_0(\rho r) - \frac{\sqrt{2}}{\sqrt{\pi\rho r}} \cos\left(\rho r - \frac{\pi}{4}\right) \right] dr \\ &= \frac{1}{\rho} \int_0^{\infty} f(r) H(\rho r) dr \end{aligned} \quad (5)$$

1) A more recent expansion with the same leading behavior can be found in Watson. [2]

with $H(\rho r) = \rho r \left[J_0(\rho r) - \frac{\sqrt{2}}{\sqrt{\pi \rho r}} \cos(\rho r - \frac{\pi}{4}) \right]$. $H(x)$ is plotted in Figure III.3.1. It looks very much like a slowly decaying sinusoid. $\epsilon(\rho)$ decays with ρ both because $H(\rho r)$ decays (slowly) with ρ and because of the of the $1/\rho$ term. Because of the sinusoidal behavior of $H(\rho r)$ the error term of Equation (5) can be large at those frequencies where $f(r)$ has a lot of energy.

By using the expression of Lipschitz we can develop an asymptotic Hankel transform with an error term that decays much faster than the error term for the conventional asymptotic method. This expression also makes it relatively easy to judge the validity of the conventional asymptotic transform after it has been performed because it presents the leading error terms of that transform as a function of the transform itself.

We substitute the expression of (1) for $J_0(\rho r)$ in the Hankel transform to see that:

$$F(\rho) = \frac{\sqrt{2}}{\sqrt{\pi \rho}} \left[\int_0^{\infty} f(r) \sqrt{r} \cos(\rho r - \frac{\pi}{4}) dr + \frac{1}{8\rho} \int_0^{\infty} \frac{f(r)}{\sqrt{r}} \sin(\rho r - \frac{\pi}{4}) dr - \frac{9}{128} \frac{1}{\rho^2} \int_0^{\infty} \frac{f(r)}{r^{3/2}} \cos(\rho r - \frac{\pi}{4}) dr + \frac{3}{64} \frac{1}{\rho^3} \int_0^{\infty} \frac{f(r)}{r^{5/2}} \theta(r) dr \right] \quad (6)$$

If we use

$$\begin{aligned} \cos(\rho r - \frac{\pi}{4}) &= \frac{1}{\sqrt{2}} [\cos(\rho r) + \sin(\rho r)] \\ \sin(\rho r - \frac{\pi}{4}) &= \frac{1}{\sqrt{2}} [\sin(\rho r) - \cos(\rho r)] \end{aligned} \quad (7)$$

then Equation (6) becomes

$$\begin{aligned} F(\rho) &= \frac{1}{\sqrt{\pi \rho}} \left[\int_0^{\infty} f(r) \sqrt{r} \cos(\rho r) dr + \int_0^{\infty} f(r) \sqrt{r} \sin(\rho r) dr - \frac{1}{8\rho} \int_0^{\infty} \frac{f(r)}{\sqrt{r}} \sin(\rho r) dr + \frac{1}{8\rho} \int_0^{\infty} \frac{f(r)}{\sqrt{r}} \cos(\rho r) dr - \frac{9}{128} \frac{1}{\rho^2} \int_0^{\infty} \frac{f(r)}{r^{3/2}} \cos(\rho r) dr - \frac{9}{128} \frac{1}{\rho^2} \int_0^{\infty} \frac{f(r)}{r^{3/2}} \sin(\rho r) dr + \frac{3}{64} \frac{1}{\rho^3} \int_0^{\infty} \frac{f(r)}{r^{5/2}} \theta(\rho r) dr \right] \end{aligned} \quad (8)$$

If we now define

$$\begin{aligned} F_c(\rho) &= \int_0^{\infty} f(r) \sqrt{r} \cos(\rho r) dr \\ F_s(\rho) &= \int_0^{\infty} f(r) \sqrt{r} \sin(\rho r) dr \end{aligned} \quad (9)$$

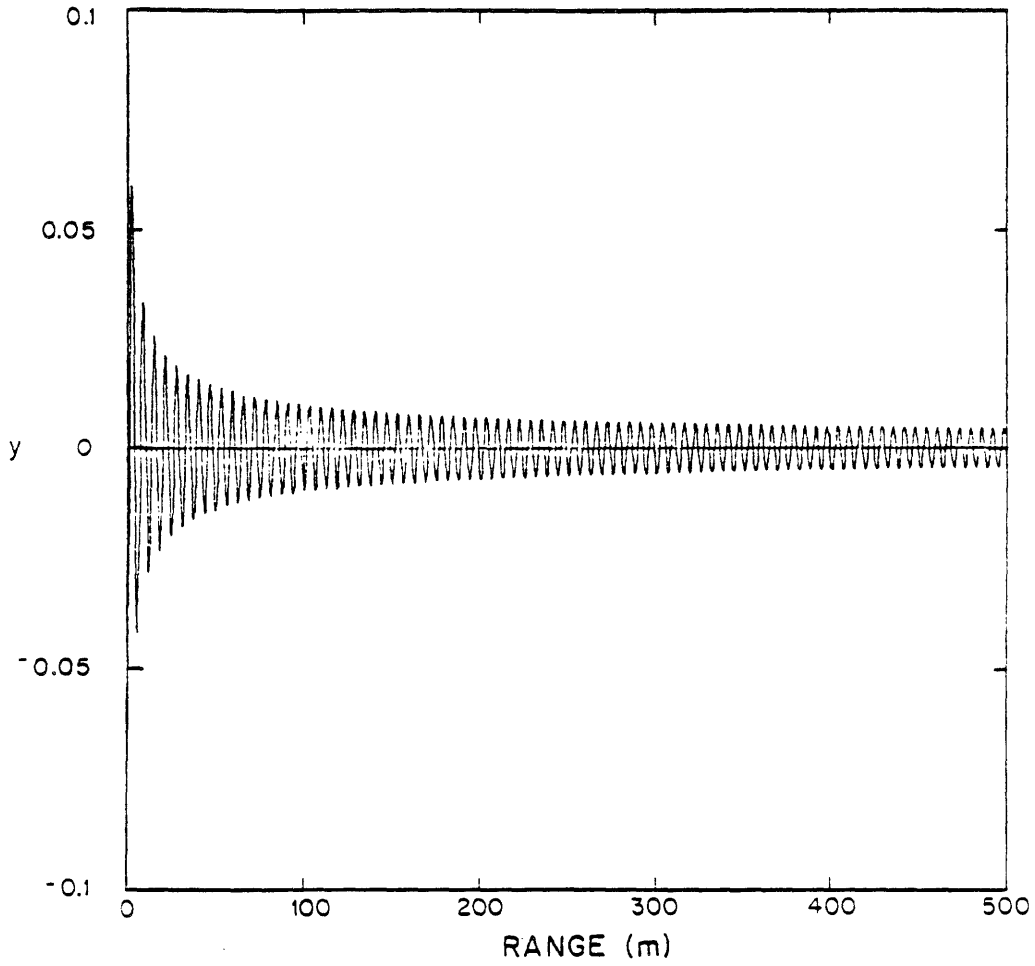


Figure III.3.1 Plot of the error kernel for the asymptotic transform method

and note that

$$\begin{aligned} \frac{\partial}{\partial \rho} \int_0^{\infty} \frac{f(r)}{\sqrt{r}} \cos(\rho r) dr &= - \int_0^{\infty} f(r) \sqrt{r} \sin(\rho r) dr = -F_s(\rho) \\ \frac{\partial}{\partial \rho} \int_0^{\infty} \frac{f(r)}{\sqrt{r}} \sin(\rho r) dr &= \int_0^{\infty} f(r) \sqrt{r} \cos(\rho r) dr = F_c(\rho) \\ \frac{\partial^2}{\partial \rho^2} \int_0^{\infty} \frac{f(r)}{r^{3/2}} \cos(\rho r) dr &= -F_c(\rho) \\ \frac{\partial^2}{\partial \rho^2} \int_0^{\infty} \frac{f(r)}{r^{3/2}} \sin(\rho r) dr &= -F_s(\rho) \end{aligned} \quad (10)$$

then

$$\begin{aligned} F(\rho) = \frac{1}{\sqrt{\rho\pi}} \left[F_c(\rho) + F_s(\rho) + \frac{1}{8\rho} \int_0^{\rho} F_s(\xi) d\xi + \frac{1}{8\rho} \int_0^{\rho} F_c(\xi) d\xi + \frac{9}{128\rho^2} \int_0^{\rho} \int_0^{\xi} F_c(\xi_1) d\xi_1 d\xi \right. \\ \left. + \frac{9}{128\rho^2} \int_0^{\rho} \int_0^{\xi} F_s(\xi_1) d\xi_1 d\xi + \frac{3}{64\rho^3} \int_0^{\infty} \frac{f(r)}{r^{5/2}} \theta(\rho r) dr \right] \end{aligned} \quad (11)$$

We can combine terms above by defining

$$F_1(\rho) = F_c(\rho) + F_s(\rho) \quad (12)$$

so Equation (11) becomes

$$F(\rho) = \frac{1}{\sqrt{\rho\pi}} \left[F_1(\rho) + \frac{1}{8\rho} \int_0^{\rho} F_1(\xi) d\xi + \frac{9}{128} \frac{1}{\rho^2} \int_0^{\rho} \int_0^{\xi} F_1(\xi_1) d\xi_1 d\xi + \frac{3}{64\rho^3} \int_0^{\infty} \frac{f(r)}{r^{5/2}} \theta(\rho r) dr \right] \quad (13)$$

The indefinite integrals above can be converted to definite integrals by integrating from 0 to infinity and adding on the values necessary to force the resulting equation to match Equation (8) at $\rho = 0$:

$$\int_0^{\rho} F_1(\xi) d\xi = \int_0^{\rho} F_1(\xi) d\xi + C_1 \quad \text{with } C_1 = \int_0^{\infty} \frac{f(r)}{\sqrt{r}} dr \quad (14)$$

$$\int_0^{\rho} \int_0^{\xi} F_1(\xi_1) d\xi_1 d\xi = \int_0^{\rho} \left[\int_0^{\xi} F_1(\xi) d\xi + C_1 \right] d\xi + C_2 \quad \text{with } C_2 = \int_0^{\infty} \frac{f(r)}{r^{3/2}} dr \quad (15)$$

Performing the integrations over the constants and replacing the iterated integral we are left with the expression

$$F(\rho) = \frac{1}{\sqrt{\pi\rho}} \left\{ F_1(\rho) + \frac{1}{\rho} \left[\frac{1}{8} \int_0^{\rho} F_1(\xi) d\xi + \frac{25}{128} C_1 \right] + \frac{9}{128} \frac{1}{\rho} \left[\int_0^{\rho} (\rho - \xi) F_1(\xi) d\xi + C_2 \right] + \frac{3}{64\rho^3} \int_0^{\infty} \frac{f(r)}{r^{5/2}} \theta(\rho r) dr \right\} \quad (16)$$

The first term can be recognized as the usual asymptotic expression for the Hankel transform.

The second and third terms are corrections to this expression which can in principle be determined from it. The final term is the remaining error term but which is considerably smaller than the term associated with the usual asymptotic expression.

If it were desired to calculate the second and third terms directly as a Fourier transform, the same procedure could be used as will be described in Section (III.7) where it is applied to calculating the Abel transform.

Equation (16) can also be interpreted as providing first and second order error estimates for the classical asymptotic transform. These estimates allow the error associated with the classical method to be estimated (to first and second order) from a knowledge of only the resulting transform. Such estimates permit one to interpret the result of an asymptotic transform with a questionable appearance.

III.5) *A Combined Transform Method*

The Fourier-Bessel series and the backsmear methods both permit the calculation of the Hankel transform on any output grid. The computational cost of each of these methods increases linearly with the number of points computed. The asymptotic method is fast and usually generates good estimates of the Hankel transform when ρ is large. A combined scheme is possible which uses a slow method such as the Fourier-Bessel series or the backsmear to compute the Hankel transform point by point for low values of ρ and which switches to the asymptotic transform for large values of ρ . Such a method has been proposed in the literature. [8]

The main issue with such a scheme is the point at which the algorithm should cease computing the transform point by point with the slow method and begin to accept the output of the asymptotic transform. At present there is no reliable method for doing this. It has been suggested in the literature that the transition be made at the first point for which the slow algorithm produces a transform value which matches the value of the asymptotic transform within a specified tolerance. [8] This scheme for switching to the asymptotic transform would be entirely ade-

quate if the error made by the asymptotic algorithm were monotonically decreasing in the transform variable, ρ . This error is not always monotonically decreasing, however, as we will illustrate by constructing a function for which it is not. The existence of such a function indicates that the switching method proposed in the literature [8] will not always work. In fact, for the function we construct, the error made by the asymptotic method will be zero at a point we specify. The switching scheme proposed would begin to accept the asymptotic transform before this point even though the error made by the asymptotic transform beyond this point might be greater than the specified tolerance.

As in Section (III.4) we write the error associated with the asymptotic transform as:

$$\epsilon(\rho) = \frac{1}{\rho} \int_0^{\infty} f(r) H(\rho r) dr \quad (1)$$

where $H(\rho r) \equiv \rho r \left[J_0(\rho r) - \frac{\sqrt{2}}{\sqrt{\pi \rho r}} \cos\left(\rho r - \frac{\pi}{4}\right) \right]$ and was plotted in Figure III.3.1. In order to construct a function, $f(r)$, such that $\epsilon(\rho)$ is not monotonically decreasing we first choose some small δ and set

$$f(r) \equiv \begin{cases} 1 & 0 < r < \delta \\ -\frac{\frac{1}{\rho_0} \int_0^{\delta} H(\rho_0 r) dr}{\frac{1}{\rho_0} \int_0^{\infty} H(\rho_0 r) dr} & \delta < r < \infty \end{cases} \quad (2)$$

For this $f(r)$ the error made by the asymptotic transform is:

$$\begin{aligned} \epsilon(\rho) &= \frac{1}{\rho} \int_0^{\infty} H(\rho r) f(r) dr \\ &= \frac{1}{\rho} \int_0^{\delta} H(\rho r) dr - \frac{\frac{1}{\rho_0} \int_0^{\delta} H(\rho_0 r) dr}{\frac{1}{\rho_0} \int_0^{\infty} H(\rho_0 r) dr} \frac{1}{\rho} \int_0^{\infty} H(\rho r) dr \end{aligned} \quad (3)$$

When $\rho = \rho_0$ the error, $\epsilon(\rho_0)$, equals zero. In general for $\rho > \rho_0$ it will not. For this constructed function the error is not monotonically decreasing and the switching procedure described

in the literature will not work.

Until an adequate switching method has been found or until the class of functions for which the proposed switching algorithm will work has been well defined, there can be no guarantee that the combined algorithm will work properly and this method should be used with caution.

III.6) A Convolutional Method

In this section we describe a method for computing the Hankel transform that puts the Hankel transform in the form of a convolution by transforming to an exponential grid. When this grid does not involve an extraordinary number of points to adequately represent the function, the Hankel transform can be efficiently evaluated with an FFT. We will discuss the presentation of this method by Siegman [9], though other presentations are available in the literature. [10]

Siegman converts the Hankel transform into a convolution by sampling the function on an exponential grid. He begins with the Hankel transform integral

$$F(\rho) \equiv \int_0^{\infty} f(r) J_0(\rho r) r dr \quad (1)$$

After the following definitions:

$$\begin{aligned} \rho &\equiv \rho_0 e^{\nu} & \nu &= \ln\left(\frac{\rho}{\rho_0}\right) \\ r &\equiv r_0 e^{\xi} & \xi &= \ln\left(\frac{r}{r_0}\right) \end{aligned} \quad (2)$$

Equation (1) becomes:

$$\begin{aligned} F(\rho_0 e^{\nu}) &= \\ &= \int_{-\infty}^{\infty} f(r_0 e^{\xi}) J_0(\rho_0 r_0 e^{\nu+\xi}) r_0^2 e^{2\xi} d\xi \\ &= r_0^2 \int_{-\infty}^{\infty} \left[e^{2\xi} f(r_0 e^{\xi}) \right] J_0(\rho_0 r_0 e^{(\nu+\xi)}) d\xi \\ &= r_0^2 \int_{-\infty}^{\infty} \left[e^{-2\alpha} f(r_0 e^{-\alpha}) \right] J_0(\rho_0 r_0 e^{(\nu-\alpha)}) d\alpha \end{aligned} \quad (3)$$

which is the convolution of $r_0^2 e^{-2\nu} f(r_0 e^{-\nu})$ with $J_0(\rho_0 r_0 e^{\nu})$ and can be implemented with an FFT.

The strength of this technique is the efficiency with which the Fourier transform can be implemented. Its weakness stems from the requirement that $f(r)$ be sampled evenly in $e^{-\xi}$. In order to obtain the sampling density necessary to represent a function near the origin it is likely that such a density of points is necessary to represent the function at larger ranges that the computational savings are lost. Also, the presence of the gain factor $e^{-2\nu}$ might be a severe problem for the region $0 < r < 1$. It is unlikely that this transform technique would work efficiently for functions with more than moderate range-bandwidth products.

In the next section we present another Hankel transform algorithm that exploits the computational efficiency of the FFT through a change of coordinate system. It requires only that the function be represented on a square root grid, however.

III.7) The Projection-Slice Method

a) Overview

In Section II.2 we related the Hankel transform to the two dimensional Fourier transform of a circularly symmetric function. We showed that the Hankel transform can be obtained by first forming the projection, or Abel transform:

$$p(r) = A \cdot f(r) \equiv 2 \int_0^{\infty} f(\sqrt{r^2 + y^2}) dy = 2 \int_{|r|}^{\infty} \frac{f(\xi) \xi d\xi}{\sqrt{\xi^2 - r^2}} \quad (1)$$

which is then followed by a Fourier transform:

$$F(\rho) \equiv \int_0^{\infty} f(r) J_0(\rho r) r dr = \frac{1}{2\pi} \int_{-\infty}^{\infty} p(r) e^{i\rho r} dr \quad (2)$$

Oppenheim, Frisk, and Martinez [11] suggested that the computational efficiency of the FFT be exploited by implementing the Hankel transform as a numerical projection followed by an FFT. Previously, however, the projections were expensive to compute, requiring on the order of n^2 operations and function evaluations or interpolations. As part of this thesis a computationally

efficient method for computing the projections (the Abel transform) was developed. [12] When followed by an FFT the result is a computationally efficient Hankel transform requiring on the order of $N \cdot \log N$ operations.

b) *The Abel transform*

We consider the Abel transform shown below:

$$p(r) \equiv A \cdot f(r) \equiv 2 \int_{|r|}^{\infty} \frac{f(\xi) \xi d\xi}{\sqrt{\xi^2 - r^2}} \quad (1)$$

As suggested by Bracewell [1,2], we write this transform as a convolution by defining:

$$h(r) \equiv \begin{cases} 0 & r \geq 0 \\ \frac{1}{\sqrt{-r}} & r < 0 \end{cases} \quad (2)$$

and

$$\bar{p}(r) \equiv p(\sqrt{r}) \quad r \geq 0 \quad (3)$$

$$\bar{f}(r) \equiv f(\sqrt{r}) \quad r \geq 0 \quad (4)$$

which leads to the convolution formula:

$$\bar{p}(r) = \bar{f}(r) * h(r) \quad (5)$$

The Abel transform of $f(r)$, $p(r)$, is determined by:

$$p(r) = \bar{p}(r^2) \quad (6)$$

Bracewell [2] proposed evaluating (6) by shifts and sums.

Because the Fourier transform of $h(r)$ is the known analytic function:

$$H(v) = \frac{1+i}{2} \frac{1}{\sqrt{v}} \quad \text{for all } v \quad (7)$$

$\bar{p}(r)$ can be determined in principle by means of the Fourier transform:

$$\bar{p}(r) = \int_{-\infty}^{\infty} \bar{F}(v) \frac{1+i}{2} \frac{1}{\sqrt{v}} e^{i2\pi r v} dv \quad (8)$$

where $\bar{F}(v)$ is the FT of $\bar{f}(r)$. Unfortunately the singularity at $v = 0$ makes this function dif-

difficult to represent in the computer and is responsible for the long tails of $\bar{p}(r)$ which cause aliasing problems when the convolution is implemented with a Fourier transform. We avoid these difficulties by removing the $\frac{1}{\sqrt{\nu}}$ factor from the numerical part of the transform (8) in such a way that the remaining function is as well behaved as $\bar{F}(\nu)$ within the numerical portion of the transform. The singular part of the transform is performed analytically and added in after the numerical processing.

To this end the transform (8) is written

$$\begin{aligned} \bar{p}(r) &= \int_0^{\infty} \bar{F}(\nu) \frac{1+i}{2} \frac{1}{\sqrt{\nu}} e^{i2\pi r \nu} d\nu + \int_{-\infty}^0 \bar{F}(\nu) \frac{1+i}{2} \frac{1}{\sqrt{\nu}} e^{i2\pi r \nu} d\nu \quad (9a) \\ &= \frac{1+i}{2} \left\{ \int_0^{\infty} \frac{\bar{F}(\nu) - \bar{F}(0) e^{-b\nu(1-\sqrt{\nu})}}{\sqrt{\nu}} e^{i2\pi r \nu} d\nu + \bar{F}(0) \int_0^{\infty} \frac{1-\sqrt{\nu}}{\sqrt{\nu}} e^{-(b-i2\pi r)\nu} d\nu + (9b) \right. \\ &\quad \left. + \int_{-\infty}^0 \frac{\bar{F}(\nu) - \bar{F}(0) e^{b\nu(1-\sqrt{\nu})}}{\sqrt{\nu}} e^{i2\pi r \nu} d\nu + \bar{F}(0) \int_{-\infty}^0 \frac{1-\sqrt{\nu}}{\sqrt{\nu}} e^{(b+i2\pi r)\nu} d\nu \right\} \end{aligned}$$

Where b is a parameter analogous to the real part of the exponential in a Laplace transform. Our choice of b is described later.

The integrands in the first and third integrals of Equation (9b) do not have singularities at $\nu=0$. Because both the numerator and denominator of these integrands approach 0 as ν approaches 0, they can be evaluated by l' Hospital's rule to show that as ν approaches 0 they approach $\bar{F}(0)$.

Upon defining

$$L(\nu) \equiv \begin{cases} \bar{F}(0) & \nu=0 \\ (\bar{F}(\nu) - \bar{F}(0) e^{-b|\nu|(1-\sqrt{\nu})})/\sqrt{\nu} & \text{otherwise} \end{cases} \quad (10)$$

and performing analytically the two integrals that do not depend on $\bar{F}(\nu)$ we have :

$$\bar{p}(r) = \frac{1+i}{2} \left\{ \int_{-\infty}^{\infty} L(\nu) e^{i2\pi r \nu} d\nu + \bar{F}(0) \left\{ \frac{\sqrt{\pi}}{\sqrt{b-2\pi ir}} - \frac{1}{b-2\pi ir} - \frac{i\sqrt{\pi}}{\sqrt{b+2\pi ir}} - \frac{1}{b+2\pi ir} \right\} \right\} \quad (11)$$

$L(\nu)$ was defined in (10) such that $L(0) = \bar{F}(0)$ and $L(\nu) \approx \bar{F}(\nu)$ for large ν . The parameter, b , was chosen so that $L(\nu)$ moves smoothly between its limits. If b were set to 0, $L(\nu)$ would have a DC term that would transform to an impulse. Theoretically this would be canceled by the singularities in the portion of the transform performed analytically (see equation above) but computational errors would certainly cause problems. If b were infinite, $L(\nu)$ would suffer from the $1/\sqrt{\nu}$ singularity at the origin. b is chosen to smooth out the singularity somewhat between these limits. We have been using values of b such that $e^{-b\nu}$ has decayed to e^{-1} after roughly 6 samples of $\bar{F}(\nu)$.

We present three examples of functions processed with the Abel transform algorithm described above.

Example 1 (a)

The first example is the transform of the pillbox function

$$f(r) \equiv \begin{cases} 1 & |r| < 1 \\ .5 & |r| = 1 \\ 0 & |r| > 1 \end{cases} \quad (12)$$

1024 samples of this function were generated on a \sqrt{nT} grid with $T = 1/32$ and transformed. The result is shown in Figure III.7b.1 as dots superimposed over a solid line which is the transform computed analytically ($2\sqrt{1-r^2}$). The output matches the analytic solution well.

Example 2 (a)

For the second example we transformed the function

$$\frac{J_1(r)}{r} w(r) \quad (13)$$

where $w(r)$ is a Hanning window. 2048 samples on a \sqrt{nT} grid with $T = 1/2$ were input (Figure III.7b.2). Figure III.7b.3 shows the output (dots) superimposed over the correct transform (solid line). The correct Abel transform was computed by evaluating the Fourier-Bessel series [11] to

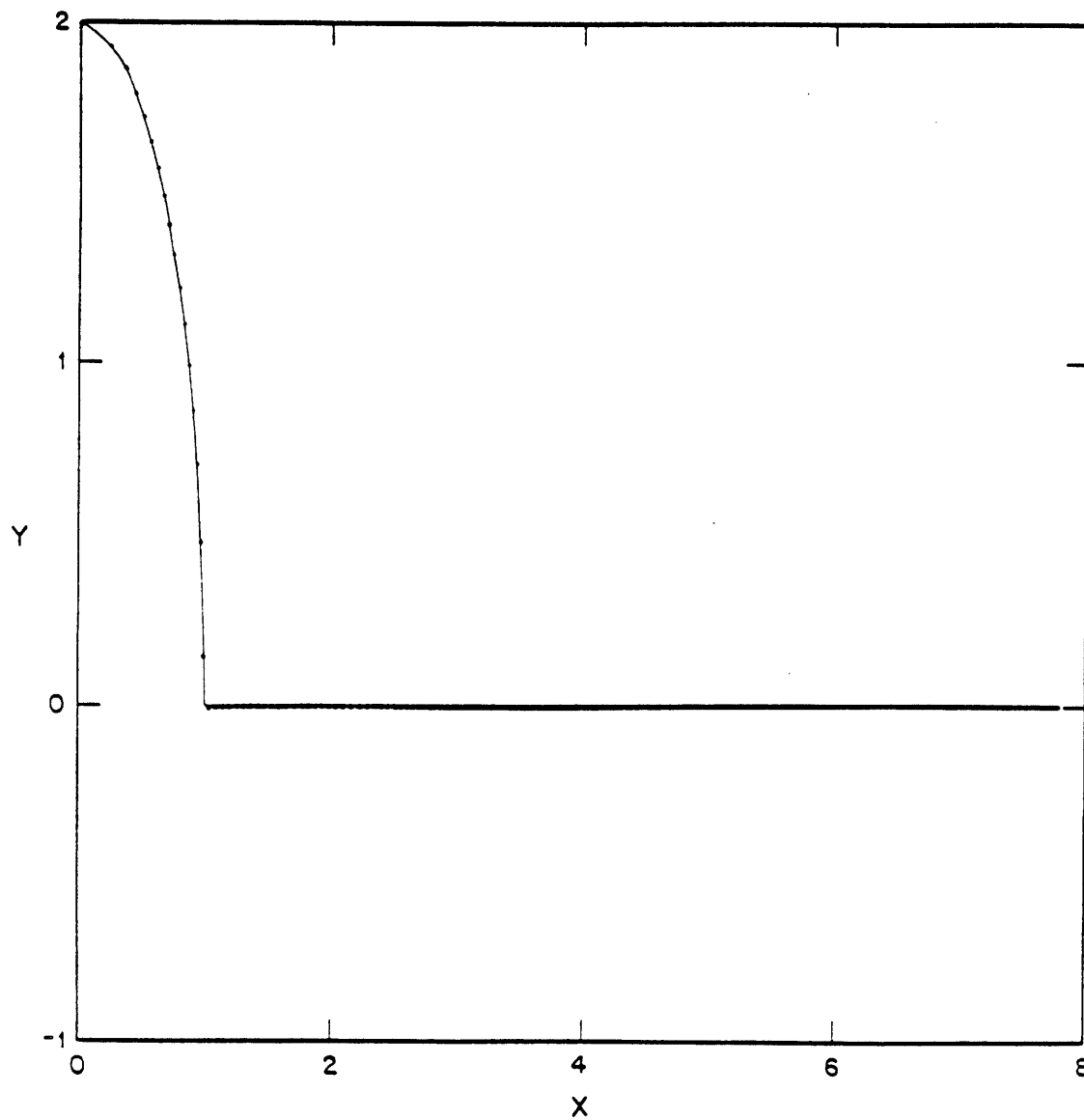


Figure III.7b.1 Superposition of the numerically generated Abel transform of a pillbox (dots) and the correct transform

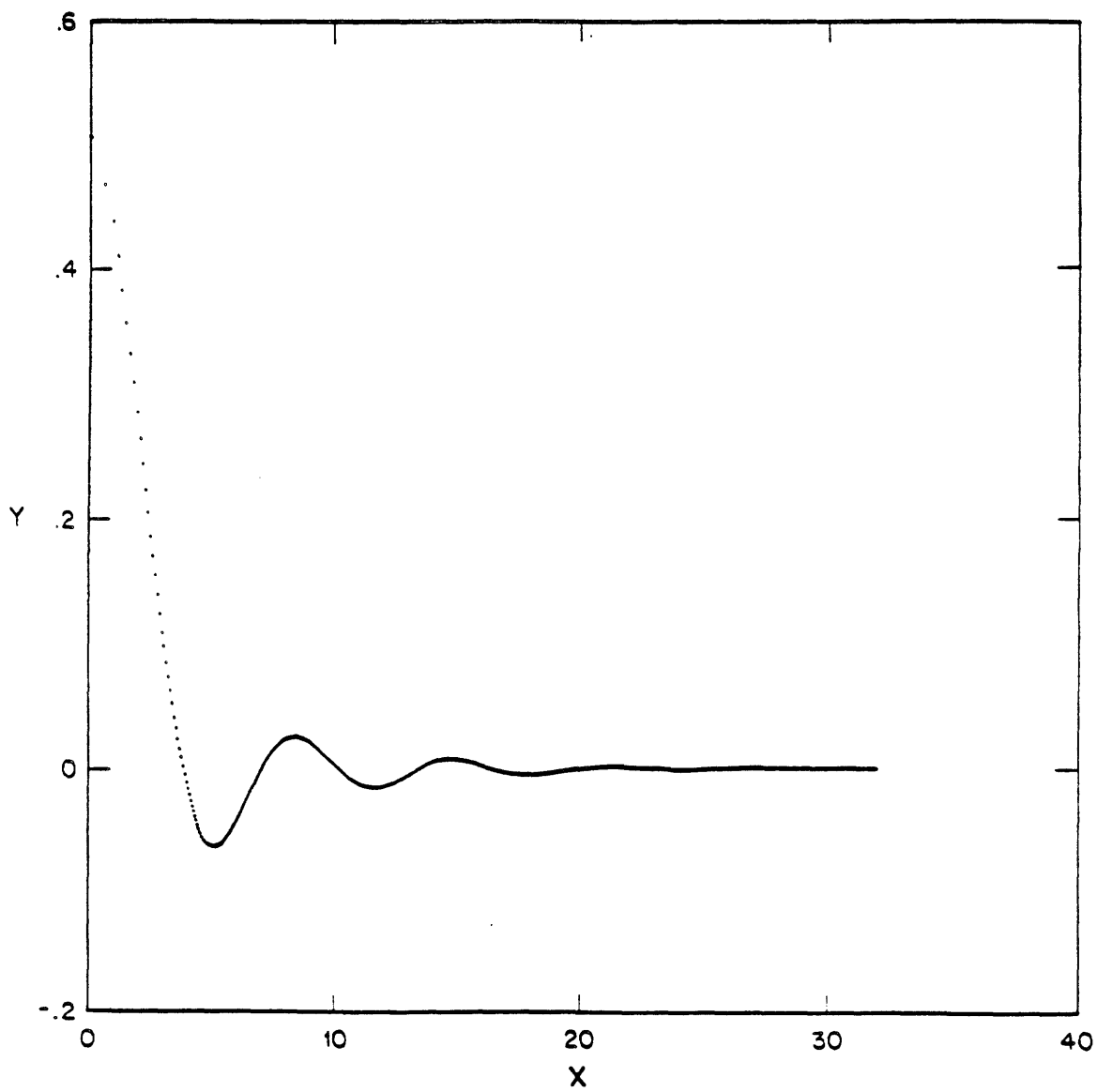


Figure III.7b.2 The input $\frac{J_1\sqrt{nT}}{\sqrt{nT}} W(nT)$ with $T = \frac{1}{2}$ and $n = 0, 1, 2, \dots, 2047$ where $W(nT)$ is a Hanning window.

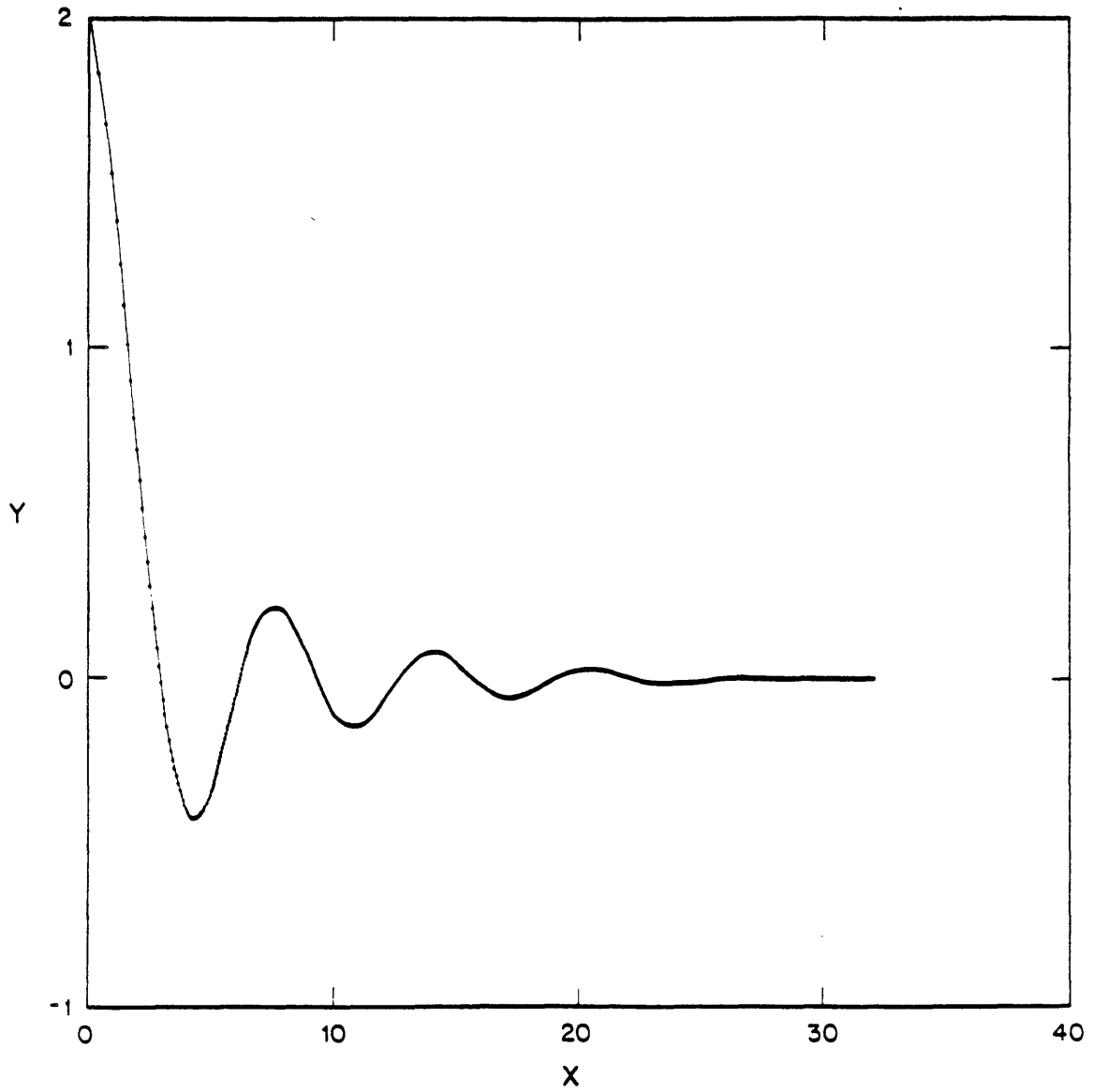


Figure III.7b.3 The Abel transform of Figure III.7b.2. The dots are the output of the proposed algorithm. The thin line is the correct output.

obtain a slow but accurate Hankel transform of the windowed input. The Hankel transform was then inverse Fourier transformed to generate the Abel transform. In the absence of the window the result would have been $\sin(r)/r$.

The output is coincident with the correct solution.

Example 3 (a)

For the third example we again transformed 2048 points of

$$\frac{J_1(r)}{r} w(r) \tag{20}$$

on the grid \sqrt{nT} but now T was chosen to be 4. This input is shown in Figure III.7b.4. Increasing the sampling interval reduced the effect of windowing on the input because a greater range of the function was represented but it also increased the sampling interval on the output. Figure III.7b.5 shows the output (dots) superimposed over the correct transform. Again, there is no discernible error.

c) *The Hankel Transform*

To complete the Hankel transform it is necessary to Fourier transform the projection obtained from the Abel transformer. Unfortunately this is available on a \sqrt{nT} grid and not the even grid required by the FFT. To generate $p(r)$ on an even grid it is necessary to interpolate. If a simple interpolation scheme is used, like sample and hold or linear interpolation, the result will be generated rapidly but may suffer some degradation. If a more sophisticated interpolator is used, better results can be expected but at the expense of greater computation time. Because the interpolation is from an uneven grid to an even grid (and not the reverse) it is difficult to characterize the error theoretically beyond the fact that the finer the initial grid the better the results. We complete the Hankel transform of the examples presented above using linear interpolation to generate the uniform grid.

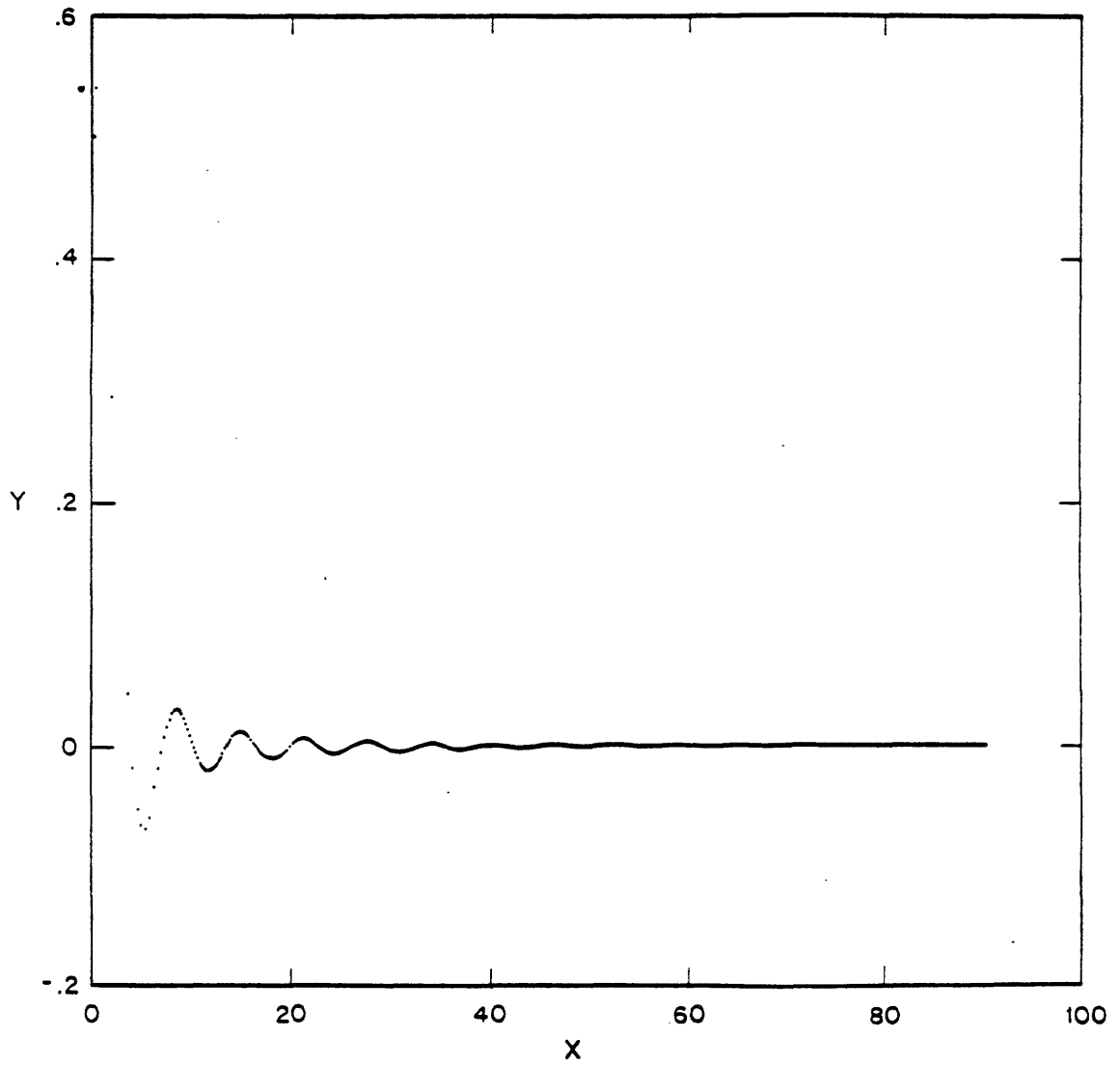


Figure III.7b.4 The input $\frac{J_1\sqrt{nT}}{\sqrt{nT}} W(nT)$ with $T=4$ and $n = 0, 1, 2, \dots, 2047$ where $W(nT)$ is a Hanning window.

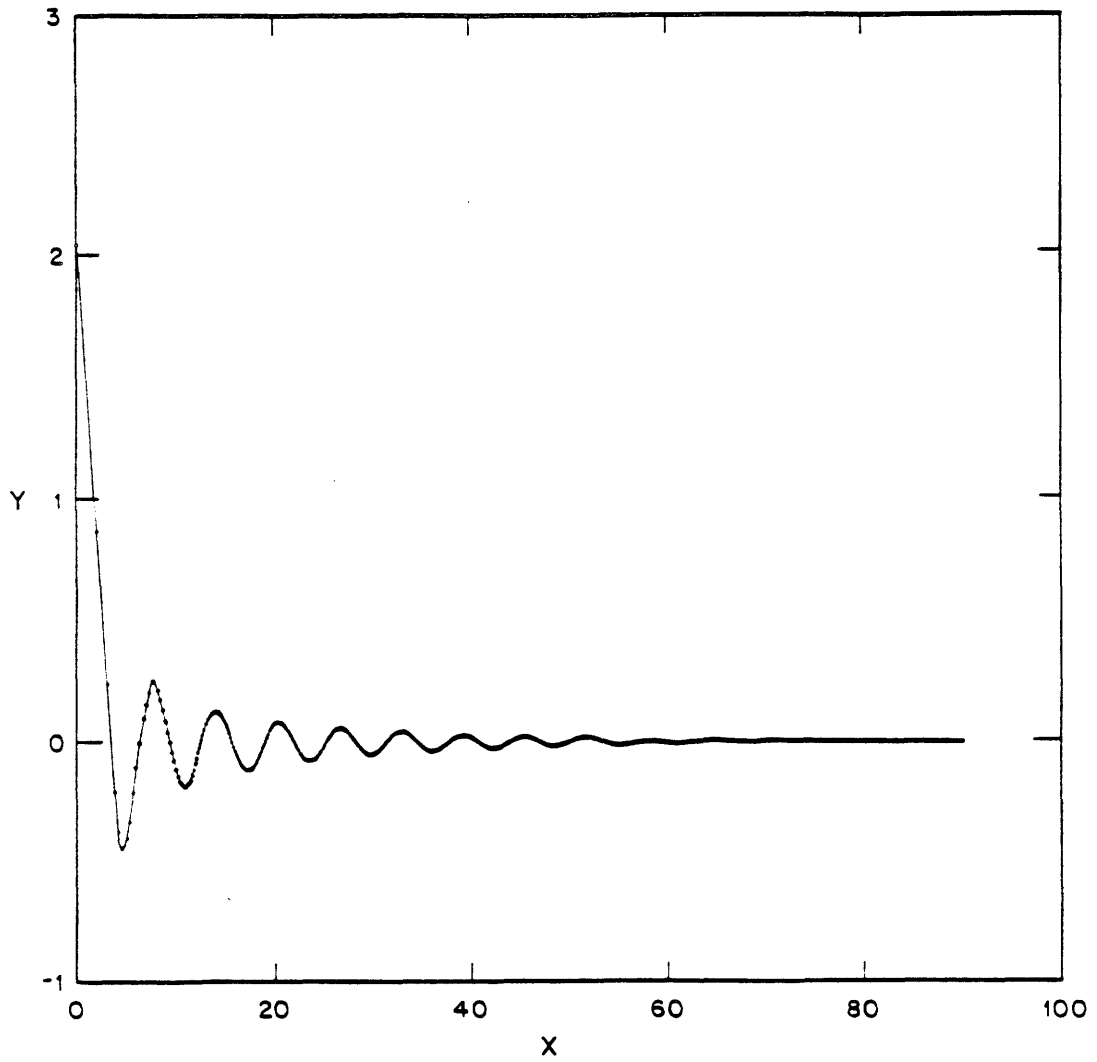


Figure III.7b.5 The Abel transform of Figure III.7b.4. The dots are the output of the proposed algorithm. The thin line is the correct output.

Example 1 (b)

Figure III.7c.1 shows the result of using a FFT on the linearly interpolated projection generated in Example 1 (a). The dots are the calculated output and are superimposed over the analytic solution (solid line). The agreement is excellent. The time required to perform the total Hankel transform (1024 input points to 1024 output points), including the required linear interpolation, was less than 31 seconds on a PDP 11-55 with a floating point processor.

Example 2 (b)

Figure III.7c.2 shows the result of Fourier transforming the linearly interpolated output of Example 2 (a). Again the dots represent the output of the Abel-Fourier scheme and the solid line is the Hankel transform as computed by the Fourier-Bessel series.[11] The agreement is excellent.

Example 3 (b)

Figure III.7c.3 compares the result of Fourier Transforming the linearly interpolated output of Example 3 (a) (dots) with the correct transform (solid). Significant distortion is apparent in this transform. Since the output of the Abel transform in example 3 (a) essentially equals the output in example 2 (a) (the correct projection) except for the sampling interval, we can associate this distortion with the linear interpolation performed before the FFT.

d) Discussion

We have found, as indicated by the examples above, that the Abel transformer works well. When its output can be successfully interpolated and is followed by a FFT the result is a fast, accurate Hankel Transform as illustrated by examples 1 and 2. As the spacing between output samples of the Abel transformer is increased, the suitability of a simple interpolation scheme becomes suspect. Example 3 was chosen to illustrate the effect of inappropriate interpolation on the resulting Hankel transform. At this point it would be prudent to determine the validity of a

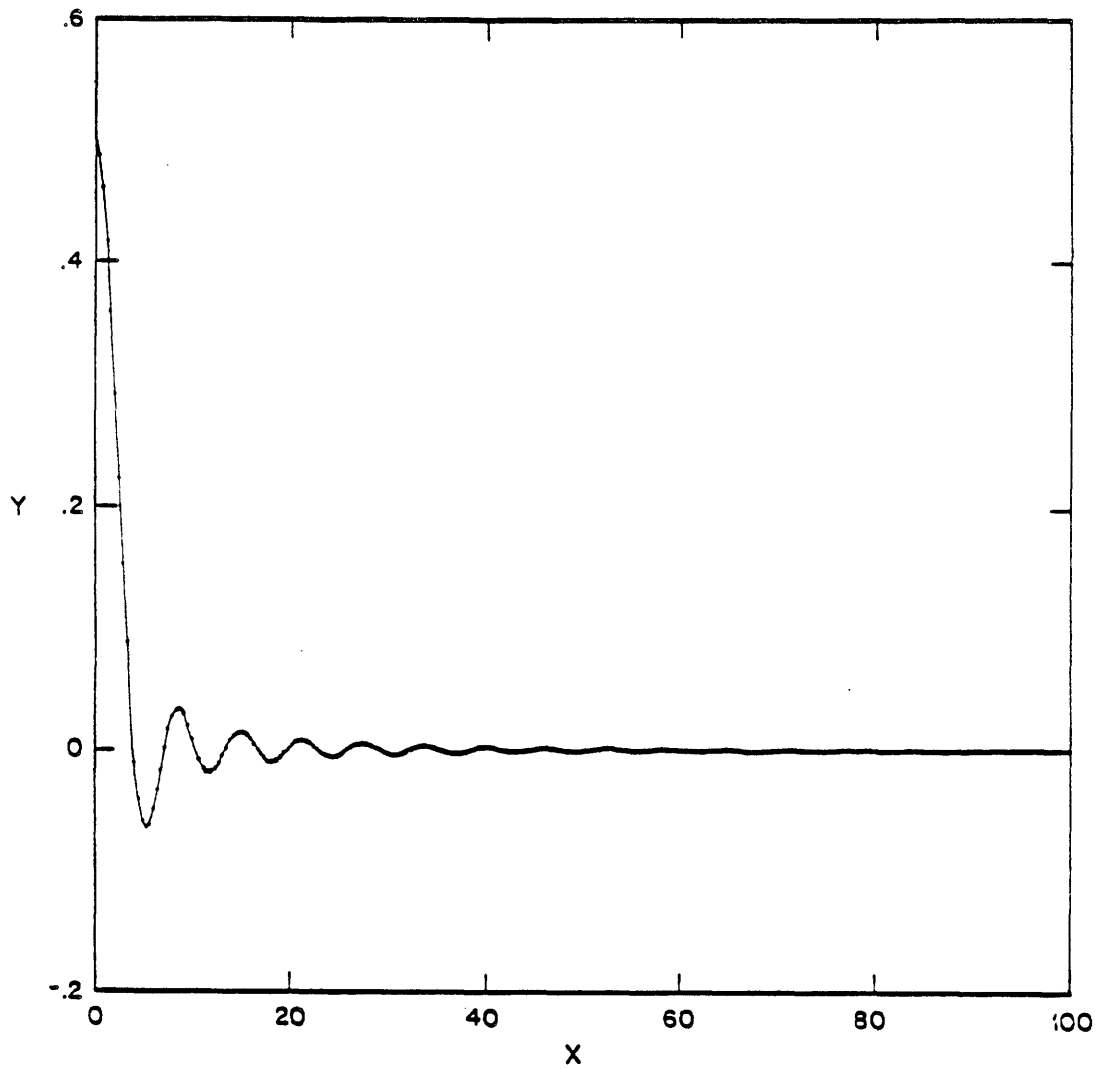


Figure III.7c.1 The Hankel transform of a pillbox computed by using an FFT on the linearly interpolated output of the Abel transformer presented in Figure III.7b.1.

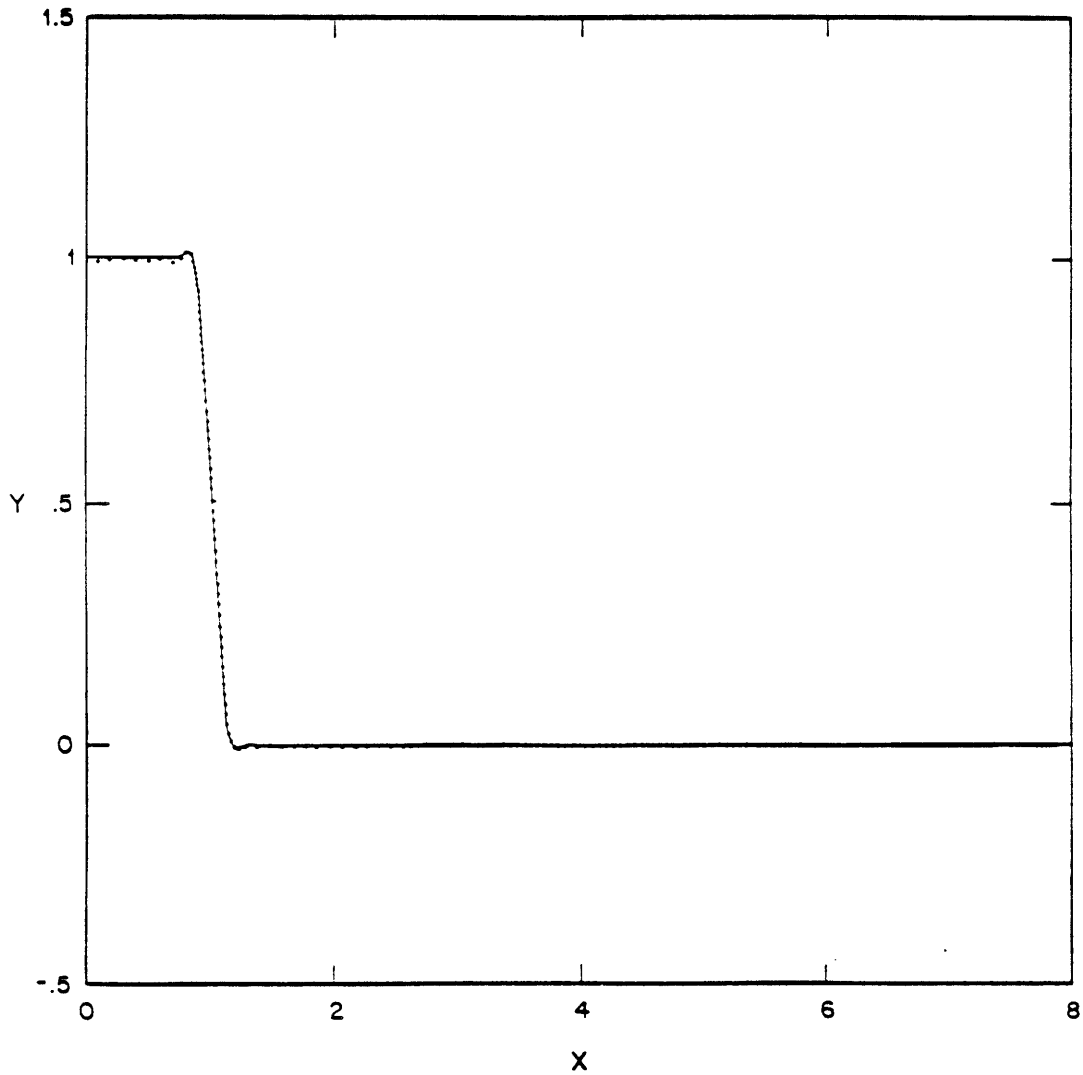


Figure III.7c.2 The Hankel transform of $\frac{J_1\sqrt{nT}}{\sqrt{nT}} W(nT)$ computed by using an FFT on the linearly interpolated output of the Abel transformer presented in Figure III.7b.3, $T = \frac{1}{2}$ case.

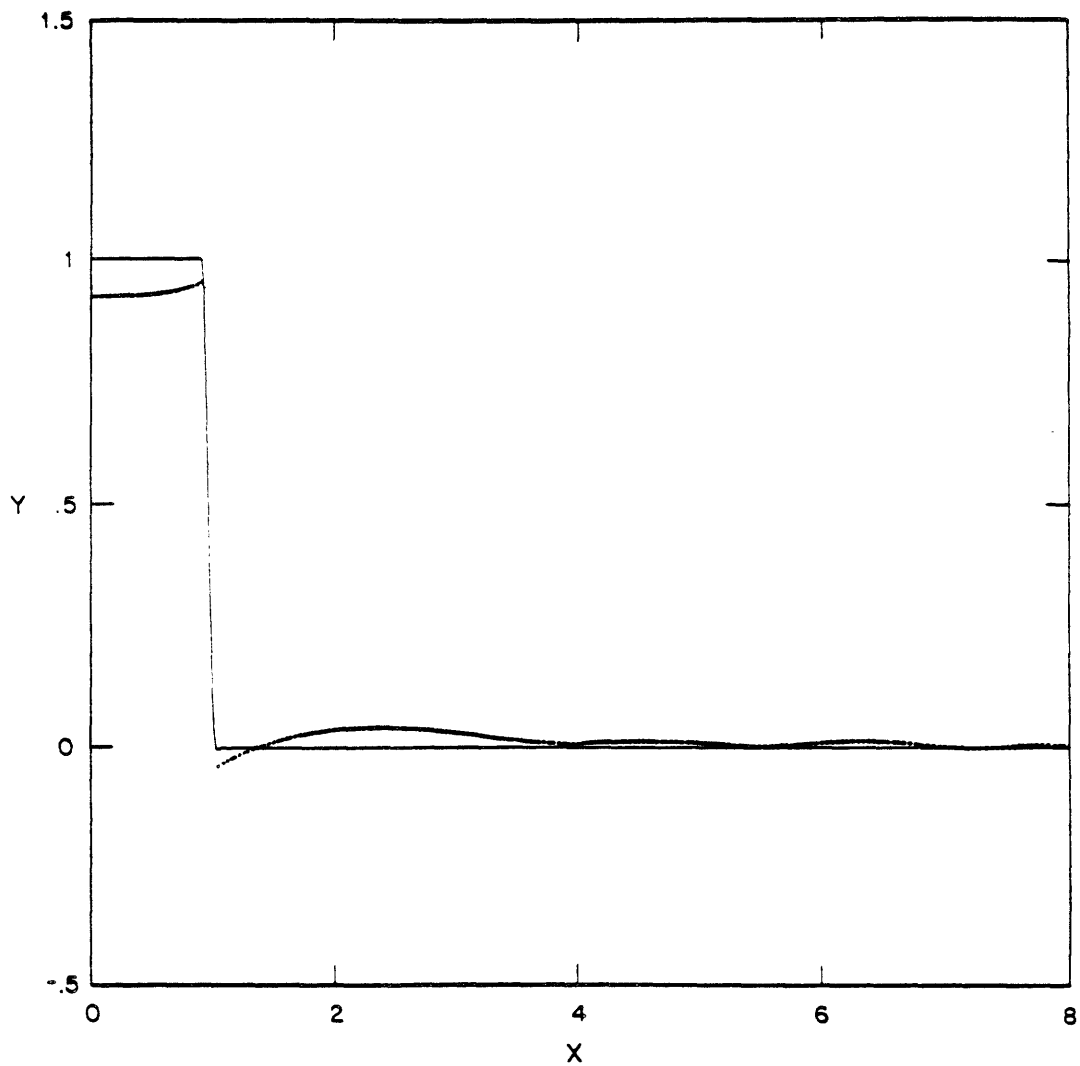


Figure III.7c.3 The Hankel transform of $\frac{J_1\sqrt{nT}}{\sqrt{nT}} W(nT)$ computed by using an FFT on the linearly interpolated output of the Abel transformer presented in Figure III.7b.5, $T = 4$ case.

Hankel transform performed with this algorithm by comparing the output for inputs of different grid spacings.

e) *Summary*

The procedure for performing the Hankel transform $H \cdot f(r) = F_H(v)$ is summarized below.

1) generate $\tilde{f}(r) \equiv f(\sqrt{r})$

2) Fourier transform to obtain $\tilde{F}(v)$

3) generate $L(v) \equiv \tilde{F}(v) - \tilde{F}(0)e^{-b|v|(1-\sqrt{v})/\sqrt{v}}$

4) perform the inverse Fourier transform and add in the analytic terms:

$$\tilde{p}(r) = \frac{1+i}{2} \left\{ IFT \cdot L(v) + \tilde{F}(0) \left\{ \frac{\sqrt{\pi}}{\sqrt{b-2\pi ir}} - \frac{1}{b-2\pi ir} - \frac{i\sqrt{\pi}}{\sqrt{b+2\pi ir}} - \frac{1}{b+2\pi ir} \right\} \right\}$$

5) interpolate to an even grid $p(r) = \tilde{p}(r^2)$

6) Fourier transform to obtain the Hankel transform

$$F_H(v) = FT \cdot p(r)$$

Each of steps 2) thru 6) requires no more than the order of $N \log(N)$ operations. Therefore the total transform can be accomplished on the order of $N \log(N)$ operations. Direct computation of projections from the 2 dimensional circularly symmetric function would have required at least N function evaluations and N sums for each of N points before the final FFT, which leads to an algorithm requiring on the order of N^2 operations. Therefore for sufficiently large N this method of calculating the projections can provide a considerable advantage in speed.

Steps 1) and 5) above indicate that in two places interpolations may be required. In many cases, however, the function to be transformed can be generated initially on a grid evenly spaced in \sqrt{r} . Further, $f(\sqrt{nT})$, as required by this algorithm, has the desirable feature that equal

areas of the underlying two dimensional function $f(r, \theta)$ are represented between samples. If stationary white gaussian noise (SWG N) corrupts the measurement of $f(\sqrt{nT})$ $n = 0, 1, \dots$ then the Hankel transform on a \sqrt{v} grid will be corrupted by SWGN (corruption of equal areas of the underlying two dimensional function produces corruption of equal areas of the underlying 2-D FT). This is not true if $f(nT)$ is corrupted by SWGN.

To implement a Hankel transform using this method it is necessary to perform the interpolations of step 5). Because of the speed of the Abel transform portion of this algorithm we have found it sufficient in many cases to simply generate an over sampled version of $\tilde{p}(r)$ and to use linear interpolation to obtain $p(r)$.

f) Conclusion

For many applications this method of calculating the Abel transform appears to permit the efficient calculation of the Hankel transform for large data files. This transform method is particularly appropriate for the evaluation of the Sommerfeld integral, in which the oscillations of the kernel increase with the independent variable. As a general transform method issues of representation on a \sqrt{r} grid must be further explored. Because of the equal area property described earlier for $f(\sqrt{r})$ and because the speed of this algorithm permits oversampling in $p(r^2)$ it is not expected that these issues will pose serious problems. It appears that the \sqrt{r} grid is of fundamental importance in the Hankel transform.

III.8) Summary

In this chapter we presented a number of numerical techniques for evaluating the Hankel transform. No one technique is ideal for all situations. When the value of the transform is desired at only a few points, the Fourier-Bessel series or the backsmeared method is appropriate. If speed is extremely important, accuracy is not, and the transform is not needed for small arguments, then the asymptotic method is justified. If the input function and its Abel transform can be well represented on a square root grid (which is the case for functions which increase in

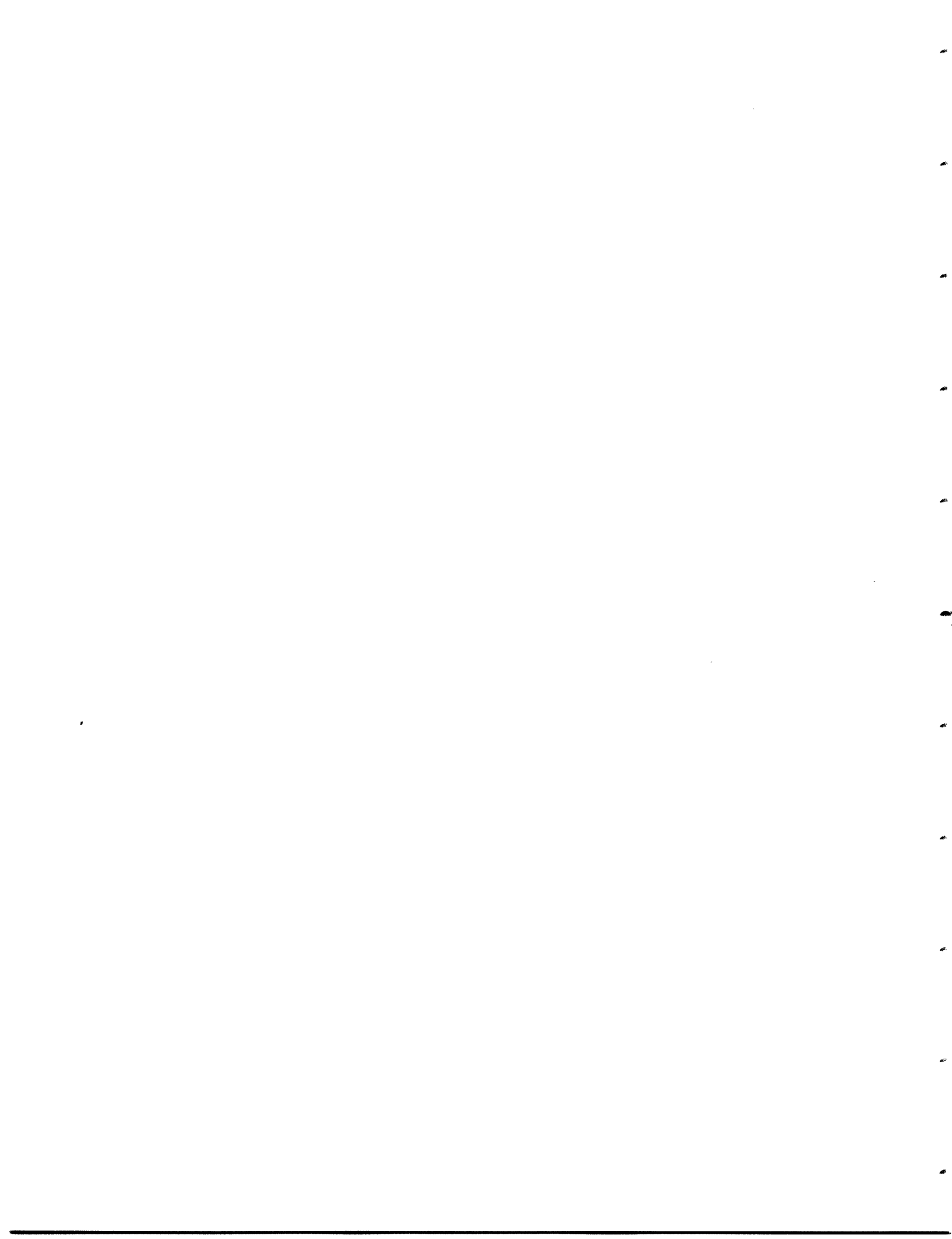
complexity with range) then the Hankel-Abel (or projection-slice) method is a good choice.

Having established the properties of the Hankel transform and examined its numerical implementation we are now ready to consider using it to generate synthetic data.

References

1. R. Bracewell, *The Fourier Transform and Its Applications*, McGraw-Hill, New York (1965).
2. G. N. Watson, *Theory of Bessel Functions 2nd Ed.*, Cambridge at the University Press, New York (1966).
3. W.H. Young, "On Series of Bessel Functions," *Proc. London Math. Soc* 2 XVIII, pp.163-200 (1920).
4. A.V. Oppenheim, G.V. Frisk, and D.R. Martinez, "An Algorithm for the Numerical Evaluation of the Hankel Transform," *Proc. IEEE* 66, pp.264-265 (1978).
5. M. Abramowitz and I.A. Stegun, H.E. Moses, and C.M. deRidder, *Properties of Dielectrics from Reflection Coefficients in One Dimension*, Lincoln Laboratory Technical Report no. 322, Washington DC (1972).
6. DiNapoli and Deavenport, "Theoretical and Numerical Green's Function Field Solution in a Plane Multilayered System," *J. Acoustical Soc. Amer.* 67, pp.92-105 (1980).
7. Lipschitz, *Journal fur Math.* 56, pp.189-196 (1859).
8. S. M. Candell, "Dual Algorithms for Fast Calculation of the Fourier-Bessel Transform," *IEEE ASSP* 29 no 5, pp.963-972 (Oct 1981).
9. Siegman, "Quasi Fast Hankel Transform," *Opt. Lett.* 1, pp.13-15 (July 1974).
10. H. K. Johansen and K. Sorensen, "Fast Hankel Transforms," *Geophys. Prosp.* 27, pp.876-901 (Dec. 1979).
11. A.V. Oppenheim, G.V. Frisk, and D. Martinez, "Computation of the Hankel Transform Using Projections," *J. Acoustical Soc. Amer.* 68 (2), pp.523-529 (1980).

12. D.R. Mook, "An Efficient Algorithm for the Numerical Evaluation of the Hankel and Abel Transforms," *IEEE ASSP*, to be published.



CHAPTER IV:

SYNTHETIC DATA GENERATION

IV.1) Overview

The generation of high quality synthetic pressure fields is an important branch of acoustic research. Because present methods can only approximately compute the fields associated with a point source for complex environments, simplified environments are often considered for which fewer approximations must be made. One important environment which lends itself well to analysis but which has sufficient complexity to be of interest for practical problems, is the horizontally stratified environment. It is an excellent model for the conditions present in the deep ocean over an abyssal plain, and consequently of direct interest to us. Currently, techniques for calculating synthetic fields arising from a CW point source in this environment exist in the literature [7, 11, 3] These techniques are based upon the numerical evaluation of the Sommerfeld integral [1], for which two major computational efforts are required. First, the plane wave reflection coefficient for the bottom profile must be numerically generated. For this the propagator matrix method [12, 8] is used. Second, the pressure field is computed as the Hankel transform of the depth-dependent Green's function (which is simply derived from the plane wave reflection coefficient). Typically, in these techniques many of the degradations associated with the numerical evaluation of the Hankel transform are not carefully controlled. In this chapter we exploit the properties of the Hankel transform derived in Chapter II to carefully control these errors. We will show in Section (IV.3a) that a major source of numerical error is aliasing, which becomes important because asymptotically the fields decay only as $\frac{1}{r}$.¹ We associate this slow rate of decay with the source singularity, $\frac{1}{\sqrt{k_0^2 - k_r^2}}$, in the depth-dependent Green's function and show how to separate this portion of the computation from the numerically computed Hankel transform.

¹) Assuming for the present that there are no trapped modes associated with low speed layers within the bottom.

The remaining numerical calculations are significantly less degraded by aliasing and are well behaved in general. They remain in the form of a Hankel transform for which we can exploit the computation efficiencies now available [9]. The result is a new hybrid procedure which is computationally efficient and significantly more accurate than existing methods. This hybrid scheme is illustrated with examples of synthetically generated fields.

In Section (IV.3b) we discuss the difficulties associated with numerically evaluating the Hankel transform of the depth-dependent Green's function when slow speed layers are present in the bottom which give rise to proper modes. Proper modes are associated with the $\frac{1}{k_r^2 - k_{r,2}^2}$ singularities (with $k_{r,2}$ near the real axis) in the depth-dependent Green's function and contribute terms to the field which decay asymptotically as $\frac{1}{\sqrt{r}}$. This very slow decay in the field causes severe aliasing problems when it is calculated using a numerical Hankel transform algorithm. In Section (IV.3b) we show how to separate the effects of proper modes from the numerical calculations by performing part of the Hankel transform analytically. We make this separation in such a manner that the portion of the field assigned to the analytical calculations is exact and finite for all ranges. This makes it possible to numerically calculate the residual numerical contribution to the field accurately and add the result to the analytically determined expression. The result of the total hybrid algorithm is a field which is accurate for all ranges and which can accurately include the effects due to proper modes arising in the presence of slow speed layers. We present an example of a field generated synthetically with this total hybrid method and show how the result is significantly better than what would have been achieved without removing the effect of the poles.

In this chapter we also develop a numerical implementation of the propagator matrix method for generating the plane wave reflection coefficient that is well behaved numerically. We begin the chapter by describing the computation of the plane wave reflection coefficient by means of the Thomson-Haskell method [12, 8].

IV.2) The Propagator Matrix Approach to Generating the Plane Wave Reflection Coefficient

a) The Method in Principle

1) Overview

To calculate the plane wave reflection coefficient we consider the response of a layered bottom to an incident plane wave as shown in Figure IV 2a.i.1. Within the n^{th} isovelocity layer we express the field as the vector:

$$\begin{bmatrix} P(z) \\ U(z) \end{bmatrix}_n J_0(k_r r) e^{-i\omega t} \quad (1)$$

where $P_n(z)$ is the pressure in the n^{th} layer and $U_n(z)$ is the normal component of the velocity. We have chosen this representation because $P(z)$ and $U(z)$ are continuous in z , even across layer interfaces. In the discussion which follows we will suppress the time and radial dependence of the field because they are the same in all layers.

In the propagator matrix approach, the impedance at the bottom layer:

$$\zeta_{N+1} = \frac{P(z_{N+1})}{U(z_{N+1})} \quad (2)$$

is available from the material parameters. In principle this impedance is used to determine the reflection coefficient at the top interface in three steps. First the field at the top interface is related to the field at the bottom interface by the propagator matrix:

$$\begin{bmatrix} P(z_0) \\ U(z_0) \end{bmatrix} = \Phi \begin{bmatrix} P(z_N) \\ U(z_N) \end{bmatrix} \quad (3)$$

Next the incident and reflected pressure waves at the surface are related to the field at the top interface and then to those at the bottom through:

$$\begin{bmatrix} P_{+,0} \\ P_{-,0} \end{bmatrix} = A \begin{bmatrix} P(z_0) \\ U(z_0) \end{bmatrix} = A \Phi \begin{bmatrix} P(z_N) \\ U(z_N) \end{bmatrix} = \begin{bmatrix} \alpha_{11} & \alpha_{21} \\ \alpha_{21} & \alpha_{22} \end{bmatrix} \begin{bmatrix} P(z_N) \\ U(z_N) \end{bmatrix} \quad (4)$$

Finally, the reflection coefficient is calculated in terms of the impedance, ζ_{N+1} , using

$$\begin{bmatrix} P_{+,0} \\ P_{-,0} \end{bmatrix} = \begin{bmatrix} \alpha_{11} & \alpha_{21} \\ \alpha_{21} & \alpha_{22} \end{bmatrix} \begin{bmatrix} 1 \\ \zeta_{N+1} \end{bmatrix} U(z_{N+1}) \quad (5)$$

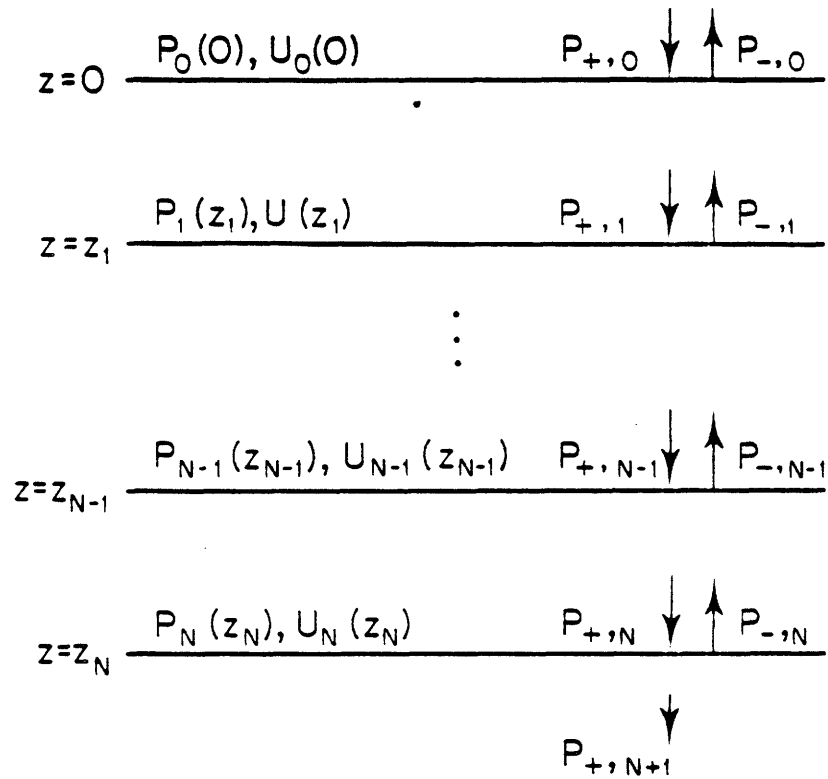


Figure IV.2a.i.1 The waves generated in a layered bottom in responses to an incident plane wave

so that

$$\Gamma = \frac{P_{-,0}}{P_{+,0}} = \frac{\alpha_{11} + \zeta_{N+1}\alpha_{12}}{\alpha_{21} + \zeta_{N+1}\alpha_{22}} \quad (6)$$

ii) The Propagator Matrix

The essential element of this approach is the propagator matrix, Φ , of Equation IV 2a.1.3. In this section we review its derivation.

Within any isovelocity layer, the field can be considered as the superposition of a positive and a negative traveling wave. The pressure field is given by

$$P(z) = P_+ e^{ik_1 z} + P_- e^{-ik_1 z} \quad (1)$$

The normal component of velocity, $U(z)$, is related to $P(z)$ through the telegraph equations [2]

For the non-normal case we use $-\frac{\partial P}{\partial z} = \rho \frac{\partial U}{\partial t} = -i\omega\rho U$ which implies that:

$$U(z) = \frac{ik_1}{i\omega\rho} P_+ e^{ik_1 z} - \frac{ik_1}{i\omega\rho} P_- e^{-ik_1 z} \quad (2)$$

or defining $Y_0 = \frac{k_1}{\omega\rho}$:

$$U(z) = Y_0 P_+ e^{ik_1 z} - Y_0 P_- e^{-ik_1 z} \quad (3)$$

In matrix form Equations (1) and (3) become:

$$\begin{bmatrix} P(z) \\ U(z) \end{bmatrix} = \begin{bmatrix} e^{ik_1 z} & e^{-ik_1 z} \\ Y_0 e^{ik_1 z} & -Y_0 e^{-ik_1 z} \end{bmatrix} \begin{bmatrix} P_+ \\ P_- \end{bmatrix} \quad (4)$$

If $\begin{bmatrix} P(z_1) \\ U(z_1) \end{bmatrix}$ is known at some point in the layer then $\begin{bmatrix} P(z_2) \\ U(z_2) \end{bmatrix}$ can be computed in principle by

inverting Equation (4) to find $\begin{bmatrix} P_+ \\ P_- \end{bmatrix}$ in terms of $\begin{bmatrix} P(z_1) \\ U(z_1) \end{bmatrix}$ and then calculating $\begin{bmatrix} P(z_2) \\ U(z_2) \end{bmatrix}$ from $\begin{bmatrix} P_+ \\ P_- \end{bmatrix}$.

Combining these operations into one step gives:

$$\begin{bmatrix} P(z_2) \\ U(z_2) \end{bmatrix} = \begin{bmatrix} e^{ik_1 z_2} & e^{-ik_1 z_2} \\ Y_0 e^{ik_1 z_2} & -Y_0 e^{-ik_1 z_2} \end{bmatrix} \begin{bmatrix} e^{ik_1 z_1} & e^{-ik_1 z_1} \\ Y_0 e^{ik_1 z_1} & -Y_0 e^{-ik_1 z_1} \end{bmatrix}^{-1} \begin{bmatrix} P(z_1) \\ U(z_1) \end{bmatrix} \quad (5)$$

which gives us:

$$\begin{bmatrix} P(z_2) \\ U(z_2) \end{bmatrix} = \begin{bmatrix} \cos k_z(z_2-z_1) & \frac{i}{Y_0} \sin k_z(z_2-z_1) \\ iY_0 \sin k_z(z_2-z_1) & \cos k_z(z_2-z_1) \end{bmatrix} \begin{bmatrix} P(z_1) \\ U(z_1) \end{bmatrix} \quad (6)$$

The values of k_z and Y_0 are functions of the material parameters of the layer under consideration. In particular if c_n is the sound speed in layer n , ρ_n its density, k_r the horizontal wave number of the incident plane wave (by Snell's law common to all layers), and ω the temporal frequency of the CW source, then $k_n = \frac{\omega}{c_n}$, $k_z = \sqrt{k_n^2 - k_r^2}$, and $Y_0 = \frac{k_z}{\omega \rho}$.

To indicate explicitly the dependence on the material properties of the n^{th} layer we write:

$$\begin{bmatrix} P(z_2) \\ U(z_2) \end{bmatrix} = \Phi_n(z_2-z_1) \begin{bmatrix} P(z_1) \\ U(z_1) \end{bmatrix} \quad (7)$$

when z_2 and z_1 are both within layer n .

To calculate the field at the top interface in terms of the field at the bottom interface, as shown in Figure IV.2a.i.1, we can use the previous discussion which was applicable only to a single layer, to relate the field at z_n to the field at z_{n-1} :

$$\begin{bmatrix} P(z_{n-1}) \\ U(z_{n-1}) \end{bmatrix} = \Phi_n(z_{n-1}-z_n) \begin{bmatrix} P(z_n) \\ U(z_n) \end{bmatrix} = \Phi_n \begin{bmatrix} P(z_n) \\ U(z_n) \end{bmatrix} \quad (8)$$

We then iterate the procedure through all the layers to find

$$\begin{bmatrix} P(z_0) \\ U(z_0) \end{bmatrix} = \Phi_1 \Phi_2 \cdots \Phi_n \begin{bmatrix} P(z_n) \\ U(z_n) \end{bmatrix} = \Phi \begin{bmatrix} P(z_n) \\ U(z_n) \end{bmatrix} \quad (9)$$

b) Numerical Implementation

1) The modified propagation matrix

The bulk of computation associated with the propagator matrix approach is the accumulation of the matrices $\Phi_1 \Phi_2 \cdots \Phi_n$. When these are accumulated on the computer, the actual operation is $\Phi_1(\Phi_2(\cdots \Phi_n))$. It is possible for the scale of the accumulated product to differ dramatically from any particular Φ_i . Because of the limited dynamic range in the computer it is advisable to scale terms to make them comparable before accumulation. Fortunately the final cal-

calculation for the reflection coefficient depends only on ratios of elements in Φ . For this reason we normalize each of the Φ_i so that its largest value equals 1. This procedure alone could cause another problem stemming from the different scales in general for P and U , which is due to their different units. To bring P and U into the same units we do not actually relate

$$\begin{bmatrix} P(z_{n-1}) \\ U(z_{n-1}) \end{bmatrix} \text{ to } \begin{bmatrix} P(z_n) \\ U(z_n) \end{bmatrix} \quad (1)$$

but rather consolidate units by multiplying the normal component of velocity by the characteristic impedance of that layer. Therefore we actually calculate:

$$\begin{bmatrix} P(z_0) \\ \zeta_0 U(z_0) \end{bmatrix} = \begin{bmatrix} a_1 & b_1 \\ \xi_1 b_1 & \xi_1 a_1 \end{bmatrix} \cdots \begin{bmatrix} a_N & b_N \\ \xi_N b_N & \xi_N a_N \end{bmatrix} \begin{bmatrix} P(z_N) \\ \zeta_N U(z_N) \end{bmatrix} \quad (2)$$

where

$$\begin{aligned} k_{z,i} &\equiv \sqrt{(\omega/c_i)^2 - k_r^2} \\ \zeta_i &\equiv \frac{\omega \rho_i}{k_{z,i}} \\ \xi_i &\equiv \frac{\zeta_{i-1}}{\zeta_i} \\ a_i &\equiv \cos k_{z,i}(z_i - z_{i-1}) \\ b_i &\equiv -i \sin k_{z,i}(z_i - z_{i-1}) \end{aligned}$$

ii) Relation of the modified propagation matrix to the incident and reflected waves

We now relate the field variables to the incident plane wave and the resulting reflected plane wave by slightly modifying Equation (IV.2a.ii.4). We assume that the top interface is at $z = 0$ so that:

$$\begin{bmatrix} P(0) \\ \zeta_0 U(0) \end{bmatrix} = \begin{bmatrix} 1 & 0 \\ 0 & \zeta_0 \end{bmatrix} \begin{bmatrix} 1 & 1 \\ Y_0 & -Y_0 \end{bmatrix} \begin{bmatrix} P_{+,0} \\ P_{-,0} \end{bmatrix} \quad (1)$$

and

$$\begin{bmatrix} P_{+,0} \\ P_{-,0} \end{bmatrix} = \frac{1}{2} \begin{bmatrix} 1 & \frac{1}{Y_0} \\ 1 & \frac{-1}{Y_0} \end{bmatrix} \begin{bmatrix} 1 & 0 \\ 0 & Y_0 \end{bmatrix} \begin{bmatrix} P(0) \\ \zeta_0 U(0) \end{bmatrix} \quad (2)$$

By defining:

$$\begin{bmatrix} \phi_{11} & \phi_{12} \\ \phi_{21} & \phi_{22} \end{bmatrix} = \prod_{i=1}^N \begin{bmatrix} a_i & b_i \\ \xi_i b_i & \xi_i a_i \end{bmatrix} \quad (3)$$

and using Equation (IV.2b.i.2) we have:

$$\begin{bmatrix} P_{+,0} \\ P_{-,0} \end{bmatrix} = \frac{1}{2} \begin{bmatrix} 1 & 1 \\ 1 & -1 \end{bmatrix} \begin{bmatrix} \phi_{11} & \phi_{12} \\ \phi_{21} & \phi_{22} \end{bmatrix} \begin{bmatrix} P(z_N) \\ \zeta_N U(z_N) \end{bmatrix} \quad (4)$$

We now need to use the fact that the pressure and velocity fields in the last layer are made up of only positive traveling waves so that (referring to Equation IV.2a.ii.4) $P_{N+1} = P(z_N)$ and

$U_{N+1} = \frac{1}{\zeta_{N+1}} P(z_N)$ we have

$$\begin{bmatrix} P_{+,0} \\ P_{-,0} \end{bmatrix} = \frac{1}{2} \begin{bmatrix} \phi_{11} + \phi_{21} & \phi_{12} + \phi_{22} \\ \phi_{11} - \phi_{21} & \phi_{12} - \phi_{22} \end{bmatrix} \begin{bmatrix} 1 \\ \frac{\zeta_N}{\zeta_{N+1}} \end{bmatrix} P_{N+1} \quad (5)$$

If we now use

$$\xi_{N+1} = \frac{\zeta_N}{\zeta_{N+1}} \quad (6)$$

we have the reflection coefficient

$$\Gamma = \frac{P_{-,0}}{P_{+,0}} = \frac{\phi_{11} - \phi_{21} + \xi_{N+1}(\phi_{12} - \phi_{22})}{\phi_{11} + \phi_{21} + \xi_{N+1}(\phi_{12} + \phi_{22})} \quad (7)$$

Equations (IV.2b.ii.2) and (7) show that this approach uses only the ratios of the impedances in adjacent layers and never the impedances themselves. These ratios are much better behaved in general than the individual impedances. For this reason, because the use of P and $Y_0 U$ instead of P and U , and because of the scaling of the layer propagation matrices this implementation of the propagator matrix approach has good numerical properties.

c) Selected Properties of the Reflection Coefficient

In Figure IV.2c.2 we present a perspective plot of the log magnitude of the reflection coefficient as a function of k_r for the bottom of Figure IV.2c.1 calculated using the numerical

$$f = 220 \text{ Hz}$$

$$|z + z_0| = 2 \text{ m}$$

$$k_0 = .8975979 \text{ m}^{-1}$$

$$C_0 = 1540 \text{ m/s}$$

$$\rho_0 = 1 \text{ g/cm}^3$$

$$C_1 = 1493.8 \text{ m/s}$$

$$\rho_1 = 1.5 \text{ g/cm}^3$$

↑
10 m
↓

$$C_2 = 1700 \text{ m/s}$$

$$\rho_2 = 2.0 \text{ g/cm}^3$$

Figure IV.2c.1 The bottom parameters used to generate the reflection coefficient shown in Figure IV.2c.2

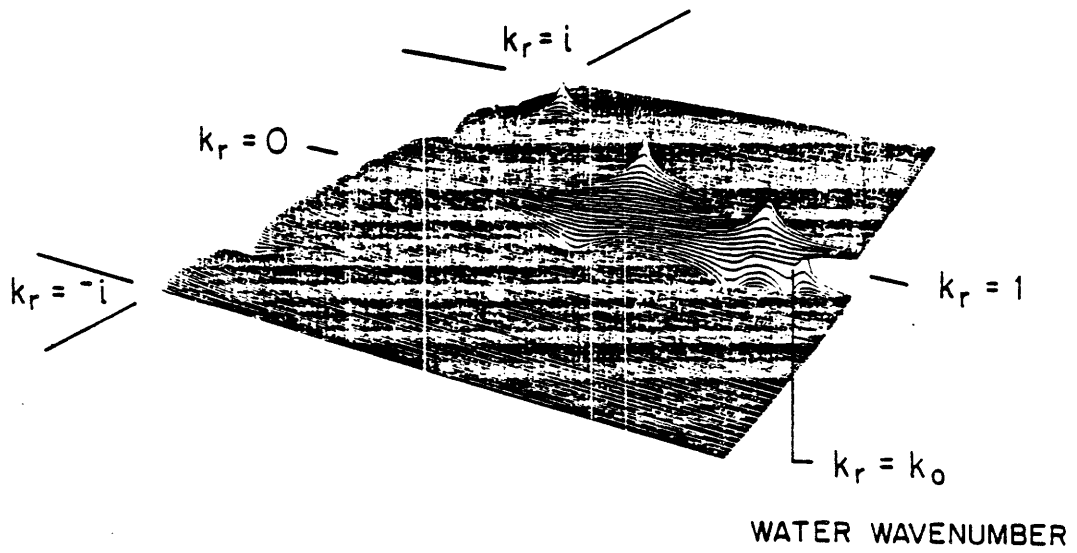


Figure IV.2c.2 Perspective plot of the log magnitude of the plane wave reflection coefficient for the bottom of Figure IV.2c.1

algorithm just described. The reflection coefficient is displayed both for those horizontal wave numbers corresponding to real angles of incidence ($0 < \text{Re}(k_r) < k_0$ where k_0 is the water wave number) and for horizontal wave numbers corresponding to complex angles of incidence ($k_0 < \text{Re}(k_r)$). The complex angles correspond to evanescent waves. Single evanescent waves do not carry any time average power flow (their Poynting vector is imaginary) and consequently the magnitude of the reflection coefficient is not limited to be less than one in the evanescent region, $k_0 < k_r$ [6]

In Figure IV.2c2 a pole is apparent in the reflection coefficient on the real k_r axis in the evanescent region. This on axis pole corresponds to a proper mode propagating in the low speed layer within the bottom. Other off axis poles corresponding to leaky modes are also apparent in the reflection coefficient. A discontinuity, or cut, can be seen extending from k_2 along the real k_r axis to infinity. This is the branch cut extending from the branch point at k_2 . Another cut extending from k_0 to infinity falls on this same line and is therefore not apparent. The origin of these branch points and cuts can be found in our derivation of the reflection coefficient where we associated

$$e^{i\sqrt{k_0^2 - k_r^2}z} \quad \text{with} \quad P_+ \quad (1)$$

and

$$e^{-i\sqrt{k_0^2 - k_r^2}z} \quad \text{with} \quad P_- \quad (2)$$

Clearly the roles of P_+ and P_- would be reversed by changing the choice of sign for the square root. For incident and reflected wave this would correspond to inverting the reflection coefficient (if no other waves were affected). The two sheets corresponding to the branch point at k_0 reflect the two choices of sign for the incident wave. We have displayed the choice associated with positive real power flow for the incident wave.

In the intermediate layers such as layer 1 of this example, changing the role of P_+ and P_- would not affect the reflection coefficient. For the intermediate layers, the physical problem does not name (or distinguish between) forward and backward traveling waves. Consequently there are

no branch points associated with intermediate layers.

If the opposite sign were chosen for the square root, $\sqrt{k_{N+1}^2 - k_r^2}$, associated with the emerging wave, $P_{+,N+1}$ from the bottom of the stack of layers (into the isovelocity half space) the direction of energy flow associated with that wave would change. Unlike the intermediate layer, there is no returning wave in the isovelocity half space. Consequently, the physical problem would change. For this reason we see a branch point at k_{N+1} reflecting the two different "physical" problems.

In Figure IV.2c2 we have chosen to display the Riemann sheet for which both $\text{Re}(\sqrt{k_0^2 - k_r^2}) > 0$ and $\text{Re}(\sqrt{k_{N+1}^2 - k_r^2}) > 0$. On this sheet only waves with real power flow in the positive direction are associated with P_+ . This constrains our incident waves to be those with power flow from the source to the layered bottom and specifies that there is no power flow returning from infinity.

When we perform the integrations discussed later we must choose which side of the cuts to integrate upon. For reasons of convergence we choose the side for which $\text{Im}(\sqrt{k_j^2 - k_r^2}) > 0$ when $j = 0$ and $N + 1$, is satisfied. Consequently, whenever we integrate the reflection coefficient in the complex k_r plane, we always satisfy both $\text{Re}(\sqrt{k_j^2 - k_r^2}) > 0$ and $\text{Im}(\sqrt{k_j^2 - k_r^2}) > 0$ for $j = 0$ and $N + 1$.

IV.3) Evaluating the Sommerfeld Integral

Once the plane wave reflection coefficient, $\Gamma(k_r)$, has been computed it is necessary to evaluate the Sommerfeld integral:

$$P_R(r) = \int_0^{\infty} \frac{i}{\sqrt{k_0^2 - k_r^2}} \Gamma(k_r) e^{i\sqrt{k_0^2 - k_r^2}|z+z_0|} J_0(rk_r) k_r dk_r \quad (1)$$

in order to compute the reflected pressure field. The Sommerfeld integral is in the form of a Hankel transform of the depth dependent Green's function,

$$G(k_r, z, z_0) = \frac{i}{\sqrt{k_0^2 - k_r^2}} \Gamma(k_r) e^{i\sqrt{k_0^2 - k_r^2}|z+z_0|}. \text{ The properties of the Hankel transform were}$$

developed in Chapter II. In Sections (6) and (7) of that chapter we discussed the effect of truncating the integration at some finite value, and the effect of sampling. The truncation was accomplished by multiplying the function to be transformed by some finite length window. For the generation of synthetic data we find that windowing of the Green's function is not an important consideration in general because when $z+z_0 > 0$, $G(k_r, z, z_0)$ decays exponentially in k_r for $k_r > k_0$. Except when $z+z_0$ is very small we can integrate Equation (1) until the Greens function is negligible and truncate at that point. It is not necessary to multiply by a windowing function.

The issue of sampling and the associated degradation introduced into the transform, aliasing, can be very much a problem however.

a) *The Source Singularity*

In order to highlight the issues associated with the source singularity, $\frac{i}{\sqrt{k_0^2 - k_r^2}}$, and the propagation terms in the Sommerfeld integral, we first consider the evaluation of Equation (IV.3.1) for a hard bottom case where $\Gamma(k_r) = 1$.

For the hard bottom case the pressure field is given by the known integral:

$$P_R(r) = \int_0^\infty \frac{i}{\sqrt{k_0^2 - \xi^2}} e^{i\sqrt{k_0^2 - \xi^2}|z+z_0|} J_0(\xi r) \xi d\xi = \frac{e^{ik_0\sqrt{r^2+(z+z_0)^2}}}{\sqrt{r^2+(z+z_0)^2}} \quad (2)$$

We evaluated this integral numerically with the Fourier-Bessel series to obtain an estimate for the field:

$$\hat{P}_R(r) = \frac{2}{A^2} \sum_1^N \frac{G\left(\frac{\lambda_n}{A}, z, z_0\right) J_0\left(r \frac{\lambda_n}{A}\right)}{J_1^2(\lambda_n)} \quad 0 < r < A \quad (3)$$

where for this example, A was chosen to be 2000 and $|z+z_0| = 2$. In Figure (IV.3a.1) we compare the log magnitude of the result (dots) with the known transform (solid curve).¹ We see that the magnitude of the numerically generated field, $\hat{P}_R(r)$, oscillates rapidly in contrast with the

¹The output of the Fourier-Bessel series has been displayed to twice its region of validity to better illustrate the source of degradation.

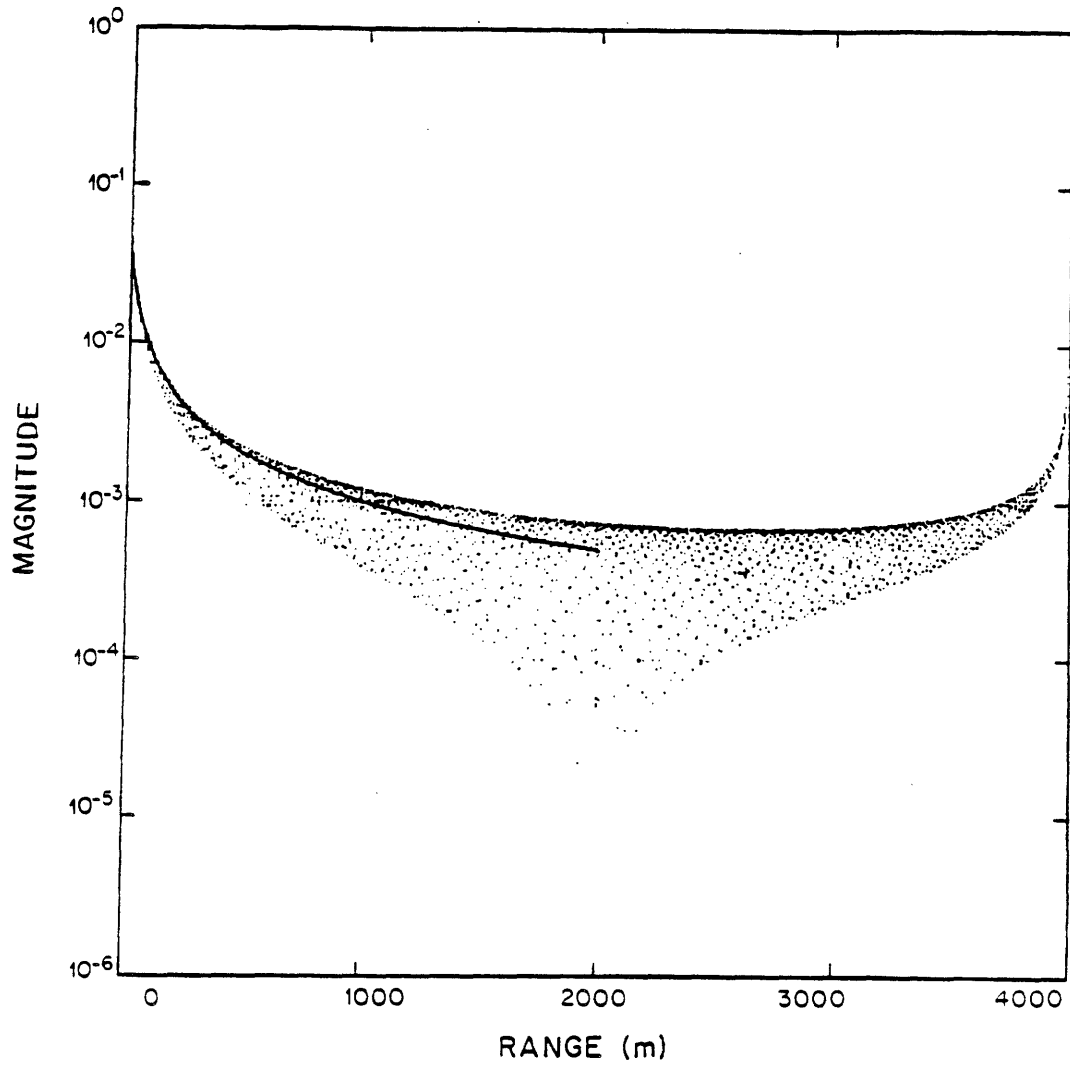


Figure IV.3a.1 A comparison of the log magnitude of the reflected field generated by a point source over a hard bottom (solid line) to the field numerically computed using the Fourier-Bessel series (scatter) which is shown to twice its presumed region of validity

true Hankel transform. As we will now show these oscillations are due to aliasing in the numerically computed Hankel transform.

In Section (II.7) we showed that the effect of sampling on the Hankel transform is to approximately produce an aliased estimate of the true transform, $\sqrt{r}P_R(r)$. Since for this example, $P_R(r)$ decays asymptotically as $1/r$, $\sqrt{r}P_R(r)$ decays asymptotically only as $1/\sqrt{r}$. What we see in Figure (IV.3a.1) is given approximately by:

$$0 < r < 2A \quad |\hat{P}_R(r)| \approx \left| \frac{1}{\sqrt{r}} \left[\sqrt{r} \frac{e^{ik_0\sqrt{r^2+(z+z_0)^2}}}{\sqrt{r^2+(z+z_0)^2}} - \sqrt{2A-r} \frac{e^{ik_0\sqrt{(2A-r)^2+(z+z_0)^2}}}{\sqrt{(2A-r)^2+(z+z_0)^2}} \right] \right| \quad (4)$$

When r is much greater than $z+z_0$, $\hat{P}_R(r)$ is approximately:

$$0 < r < 2A \quad |\hat{P}_R(r)| \approx \left| \frac{1}{\sqrt{r}} \left[\frac{e^{ik_0r}}{\sqrt{r}} - \frac{e^{ik_0|2A-r|}}{\sqrt{2A-r}} \right] \right| \quad (5)$$

Since we are in the region $r < 2A$ this can be rewritten:

$$0 < r < 2A \quad |\hat{P}_R(r)| \approx \left| \frac{1}{\sqrt{r}} \left[\frac{e^{ik_0r}}{\sqrt{r}} - \frac{e^{ik_02A}}{\sqrt{2A-r}} e^{-ik_0r} \right] \right| \quad (6)$$

We can write Equation (6) in terms of the desired transform and a modulation term as:

$$|\hat{P}_R(r)| \approx \left| \frac{1}{\sqrt{r}} \left[\left(\frac{1}{\sqrt{r}} - \frac{e^{ik_02A}}{\sqrt{2A-r}} \right) e^{ik_0r} + 2i \frac{e^{ik_02A}}{\sqrt{2A-r}} \sin k_0r \right] \right| \quad (7)$$

Which upon defining $\epsilon(r) \equiv \frac{e^{ik_02A}}{\sqrt{2A-r}}$

$$|\hat{P}_R(r)| \approx \left| \left[\frac{1}{r} - \frac{\epsilon(r)}{\sqrt{r}} \right] e^{ik_0r} + 2i \frac{\epsilon(r)}{\sqrt{r}} \sin k_0r \right| \quad (8)$$

When $r \ll 2A$ $\epsilon(r)$ is small, so that the magnitude of $\hat{P}_R(r)$ appears as roughly the correct transform with a modulation term.

We note at this point that if we had sampled the output of our transform at an integral multiple of $2\pi/k_0$ we would not have seen these oscillations. At this sampling rate the cosine would have appeared as a DC offset in the magnitude of the pressure field. If the output sampling rate were near but not exactly an integral multiple of $2\pi/k_0$ the $\cos(k_0r)$ would have appeared as a low frequency modulation because the sampling is in effect demodulating the cosine down to a

low (but not now zero) frequency. This result is an important one because frequently pressure fields are generated by using an FFT based approximation to the Hankel transform (IV.3.1) and the water wave number is the maximum wave number used [5,4] The grid resulting from such processing is exactly an integral multiple of $2\pi/k_0$. Carrying the integration to higher wave number would make evident the modulation in the answer by automatically providing the output on a finer grid.

The problem of aliasing arose because the field being computed decayed only as $\frac{1}{r}$ which forces us to use a very high sampling rate to properly sample the Hankel transform. We now note that this $\frac{1}{\sqrt{r}}$ decay is due to the $\frac{1}{\sqrt{k_0^2 - k_r^2}}$ singularity in the Green's function. It is well known that the asymptotic, or far field, character of such a transform is determined by the singularities of the kernel over the path of integration [10]. The Green's function which is transformed in Equation (IV.3.1) was

$$G(k_r, z, z_0) \equiv \frac{i}{\sqrt{k_0^2 - k_r^2}} e^{i\sqrt{k_0^2 - k_r^2}|z|} \quad (9)$$

The asymptotic character of the transform, $P(r)$, is dominated by the singularity

$$\frac{1}{\sqrt{k_0^2 - k_r^2}} \quad (10)$$

The integral

$$\frac{e^{ik_0\sqrt{r^2+z^2}}}{\sqrt{r^2+z^2}} = \int_0^\infty \frac{i}{\sqrt{k_0^2 - k_r^2}} e^{i\sqrt{k_0^2 - k_r^2}|z|} J_0(k_r r) k_r dk_r \quad (11)$$

shows us that this singularity is in fact associated with the $1/r$ decay rate. Physically this singularity was due to the angular spectrum of the point source. The $1/r$ decay associated with this singularity is often associated with the point source by noting that the field around a point source must decay at that rate in a manner such that the intensity, which decays as the field squared, integrated over any three dimensional shell enclosing the point source, would not be a function of r .

The source of slow asymptotic decay we have isolated suggests a procedure for reducing the problem of aliasing. We remove the source singularity from the kernel, numerically transform what is left, and add the result to the analytically determined transform of the source singularity. When we remove the singularity we must do so in a manner such that the numerical transform we must perform is well behaved. We allow for a general $\Gamma(k_r)$ but at this time assume that $\Gamma(k_r)$ has no singularities along the real k_r axis with asymptotic contributions to the field capable of dominating those of the $\frac{i}{\sqrt{k_0^2 - k_r^2}}$ singularity.

To this end we rewrite integral (IV.3.1) as:

$$P_R(r) = \int_0^{\infty} \Gamma(k_r) \frac{i}{\sqrt{k_0^2 - k_r^2}} e^{i\sqrt{k_0^2 - k_r^2}|z+z_0|} J_0(k_r r) k_r dk_r = \quad (12)$$

$$\int_0^{\infty} [\Gamma(k_r) - \Gamma(k)] \frac{i}{\sqrt{k_0^2 - k_r^2}} e^{i\sqrt{k_0^2 - k_r^2}|z+z_0|} J_0(k_r r) k_r dk_r + \Gamma(k) \int_0^{\infty} \frac{i}{\sqrt{k_0^2 - k_r^2}} e^{i\sqrt{k_0^2 - k_r^2}|z+z_0|} J_0(k_r r) k_r dk_r \quad (13)$$

If we define:

$$L(k_r) \equiv [\Gamma(k_r) - \Gamma(k)] \frac{i}{\sqrt{k_0^2 - k_r^2}} e^{i\sqrt{k_0^2 - k_r^2}|z+z_0|} \quad (14)$$

so that $L(k_r)$ does not have the $1/\sqrt{k_0^2 - k_r^2}$ singularity at $k_r = k_0$,¹ then we can write Equation (13) as:

$$P_R(r) = \int_0^{\infty} L(k_r) J_0(k_r r) k_r dk_r + \Gamma(k) \frac{e^{ik\sqrt{r^2+(z+z_0)^2}}}{\sqrt{r^2+(z+z_0)^2}} \quad (15)$$

Because $L(k_r)$ does not have this singularity along the path of integration the output of the numerical transform will decay at a rate faster than $1/r$. The asymptotic $1/r$ decay is provided by

We show in the appendix that if the impedance and its first derivative at the interface is finite for $k_r = k_0$ then the

$$\lim_{k_r \rightarrow k_0} L(k_r) = \frac{Z_1}{\omega \rho_0}$$

where Z_1 is the impedance of the bottom at $k_r = k_0$, ω is 2π source frequency, and ρ_0 is the density of the water. For an isovelocity half space this expression reduces to

$$L(k_0) = \frac{\rho_1}{\rho_0 \sqrt{k_1^2 - k_0^2}}$$

Which is finite.

the analytic term which can be recognized as the specular reflection when r is very large (glancing incidence). These observations are confirmed in the examples which follow.

In the following examples we illustrate the generation of synthetic pressure fields through the hybrid algorithm implied by Equation (15) where the integral is performed with a numerical Hankel transform algorithm and the analytical expression is the result of integrating the singularity.

i) *Hard Bottom*

This is the degenerate example because for $\Gamma(k_r)$ constant, the entire transform is performed analytically. The result of the analytic transform was compared to the direct numerical transform Figure (IV.3a.1).

ii) *Slow bottom*

Figure (IV.3a.ii.1) shows the bottom parameters for this example. Figure (IV.3a.ii.2) shows the result of the hybrid calculation (solid line) versus a direct numerical calculation. The improvement is dramatic. Figure (IV.3a.ii.3) compares the hybrid field of Figure (IV.3a.ii.2), with its numerically generated component. As can be seen, the near field is dominated by the numerically generated component. As range increases this numeric term begins to suffer from aliasing problems but the analytic term begins to dominate, minimizing the effect of aliasing on the computed field at large ranges.

iii) *Fast Bottom*

Figure (IV.3a.iii.1) shows the parameters of the fast bottom for this example. Figure (IV.3a.iii.2) shows the hybrid calculation versus the direct numerical calculation. Figure (IV.3a.iii.3) presents the hybrid field and its numeric component. The improvements are similar to the fast bottom case.

b) *Poles Due to Slow Speed Layers*

$$f = 220 \text{ Hz}$$

$$|z + z_0| = 2 \text{ m}$$

$$k_0 = .8975979 \text{ m}^{-1}$$

$$C_0 = 1540 \text{ m/s}$$

$$\rho_0 = 1 \text{ g/cm}^3$$

$$C_1 = 1493.8 \text{ m/s}$$

$$\rho_1 = 1.5 \text{ g/cm}^3$$

Figure IV.3a.ii.1 Parameters of bottom used for slow bottom example

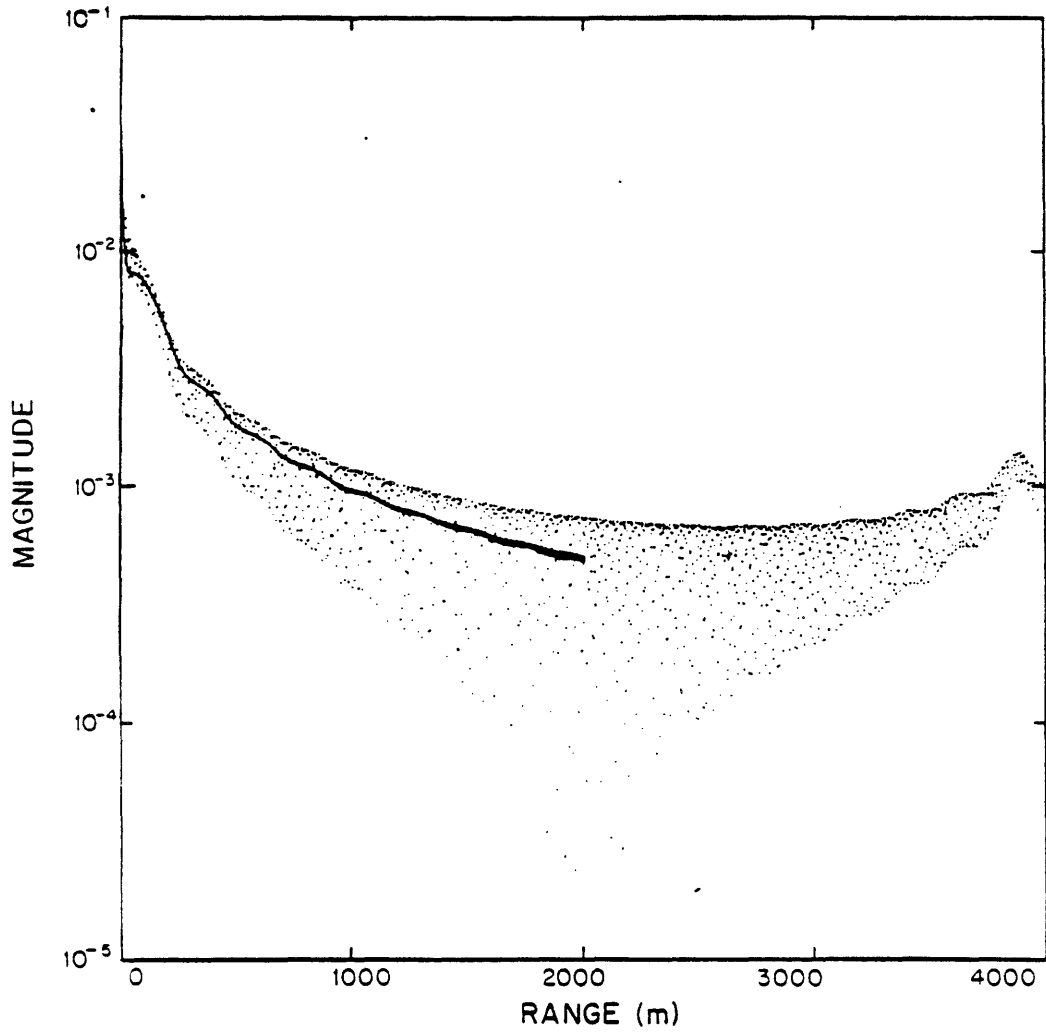


Figure IV.3a.ii.2 Log magnitude of field calculated using hybrid method (solid line) versus direct calculation (scatter) for slow bottom example

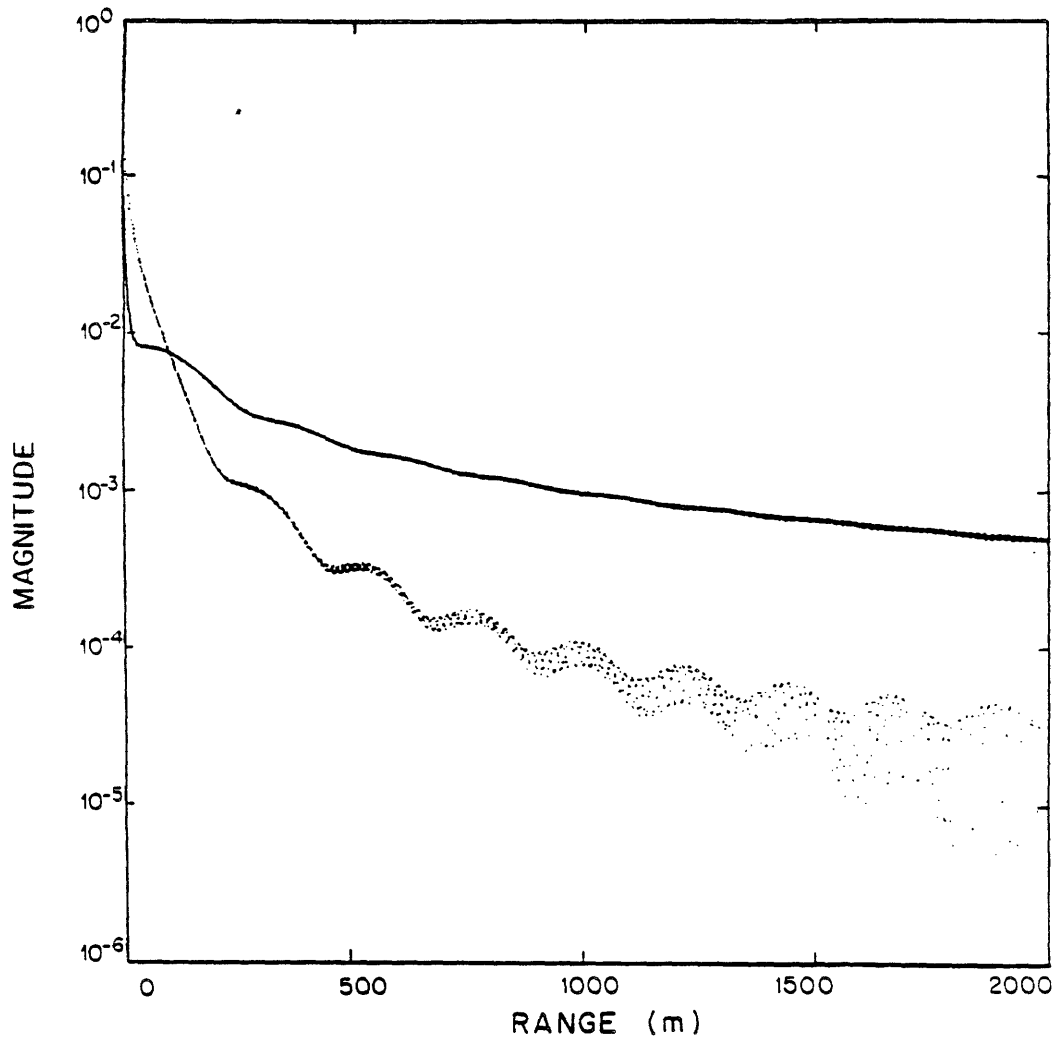


Figure IV.3a.ii.3 Comparison of hybrid field calculated for slow bottom example and its numerically generated component

$$f = 220 \text{ Hz}$$

$$|z + z_0| = 2 \text{ m}$$

$$k_0 = .8975979 \text{ m}^{-1}$$

$$C_0 = 1540 \text{ m/s}$$

$$\rho_0 = 1.0 \text{ g/cm}^3$$

$$C_1 = 1700 \text{ m/s}$$

$$\rho_1 = 2.0 \text{ g/cm}^3$$

Figure IV.3a.iii.1 Parameters of bottom used for fast bottom example

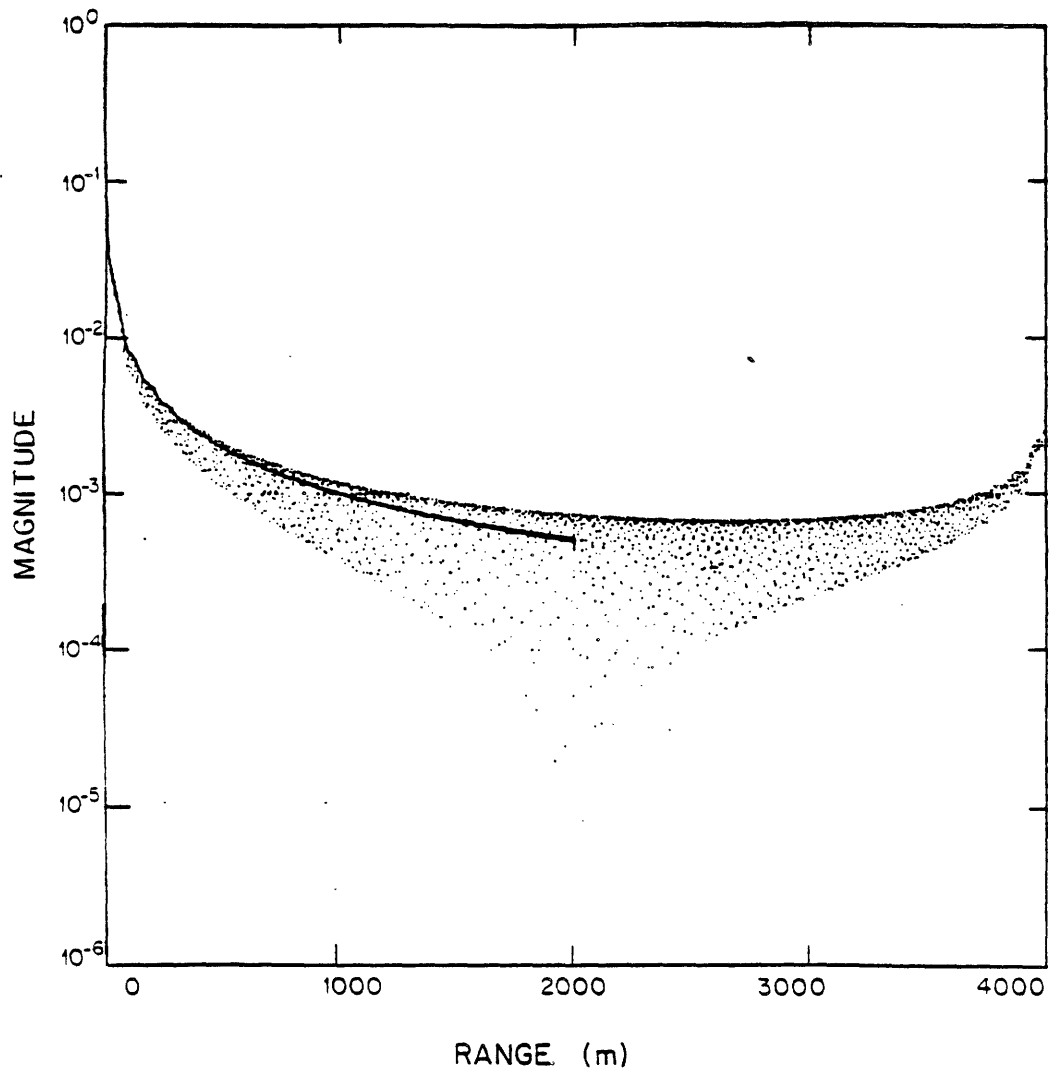


Figure IV.3a.iii.2 Log magnitude of field calculated using hybrid method (solid line) verses direct calculation (scatter) for fast bottom example

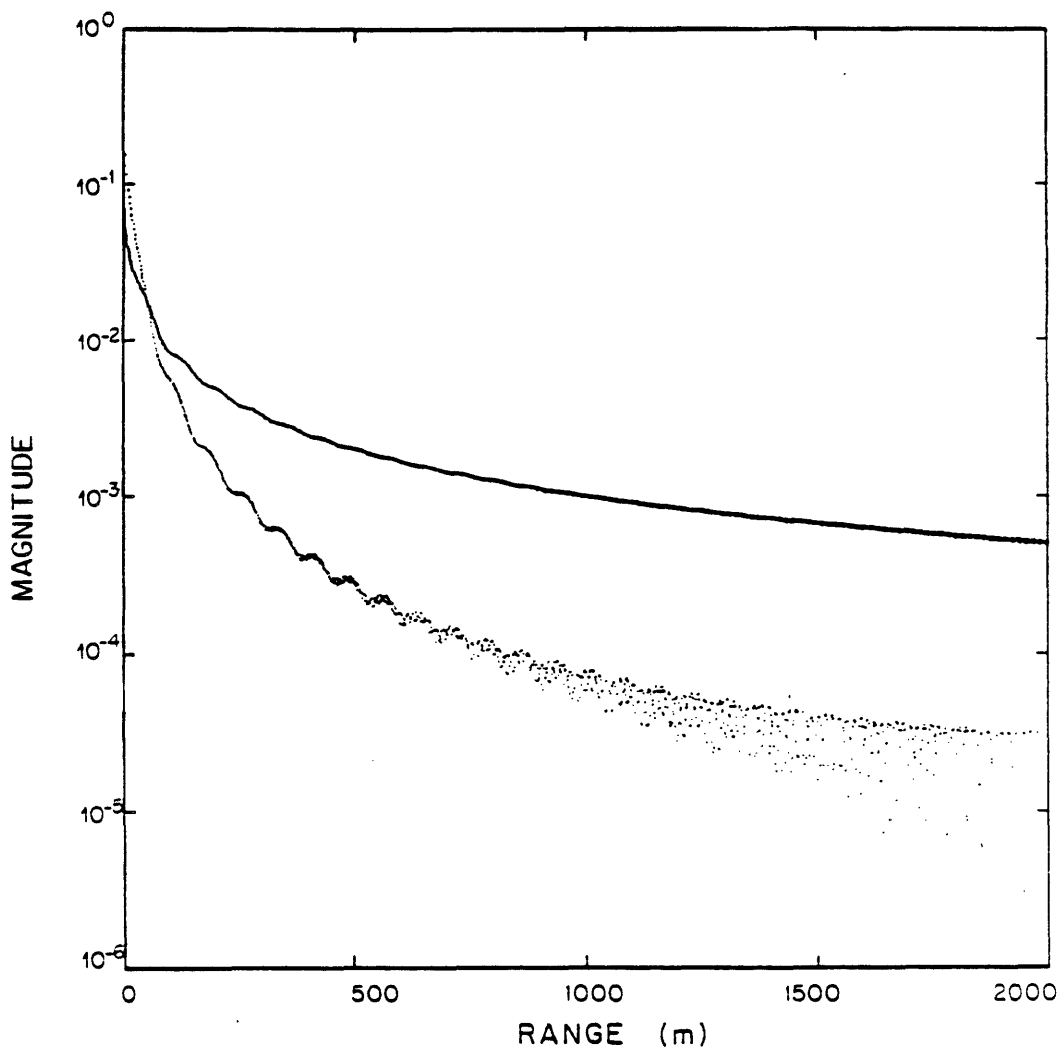


Figure IV.iii.3 Comparison of hybrid field calculated for fast bottom example with its numerically generated component

Figure (IV.3b.1) shows the parameters of a slow speed layer between two isovelocity half spaces. These are the same parameters used to generate the perspective plot of the reflection coefficient presented in Figure (IV.2c.2). Figures (IV.3b.2a) and (IV.3b.2b) show the magnitude and phase of the reflection coefficient for this bottom as a function of horizontal wave number. We see that for this example the reflection coefficient has a singular point beyond the water wave number, k_0 . That singularity is a simple pole associated with a proper mode excited in the low speed layer. Such a proper mode can appear only for $k_0 < k_r < k_{N+1}$. In this region conservation of energy is not violated because the waves are evanescent. Proper modes are generated when the low speed layer acts like a dielectric waveguide. When this happens energy diffuses (tunnels) from the point source to the low speed layer but does not otherwise propagate vertically. Energy from the field is now constrained to decay in only two dimensions instead of three and we expect that the field associated with the pole will decay asymptotically as $\frac{1}{\sqrt{r}}$ so that the integral of the flux over any two-dimensional ring surrounding the source remains constant.

Poles such as this disrupt the asymptotic character of the field derived in the previous section. As before we would like to analytically determine the contribution of these poles and remove them as we removed the $\frac{i}{\sqrt{k_0^2 - k_r^2}}$ singularity. To do so it is necessary to evaluate the integral:

$$I(r, z+z_0; k_{r_i}) \equiv \int_0^\infty \left[\frac{1}{k_r^2 - k_{r_i}^2} \right] \frac{i}{\sqrt{k^2 - k_r^2}} e^{i\sqrt{k^2 - k_r^2}|z+z_0|} J_0(k_r, r) k_r dk_r \quad (1)$$

In Appendix (I) we show that for $\text{Im}(k_{r_i}) \geq 0$ (associated with no return from $r = \infty$)

$I(r, z+z_0; k_{r_i})$ is given by:

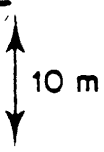
$$I(r, z+z_0; k_{r_i}) = \frac{-1}{2\beta} \int_{-\infty}^{\infty} \frac{e^{ik\sqrt{r^2 + \xi^2}}}{\sqrt{r^2 + \xi^2}} e^{-\beta|z+z_0 - \xi|} d\xi - \frac{i\pi}{2\beta} H_0^{(1)}(k_{r_i}, r) e^{-\beta|z+z_0|} \quad (2)$$

where

$$\beta \equiv +\sqrt{k_{r_i}^2 - k_0^2} \quad (3)$$

$$f = 220 \text{ Hz}$$
$$|z + z_0| = 2 \text{ m}$$
$$k_0 = .8975979 \text{ m}^{-1}$$

$$C_0 = 1540 \text{ m/s}$$
$$\rho_0 = 1 \text{ g/cm}^3$$

$$C_1 = 1493.8 \text{ m/s}$$
$$\rho_1 = 1.5 \text{ g/cm}^3$$


$$C_2 = 1700 \text{ m/s}$$
$$\rho_2 = 2.0 \text{ g/cm}^3$$

Figure IV.3b.1 Parameters of bottom used for slow speed layer example

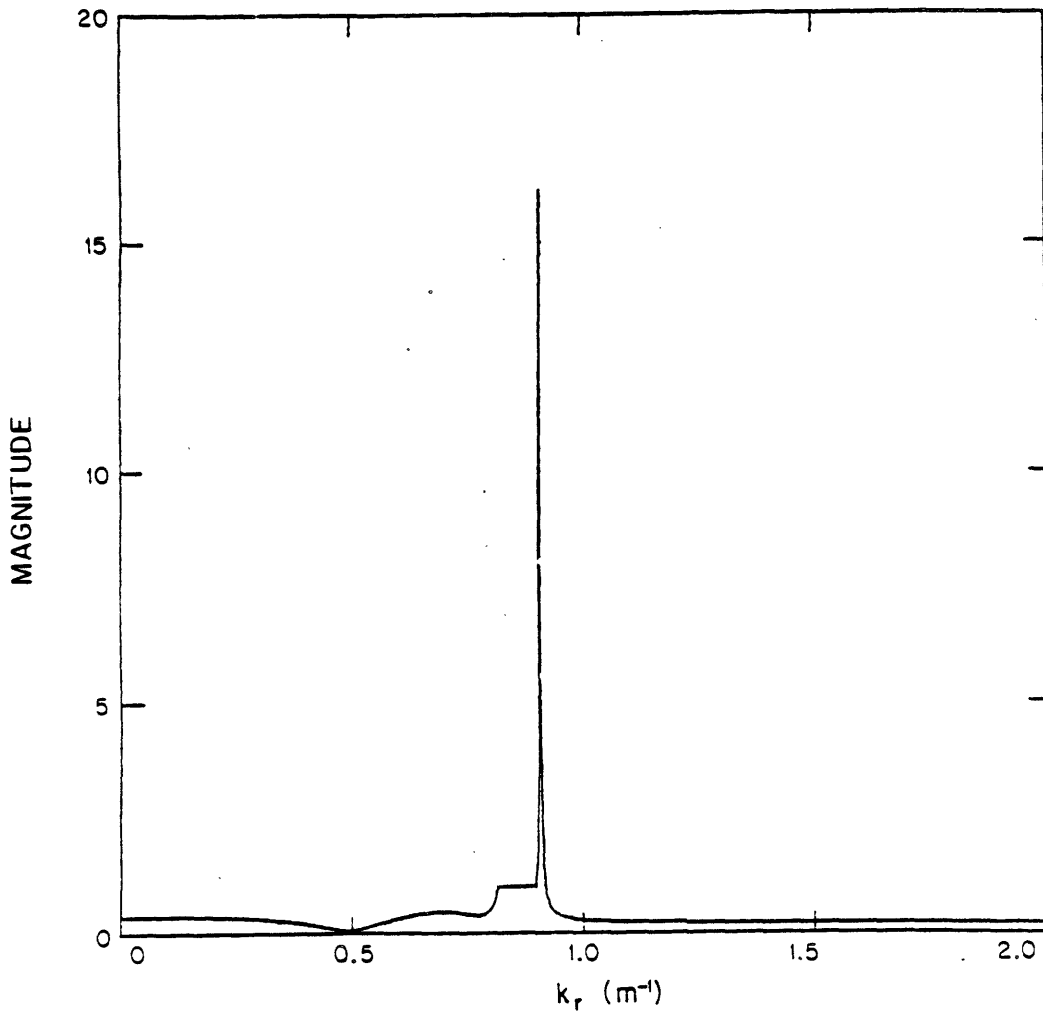


Figure IV.3b.2a Magnitude of reflection coefficient calculated for slow speed layer example

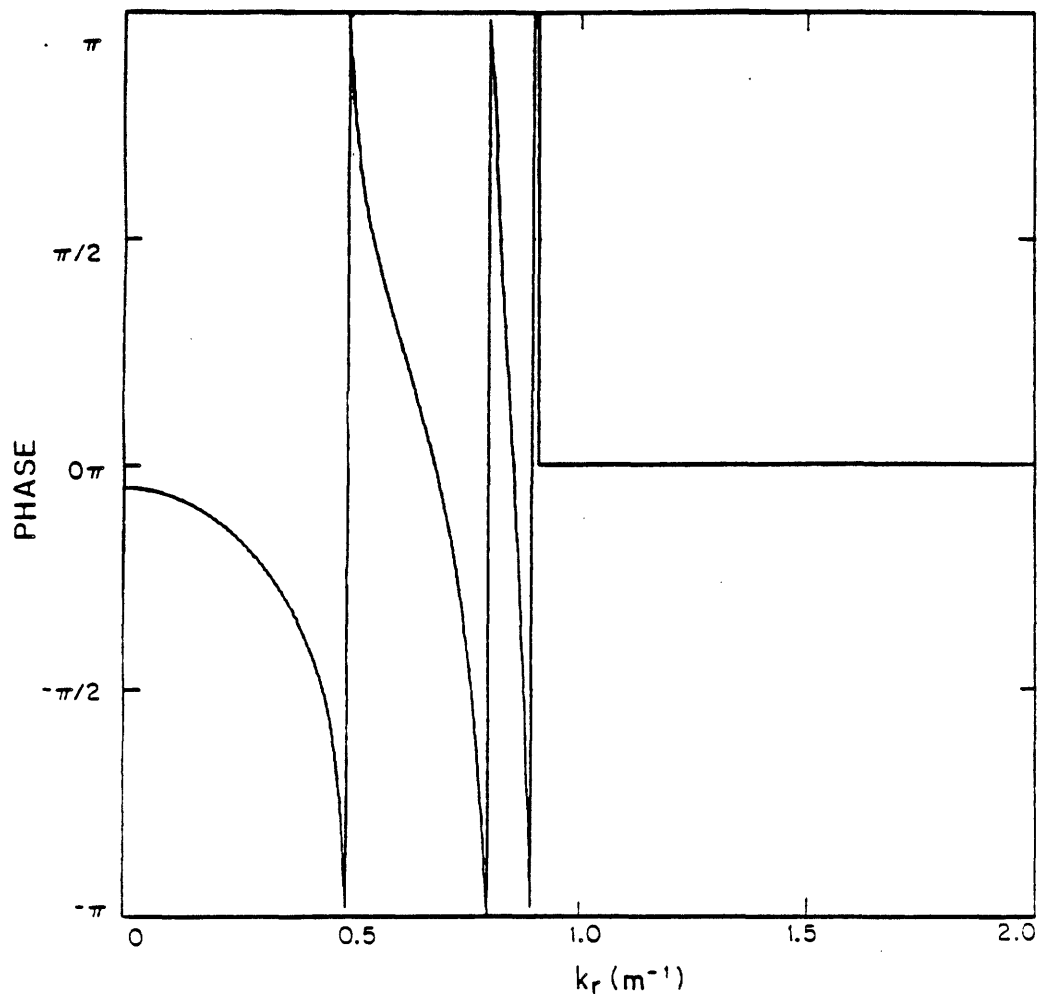


Figure IV.3b.2b Phase of reflection coefficient calculated for slow speed layer example

The first integral is easily evaluated on the computer. In addition as r becomes large the first term rapidly approaches:

$$\frac{-1}{2\beta^2} \frac{e^{ik_0\sqrt{r^2+(z+z_0)^2}}}{\sqrt{r^2+(z+z_0)^2}} \quad (4)$$

The second term decays as $1/\sqrt{r}$ when k_{r_i} is real.

Equation (2) is also correct for $\text{Im}(k_{r_i}) > 0$, but when $\text{Im}(k_{r_i}) \gg 0$ the poles no longer contribute asymptotically as $1/\sqrt{r}$ because the Hankel function decays exponentially. Under these conditions

$$H_0^{(1)}(k_{r_i}r) \approx \sqrt{2/\pi k_{r_i}r} e^{i(k_{r_i}r - \pi/4)} \equiv \frac{C(k_{r_i})}{\sqrt{r}} e^{i[k_{r_i} + ik_{r_i}']r} \quad (5)$$

$$= \frac{C(k_{r_i})}{\sqrt{r}} e^{-k_{r_i}r} e^{ik_{r_i}r} \quad (6)$$

As $\text{Im}(k_{r_i})$ becomes large the exponential decay dominates the $1/\sqrt{r}$ decay even over the finite range that concerns us. It is for this reason that we consider only those poles near the real axis (close to the path of integration) and leave the others to the numerical part of the transform.

With $I(r, z+z_0; k_{r_i})$ so defined, the reflected pressure field can be written:

$$P_R(r) = \int_0^\infty \frac{i}{\sqrt{k_0^2 - k_r^2}} \left[\Gamma(k_r) - \sum_i \frac{a_i}{k_r^2 - k_{r_i}^2} \right] e^{i\sqrt{k^2 - k_{r_i}^2}z + z_0} J_0(k_r r) k_r dk_r + \sum_i a_i I(r, z+z_0; k_{r_i}) \quad (7)$$

Where the expression in brackets no longer has any poles near the line of integration and so can be evaluated as before.

In order to remove the poles as required in Equation (7) it is necessary to determine with precision the pole locations, k_{r_i} , and their scales, $(a_{-i})_i$. The pole locations can be found using standard complex root finding techniques, though care must be taken to provide the root finding algorithm with values of the reflection coefficient on the Riemman surface so that it appears analytic except at isolated singularities. This means that the branches chosen for the square roots must be taken in such a manner that a branch cut is never placed between points simultaneously considered by the root finder. Once the root locations are known, the scale factors can be found

for those singularities far from any others by determining a least squares fit to:

$$\Gamma(k_{r_j}) = \frac{(a_{-1})_i}{k_{r_j}^2 - k_{r_i}^2} \quad j = 1, 2, \dots, N \quad (8)$$

provided that the k_{r_j} are taken sufficiently close to k_{r_i} that $\Gamma(k_r)$ is well approximated by just one pole in that region.

If many poles are clustered together, they can be determined simultaneously by solving:

$$\Gamma(k_{r_j}) = \sum_{i \in \mathbb{I}} \frac{(a_{-1})_i}{k_{r_j}^2 - k_{r_i}^2} \quad j = 1, 2, \dots, N \quad (9)$$

for N sufficiently large. If a pole is near a branch cut then the poles on the other side of the cut, on the opposite sheet, and near the cut must also be considered to be near that pole.

Figures (IV.3b.3a) and (IV.3b.3b) show the magnitude and phase of the reflection coefficient of Figure (IV.3b.2a) minus the pole contribution:

$$\Gamma(k_r) - \frac{a_{-1}}{(k_r^2 - k_{r_i}^2)} \quad (10)$$

For this example $a_{-1} = 1.689712 * 10^{-2} + i 5.027826 * 10^{-4}$ and $k_{r_i} = 9.069830 * 10^{-1} + i 2.488749 * 10^{-5}$.

Note the difference in scale between Figures (IV.3b.2a) and (IV.3b.3a). The small notch visible at $k_r \approx k_{r_i}$ is due to a small amount of error in the estimate of k_{r_i} .

A notable feature of Figure (IV.3b.3a) is the unmasking of the off axis zeros in the region $k_{N+1} < k_r < k_0$ where previously $|\Gamma(k_r)| = 1$. These zeros can be clearly seen in the perspective plot of the total reflection coefficient in the complex plane that was presented in Figure (IV.2c.2).

Figure (IV.3b.4) presents the hybrid field (solid line) versus the field calculated without removing the pole from the reflection coefficient (but otherwise removing the $1/\sqrt{k_0^2 - k_r^2}$ singularity as in the previous hybrid examples). The spread in the directly computed field due to aliasing is severe because aliasing in the Hankel transform severely affects a function that decays as

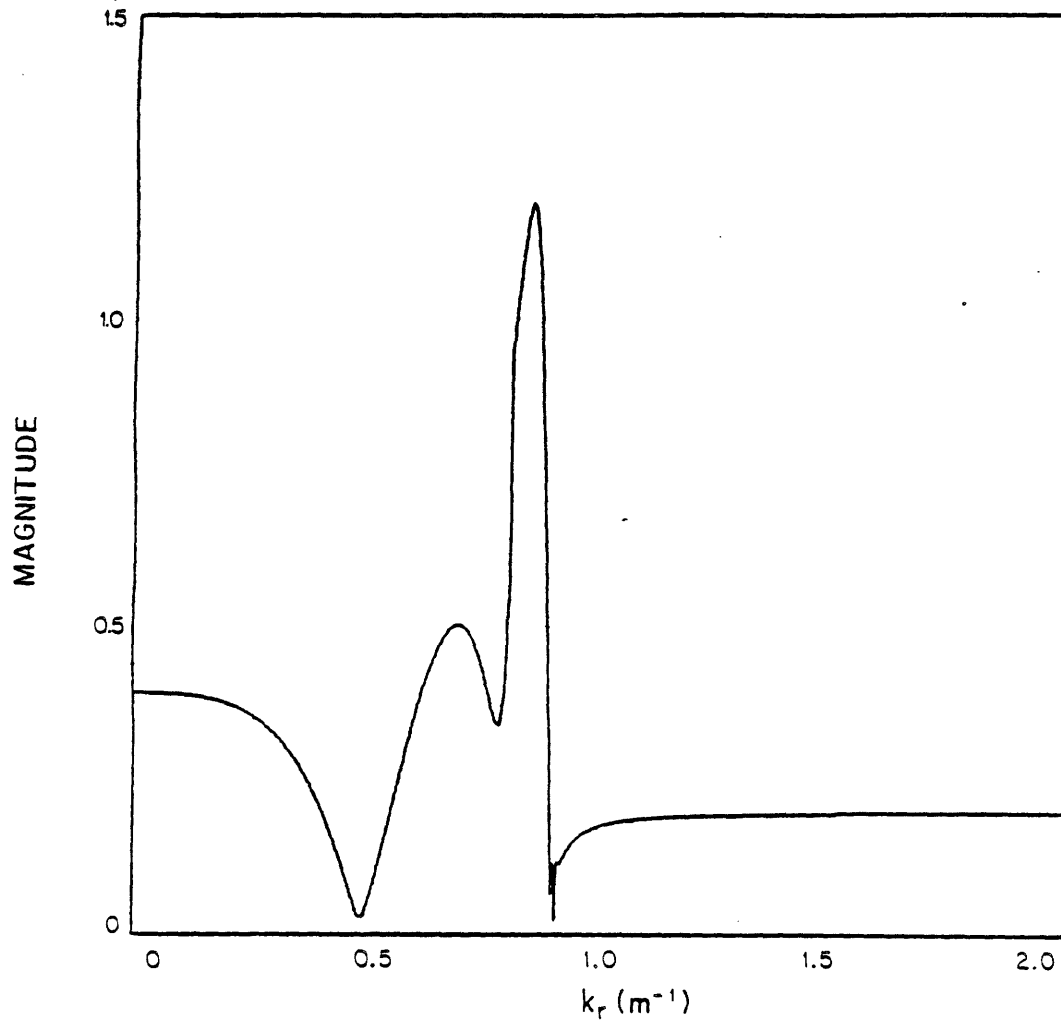


Figure IV.3b.3a Magnitude of reflection coefficient for slow speed layer example after the pole has been removed

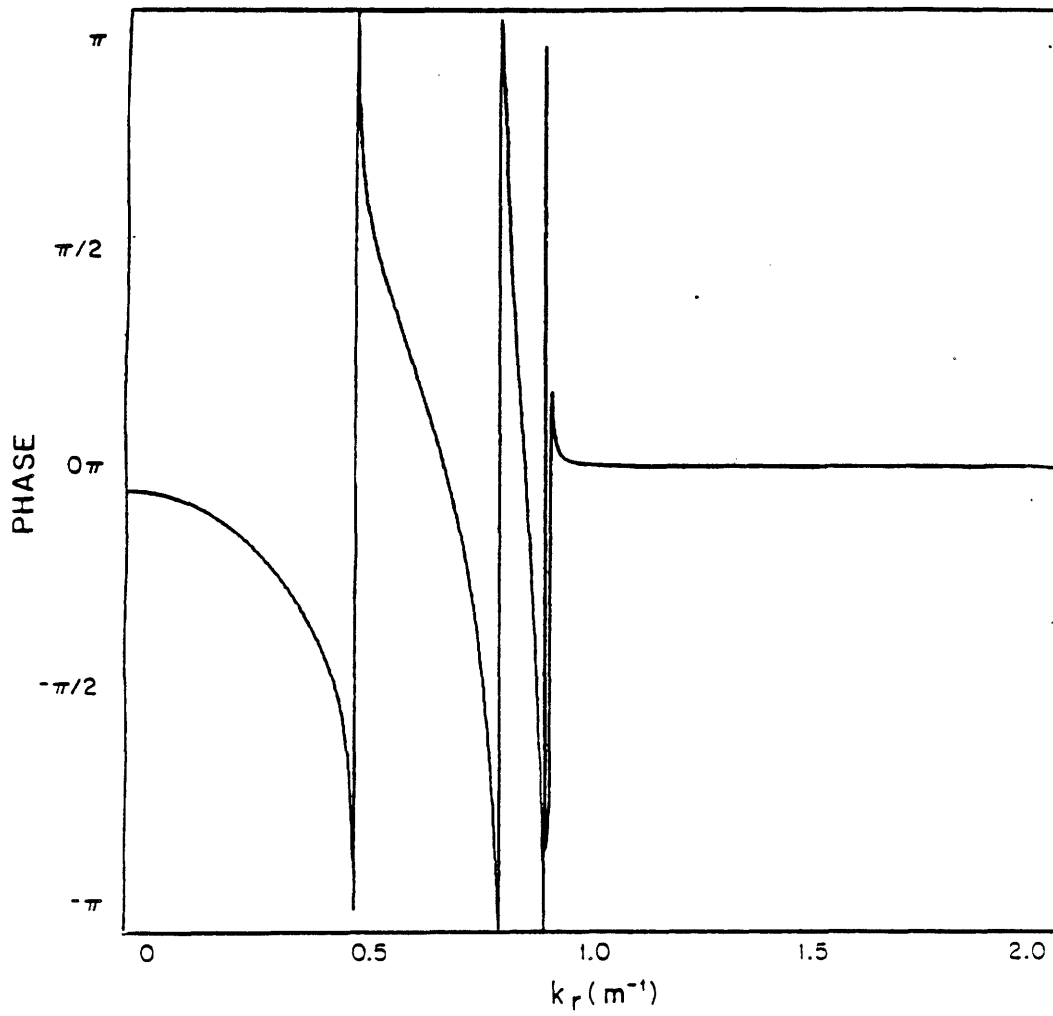


Figure IV.3b.3b Phase of reflection coefficient for slow speed layer example after the pole has been removed

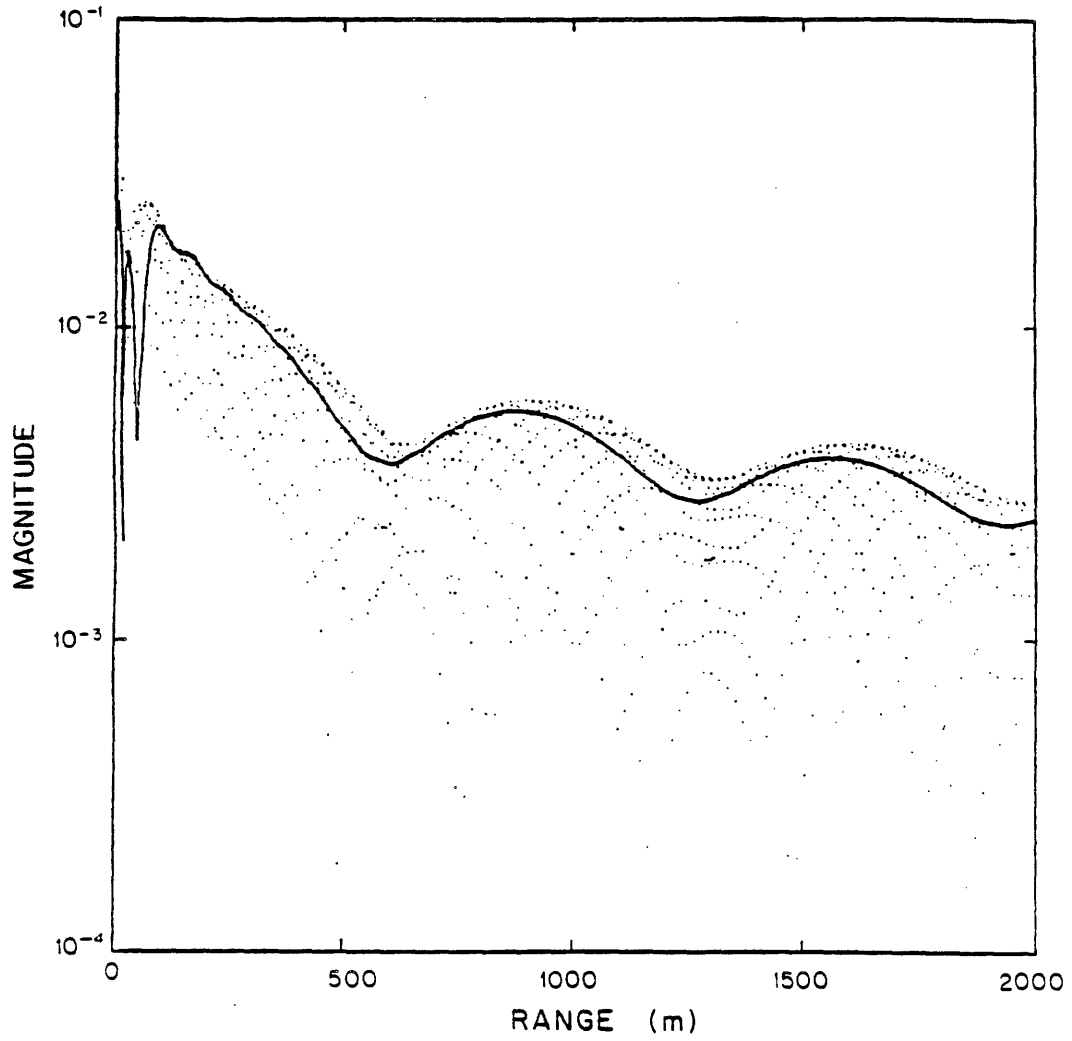


Figure IV.3b.4 Log-magnitude of the field calculated using the total hybrid method with pole removal (solid line) versus the field calculated without pole removal (scatter)

$1/\sqrt{r}$. The hybrid field does not exactly follow the contour of the top of the spread just as the hybrid computations in the previous examples did not exactly follow those contours when the aliasing became severe. Figure (IV.3b.5) presents the log-magnitude of the analytically generated pole contribution (solid line) and the remainder of the field exclusive of the pole contribution. The non-pole contribution is most significant for short ranges, while for this near bottom geometry the pole contribution dominates farther out.

The expression for $I(r, z+z_0; k_r)$ in Equation (2) shows that the contribution of the pole to the field decreases exponentially with $|z+z_0|$. In this example $|z+z_0| = 2$ to emphasize the near field behavior associated with the pole. For larger values of $|z+z_0|$ the pole contribution would be considerable less. Equation (2) can be used to estimate the magnitude of the pole contribution if the pole location, k_r , and $|z+z_0|$ are known.

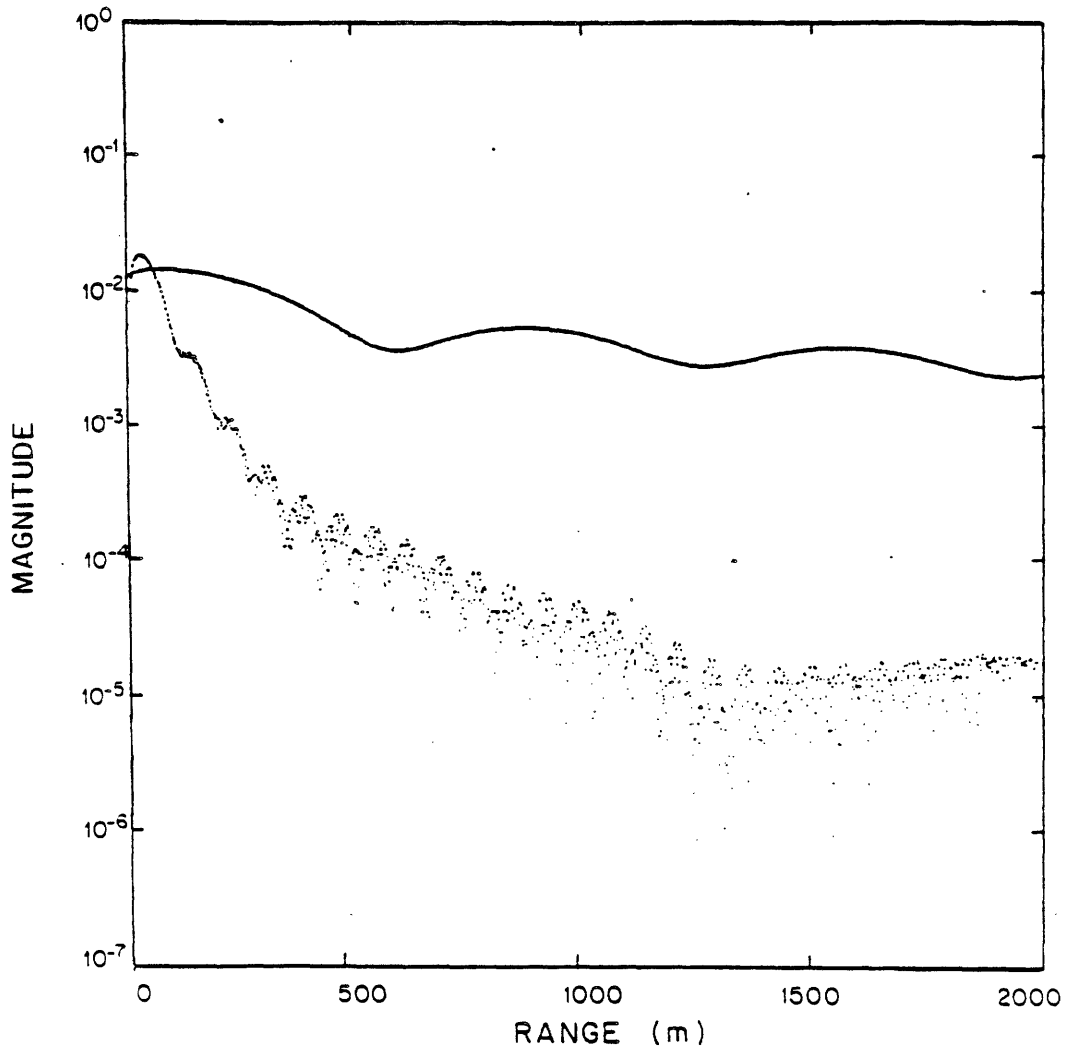


Figure IV.3b.5 Log-magnitude of field calculated with total hybrid method (solid line) versus the

References

1. K. Fuchs and G. Muller, "Computation of Synthetic Seismograms with the Reflectivity Method and Comparison with Observations," *Geophys. J.R. Astr.* 23, pp.417-433 (1971).
2. R. Stephen, "Synthetic Seismograms For the Case of the Receiver Within the Reflectivity Zone," *Geophys. J.R. Astr.*, pp.169-181 (1977).
3. Brekhovskikh, *Waves in Layered Media*, Academic Press, New York (1960).
4. K. Aki and P.G. Richards, *Quantitative Seismology Theory and Methods*, W.H. Freeman and Co., San Fransisco (1980).
5. W.T. Thomson, "Transmission of Elastic Waves Through a Stratified Solid Medium," *J. Applied Physics* 21, pp.89- (1950).
6. N.A. Haskell, "The Dispersion of Surface Waves in Multilayered Media," *Bull. of the Seismological Soc. of America* 43, pp.17-34 (1953).
7. D.R. Mook, "An Efficient Algorithm for the Numerical Evaluation of the Hankel and Abel Transforms," *IEEE ASSP*, to be published.
8. L.L. Beranek, *Acoustics*, McGraw-Hill Book Co., New York (1954).
9. G.V. Frisk, "Inhomogeneous Waves and the Plane Wave Reflection Coefficient," *J. Acoustical Soc. Amer.* 66 (1), pp.219-234 (1979).
10. F. R. DiNapoli, "Acoustic Propagation in a Stratified Medium," *Nucl Report No. 1046 Navy Underwater Sound Laboratory* (August 13, 1969).
11. DiNapoli and Deavenport, "Theoretical and Numerical Green's Function Field Solution in a Plane Multilayered System," *J. Acoustical Soc. Amer.* 67, pp.92-105 (1980).
12. Papoulis, *Systems and Transforms with Applications in Optics*, McGraw-Hill, New York (1968).

CHAPTER V: THE INVERSION PROCEDURE

V.1) Overview

In Chapter II we developed the properties of the Hankel transform. These properties provided our foundation for the development of an accurate procedure to numerically generate synthetic pressure fields, presented in Chapter IV. In this chapter we will use the results of Chapter II to explore the problem of determining the plane wave reflection coefficient from measurements of the pressure field arising in a horizontally stratified environment in response to a CW point source. The estimation of the plane wave reflection coefficient from measurements of the field is an extremely important problem. Determining the plane wave reflection coefficient is an essential step in the inversion of pressure field data to obtain the parameters of the bottom. In this context it is of interest to geophysicists and others who wish to determine the composition of the ocean bottom. The plane wave reflection coefficient is also used as a geometry independent characterization of the bottom. As such, if it is estimated in a region from one set of acoustic measurements, then the fields associated with an arbitrary source-receiver geometry in that region can be determined. This is of great value in problems of acoustic imaging.

The inversion procedure that we consider in this chapter was proposed by Frisk, Oppenheim, and Martinez [1]. It requires as input, coherent measurements of the pressure field as a function of range resulting from a CW point source over a horizontally stratified ocean bottom. From this the (complex) reflected pressure field, $P_R(r)$, is extracted. The Hankel transform of this field is computed to provide the depth-dependent Green's function as a function of horizontal wave number:¹

$$G(k_r, z, z_0) = \int_0^{\infty} P_R(r) J_0(k_r r) r dr \quad (1)$$

Finally, the plane wave reflection coefficient is obtained by multiplying the Green's function by

¹We will sometimes shorten "depth-dependent Green's function" to "Green's function".

terms which compensate for the source spectrum and for the source-receiver distance:

$$\Gamma(k_r) = -i \sqrt{k_0^2 - k_r^2} e^{-i \sqrt{k_0^2 - k_r^2} |z+z_0|} G(k_r, z, z_0) \quad (2)$$

This entire procedure is summarized in Figure (V.1.1).

In this chapter we will concentrate on the estimation of the depth-dependent Green's function. We divide the issues addressed directly into the categories of source-field subtraction, sampling, windowing, and source-height variation. The issue of source-field subtraction arises because the plane wave reflection coefficient is directly related to the reflected pressure field and not the total pressure field, which is measured. The issue of sampling covers the effects caused by having the pressure field available for computation only on a discrete set of points. We discuss both the effect that sampling rate has on the estimate of the depth-dependent Green's function and the practical problem of interpolation, which is required to move the field from one grid to another (often to compensate for missing data points). We develop a phase unwrapping procedure that allows us to interpolate the magnitude and unwrapped phase, which vary slowly compared to the quadrature components.

In the section on windowing we discuss the effect that having the pressure field available only to a finite range has on the estimate of the depth dependent Green's function. We determine the range over which the data must be known in order to accurately determine the depth-dependent Green's function. We do this by using the properties of the Hankel transform developed in Section (II.6).

In the section on source-height variation we exploit the results of Section (II.6) once again, but this time we use them to determine the effect that variations in the source-height has on the estimate for the depth-dependent Green's function. Such variations are inevitable during the acquisition of real data. We illustrate these effects by considering the effect of three specific variations.

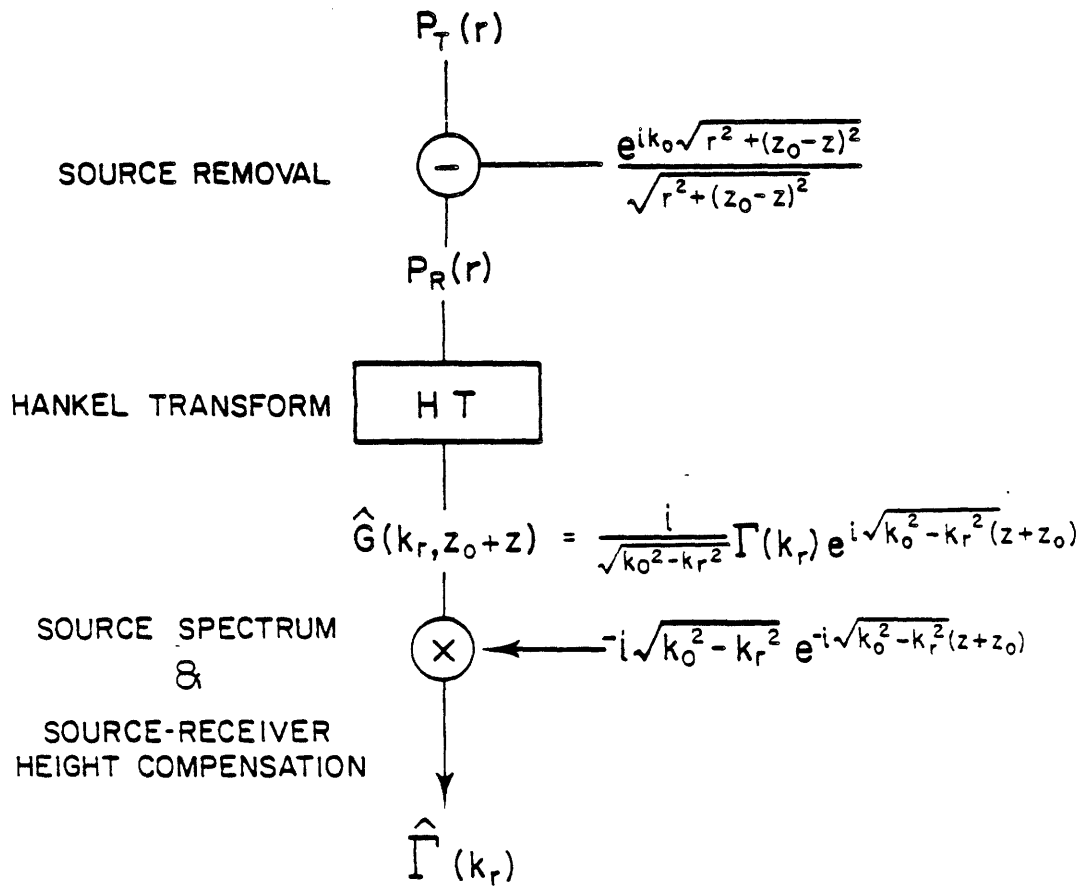


Figure V.1.1 The inversion procedure to estimate the plane wave reflection coefficient from the total field generated by a CW point source over a horizontally stratified bottom

V.2) Source-field subtraction

In this section we consider the removal of the source field when the source-receiver geometry is known. In Figure (V.1.1) we showed the source field removed before the Hankel transform. We did this because conceptually we wish to deal with the reflected field alone. In this section we show that numerically it is better to remove the source field in the transform domain, after the Hankel transform of the total field has been computed.

Because the Hankel transform is a linear operator, in principal the estimate for the Green's function can be made by subtracting the source field either before transforming:

$$G(k_r, z, z_0) = \int_0^{\infty} \left[P_T(r) - \frac{e^{ik_0 \sqrt{r^2 + (z-z_0)^2}}}{\sqrt{r^2 + (z-z_0)^2}} \right] J_0(k_r r) r dr \quad (1)$$

or by subtracting in the transform domain:

$$G(k_r, z, z_0) = \int_0^{\infty} P_T(r) J_0(k_r r) r dr - \int_0^{\infty} \frac{e^{ik_0 \sqrt{r^2 + (z-z_0)^2}}}{\sqrt{r^2 + (z-z_0)^2}} J_0(k_r r) r dr \quad (2)$$

which becomes upon performing the second integral analytically:

$$G(k_r, z, z_0) = \int_0^{\infty} P_T(r) J_0(k_r r) r dr - \frac{i}{\sqrt{k_0^2 - k_r^2}} e^{i\sqrt{k_0^2 - k_r^2} |z-z_0|} \quad (3)$$

If $P_T(r)$ is available only over the finite range $0 < r < r_{\max}$ then the field integrals can only be carried out to r_{\max} . Substituting r_{\max} for ∞ in Equations (1) and (3) will make these two formulations no longer equivalent because the analytically performed integration is not windowed.

The function transformed in Equation (1) is the reflected pressure field, $P_R(r)$. In Section (IV.3) we argued that the reflected field decayed asymptotically as $\frac{1}{r}$.¹ If the total field, $P_T(r)$, decays asymptotically faster than $\frac{1}{r}$, we can expect that the formulation of Equation (3) to suffer less from windowing effects than the formulation of Equation (1). We will now show that the total field does in fact decay faster than the reflected field alone. In fact, by transforming the

¹ In the absence of trapped modes.

total pressure field and then subtracting the source contribution in the Hankel domain, we have performed the dual to the removal of the $\frac{1}{\sqrt{k_0^2 - k_r^2}}$ singularity discussed in Section (IV.3a).

Before we begin, an analogy to a similar procedure for determining the Fourier transform of a function known only over a finite range but with a large, known constant offset might provide some insight. If such a function is (Fourier) transformed directly, the offset will transform to an impulse at the origin which is smeared into the rest of the transform. The smearing will occur because the transform is taken over only a finite aperture (windowing). The alternative is to subtract the offset from the function, transform the result, and add an impulse (with a strength which is determined analytically from the known offset) to the origin. This second procedure will give superior results because the transform of the offset is not degraded.

Transforming the reflected field alone is analogous to generating the Fourier transform directly from the the field with the known offset. In the case of the reflected field, however, instead of a simple constant offset, the function has a known asymptotic behavior. It decays as $\frac{1}{r}$. We are about to show that adding the source field to the reflected pressure field is analogous to subtracting the offset in the Fourier transform example. In the Hankel transform case we are actually considering it corresponds to subtracting a term with the same asymptotic $\frac{1}{r}$ behavior. The difference will decay faster than $\frac{1}{r}$.

We begin by considering the Green's function associated with the total field for $z_0 > z$ which is given by:

$$G_T(k_r, z, z_0) = \frac{i}{\sqrt{k_0^2 - k_r^2}} \left[\Gamma(k_r) e^{i\sqrt{k_0^2 - k_r^2}(z_0+z)} + e^{i\sqrt{k_0^2 - k_r^2}(z_0-z)} \right] \quad (4)$$

The $\frac{ie^{i\sqrt{k_0^2 - k_r^2}(z_0-z)}}{\sqrt{k_0^2 - k_r^2}}$ term is the source term. If we rewrite Equation (4) in terms of the reflection coefficient at k_0 , it will be more clear why adding this term in the transform domain corresponds to subtracting the asymptotic behavior in the pressure domain. We must use the fact

that for all bottoms $\Gamma(k_0) = -1$ (except the degenerate case $\Gamma(k_r) \equiv 1$). We write Equation (4) as:

$$G_T(k_r, z, z_0) = \frac{i}{\sqrt{k_0^2 - k_r^2}} \left[\Gamma(k_r) - \Gamma(k_0) e^{-2i\sqrt{k_0^2 - k_r^2}(z)} \right] e^{i\sqrt{k_0^2 - k_r^2}(z_0 - z)} \quad (5)$$

As we discussed in Section (IV.3) the asymptotic behavior in the pressure domain is determined by the behavior at the singularities in the transform domain. [2] At $k_r = k_0$ the phase term, $e^{-2i\sqrt{k_0^2 - k_r^2}(z)}$, equals 1 so that unlike the Green's function associate with the reflected field alone, the numerator of the total Green's function approaches zero as k_r approaches the $\frac{1}{\sqrt{k_0^2 - k_r^2}}$ singularity at k_0 . We wish now to determine the contribution of the singularity at $k_r = k_0$ in the total Green's function in order to show that the "softening" introduced by the addition of the source term has made the associated total field more range limited. We can bypass a great number of issues by instead considering the asymptotics of the simplified Green's function:

$$G_T^{simple}(k_r, z, z_0) = \frac{i}{\sqrt{k_0^2 - k_r^2}} \left[-1 - \Gamma(k_0) e^{-2i\sqrt{k_0^2 - k_r^2}(z)} \right] e^{i\sqrt{k_0^2 - k_r^2}(z_0 - z)} \quad (6)$$

By considering Equation (6) we exclude those issues associated with $\dot{\Gamma}(k_r)$. Our examples in the synthetic data generation section showed that these terms do not give rise to terms which decay as slowly as $\frac{1}{r}$.

Equation (6) is the Green's function for a dipole and has the known Hankel transform:

$$P_d(r) = \frac{e^{ik_0\sqrt{r^2 + (z - z_0)^2}}}{\sqrt{r^2 + (z - z_0)^2}} - \frac{e^{ik_0\sqrt{r^2 + (z + z_0)^2}}}{\sqrt{r^2 + (z + z_0)^2}} \quad (7)$$

It is well known that this field decays asymptotically as $\frac{1}{r^2}$ and that this asymptotic behavior begins more quickly when z_0 is small than when it is large.

Since the total field will be more range limited than the reflected field, it is better to transform the total field numerically and subtract the (analytically determined) transform of the

incident field than it is to subtract the incident field before transforming.

V.3) Sampling

a) Overview

Typically, data is not available on the grid required for processing. In the experiment providing the data for this thesis, for example, the range values for which the data has been obtained is determined by the drift rate of the boat and the source away from the receivers. The individual samples do not occur exactly where we would like them and while the experiment was designed to provide samples as close to the Nyquist rate as possible, typically the number of samples on averages is less than we would like. Finally, there are isolated cases of missing samples, a reality of data collection. Section (V.3b) discusses the issues associated with the average sampling rate. The issues associated with the grid in general are discussed in Section (V.3c).

b) Sampling rate

In Chapter (II.7) we saw that when $f(r)$ is sampled on approximately a linear grid and the transform:

$$F(\rho) = \int_0^{\infty} f(r) J_0(\rho r) r dr \quad (1)$$

is computed from these samples, then $f(r)$ must be sampled on a grid at least as fine as $\frac{\pi}{A}$ in order to correctly perform the transform for $F(\rho)$ negligible $\rho > A$. In this chapter we consider the transform of the pressure field, to obtain the depth-dependent Green's function. This transform has the form:

$$G(k_r, z+z_0) \equiv \frac{i \Gamma(k_r)}{\sqrt{k_0^2 - k_r^2}} e^{i\sqrt{k_0^2 - k_r^2}|z+z_0|} = \int_0^{\infty} P_R(r) J_0(k_r r) r dr \quad (2)$$

$G(k_r, z+z_0)$ is negligible for $k_r > k_0 + \epsilon^1$ except possibly near the poles of $\Gamma(k_r)$ (for some

1) For some small $\epsilon > 0$.

small ϵ) because when $k_r > k_0$, it decays exponentially. Consequently when there are no poles in $\Gamma(k_r)$ for real k_r , then the pressure field need only be available on a grid as fine as $\frac{n\pi}{A}$ with $A \equiv k_0 + \epsilon$ to accurately determine $G(k_r, z + z_0)$ in the region $0 < k_r < k_0$. If we wish to obtain $G(k_r, z + z_0)$ in the region where it is exponentially decreasing ($k_r > k_0$), however, we must sample fast enough to represent the signal in that region as well.

If a pole is present in $\Gamma(k_r)$ at $k_r = k_{r_i}$ the Green's function will be significant near k_{r_i} despite the exponential decay. If the presence of the pole is ignored and the field is transformed on the grid $\frac{n\pi}{k}$, then the pole will be aliased into the Green's function at lower wave numbers.

If there is only one pole present we can write the Green's function, $G(k_r)$ (we suppress the z variation) as:

$$G(k_r) \equiv \hat{G}(k_r) + \frac{a_{-1}}{k_r^2 - k_{r_i}^2} \quad \text{for } k_{r_i} > k \quad (3)$$

The results of Chapter (II.7) show that if the pressure field is transformed on the grid $\frac{\lambda_n}{k}$, then the aliased Green's function computed will approximately be given in the region $0 < k_r < k$ by:

$$\hat{G}(k_r) \approx G(k_r) - \sqrt{2k/k_r - 1} G(2k - k_r) \approx \hat{G}(k_r) - \sqrt{2k/k_r - 1} \frac{a_{-1}}{(2k - k_r)^2 - k_{r_i}^2} \quad (4)$$

so that the Greens function at $2k_0 - k_{r_i}$ will be corrupted.

If the amplitude, a_{-1} , is very small (which would be the case for large source-receiver geometries) and some smearing is present due to windowing (the field is not measured out to ranges where the trapped mode dominates), we may not see the pole's effect and it can safely be ignored.

In general the possibility of trapped modes must be considered before deciding upon a sampling rate, particularly in geometries with small source-receiver heights. For such geometries it is not always sufficient to sample at $\frac{n\pi}{k_0}$.

c) *Sampling grid*

When data is not available on the grid required for processing we must first interpolate. Successful interpolation is possible only if the signal is adequately represented by the original samples. If we know only that our signal has a Hankel transform which is negligible beyond some bandwidth, A , then the signal is adequately represented by samples on the grid $\frac{\lambda_n}{C}$ for $C \geq A$ and where λ_n $n = 0, 1, 2, \dots$ are the ordered zeros of $J_0(r)$. [2] This is true in theory. In practice, if the the samples are not originally spaced as required, it may be impossible to actually perform the interpolation onto another grid. If the samples are only available on the grid $\frac{\lambda_n}{C}$ with $C < A$, then it is not possible to interpolate without making additional assumptions.

We will show that for the class of pressure fields examined, an additional assumption seems reasonable. This assumption makes interpolation possible even when the sampling rate is slightly too low. We will assume that the magnitude and phase of our pressure fields are smooth compared to their quadrature components. Figure (V.3c.1) shows the magnitude of the pressure field associated with a point source over a pressure release bottom. Between calculated points the curve varies so little and so regularly that a plot of the points appears to be a smooth line. Figure (V.3c.2) shows the result of first subsampling the points plotted in Figure (V.3c.1) (which were available on the grid $\frac{\lambda_n}{2}$) by a factor of two, and then interpolating back onto the original grid using splines.¹ The differences between the two curves are negligible.

We can compare this successful interpolation to the result of subsampling the quadrature components, spline interpolating, and computing the magnitude. The result of this operation is shown in Figure (V.3c.3). The apparently smooth line comes from the subsampled set of values which the splines was constrained to match in the quadrature components. It actually consists of

1) Splines were used because the original grid is given by λ_n/A , where λ_n are the ordered zeros of $J_0(x)$. This grid is uneven and makes other interpolation schemes less desirable.

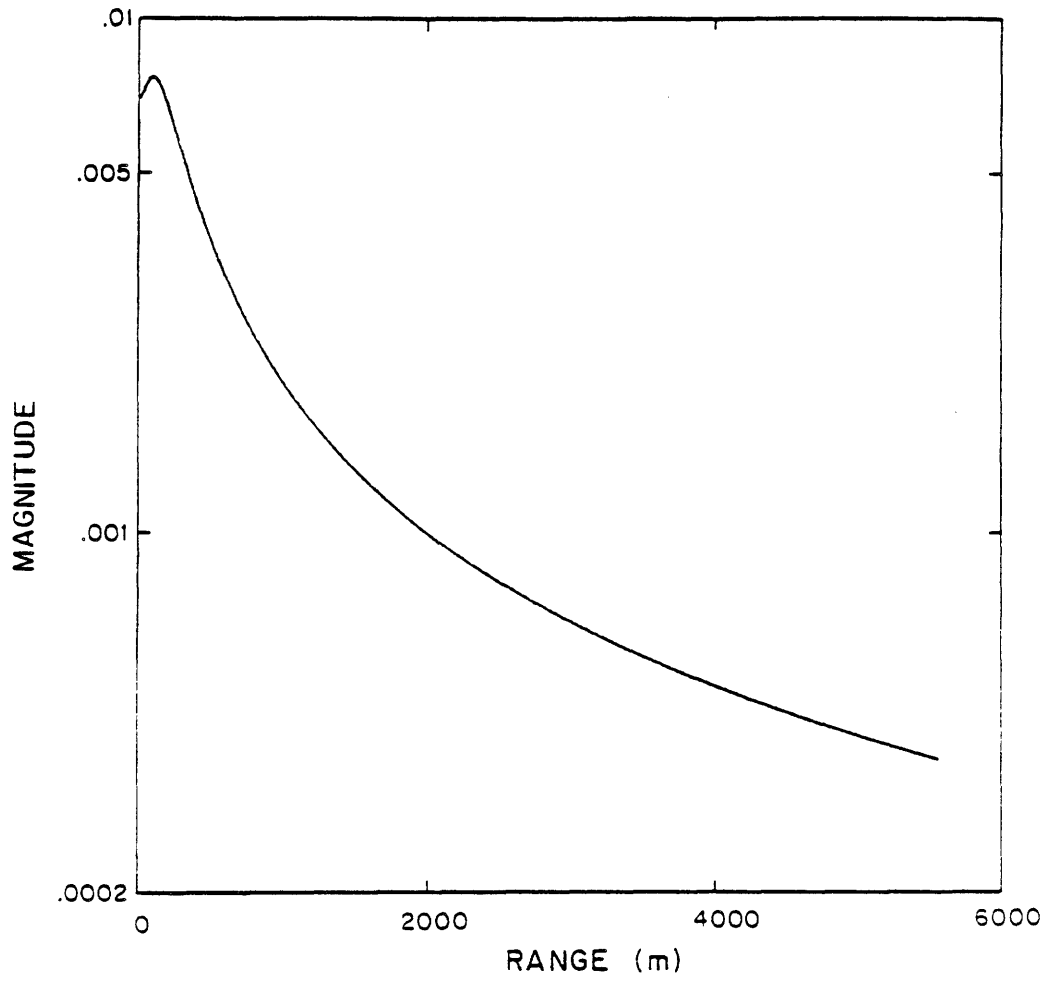


Figure V.3c.1 Log-magnitude of pressure field for a CW point source over a pressure release bottom

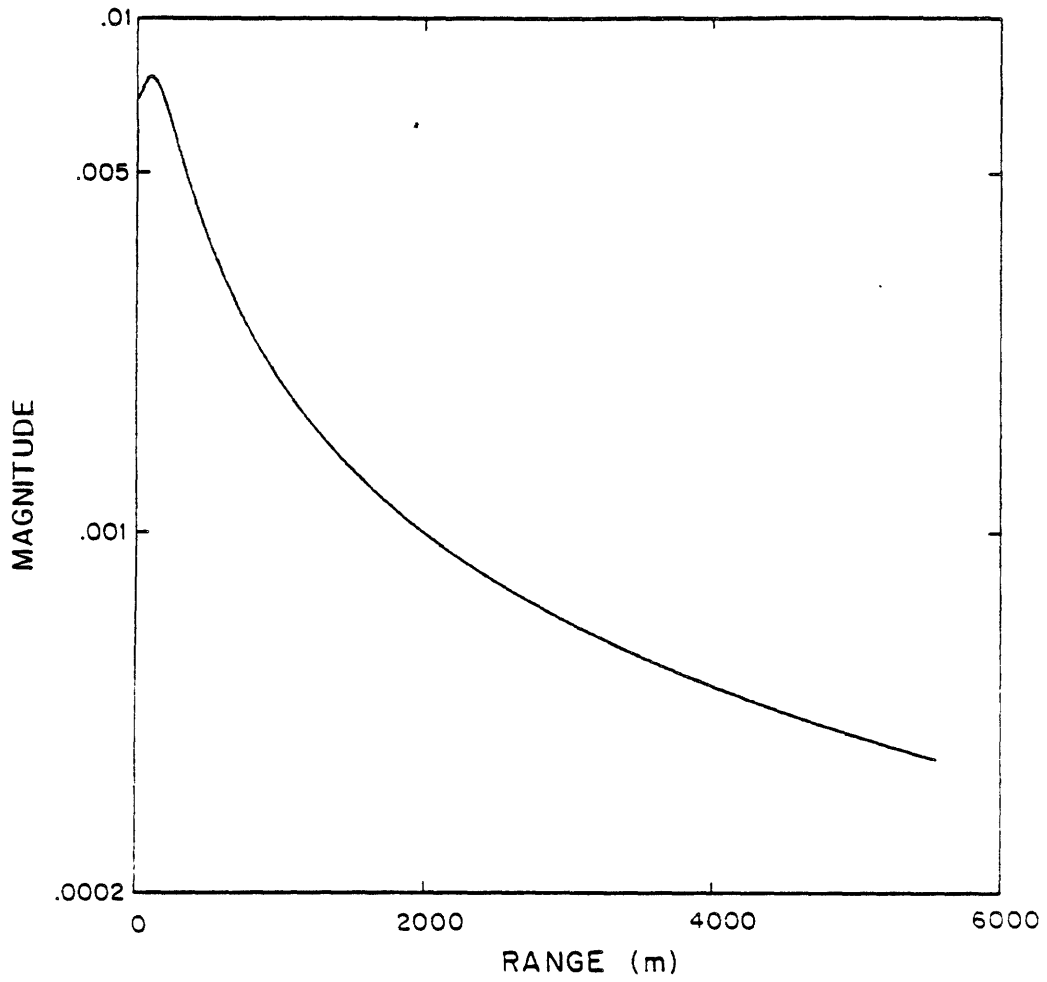


Figure V.3c.2 The result of subsampling and interpolating the magnitude function shown in Figure V.3c.1

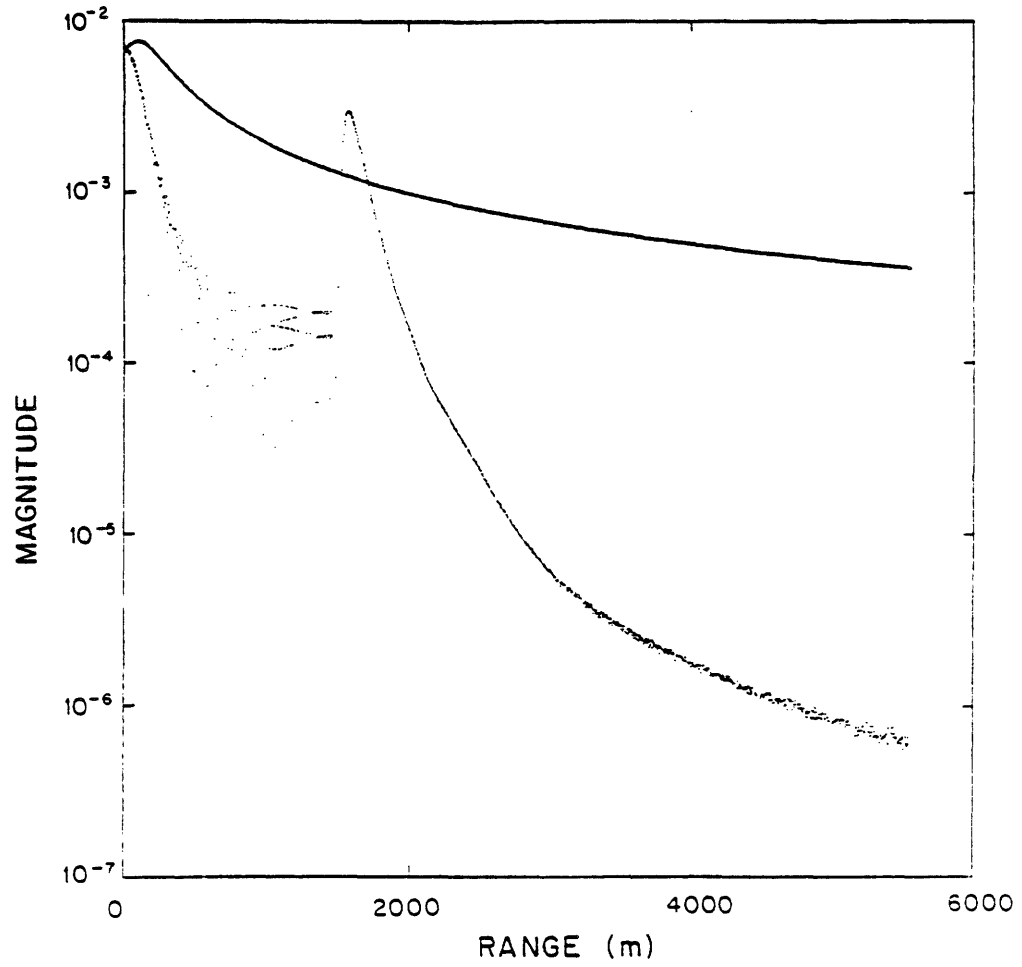


Figure V.3c.3 The result of subsampling the function with magnitude shown in Figure V.3c.1, interpolating the quadrature components, and generating the magnitude.

every other point of the displayed curve. The surrounding scatter is the magnitude of interpolated points supplied by the splines. Clearly, splines did not successfully interpolate the quadrature components.

Figure (V.3c.4) shows the phase of Figure (V.3c.1) computed by

$$\hat{\theta} = \tan^{-1} \left[\frac{P_i}{P_r} \right] \quad (1)$$

where P_i is the imaginary component of the field and P_r is the real component. The rapid variation in $\hat{\theta}$ suggests that it is not adequately represented by the grid upon which it is presented. $\hat{\theta}$ is not the only representation of the phase of the pressure field, however.

d) *Unwrapping the Phase*

The phase displayed in Figure (V.3c.4) is the principal value of the phase, often referred to as the wrapped phase. The wrapping comes about because of the ambiguity concerning which phase should be associated with the quadrature components. If θ satisfies:

$$M e^{i\theta} = P_r + i P_i \quad (1)$$

then so must $\theta + 2\pi m$ where m is any integer, since

$$M e^{i(\theta + 2\pi m)} = M e^{i\theta} e^{2\pi i m} = M e^{i\theta} = P_r + i P_i \quad (2)$$

Given just P_r and P_i there is no way to determine the correct value of m . The arctan routine used by Fortran follows the convention of choosing m such that

$$-\pi < \hat{\theta} \equiv \theta + 2\pi m < \pi \quad (3)$$

The output value $\hat{\theta}$ is the principal value of the phase, or the wrapped phase.

If the phase of the pressure field were approximately increasing at a rate of $k_0 R$ where $R \equiv \sqrt{r^2 + (z - z_0)^2}$ and the field were sampled at the Nyquist rate of $1/2k_0$, then the phase difference between samples would be roughly π and the wrapped phase every sample or two would suffer a jump to a different m in order to satisfy the condition $-\pi < \theta + 2\pi m < \pi$. This would obscure any underlying regular behavior that we expect from most physical phenomena. These frequent jumps are responsible for the rapid oscillation apparent in the phase

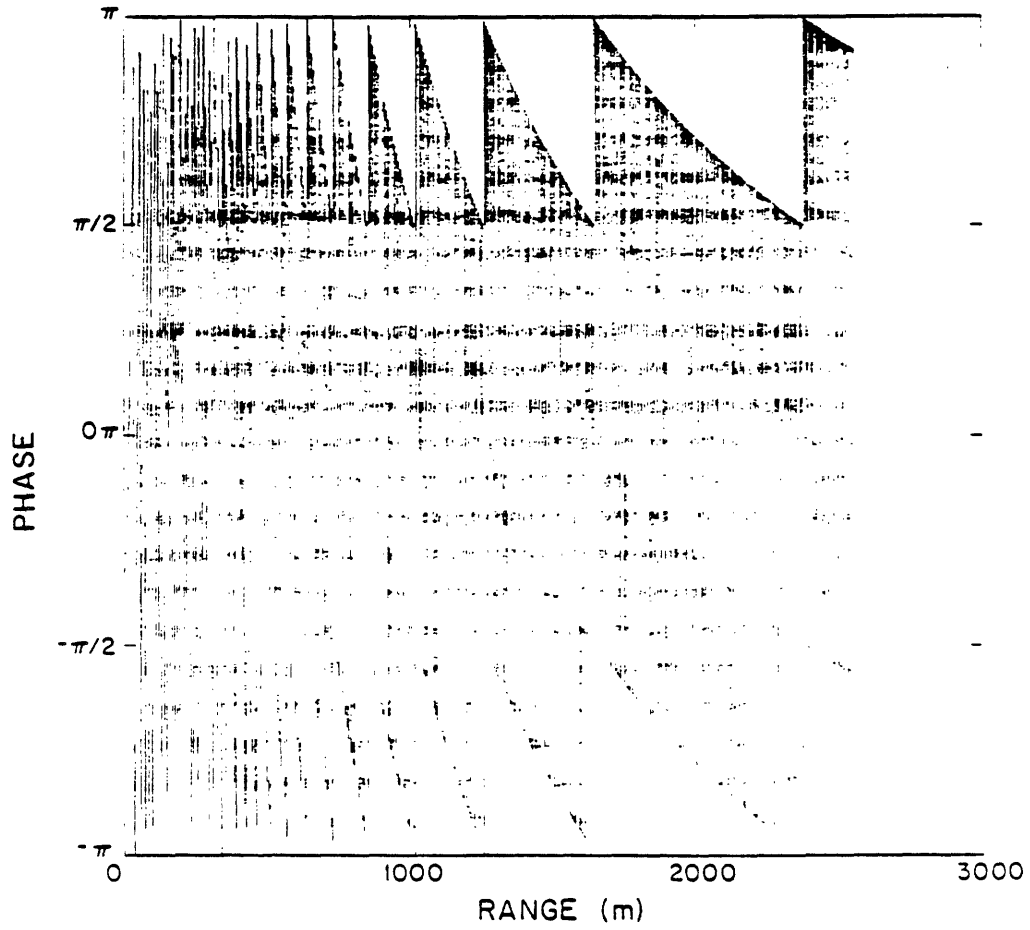


Figure V.3c.4 The principal value of the phase of the field associated with Figure V.3c.1

of Figure (V.3c.4). We wish to compensate for the wrapping that takes place when the principal value of the phase is generated. To do so we must make use of our knowledge of how the phase is varying from point to point.

We conjecture that the phase of the total field is dominated by a component at the water wave number associated with the dominant specular path and that the remaining portion of the phase is slowly varying compared to the sampling rate. We write

$$P_T(r) = M(r)e^{i\theta(r)} \quad (4)$$

where $M(r)$ and $\theta(r)$ are real, and write

$$\theta(r) = k_0R + \epsilon(r) \quad (5)$$

where $R \equiv \sqrt{r^2 + (z - z_0)^2}$. We will call k_0R the modeled portion of the phase and $\epsilon(r)$ the residual phase. We are going to show that as long as the residual phase is sampled fast enough, we can reconstruct the true phase.

In this notation the difference in true phase value from sample to sample can be written:

$$\theta(r_n) - \theta(r_{n-1}) = k_0(R_n - R_{n-1}) + \epsilon(R_n) - \epsilon(R_{n-1}) \quad (6)$$

so that

$$\theta(r_n) - \theta(r_{n-1}) - k_0(R_n - R_{n-1}) = \epsilon(R_n) - \epsilon(R_{n-1}) \quad (7)$$

Precisely stated, our requirement that the residual phase be slowly varying compared to the sampling rate is:

$$|\epsilon(R_n) - \epsilon(R_{n-1})| < \pi \quad \text{for all } R_n \quad (8)$$

To unwrap the phase we first form:

$$\begin{aligned} & \hat{\theta}(r_n) - \hat{\theta}(r_{n-1}) - k_0(R_n - R_{n-1}) \\ &= \theta(r_n) - m_n 2\pi - \theta(r_{n-1}) - m_{n-1} 2\pi - k_0(R_n - R_{n-1}) \\ &= \theta(r_n) - \theta(r_{n-1}) - 2\pi(m_n - m_{n-1}) \\ &= \epsilon(R_n) - \epsilon(R_{n-1}) \end{aligned} \quad (9)$$

from the measured data. We now do the unwrapping by defining $m_0 \equiv 0$ and picking the integers, m_n , ($n = 1, 2, \dots$) sequentially to satisfy:

$|\hat{\theta}(r_n) - \hat{\theta}(r_{n-1}) - k_0(R_n - R_{n-1}) - 2\pi(m_n - m_{n-1})| = |\epsilon(R_n) - \epsilon(R_{n-1})| < \pi$ (10)
and define the unwrapped phase to be:

$$\theta(r_n) \equiv \hat{\theta}(r_n) + (m_n)2\pi \quad (11)$$

Figure (V.3d.1) shows the result of running this algorithm on the phase of the synthetic data with magnitude shown in Figure (V.3c.1) and wrapped phase shown in Figure (V.3c.4). The resulting phase is dominated by the linear term k_0R we defined in our model. Figure (V.3d.2) shows the residual phase. The smooth and small variation of the residual phase over the intervals $[r_{n-1}, r_n]$ for all n , is a strong confirmation of our phase unwrapping assumption.

Figures (V.3d.3a) and (V.3d.3b) present the magnitude and residual phase of the fast bottom example of Section (IV.3a). For this example, too, the residual phase is well behaved.

Figures (V.3d.4a) and (V.3d.4b) present the magnitude and residual phase of the slow speed layer example of Section (IV.3b). For this example, too, the residual phase is well behaved. The field in this example was shown to be dominated in the far field by the contribution due to the pole beyond the water wave number. The upward slope of the residual phase apparent in Figure (V.3d.4b) reflects the fact that this pole is contributing the dominant component to the phase (in the far field) which is slightly larger than the k_0R term subtracted out.

e) Interpolating the magnitude and unwrapped phase

In Figures (V.3c.1) and (V.3c.2) we showed that the magnitude of the dipole field could be up-sampled from the grid $\frac{\lambda_n}{1}$ to $\frac{\lambda_n}{2}$. In Section (V.3d) we saw that the unwrapped and residual phase components enjoy smooth, regular variation ideally suited for interpolation. Figure (V.3e.1) shows the residual phase for the dipole field up-sampled from the $\frac{\lambda_n}{1}$ to the $\frac{\lambda_n}{2}$ grid. It is indistinguishable from the residual phase generated on the $\frac{\lambda_n}{2}$ grid shown in Figure (V.3d.2).

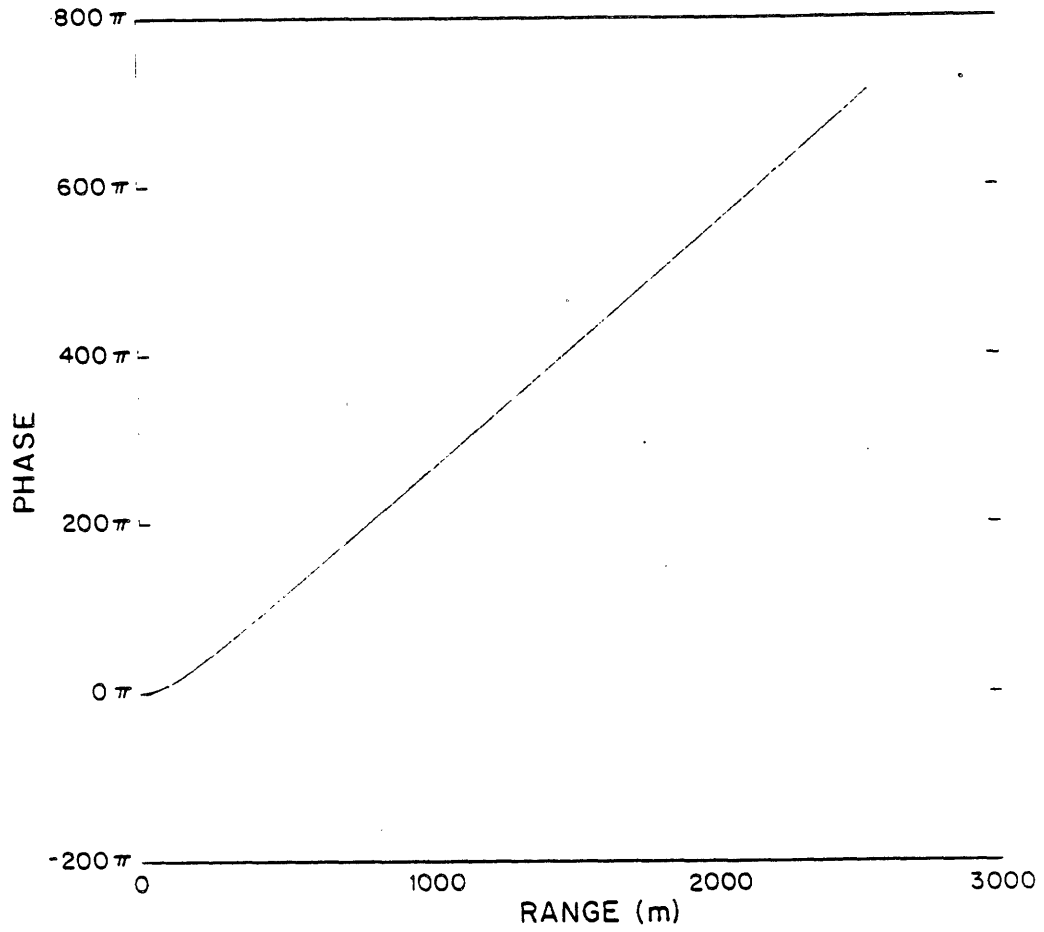


Figure V.3d.1 Unwrapped phase corresponding to Figure V.3c.4

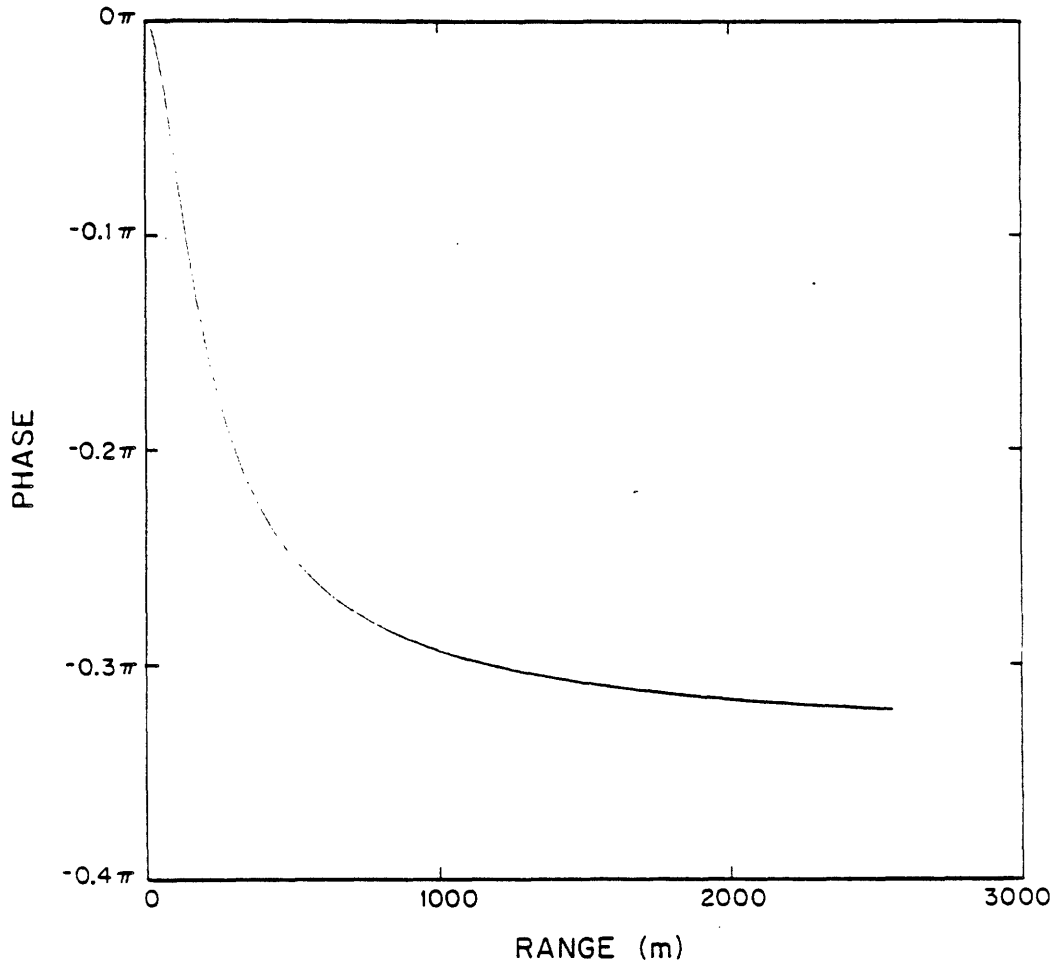


Figure V.3d.2 Residual phase corresponding to Figure V.3c.4

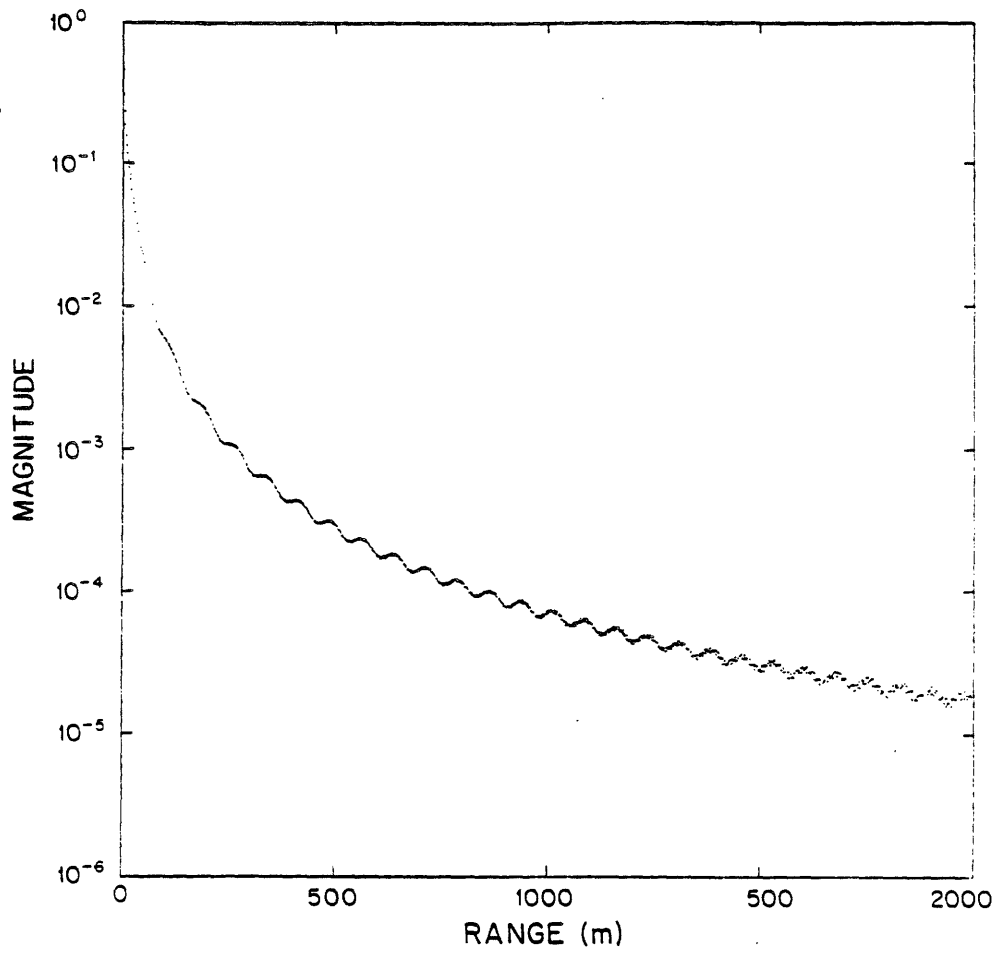


Figure V.3d.3a Log-magnitude of field for fast bottom example

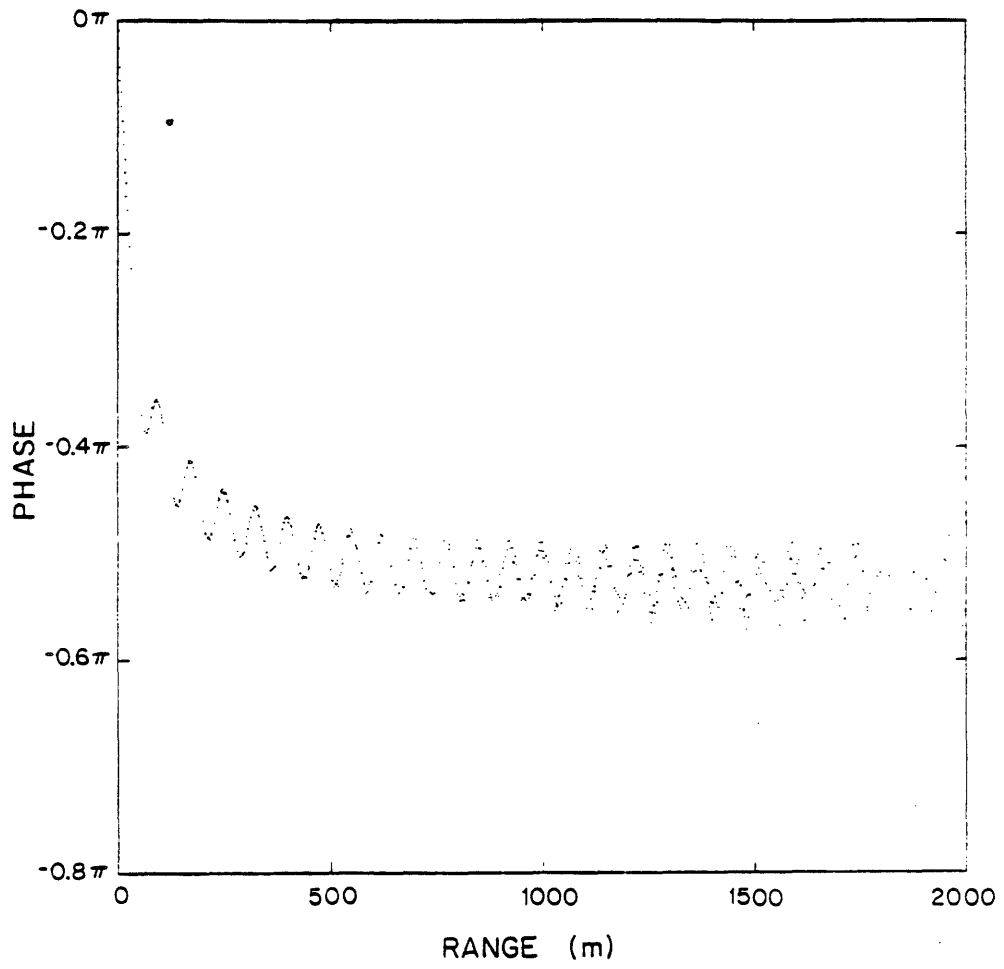


Figure V.3d.3b Residual phase of field for fast bottom example

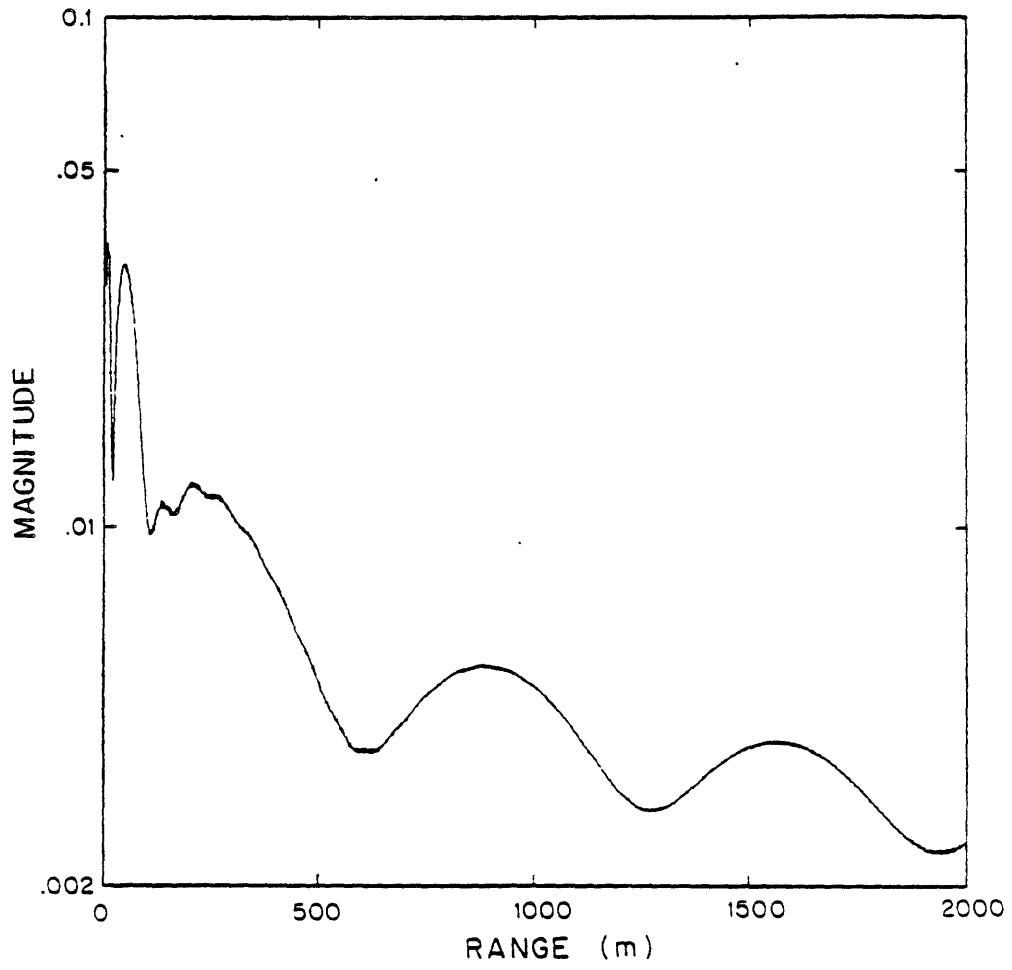


Figure V.3d.4a Log-magnitude of field for slow bottom example

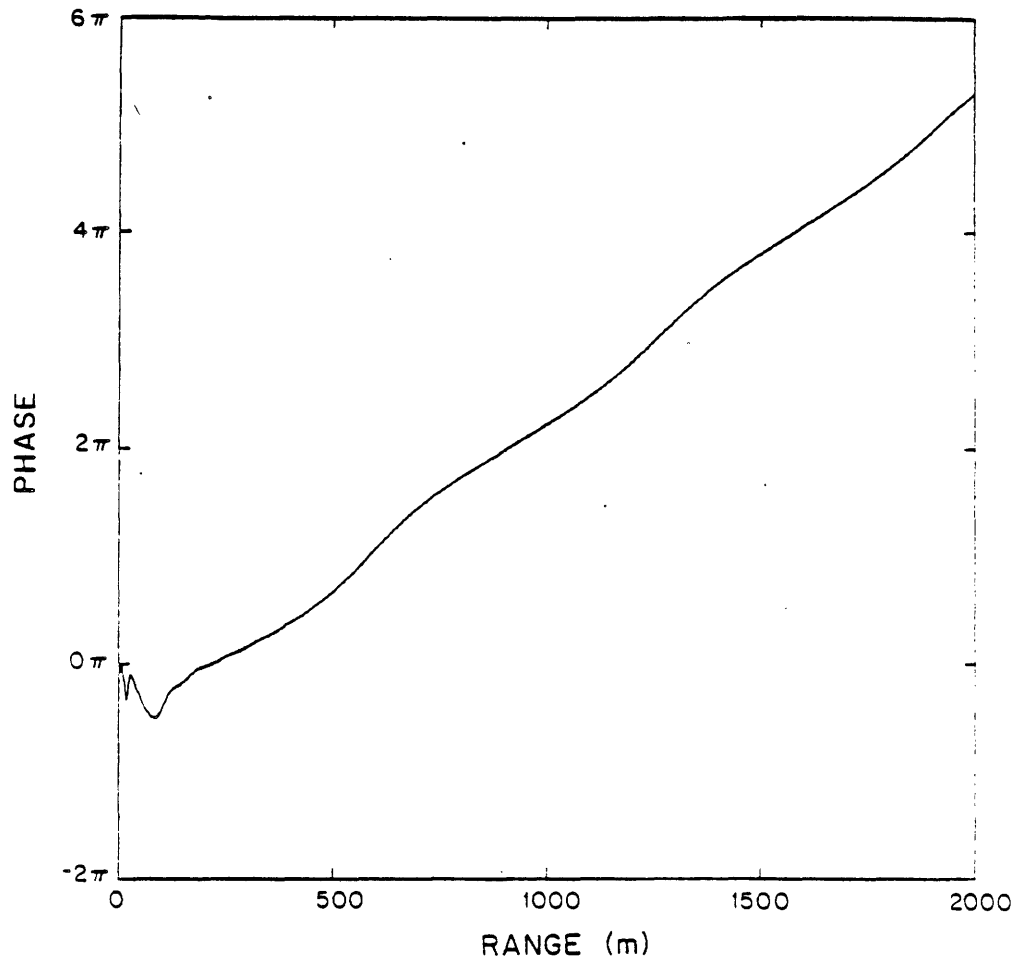


Figure V.3d.4b Residual phase for slow bottom example.

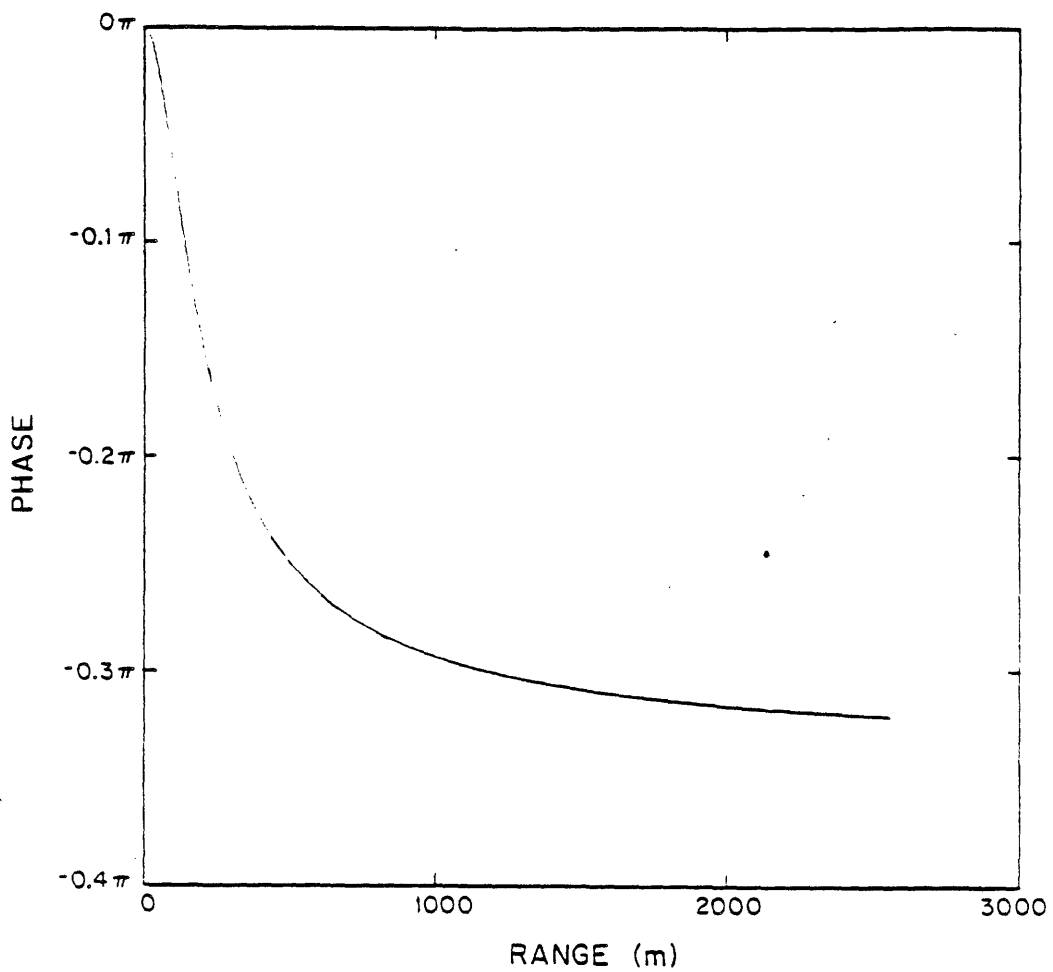


Figure V.3e.1 Residual phase for up-sampled pressure release example

We now show that for the dipole field we can actually interpolate the magnitude and unwrapped phase to increase the sampling rate of the quadrature components of the field. This allows us to determine the Green's function to a higher horizontal wave number than the Nyquist criteria applied to our original sampling scheme would have us believe.

We recall from Section (II.7) that if the pressure field for the dipole on the grid $\frac{\lambda_n}{1}$ were transformed and displayed in the range $0 < k_r < 2$ the result would be severely aliased and completely inaccurate in the region $1 < k_r < 2$. To obtain a transform accurate on $0 < k_r < 2$, the quadrature components must be at least sampled on the grid $\frac{\lambda_n}{2}$. We can still obtain the transform in the range $0 < k_r < 2$, never-the-less, by interpolating the field onto the grid $\frac{\lambda_n}{2}$ through its magnitude and unwrapped phase. Figures (V.3e.2a) and (V.3e.2b) show the magnitude and phase of the transform generated by such a procedure. First the magnitude and residual phase of $p(\frac{\lambda_n}{1})$ were generated. These were up-sampled as just discussed. From this up-sampled magnitude and residual phase (and the modeled, $k_0 R$, portion of the phase) the associated quadrature components were generated. This was transformed. Figures (V.3e.3a) and (V.3e.3b) show the magnitude and phase of the Hankel transform of $p(\frac{\lambda_n}{1})$ generated without interpolation. Only small differences in the magnitude are apparent. The phase curves also display only small differences though in the inhomogeneous region (where the phase is oscillating rapidly as evidenced by the two parallel lines) the small difference has caused a slightly different picture of the oscillations. By contrast, Figures (V.3e.4a) and (V.3e.4b) present the magnitude and phase of the Hankel transform of $p(\frac{\lambda_n}{1})$ up-sampled by direct spline interpolation of its quadrature components. Clearly, once again, a direct interpolation of the quadrature components did not work.

We apply this scheme for interpolating the magnitude and residual phase to the field of the fast bottom example of Section (IV.3a). We first generate the magnitude and unwrapped phase

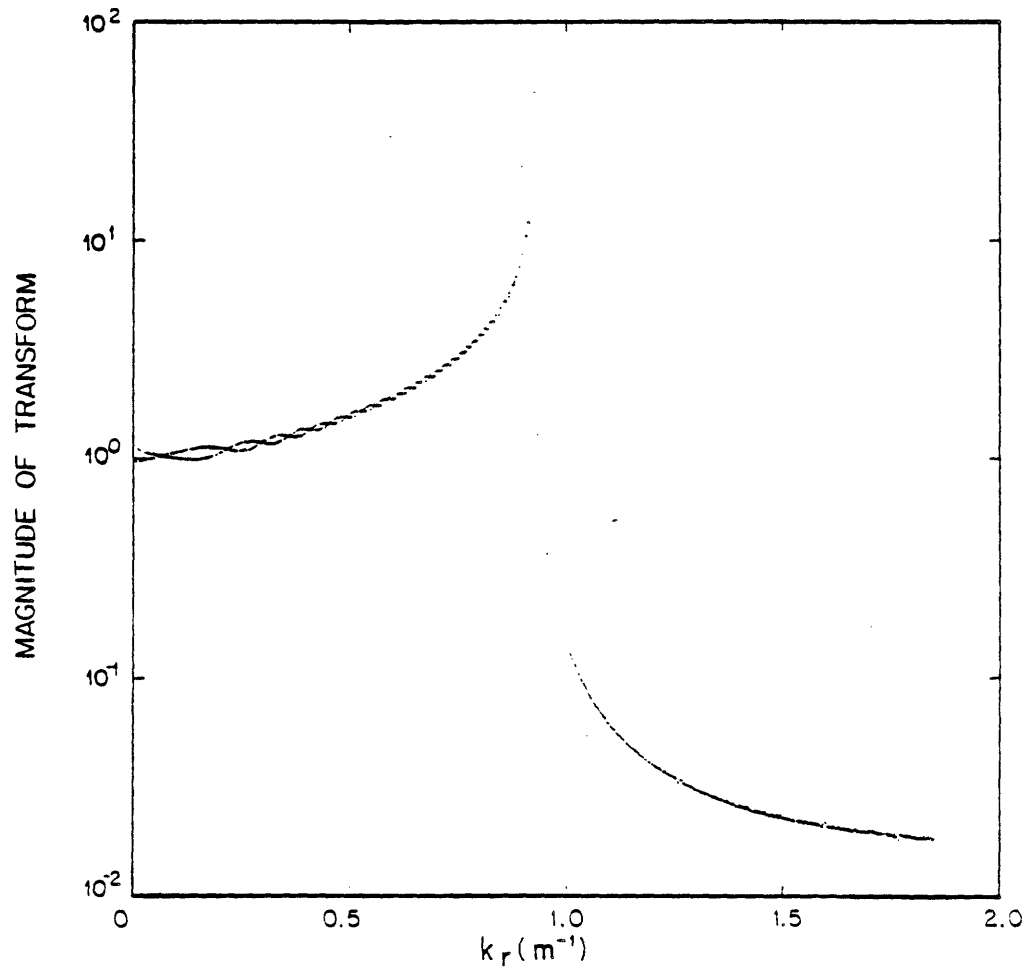


Figure V.3e.2a Log-magnitude of Hankel transform of up-sampled field for pressure release example shown in Figures V.3c.2 and V.3e.1

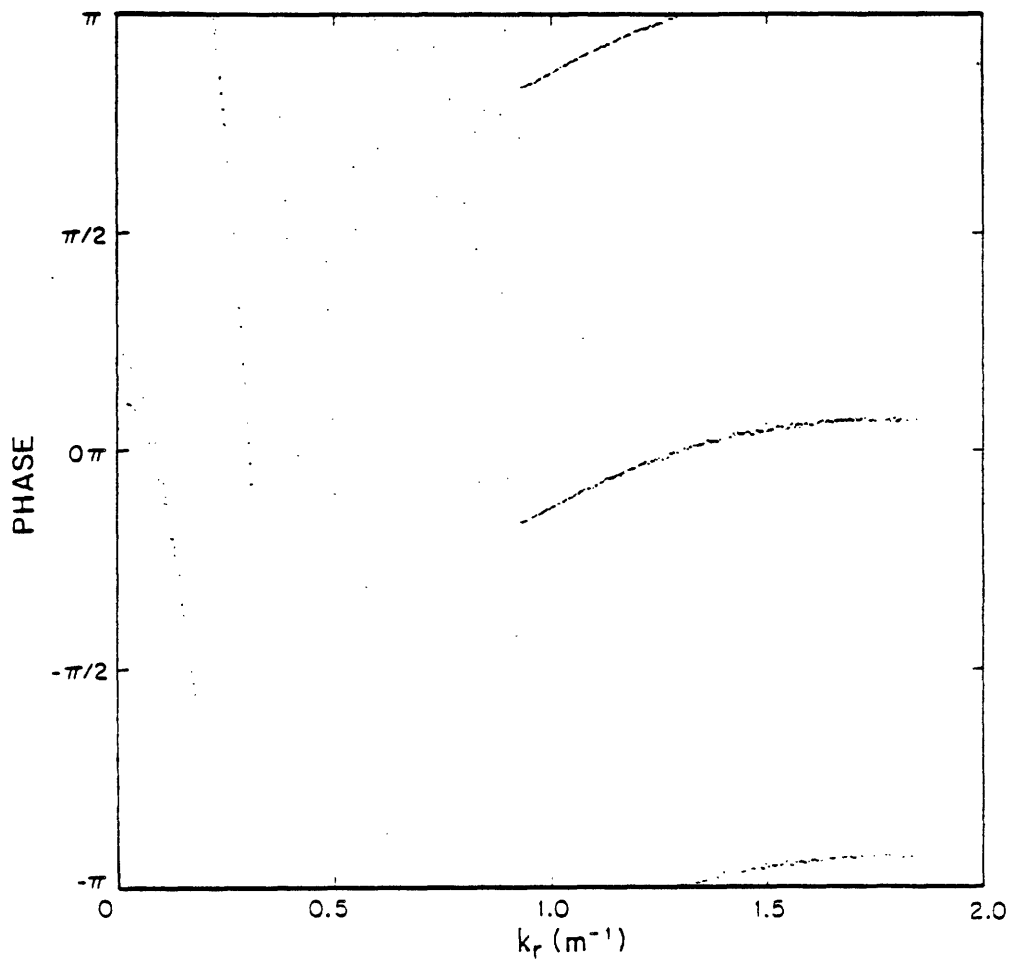


Figure V.3e.2b Phase of Hankel transform of up-sampled field for pressure release example shown in Figures V.3c.2 and V.3e.1

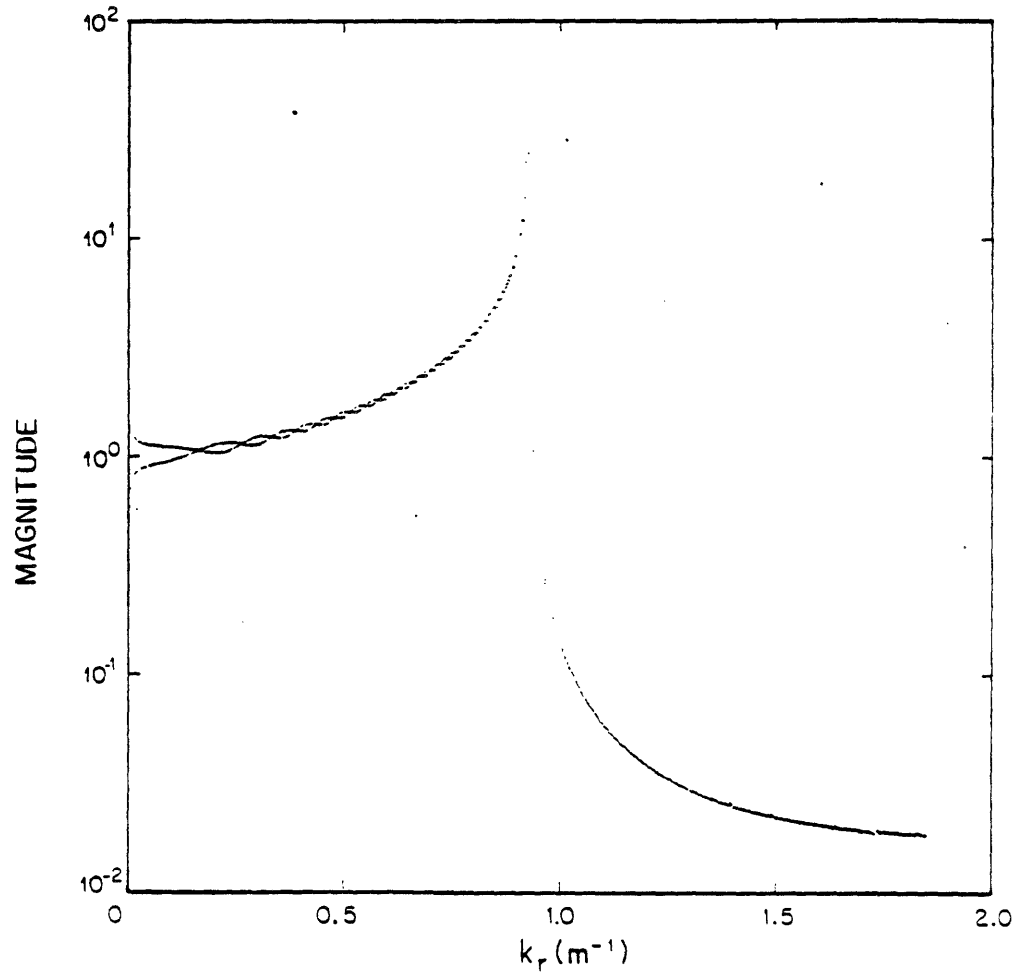


Figure V.3e.3a Log-magnitude of Hankel transform of field for pressure release example without up-sampling

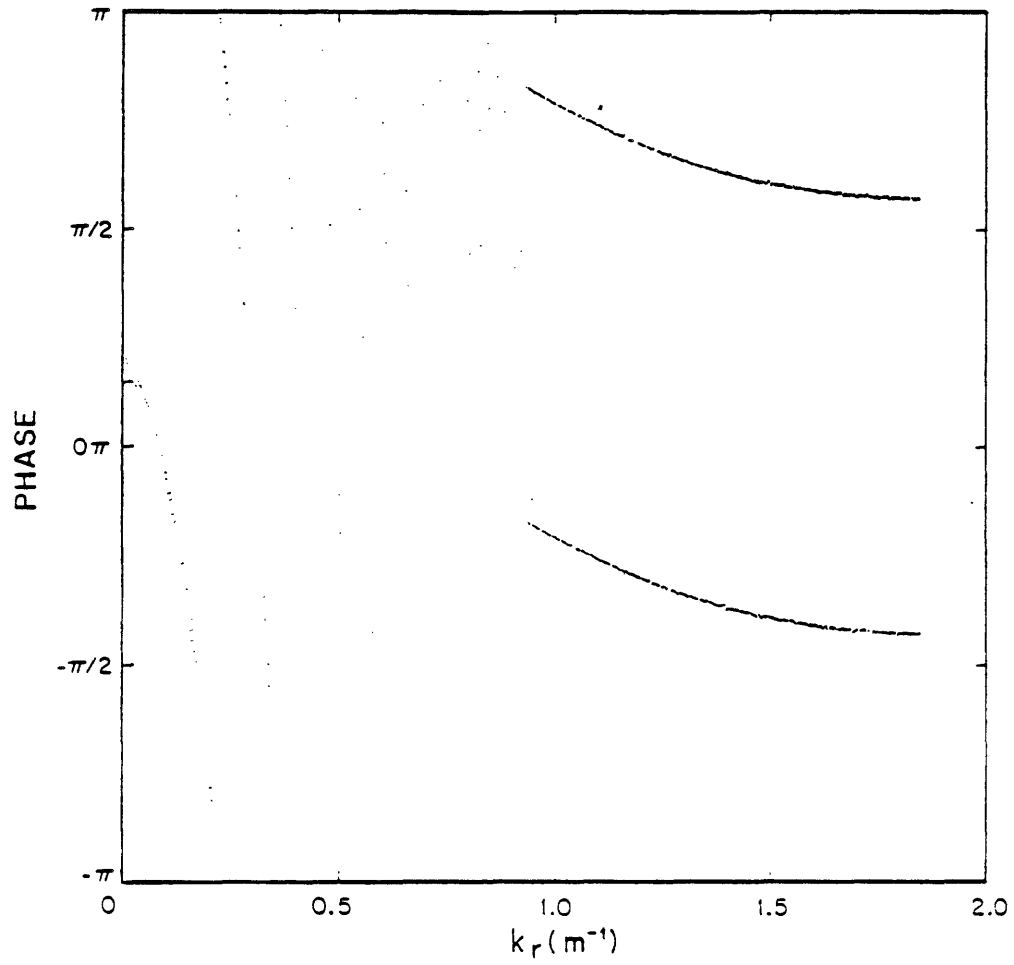


Figure V.3e.3b Phase of Hankel transform of field for pressure release example without up-sampling

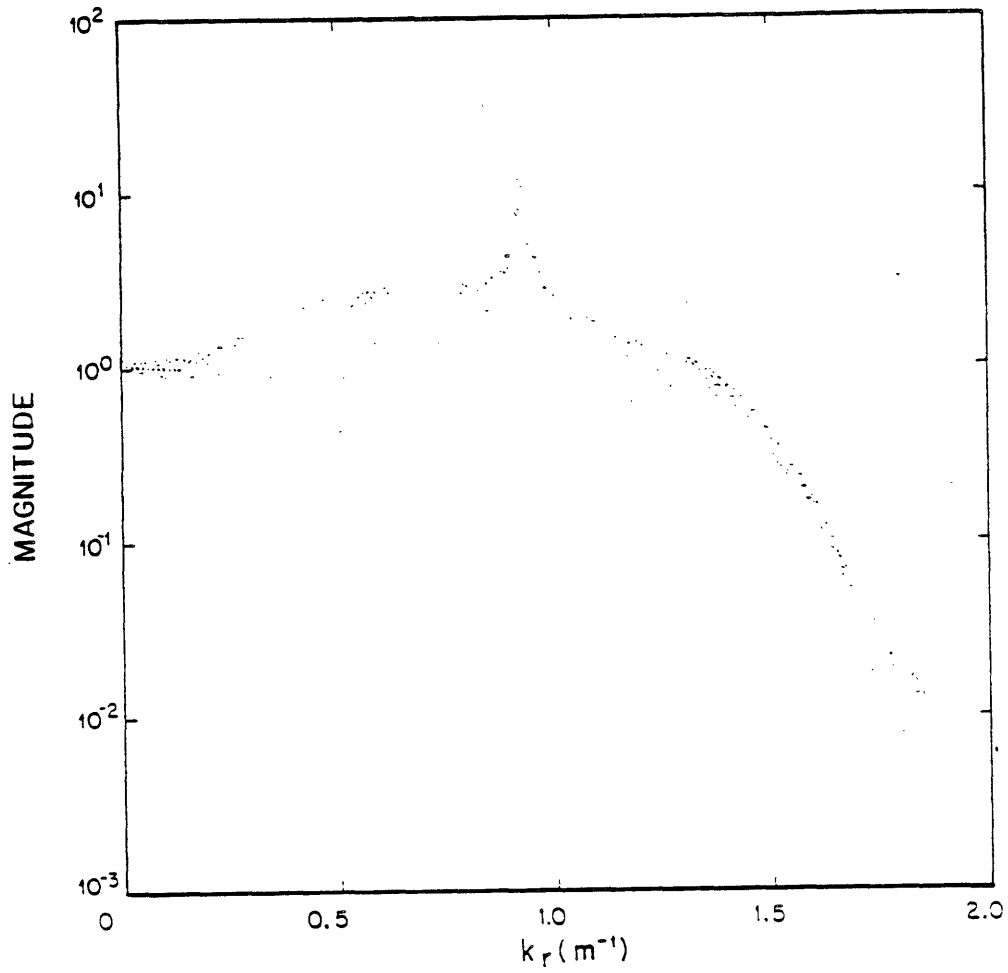


Figure V.3e.4a Log-magnitude of Hankel transform of field for the pressure release example that has been up-sampled through its quadrature components

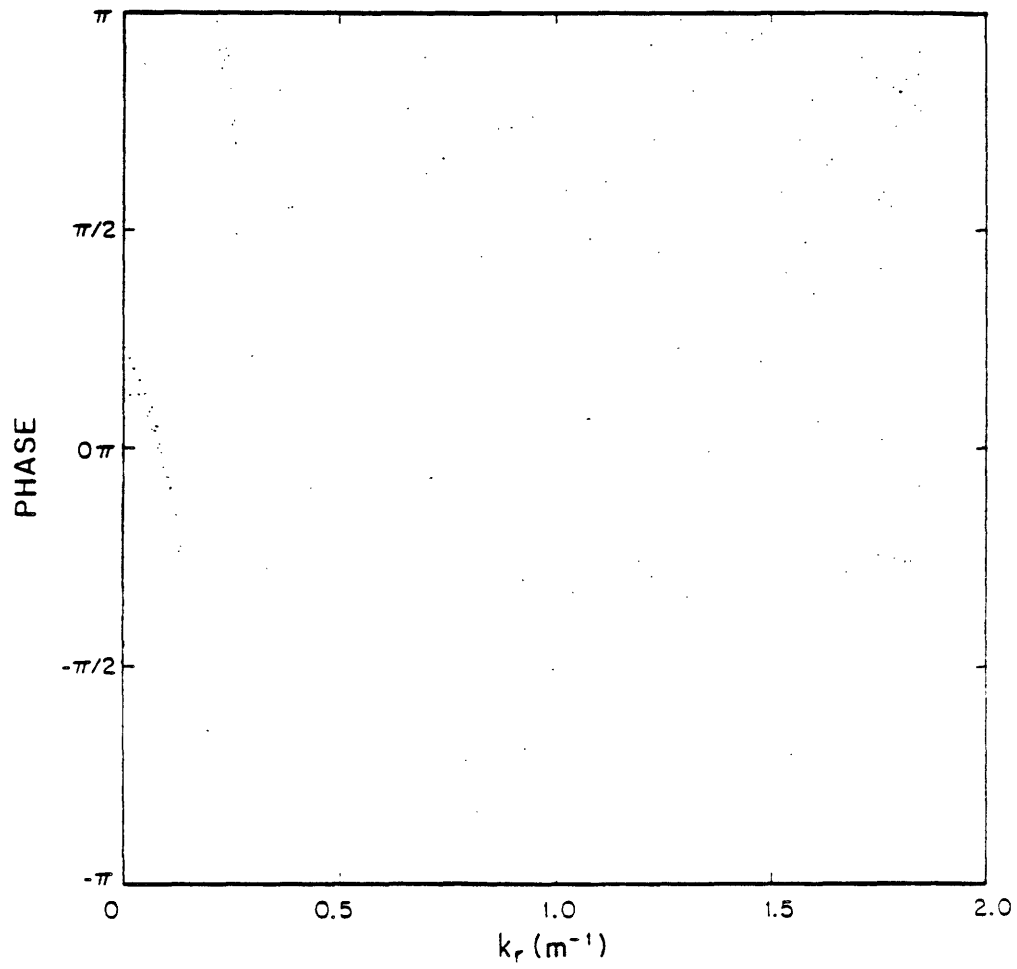


Figure V.3e.4b Phase of Hankel transform of field for the pressure release example that has been up-sampled through its quadrature components

of $p\left(\frac{\lambda_n}{2^3}\right)$, interpolate up to the grid $\frac{\lambda_n}{2}$, generate the quadrature components, and then Hankel transform. The magnitude and phase of the result is shown in Figures (V.3e.5a) and (V.3e.5b). The magnitude and phase of the correct transform (of $p\left(\frac{\lambda_n}{2}\right)$ generated without using this interpolation scheme) is shown in Figures (V.3e.6a) and (V.3e.6b). We see that the Hankel transform of the up-sampled data and the Hankel transform of the data originally available on the fine grid do not agree exactly. Figures (V.3e.7a) and (V.3e.7b) present the magnitude and phase of their complex difference and Figure (V.3e.8) presents the magnitude of the Hankel transform of that complex difference. This transform represents the errors made in the pressure domain by our up-sampling procedure that gave rise to the error in the Green's function. We see that practically all the error energy was concentrated at the origin. This error could be due to a breakdown in our phase unwrapping assumption near the origin or to a poor handling of the rapid change in magnitude by the splines. This problem can be corrected by a dense sampling of the original field near the origin so that there is no room for interpolation error there.

f) *Phase unwrapping errors*

At this point we consider briefly the kinds of error that might be expected when the assumption underlying this phase unwrapping technique is violated. If for some n

$$|\theta(R_n) - \theta(R_{n-1}) - k_0(R_n - R_{n-1})| > \pi \quad (1)$$

the wrong m_n will be chosen. From that point on, each m_k ($k = n, n+1, \dots$) chosen by the procedure will also be wrong by the same amount. A plot of this error is a step function of height $\hat{m}_n - m_n$ centered at n as shown in Figure (V.3f.1). If multiple violations occur, the error will look like the sum of step functions as illustrated in Figure (V.3f.2). The smoothness apparent in the residual phase in all of our examples suggests that no errors have occurred.

If the phase unwrapping scheme is used to interpolate the field, these errors are not serious. As part of the interpolation procedure, the quadrature components are regenerated from the

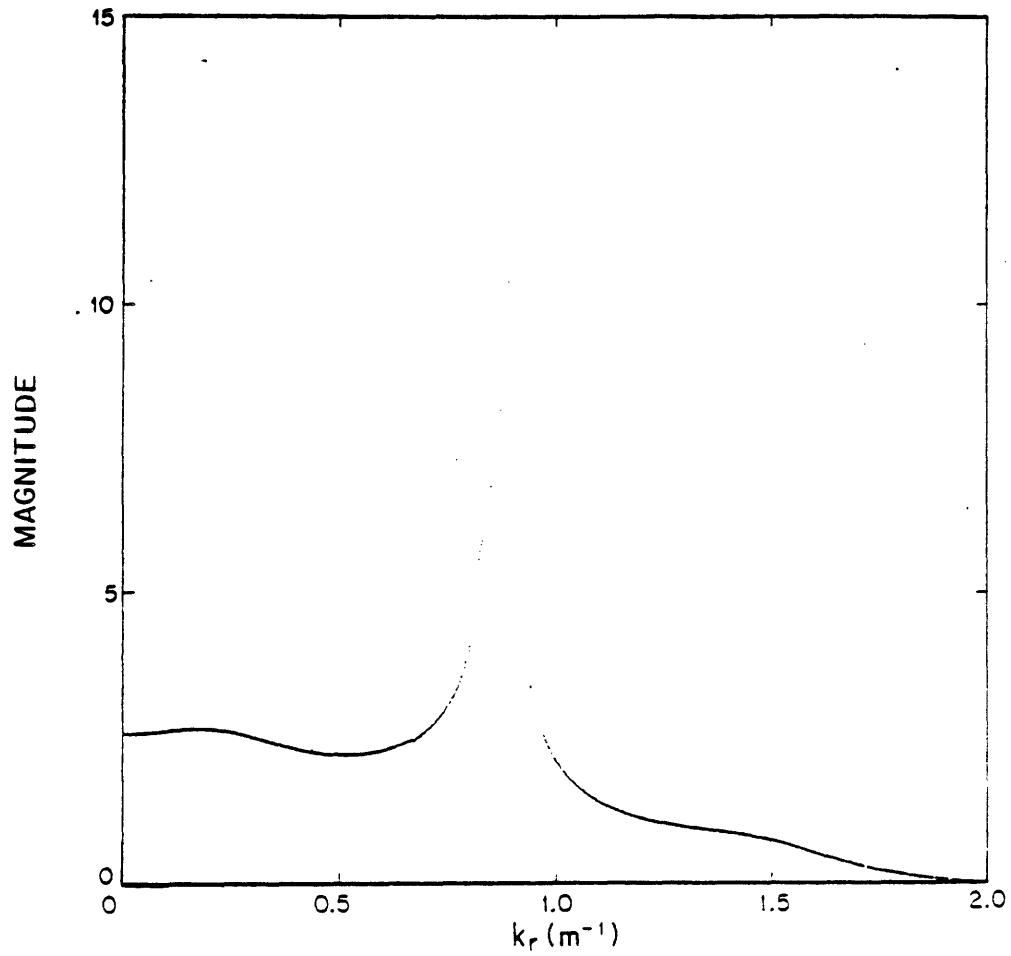


Figure V.3e.5a Log-magnitude of Hankel transform of the field for the fast bottom example after it has been up-sampled through its magnitude and residual phase

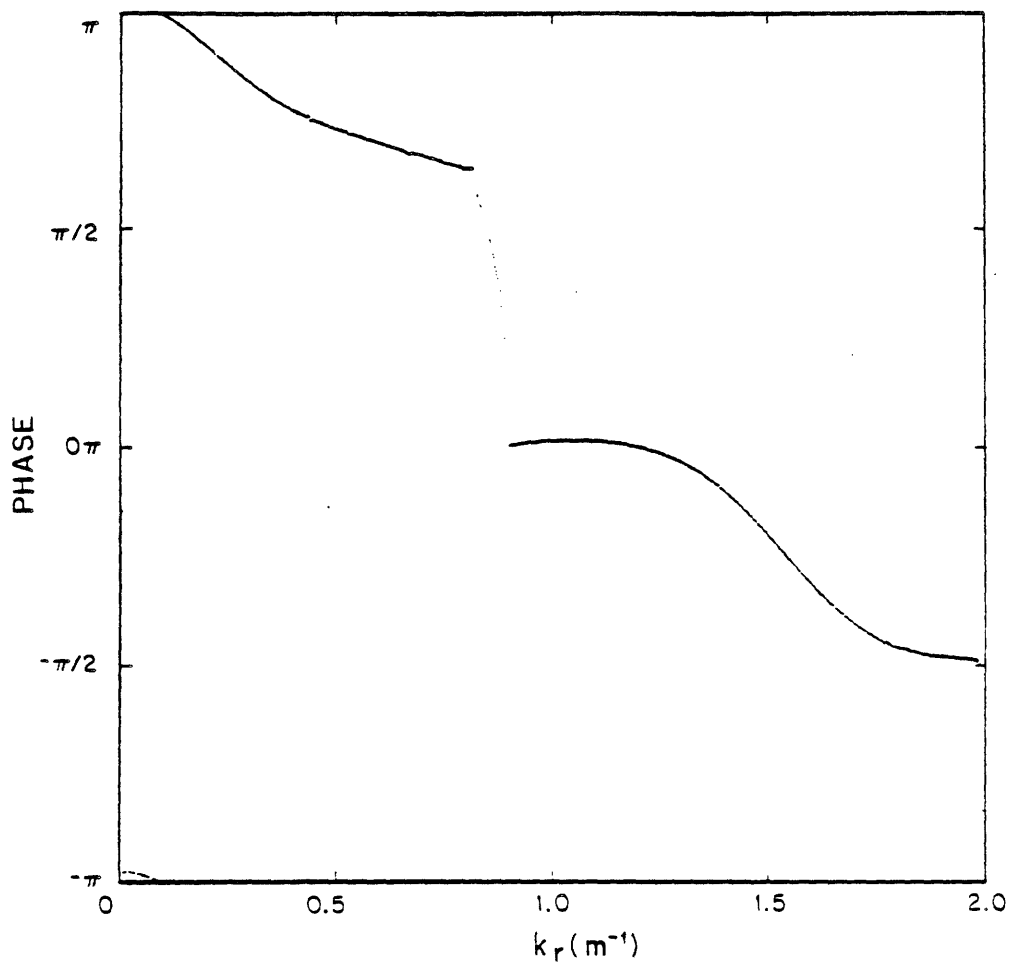


Figure V.3e.5b Phase of Hankel transform of the field for the fast bottom example after it has been up-sampled through its magnitude and residual phase

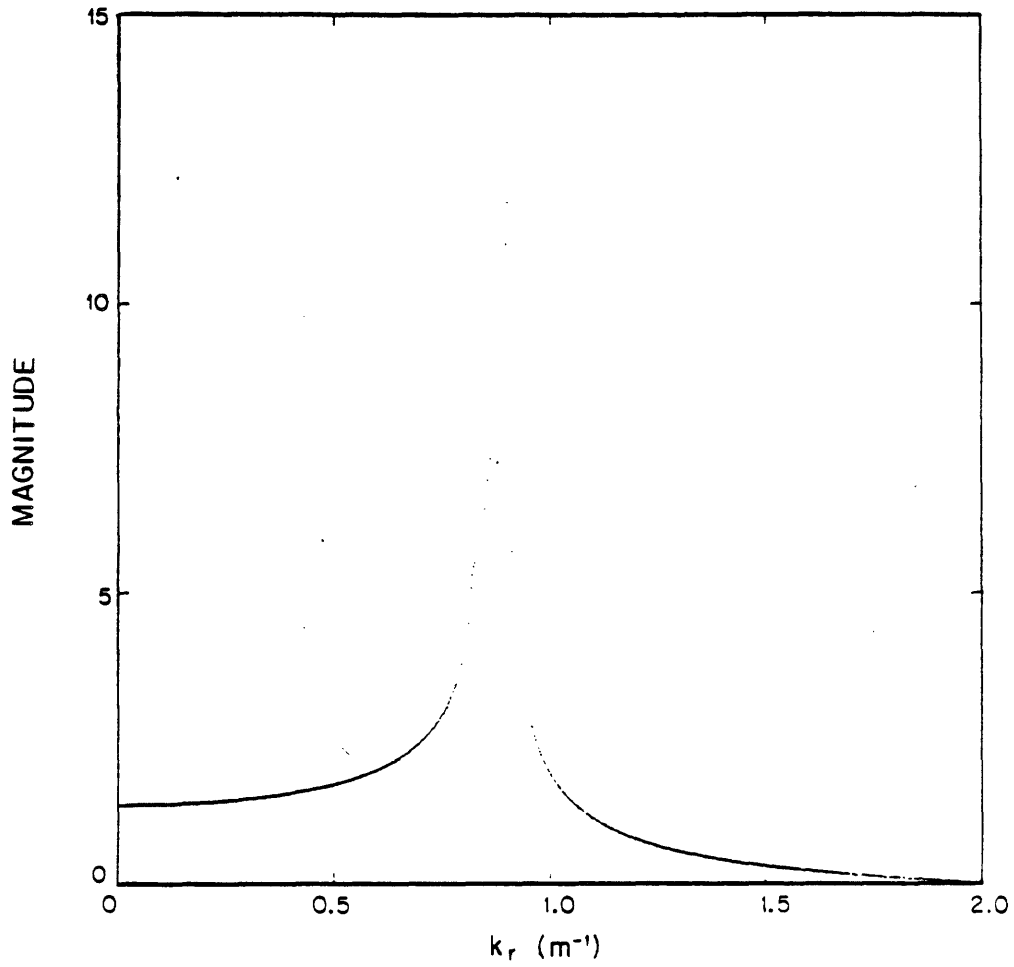


Figure V.3e.6a Log-magnitude of Hankel transform of the field for the fast bottom example generated originally on a fine grid

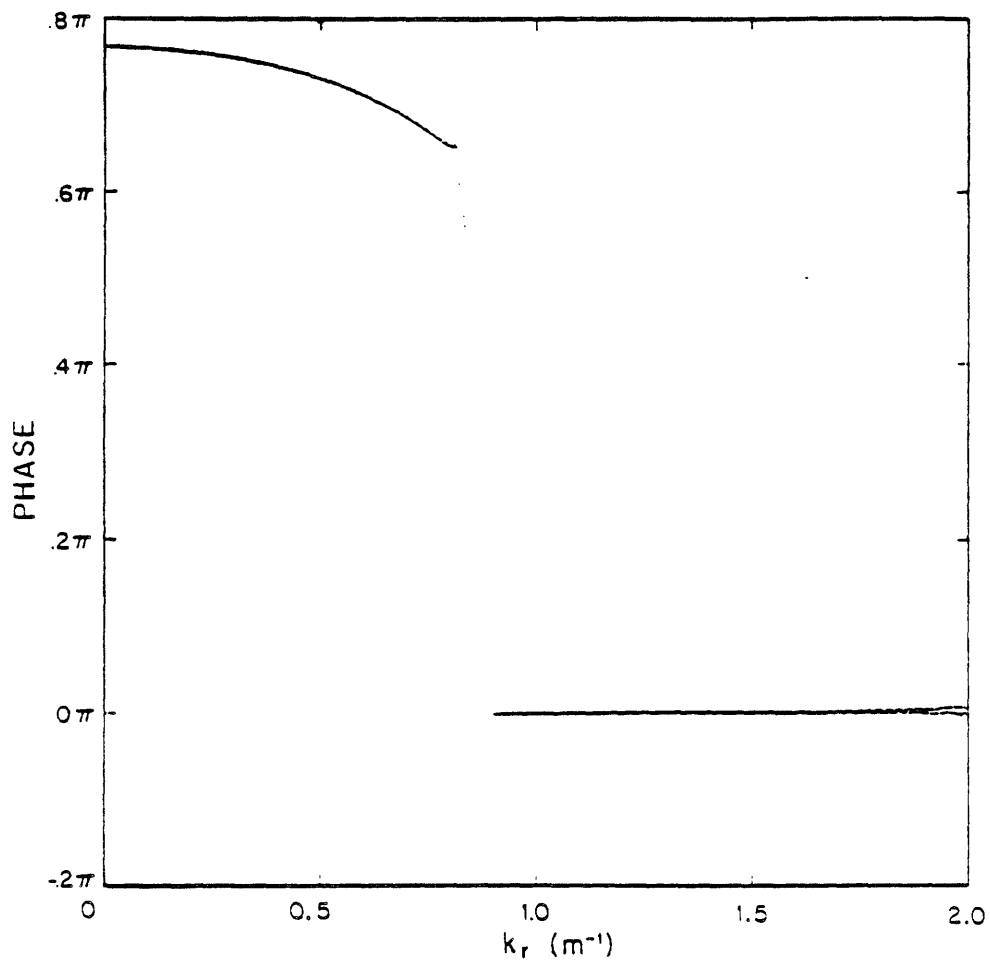


Figure V.3e.6b Phase of Hankel transform of the field for the fast bottom example generated originally on a fine grid

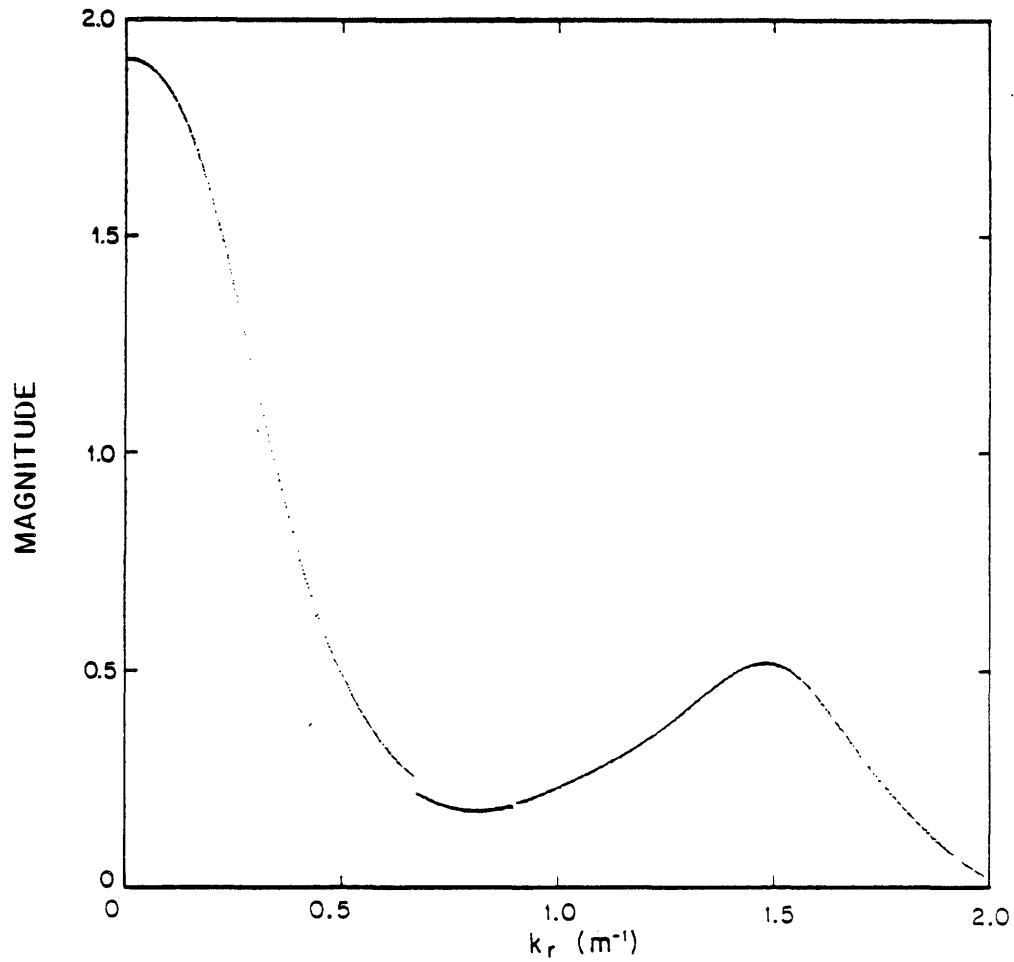


Figure V.3e.7a Magnitude of the complex error in the Hankel transform of the up-sampled field for the fast bottom example

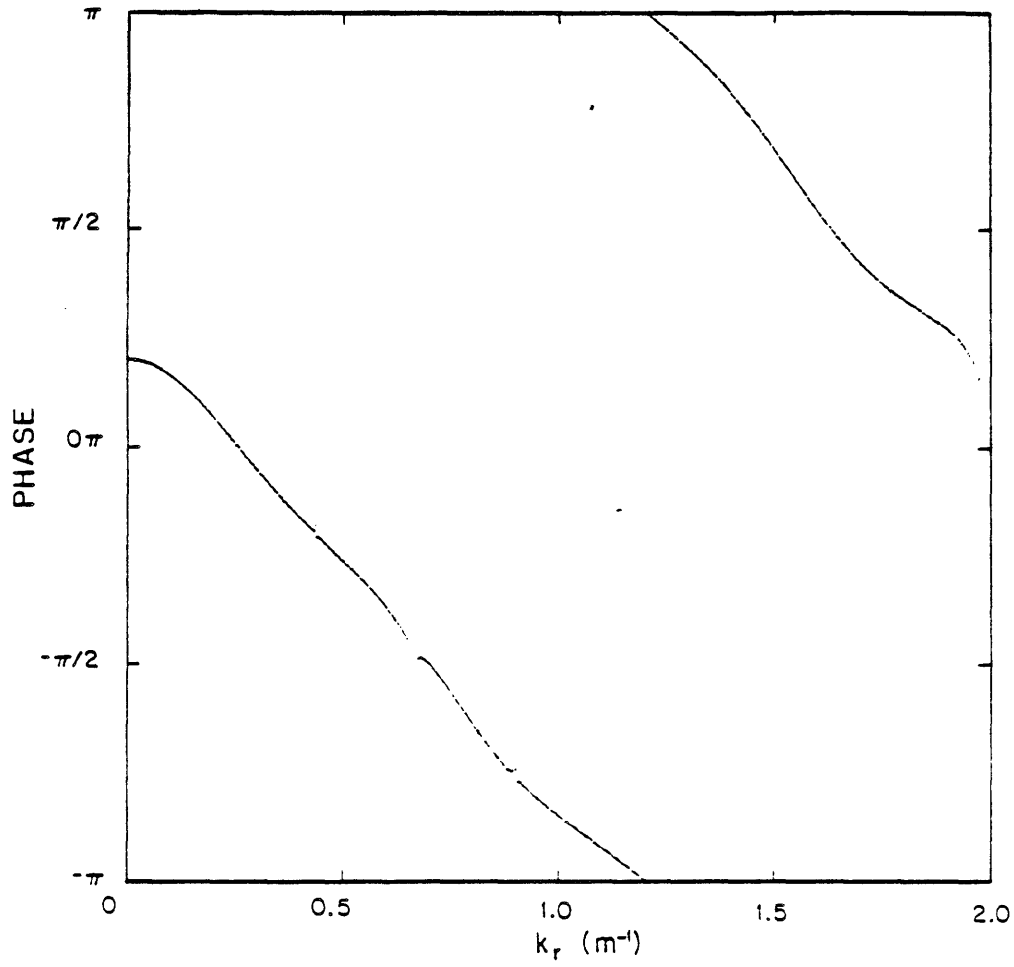


Figure V.3e.7b Phase of the complex error in the Hankel transform of the up-sampled field for the fast bottom example

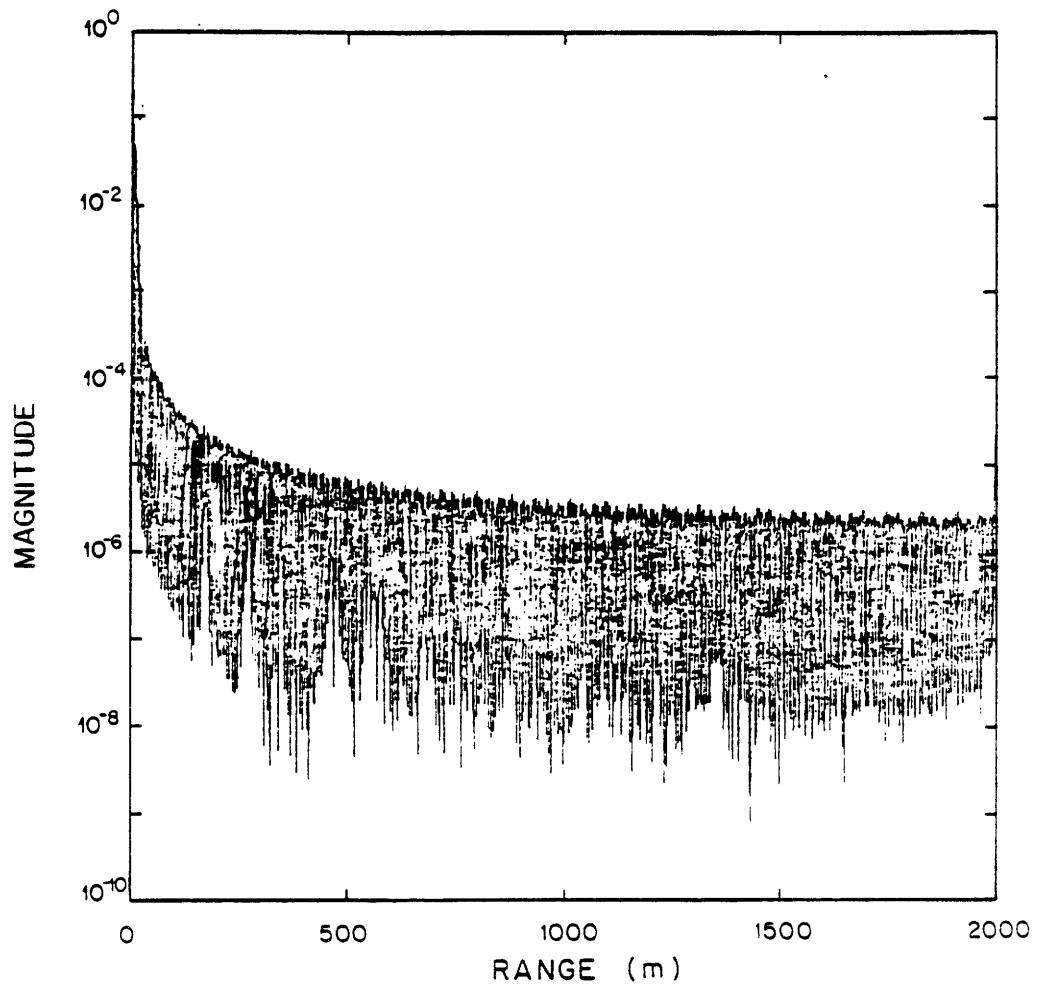


Figure V.3e.8 Magnitude of Hankel transform of the error shown in Figures V.3e.7a and V.3e.7b

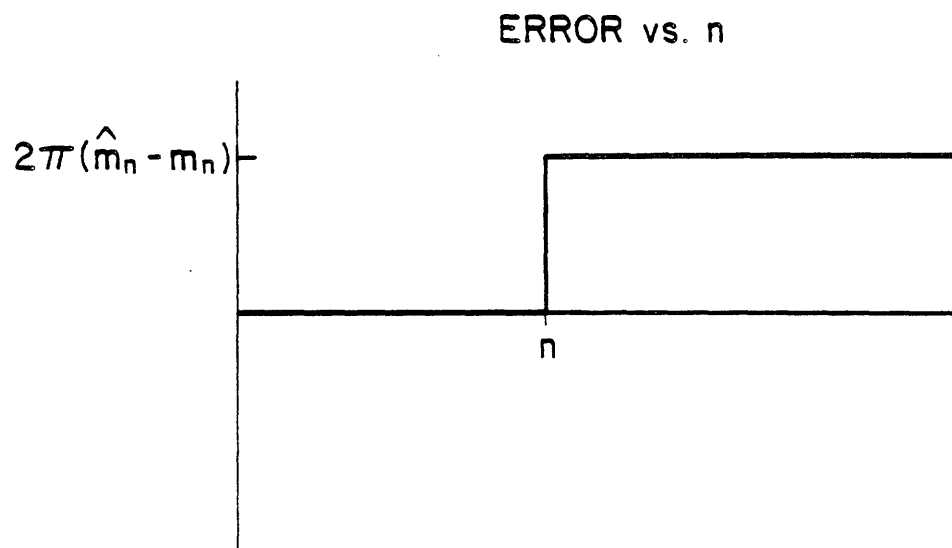


Figure V.3f.1 Error present in unwrapped phase when underlying assumption is violated between R_{n-1} and R_n .

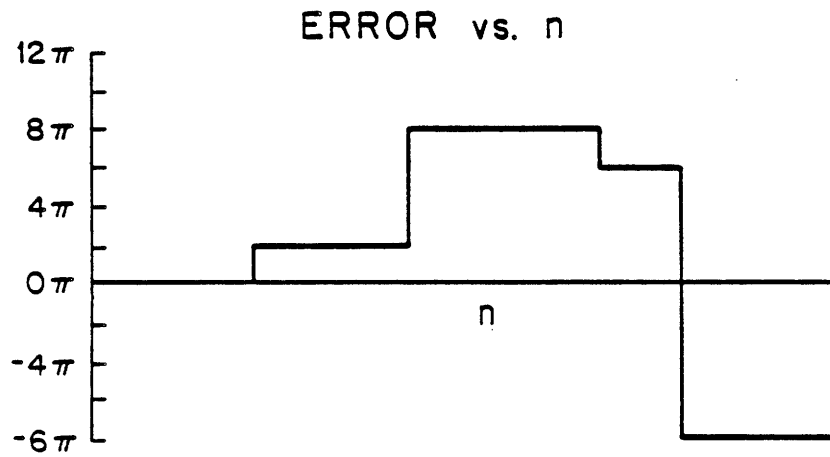


Figure V.3f.2 Error present in unwrapped phase when there are multiple violations in the phase unwrapping underlying assumption.

interpolated magnitude and phase. The error curve shown in Figure (V.3f.2) would have no affect on the quadrature components regenerated from the unwrapped phase. In general, after the interpolation, the error curve will not be a simple sum of steps but will be smeared by the interpolator. This will usually affect the quadrature components. If the interpolator is well chosen, the leakage will be small and limited to the area near the error. Finally we note that errors in the phase unwrapping scheme will occur when the unmodeled portion of the phase is varying rapidly between samples. When this happens the interpolator is likely to have difficulties even without errors in the unwrapped phase and this scheme is probably not appropriate.

V.4) Windowing

In Section (II.6) we stated that in terms of resolution the Hankel transform behaves very much like a Fourier transform. We wish to consider the resolution required to generate the Green's function and the window that this implies.

The total Green's function is given by

$$G_T(k_r, z) = \frac{i}{\sqrt{k_0^2 - k_r^2}} \left[\Gamma(k_r) e^{i\sqrt{k_0^2 - k_r^2}(z+z_0)} + e^{i\sqrt{k_0^2 - k_r^2}(z-z_0)} \right] \text{ when } z > z_0 \quad (1)$$

The most rapid variations in G_T (excluding possible poles in the reflection coefficient beyond the water wave number) occur near $k_r = k_0$. When $\Gamma(k_r)$ is smooth compared to $\frac{e^{i\sqrt{k_0^2 - k_r^2}(z+z_0)}}{\sqrt{k_0^2 - k_r^2}}$

the rapidity of these variations is dominated by the $\frac{e^{i\sqrt{k_0^2 - k_r^2}(z+z_0)}}{\sqrt{k_0^2 - k_r^2}}$ term. With a windowed

sample of the pressure field we can not hope to determine the exact behavior of G at $k_r = k_0$,

when $z + z_0$ is large the rapid variation in G is due to primarily the $e^{i\sqrt{k_0^2 - k_r^2}(z+z_0)}$ term. We can obtain an ad hoc estimate of the resolution we require by considering the *lobe widths* associated with the phase for k_r near k_0 .

That is we define $k_{r,n}$ by the relation:

$$\sqrt{k_0^2 - k_{r,n}^2}(z + z_0) \equiv n\pi \quad (2)$$

and define the lobe, δ_n by:

$$\delta_n \equiv k_{r,n-1} - k_{r,n} \quad (3)$$

If we use $(k_0 - k_{r,n})(k_0 + k_{r,n}) = \left(\frac{n\pi}{z + z_0}\right)^2$ then when $k_{r,n} \approx k$ we have:

$$(k_0 - k_{r,n}) \approx \frac{1}{2k_0} \left[\frac{n\pi}{z + z_0} \right]^2 \quad (4)$$

and

$$\delta_n \approx \frac{1}{2k_0} \left[\frac{\pi}{z + z_0} \right]^2 (n^2 - (n-1)^2) = \frac{1}{2k_0} \left[\frac{\pi}{z + z_0} \right]^2 (2n-1)$$

Section (II.6c) indicates that the required window width, B , is related to the desired resolution approximately as:

$$B \approx \frac{3}{\delta} \equiv \frac{3}{\delta_n} = \frac{3(z + z_0)^2}{\pi^2} \frac{1}{2k_0} \frac{1}{2n-1} \quad (6)$$

Thus to resolve the lobe closes to k when $z + z_0 = 136$ and $k_0 = .9246$ we require a window of about:

$$B = 3 * \left\{ \frac{136}{\pi} \right\}^2 \frac{1}{(2)(.9246)} = 3 * (1013) = 3040 \text{ meters} \quad (7)$$

V.5) Source-Height Variation

a) General expression

The procedure proposed to estimate the plane wave reflection coefficient, $\Gamma(k_r)$, and shown in Figure (V.1.1), requires that the pressure field be measured with the source at a fixed height, z_0 . [1] Frequently, experimental conditions cause the source-height to vary. In this section we will explore the effect that a varying source-height has on the estimate, $\hat{\Gamma}(k_r)$.

Instead of considering the effect of a varying source-height on the estimate for the plane wave reflection coefficient directly, we will consider its effect on the depth-dependent Green's function given by:¹

1) We will suppress the dependence of the depth-dependent Green's function on z and z_0 .

$$G(k_r) = \int_0^{\infty} P_R(r; z) J_0(k_r r) r dr = \frac{i\Gamma(k_r)}{\sqrt{k_0^2 - k_r^2}} e^{i\sqrt{k_0^2 - k_r^2}(z+z_0)} \quad (1)$$

which is the Hankel transform of the reflected pressure field. By considering the effect on the depth-dependent Green's function we can make use of the properties of the Hankel transform that we derived in Chapter II. The plane wave reflection coefficient is determined by multiplying the estimate of the depth-dependent Green's function by terms which compensate for the source strength and the source-receiver separation as was shown in Equation (V.1.2).

We consider the effect of a source height given by

$$z_0(r) = z_0 + h(r) \quad (2)$$

To explore the effect of Hankel transforming a pressure field measured at a source height that is a function of range, we write the Green's function estimated by Hankel transforming this field as:

$$\begin{aligned} \hat{G}(k_r) &= \\ &= \int_0^{\infty} P_R(r, z(r)) J_0(k_r r) r dr \\ &= \int_0^{\infty} \left[\int_0^{\infty} \frac{i\Gamma(\xi)}{\sqrt{k_0^2 - \xi^2}} e^{i\sqrt{k_0^2 - \xi^2}(z+z_0+h(r))} J_0(\xi r) \xi d\xi \right] J_0(k_r r) r dr \\ &= \int_0^{\infty} \frac{i\Gamma(\xi)}{\sqrt{k_0^2 - \xi^2}} e^{i\sqrt{k_0^2 - \xi^2}(z+z_0)} \left[\int_0^{\infty} e^{i\sqrt{k_0^2 - \xi^2}h(r)} J_0(\xi r) J_0(k_r r) r dr \right] \xi d\xi \end{aligned} \quad (3)$$

We now define:

$$H(k_r, \xi) \equiv \xi \int_0^{\infty} e^{i\sqrt{k_0^2 - \xi^2}h(r)} J_0(\xi r) J_0(k_r r) r dr \quad (4)$$

which with (3) becomes:

$$\hat{G}(k_r) = \int_0^{\infty} G(\xi) H(k_r, \xi) d\xi \quad (5)$$

Equations (4) and (5) exactly describe the effect that source-height variation has on the estimate of the depth-dependent Green's function. As written, however, they do not provide much insight into what variations are tolerable or into the qualitative effect of source-height variation. To provide us with this insight we develop an approximate expression for $H(k_r, \xi)$ by

using the windowing result of Section (II.6). We do this by considering $e^{i\sqrt{k_0^2 - \xi^2}h(r)}$ as a window. The result will be reasonable provided that the Fourier transform (in r) of $e^{i\sqrt{k_0^2 - \xi^2}h(r)}$ is narrow, as discussed in Section (II.6b).

We write

$$H(k_r, \xi) \equiv \xi \int_0^\infty e^{i\omega h(r)} J_0(\xi r) J_0(k_r r) r dr \quad \text{with} \quad \omega \equiv \sqrt{k_0^2 - \xi^2} \quad (6)$$

The Hankel transform of $J_0(\xi r)$ equals $\frac{\delta(k_r - \xi)}{k_r}$ so that :

$$\sqrt{k_r} H(k_r, \xi) \approx \xi \left[\left(\sqrt{k_r} \frac{\delta(k_r - \xi)}{k_r} \right) * W_\xi(k_r) \right] = \sqrt{\xi} W_\xi(k_r - \xi) \quad (7)$$

where

$$W_\xi(k_r) \equiv \int_{-\infty}^\infty e^{i\sqrt{k_0^2 - \xi^2}h(r)} e^{ik_r r} dr \quad (8)$$

This provides us with approximate expressions for the kernel, $H(k_r, \xi)$, and an approximate expression for the estimated Green's function in terms of the actual Green's function:

$$\begin{aligned} H(k_r, \xi) &\approx \frac{\sqrt{\xi}}{\sqrt{k_r}} W_\xi(k_r - \xi) \\ \hat{G}(k_r) &\approx \frac{1}{2\pi} \frac{1}{\sqrt{k_r}} \int_0^\infty \sqrt{\xi} G(\xi) W_\xi(k_r - \xi) d\xi \end{aligned} \quad (9)$$

In the following sections we apply this result to some special cases.

b) Particular variations

i) No source-height variation

When the source-height is constant, $h(r) \equiv 0$. For this case our approximate result above gives $W_\xi(k_r - \xi) = 2\pi\delta(k_r - \xi)$ and $\hat{G}(k_r) = G(k_r)$, which is as we would expect.

ii) Linear source-height variation

If the source-height varies linearly then $h(r) = ar$ and

$$W_{\xi}(k_r) = \int_{-\infty}^{\infty} e^{i[\omega a + k_r]r} dr = 2\pi\delta(k_r + a\sqrt{k_0^2 - \xi^2})^1. \text{ This gives us}$$

$$\hat{G}(k_r) = \frac{1}{\sqrt{\rho}} \int_0^{\infty} \sqrt{\xi} G(\xi) \delta(k_r - \xi + a\sqrt{k_0^2 - \xi^2}) d\xi \quad (1)$$

To evaluate the integral we have to simplify the argument of the delta function. We define $s \equiv \xi - a + \sqrt{k_0^2 - \xi^2}$, so that

$$\xi = \frac{s + \sqrt{s^2 - (1+a^2)(s^2 - a^2k_0^2)}}{1+a^2} \quad (2)$$

Substituting into Equation (1) we have:

$$\begin{aligned} \hat{G}(k_r) &= \frac{1}{\sqrt{\rho}} \int_c^{\infty} \sqrt{\xi[s]} G(\xi[s]) \delta(k_r - s) \frac{\xi - s}{2a^2 + \xi - s} ds \\ &= \frac{1}{\sqrt{\rho}} \sqrt{\xi_0} G(\xi_0) \frac{\xi_0 - \rho}{2a^2 + \xi_0 - \rho} \end{aligned} \quad (3)$$

Where

$$\begin{aligned} \xi_0 &= \frac{k_r + \sqrt{k_r^2 - (1+a^2)(k_r^2 - a^2k_0^2)}}{1+a^2} \\ &= \frac{k_r + a\sqrt{(a^2+1)k_0^2 - k_r^2}}{a^2+1} \end{aligned} \quad (4)$$

assuming that ξ_0 is real. We see that $\hat{G}(k_r)$ is a distorted version of $G\left[\frac{k_r + a\sqrt{(a^2+1)k_0^2 - k_r^2}}{a^2+1}\right]$. This approximate analysis also correctly indicates that as the slope of the linear variation, a , goes to zero $\hat{G}(k_r)$ goes to $G(k_r)$.

iii) Sinusoidal source-height variation

When the source-height variation is given by

$$h(r) = ae^{i\alpha r} \quad (1)$$

then

$$W_{\xi}(k_r) = \int_{-\infty}^{\infty} e^{i\sqrt{k_0^2 - \xi^2}ae^{i\alpha r}} e^{ik_r r} dr = \int_{-\infty}^{\infty} e^{i\omega e^{i\alpha r}} e^{ik_r r} dr \quad (2)$$

1) Provided $\xi < k$. The integral is not defined for complex arguments and a different analysis would be

with $\omega \equiv a \sqrt{k_0^2 - \xi^2}$.

To perform the integral in Equation (2) we expand the exponential in its Taylor series to obtain:

$$\begin{aligned} W_\xi(k_r) &= \int_{-\infty}^{\infty} \sum_{n=0}^{\infty} \frac{\left\{ i\omega e^{i\alpha r} \right\}^n}{n!} e^{ik_r r} dr \\ &= \sum_{n=0}^{\infty} \frac{(i\omega)^n}{n!} \int_{-\infty}^{\infty} e^{i\alpha n r} e^{ik_r r} dr \\ &= 2\pi \sum_{n=0}^{\infty} \frac{(i\omega)^n}{n!} \delta(k_r - n\alpha) \end{aligned} \quad (3)$$

We use this to determine the effect of the real cosinusoidal variation:

$$h(r) = \frac{ae^{i\alpha r} + ae^{-i\alpha r}}{2} \quad (4)$$

Substituting (4) into Equation (V.5a.8), for cosinusoidal variation $W_\xi(k_r)$ is seen to be given by:

$$W_\xi(k_r) = \int_{-\infty}^{\infty} e^{i\sqrt{k_0^2 - \xi^2} \frac{a}{2} e^{i\alpha r}} e^{i\sqrt{k_0^2 - \xi^2} \frac{a}{2} e^{-i\alpha r}} e^{ik_r r} dr \quad (5)$$

Equation (5) is the Fourier transform of a product of terms in the form of Equation (2). Consequently we can write Equation (5) as the convolution of terms in the form of Equation (3):

$$\begin{aligned} W_\xi(k_r) &= \frac{1}{2\pi} \left[2\pi \sum_{n=0}^{\infty} \frac{(i\omega)^n}{n!} \delta(k_r - n\alpha) \right] *_{k_r} \left[2\pi \sum_{n=0}^{\infty} \frac{(i\omega)^n}{n!} \delta(k_r + n\alpha) \right] \\ &= 2\pi \sum_{n=0}^{\infty} \sum_{m=0}^{\infty} \frac{\left\{ \frac{ia\sqrt{k_0^2 - \xi^2}}{2} \right\}^{m+n}}{n!m!} \delta(k_r - (n-m)\alpha) \end{aligned} \quad (6)$$

If we perform the integration (V.5a.9) we obtain:

$$\hat{G}(k_r) \approx \left[\frac{1}{\sqrt{\rho}} \right] \left[\sum_{n=0}^{\infty} \sum_{m=0}^{\infty} \frac{\left\{ \frac{ia\sqrt{k_0^2 - (k_r - (n-m)\alpha)^2}}{2} \right\}^{m+n}}{n!m!} \sqrt{k_r - (n-m)\alpha} G(k_r - (n-m)\alpha) \right] \quad (7)$$

The cosinusoidal source-height variation with an amplitude, a , and a frequency α , has the effect of reverberating, or comb filtering, $\sqrt{k_r} G(k_r)$ in two dimensions. The impulses of the required for this case.

filter are spaced at the variation frequency α . The weightings, which we define to be $w(k_r; m, n)$, determine the envelope of the reverberation. They depend on the amplitude, a :

$$w(k_r; m, n) \equiv \frac{\left\{ \frac{ia \sqrt{k_0^2 - k_r^2}}{2} \right\}^{m+n}}{m!n!} = \frac{\left\{ \frac{ia \sqrt{k_0^2 - k_r^2}}{2} \right\}^m}{m!} \frac{\left\{ \frac{ia \sqrt{k_0^2 - k_r^2}}{2} \right\}^n}{n!} \quad (8)$$

We can write the estimate for the Green's function in terms of these weighting functions as:

$$\hat{G}(k_r) \approx \left[\frac{1}{\sqrt{\rho}} \right] \left[\sum_{n=0}^{\infty} \sum_{m=0}^n \frac{1}{k_r > (n-m)\alpha} w(k_r - (n-m)\alpha; m, n) \sqrt{k_r - (n-m)\alpha} G(k_r - (n-m)\alpha) \right] \quad (9)$$

The weighting functions, $w(k_r - (n-m)\alpha; m, n)$, are greatest when $m = n = n_{\max}$ and decay rapidly from that point in m and n . This result can be shown by replacing the factorials in (8) with Stirling's approximation (excellent even for small n : $n! \approx \sqrt{2\pi n} \left\{ \frac{n}{e} \right\}^n$) and defining

$x \equiv \frac{ia \sqrt{k_0^2 - k_r^2}}{2}$. The weighting functions then become:

$$w(k_r; m, n) = \frac{x^m}{m!} \frac{x^n}{n!} \approx \frac{1}{\sqrt{2\pi m}} \left\{ \frac{xe}{m} \right\}^m \frac{1}{\sqrt{2\pi n}} \left\{ \frac{xe}{n} \right\}^n \quad (10)$$

The $\left\{ \frac{xe}{m} \right\}^m$ term has its maximum at $m = x$ and falls off in m with greater than geometric decay. The $\frac{1}{\sqrt{m}}$ term pulls this maximum only very slightly lower.

The result is that $w(k_r; m, n)$ is large for $m, n \approx \frac{a}{2} \sqrt{k_0^2 - k_r^2}$ and small elsewhere. When

$\left| \frac{a}{2} \sqrt{k_0^2 - k_r^2} \alpha \right| \leq \left| \frac{a\alpha}{2} \right| \ll 1$ we can ignore the $(n-m)\alpha$ term in (9) so that $\hat{G}(k_r)$ is given

approximately by

$$\hat{G}(k_r) \approx \left[\frac{1}{\sqrt{\rho}} \right] \left[\sum_{n=0}^{\infty} \sum_{m=0}^n \frac{\left\{ \frac{ia \sqrt{k_0^2 - k_r^2}}{2} \right\}^{m+n}}{n!m!} \sqrt{k_r - (n-m)\alpha} G(k_r - (n-m)\alpha) \right] \quad (11)$$

By defining:

$$C(k_r; n) \equiv (i)^n \sum_{m=\max(0, -n)}^{\infty} \frac{(-1)^m \left\{ \frac{a}{2} \sqrt{k_0^2 - k_r^2} \right\}^m}{m!} \frac{\left\{ \frac{a}{2} \sqrt{k_0^2 - k_r^2} \right\}^{n+m}}{(n+m)!} \quad (12)$$

we can obtain the result, valid for $\left| \frac{a\alpha}{2} \right| \ll 1$ that

$$\sqrt{k_r} \hat{G}(k_r) \approx \sum_{k=-\infty}^{\left[\frac{k_r}{\alpha} \right]} C(k_r; n) \sqrt{k_r - n\alpha} G(k_r - n\alpha) \quad (13)$$

A perspective plot of $C(k_r, n)/(i)^n$ is presented in Figure (V.5c.1a) for the case $a = 3$ and $k_0 = .9246159$. The back of this figure corresponds to $k_r = k_0$ and consequently $k_z = 0$. The Green's function in this region corresponds to plane wave components of the field which are directed entirely in the radial direction and which do not vary in z . Figure (V.5c.1b) presents the slice of Figure (V.5c.1a) corresponding to this region, $C(k_0, n)$. $C(k_0, n)$ is zero everywhere except at $n = 0$, where it is 1. Referring to Equation (13) we see that the degraded estimate of the Green's function at $k_r = k_0$ is given by:

$$\hat{G}(k_0) = \frac{1}{\sqrt{k_0}} \sum_{n=-\infty}^{\left[\frac{k_0}{\alpha} \right]} C(k_0, n) \sqrt{k_0 - n\alpha} G(k_0 - n\alpha) \quad (14)$$

Substituting for $C(k_0, n)$ in Equation (12) we see that

$$\hat{G}(k_0) = G(k_0) \quad (15)$$

The portion of the spectrum, $k_r = k_0$, corresponds to field components that do not vary in z . It is reasonable, then, that the cosinusoidal source-height variation did not affect that portion of the angular spectrum.

In Figure (V.5c.1a) moving forward towards the leading edge corresponds to decreasing k_r and increasing k_z . With decreasing k_r , $C(k_r, n)$ becomes increasingly less impulsive, indicating greater amounts of degradation. Figure (V.5c.1c) presents the slice $C(0, n)$. This slice corresponds to that portion of the angular spectrum which has the maximum amount of vertical variation. In Figure (V.5c.1c) the value $C(0, 0)$ is not even as large as the adjacent values,

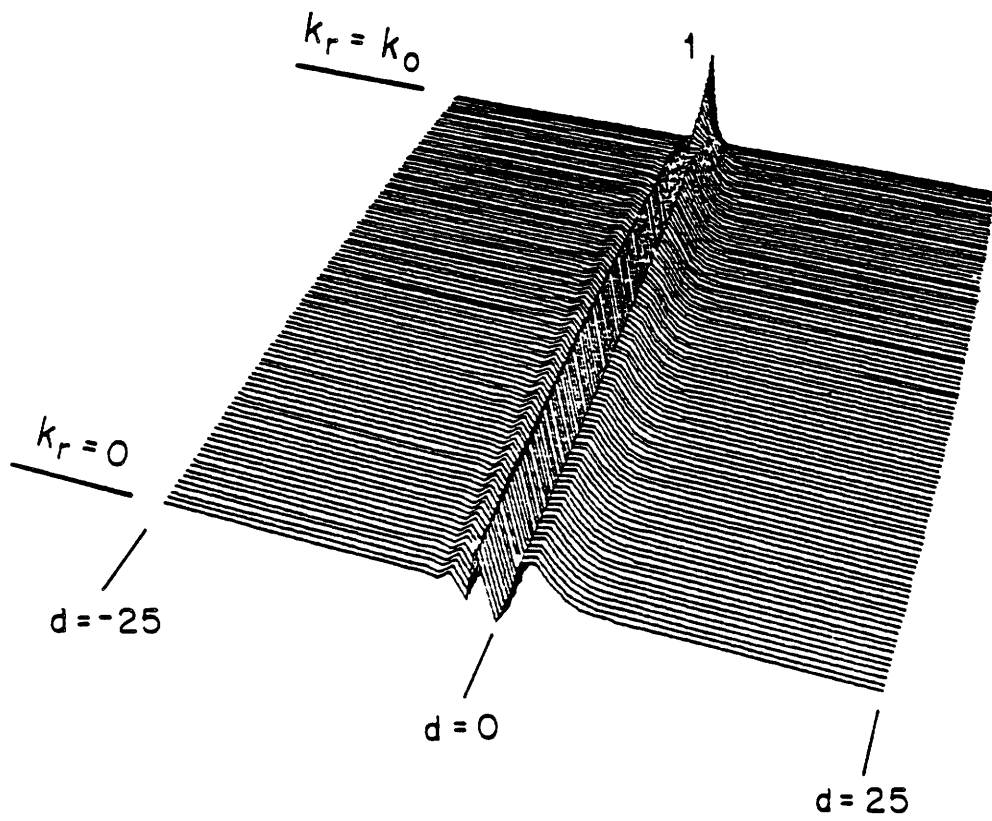


Figure V.Sc.1a Perspective plot of $C(k_r, n)/(i)^n$ with $a=3$

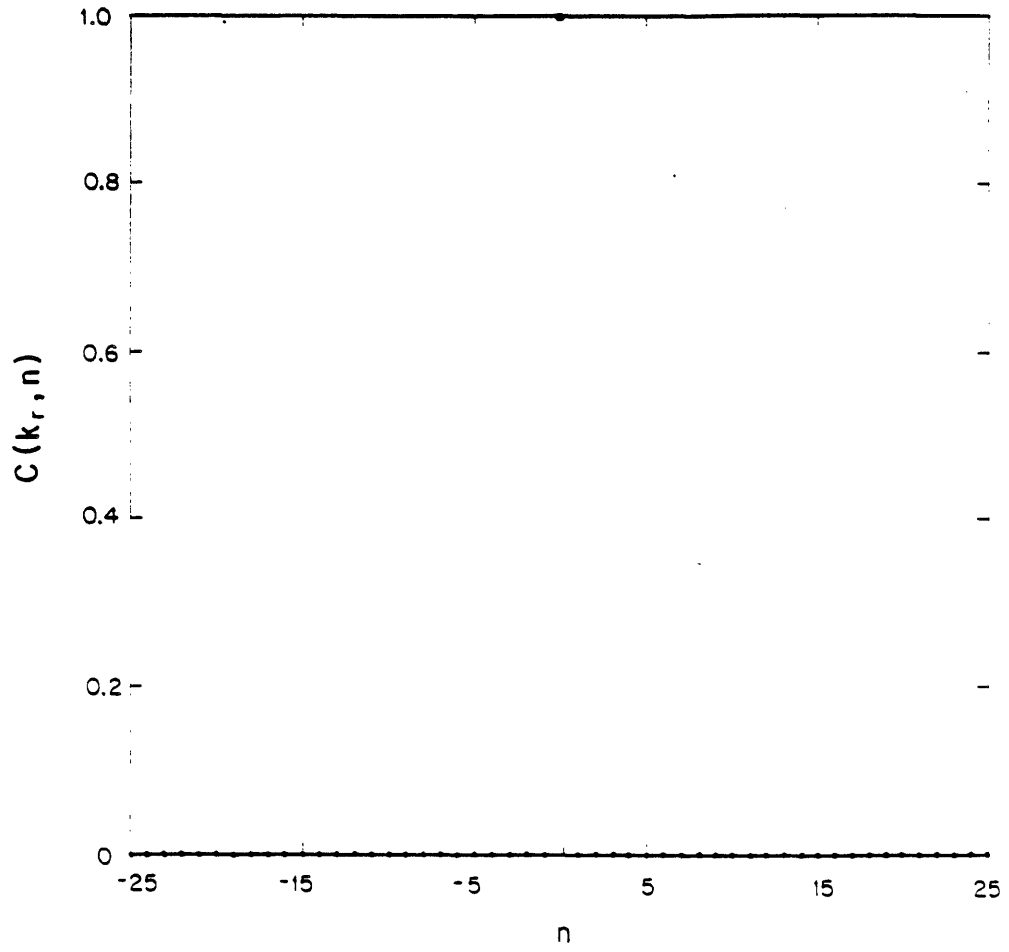


Figure V.5c.1b $C(k_0, n)$ with $a=3$

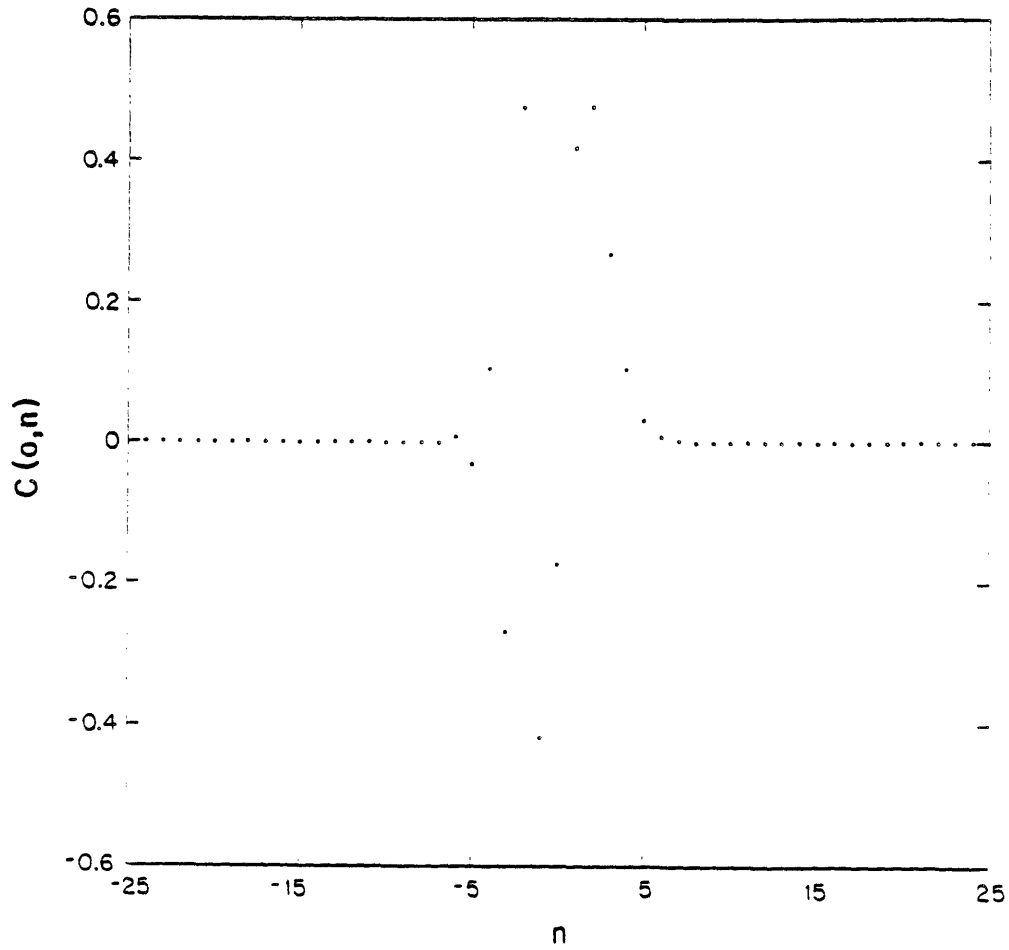


Figure V.5c.1c $C(0,n)$ with $a=3$

$C(0, -1)$ and $C(0, 1)$. The Greens function will be degraded by cosinusoidal source-height variation in this region.

Figure (V.5c.2) presents a perspective plot of $C(k_r, n)/(i)^n$ for the case $a = 12$ and $k_0 = .9246159$. Once again $C(k_0, n)$ is the discrete delta function, $\delta(n)$, and the Green's function will not be degraded at $k_r = k_0$. Because a is larger now, $\frac{a}{2}\sqrt{k_0^2 - k_r^2}$ of Equation (12) grows more rapidly as k_r becomes smaller than it did for $a = 3$. As a result the figure shows that serious degradation begins for k_r much closer to k_0 . The increased amplitude, a , has resulted in an increased amount of degradation. The product, $ak_r = a\sqrt{k_0^2 - k_r^2}$, determines the severity of this effect.

We note also that because of the $(i)^n$ factor in Equation (12), the phase of $C(k_r, n)$ increases by $\frac{\pi}{2}$ with each n . This suggests that cosinusoidal source-height variation may dramatically affect the phase of the estimated Green's function, $\hat{G}(k_r)$, even before it significantly affects the magnitude.

Thus we have seen that the effect of sinusoidal source-height variation is to comb-filter the estimate of $\sqrt{k_r}\hat{G}(k_r)$. The spacing between impulses in the comb filter is the frequency of the source-height variation. The amplitude of the source-height variation and the vertical wave number, $k_0^2 - k_r^2$, together determine the weightings of the impulses. When the product of the amplitude and the vertical wave number is small, the only contribution comes from the low lag components. As this product increases, the higher lag components begin to contribute and the comb-filtering will become increasingly apparent. If the frequency of the source-height variation is very low, causing the spacing of the impulses in the filter to be very small, the degradation will appear as a smearing.

V.5) Summary

In this chapter we have studied the issues associated with the inversion of pressure field

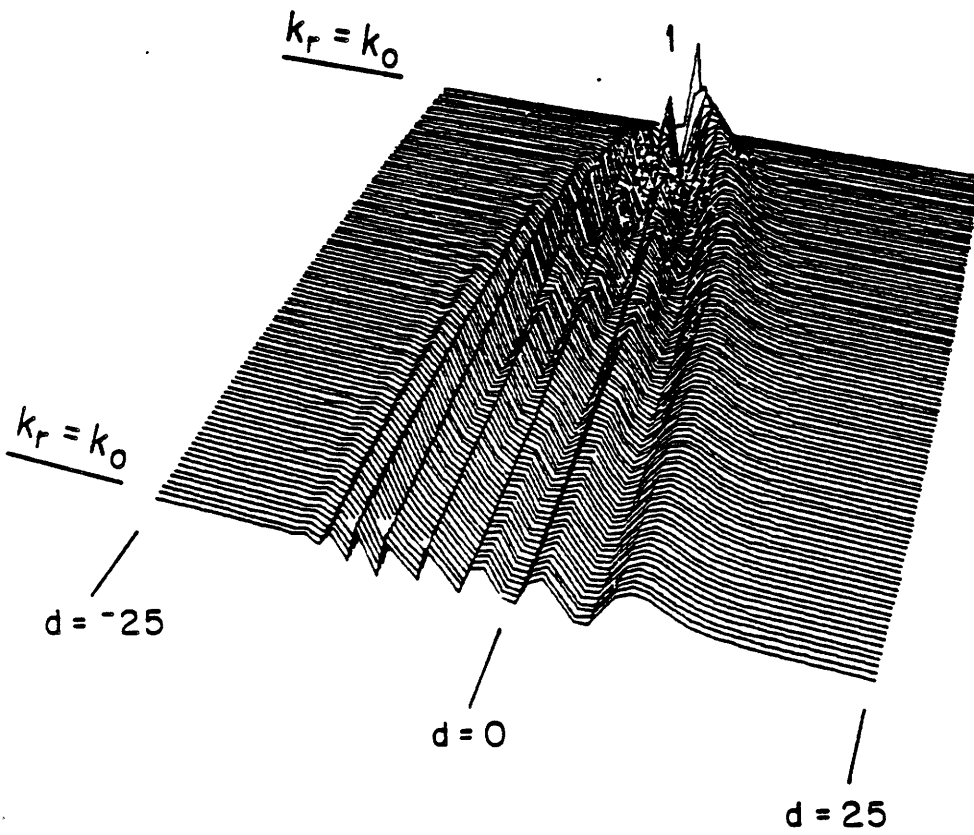


Figure V.5c.2 $C(k, n)/(i)^n$ with $a = 12$

data through the Hankel transform to estimate the depth-dependent Green's function and the plane wave reflection coefficient. We have developed a phase unwrapping procedure that allows us to interpolate the magnitude and unwrapped phase and thereby determine from the set of field samples available, the values of the field at the ranges we require for processing. We have also shown that it is better to estimate the total depth-dependent Green's function from the Hankel transform of the total field, and to later remove the effects of the source. Finally, we have examined the effects of source-height variation to help us understand the possible degradation that this effect would introduce into the depth-dependent Green's function estimated from real data.

We are ready to perform a preliminary processing of real data.

References

1. G.V. Frisk, A.V. Oppenheim, and D. Martinez, "A Technique for Measuring the Plane-Wave Reflection Coefficient of the Ocean Bottom," *J. Acoustical Soc. Amer.* 68 (2), pp.602-612 (1980).
2. Papoulis, *Systems and Transforms with Applications in Optics*, McGraw-Hill, New York (1968).

CHAPTER VI)

Inverting Real and Realistic Data

In Chapter V we described the procedure for inverting coherent field measurements arising in response to a CW point source, to obtain the plane wave reflection coefficient. In that chapter we addressed some of the practical issues that must be faced when real data is to be inverted. In this chapter we perform a preliminary inversion of real data. [1] To help interpret the results, in parallel we invert data generated synthetically for a realistic geometry and set of bottom parameters.

The real data that we invert was obtained by G. Frisk, J. Doust, and E. Hays in 1981. The associated experimental geometry was described in Section (I.6) and is presented again in Figure (VI.1). We will be using the data obtained from the lower receiver shown in this figure. In Figure (VI.2) we present a velocity profile and density parameters for a bottom that we believe is comparable to the bottom where the real data was taken. We use this geometry, velocity profile, and these density parameters to generate the synthetic data of this chapter. This synthetic data is generated using the hybrid procedure described in Chapter IV and the numerical Hankel transform that was described in Section (III.7) .¹ [2] The efficiency of this Hankel transform algorithm made it possible to obtain high quality results over a large range that would otherwise not have been practical.

We begin by generating the synthetic data for this geometry and bottom. We use the numerical procedure described in Section (IV.2) to generate the plane wave reflection coefficient, $\Gamma(k_r)$, as a function of horizontal wave number. Its magnitude and phase are presented in Figures (VI.3a) and (VI.3b). We see that a pole is present in $\Gamma(k_r)$ beyond the water wave number. This pole is due to the low speed channel just below the water-bottom interface. Because the source+receiver height is large, this pole will contribute an insignificant amount to

1) This algorithm was implemented in Fortran on a VAX-11/780 by Mike Wengrovitz.

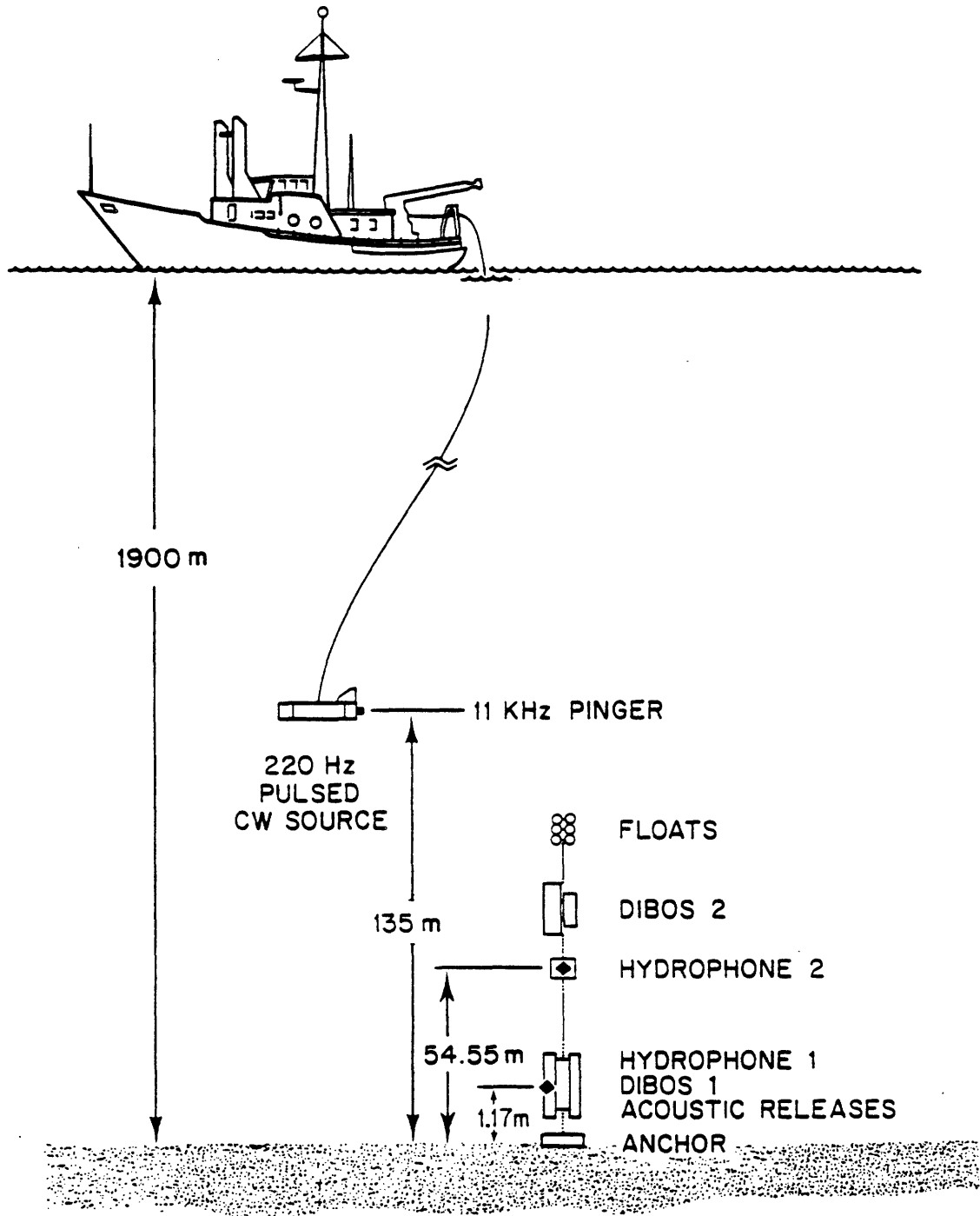


Figure VI.1 Experimental geometry associated with the real data

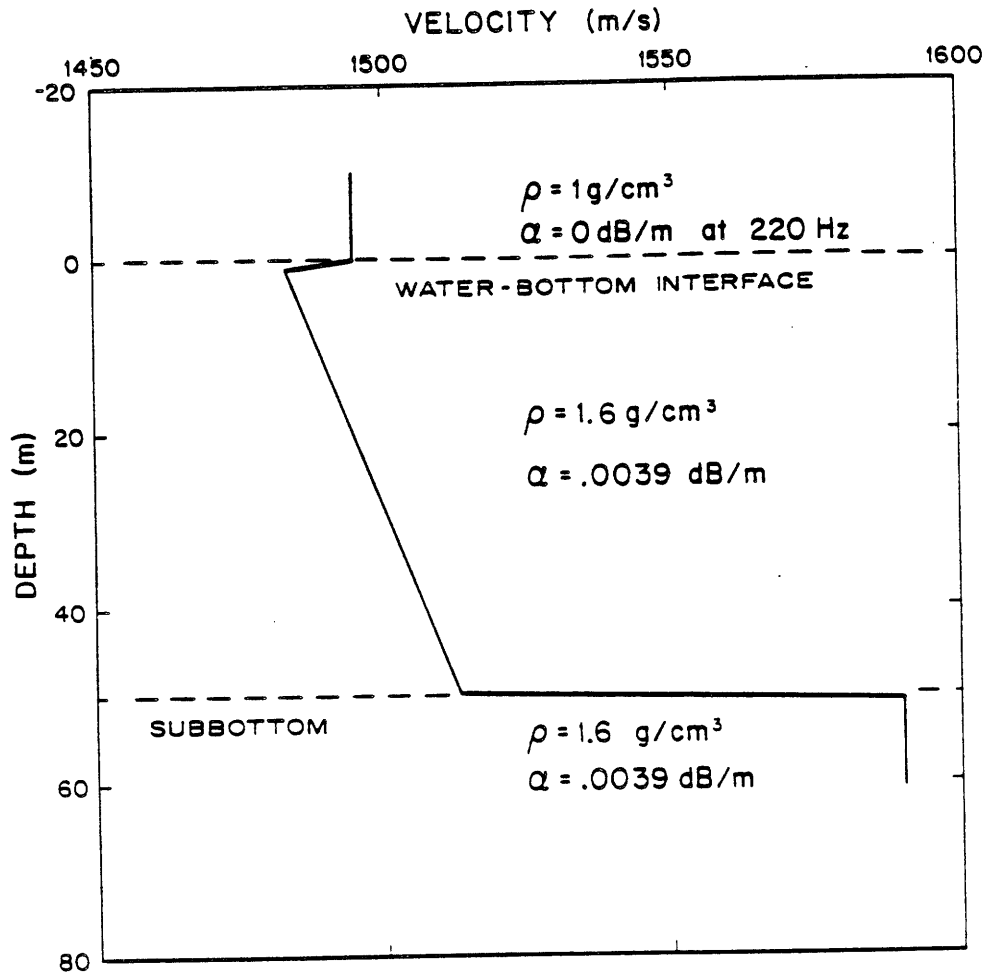


Figure VI.2 The velocity profile and density parameters for a bottom comparable to that where the real data was taken

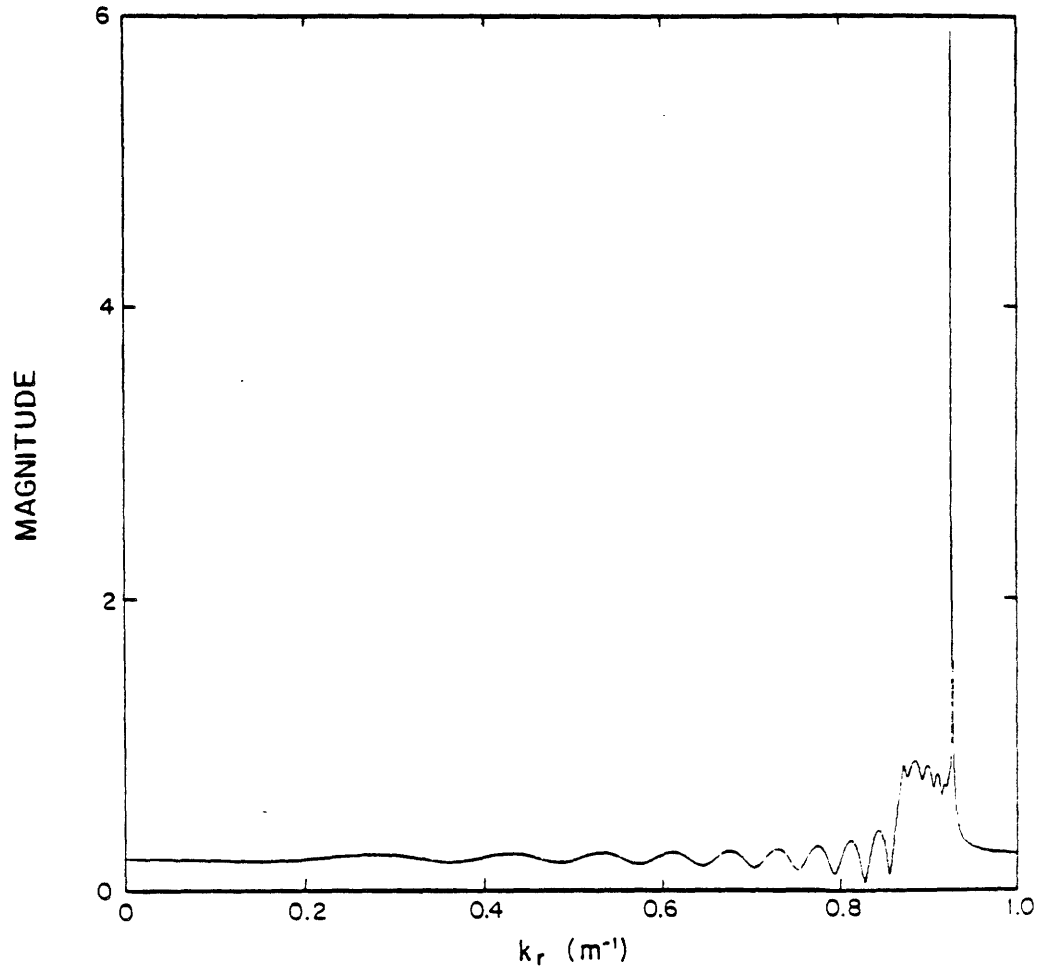


Figure VI.3a Magnitude of the reflection coefficient calculated for bottom parameters shown in Figure VI.2

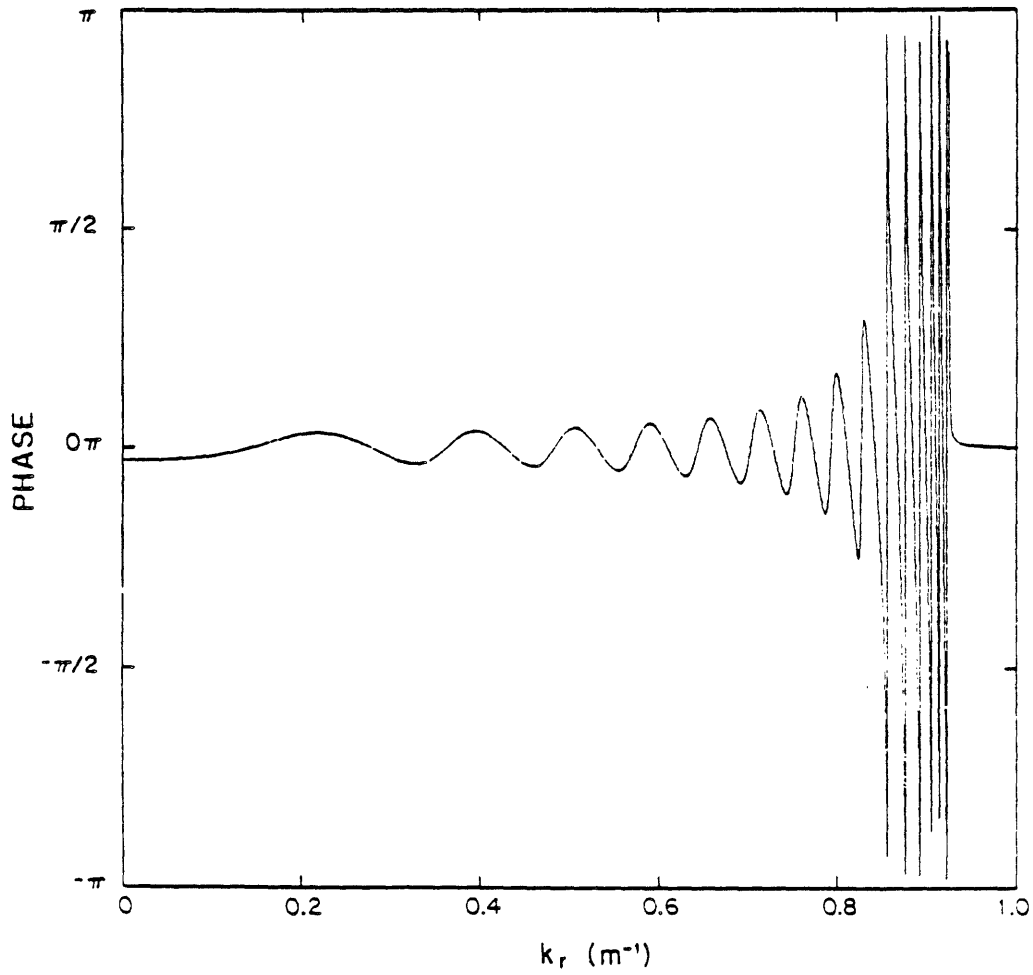


Figure VI.3b Phase of the reflection coefficient calculated for bottom parameters shown in Figure VI.2

the pressure field and need not be removed as was done in Section (IV.5b). Consequently we can generate the field with the hybrid procedure described in Section (IV.3a). The magnitude and residual phase of the associated synthetic field are presented in Figures (VI.4a) and (VI.4b). In these figures very little high frequency ripple is apparent even at large ranges, implying that the field is indeed adequately represented and not suffering from spatial aliasing.

Figures (VI.5a) and (VI.5b) present the magnitude and residual phase of the synthetic field after inclusion of the incident field. The regular behavior in these plots suggests that the magnitude and residual phase are good representations of the total field. As further confirmation of the validity of the total synthetic fields generated for this example, we present the output of a ray program that was run for this profile in Figure (VI.5c).^{1,2} The two synthetic fields are in good agreement except in the region of the caustic, $1500m < r < 2000m$, where the ray method is known to be inaccurate.

Figures (VI.6a) and (VI.6b) present the magnitude and residual phase of the real data (which includes the source field). In the region beyond the first hundred meters, the magnitude and residual phase of the real data behave regularly, which gives us confidence in them. The interference pattern apparent in the magnitude is similar to that of the synthetic data. The zeros in the magnitude are well matched by the changes in the residual phase for large ranges. The first few hundred meters of the residual phase, however, looks significantly different from the residual phase of the synthetic field. In this region, changes in the source-height have their greatest effect on the measured field because the geometry is most significantly affected by source-height variation in this region. We recall that the residual phase is given by:

$$\epsilon(r) = \hat{\theta}(r) - k_0 \sqrt{r^2 + (z - z_0)^2} \quad (1)$$

The large negative slope of the residual phase for low ranges could be due either to an estimate of k_0 which was too large, in which case the residual phase would display a negative phase everywhere, or to an estimate of $(z - z_0)^2$ which was too large. We believe that this

1) But with a slightly different source height of 125 meters rather than 135 meters.

2) I wish to thank Jim Douth for providing this synthetic field.

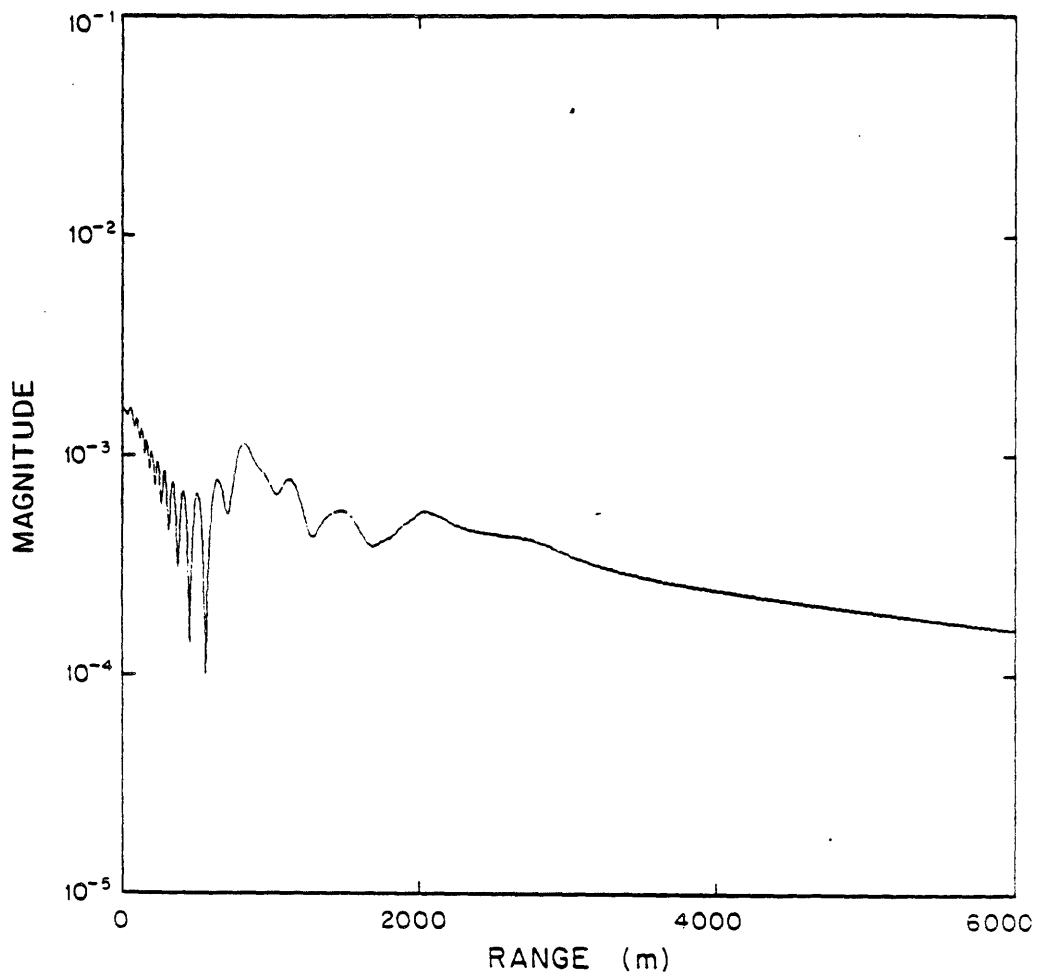


Figure VI.4a Log-magnitude of the synthetic pressure field calculated using the realistic bottom parameters and geometry

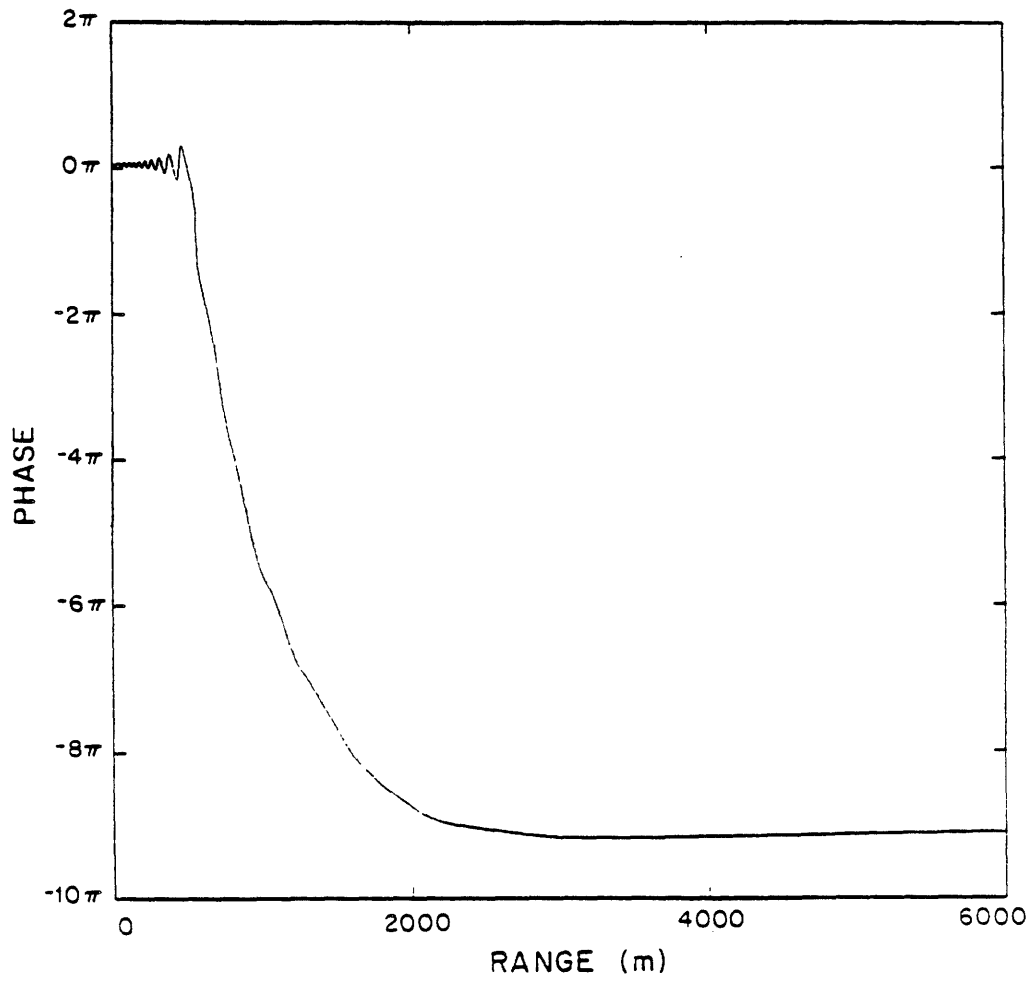


Figure VI.4b Residual phase of the synthetic pressure field calculated using the realistic bottom parameters and geometry

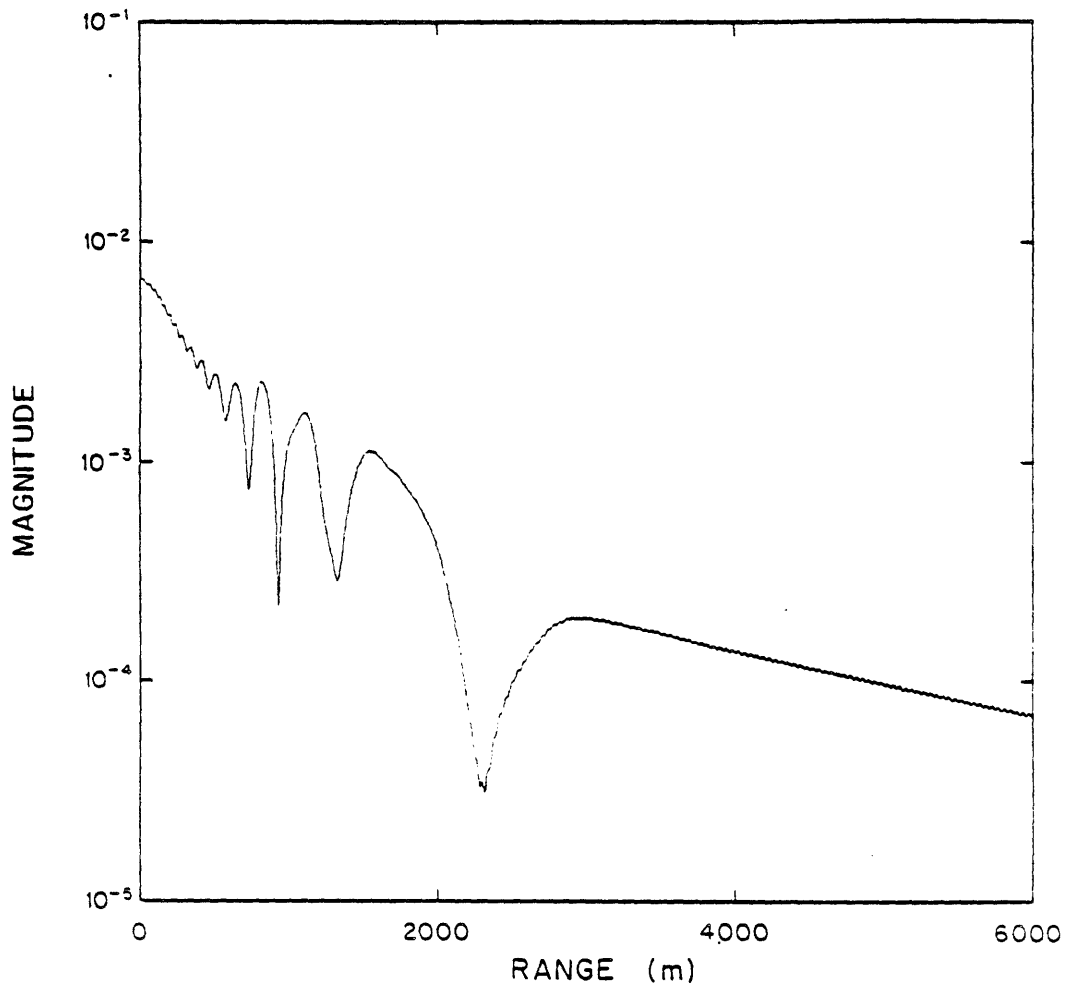


Figure VL5a Log-magnitude of the total synthetic pressure field after the inclusion of the source field

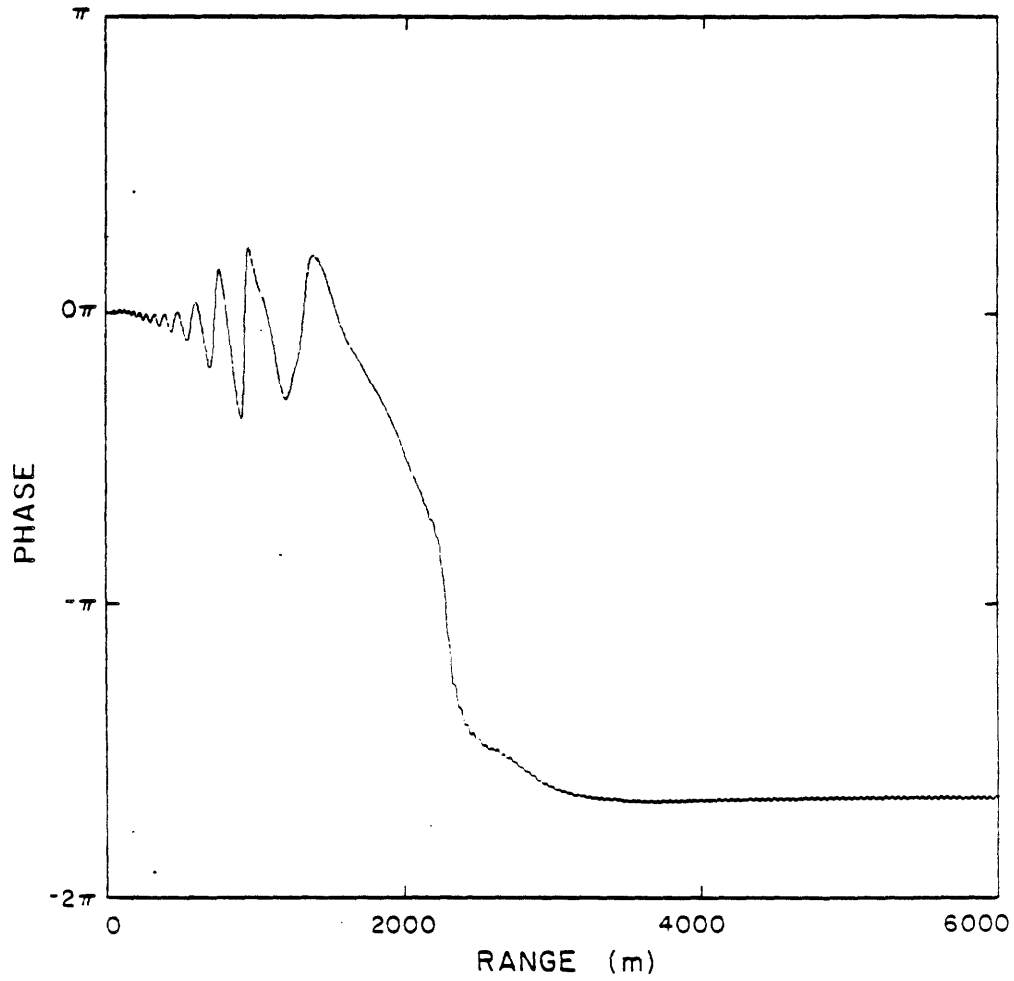


Figure VI.5b Residual phase of the total synthetic pressure field after the inclusion of the source field

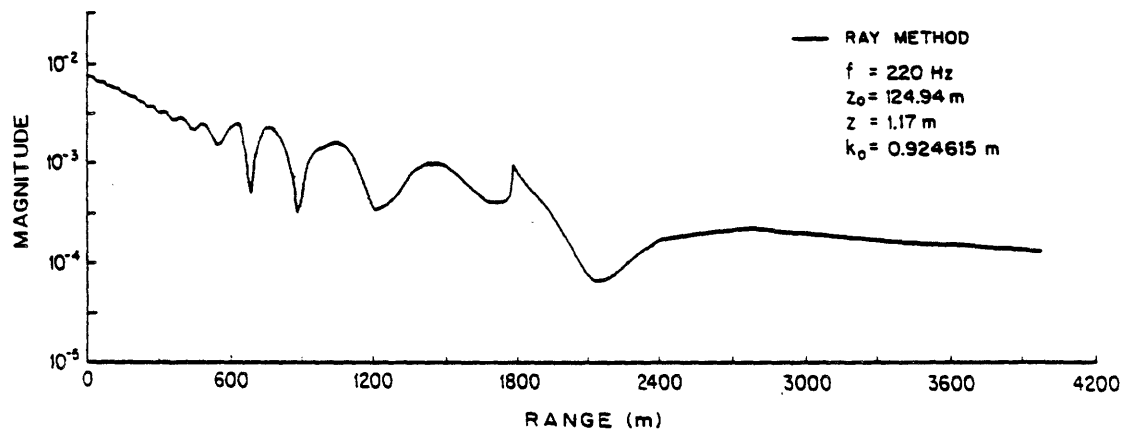


Figure VI.5c Log-magnitude of the total field calculated by a ray method

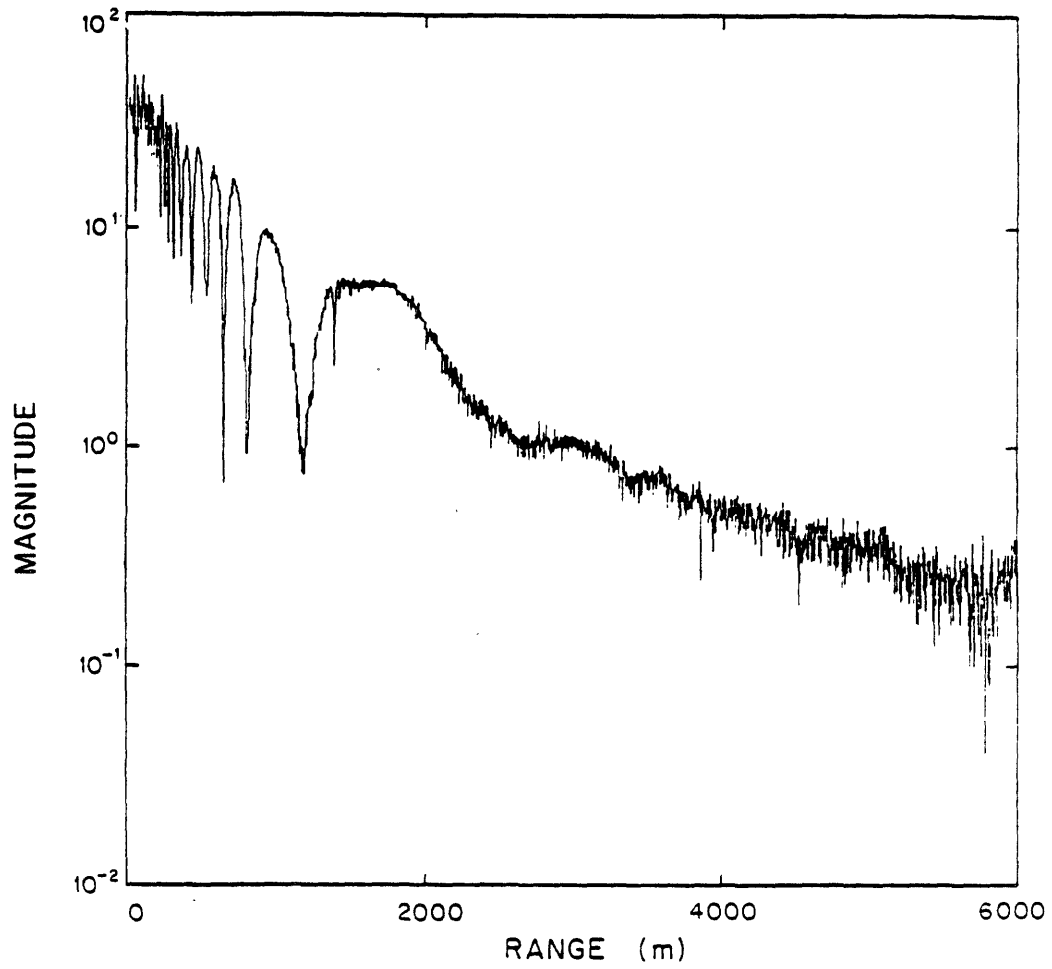


Figure VI.6a Log-magnitude of the measured pressure field

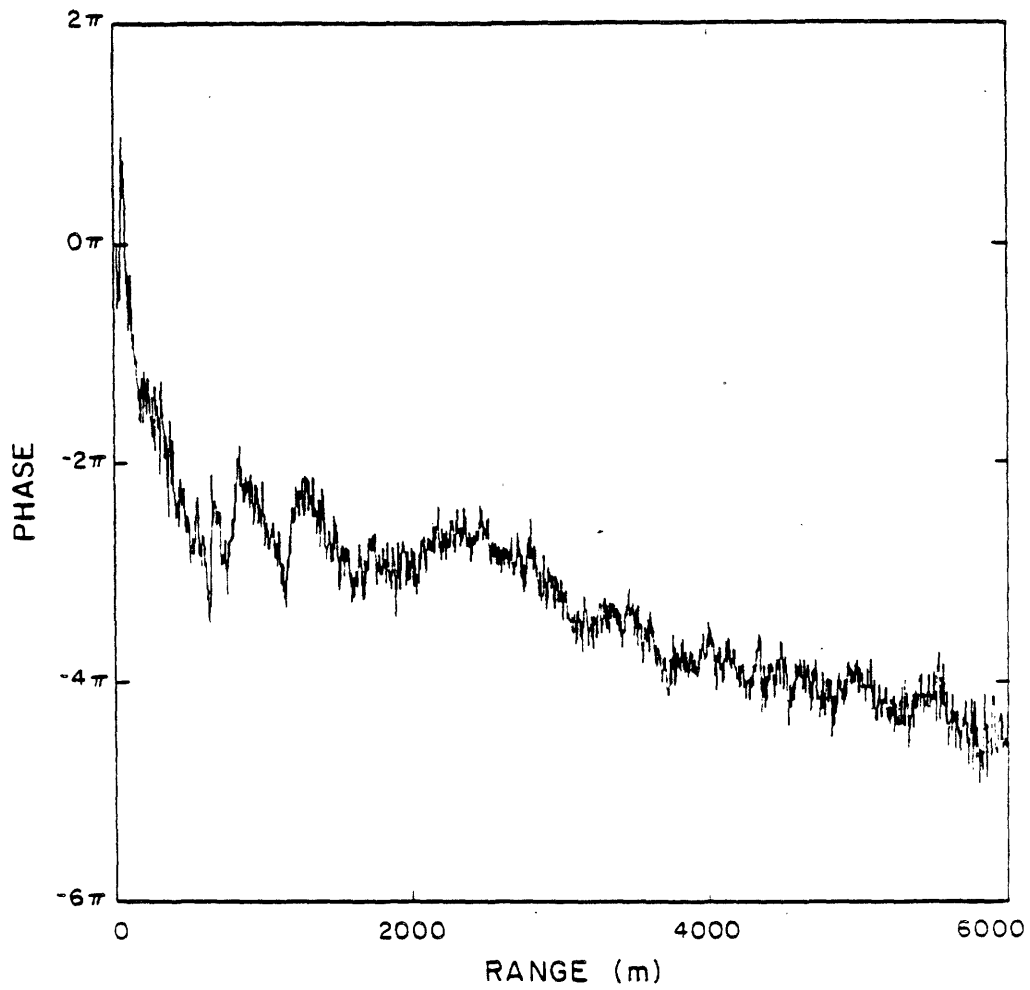


Figure VI.6b Residual phase of the measured pressure field

uncharacteristic behavior is due to imperfect knowledge of the source height in that region. The gentle negative slope of the unwrapped phase for the real data for large ranges is probably due to a slight overestimate of the water wave-number, k_0 .

Before we attempt to invert the real experimental data to estimate the depth-dependent Green's function two major factors must be considered. First, the experimental data is available only over a finite range and second, it is available only at discrete points which are not spaced properly for our processing. The first issue can be resolved by referring to Chapter V where we showed that for the source-height and geometry used to obtain the experimental data, it was only necessary to know the field out to about 3040 meters to minimize the degradation due to windowing. The experimental data is available to 6000 meters. We believe, therefore, that windowing should not prevent its successful inversion. The second issue can also be resolved by reference to Chapter V where we showed that by interpolating the magnitude and unwrapped phase it was often possible to translate the pressure field data available on one set of ranges to another. We will use the procedure developed there to interpolate the experimental data onto the set of ranges that we require for processing by the Hankel transform. In parallel we will process the synthetic data. The processed synthetic data provides a useful measure of the success of our processing because the depth-dependent Green's function that we obtain can be compared to the true depth-dependent Green's function which is known for the synthetic data, and presented in Figures (VI.7a) and (VI.7b).

Figures (VI.8a) and (VI.8b) present the magnitude and phase of the Green's function calculated by processing the synthetic data. The synthetic data was originally available on the grid $n\pi$ $n = 0, 1, 2, \dots$. It was linearly interpolated (through its magnitude and unwrapped phase as described in Section (V.3e)) onto the grid required for processing, $\frac{\lambda_n}{A}$ for $n = 0, 1, 2, \dots$ with $A = 1.2$ and where λ_n $n = 0, 1, 2, \dots$ are the zeros of $J_0(x)$.

The agreement between the estimate of the synthetic Green's function obtained by processing the synthetic field and shown in Figures (VI.8a) and (VI.8b) and the true Green's function

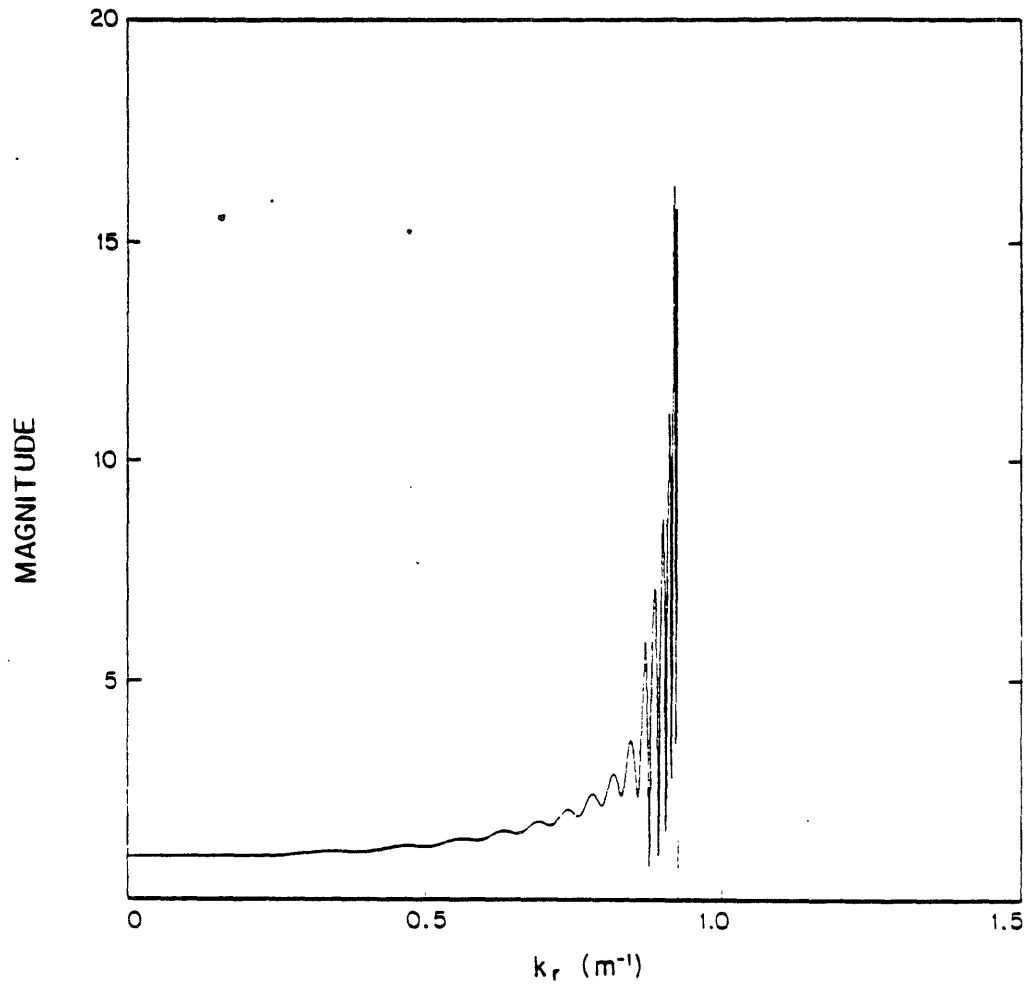


Figure VI.7a Magnitude of the true depth-dependent Green's function for the synthetic data

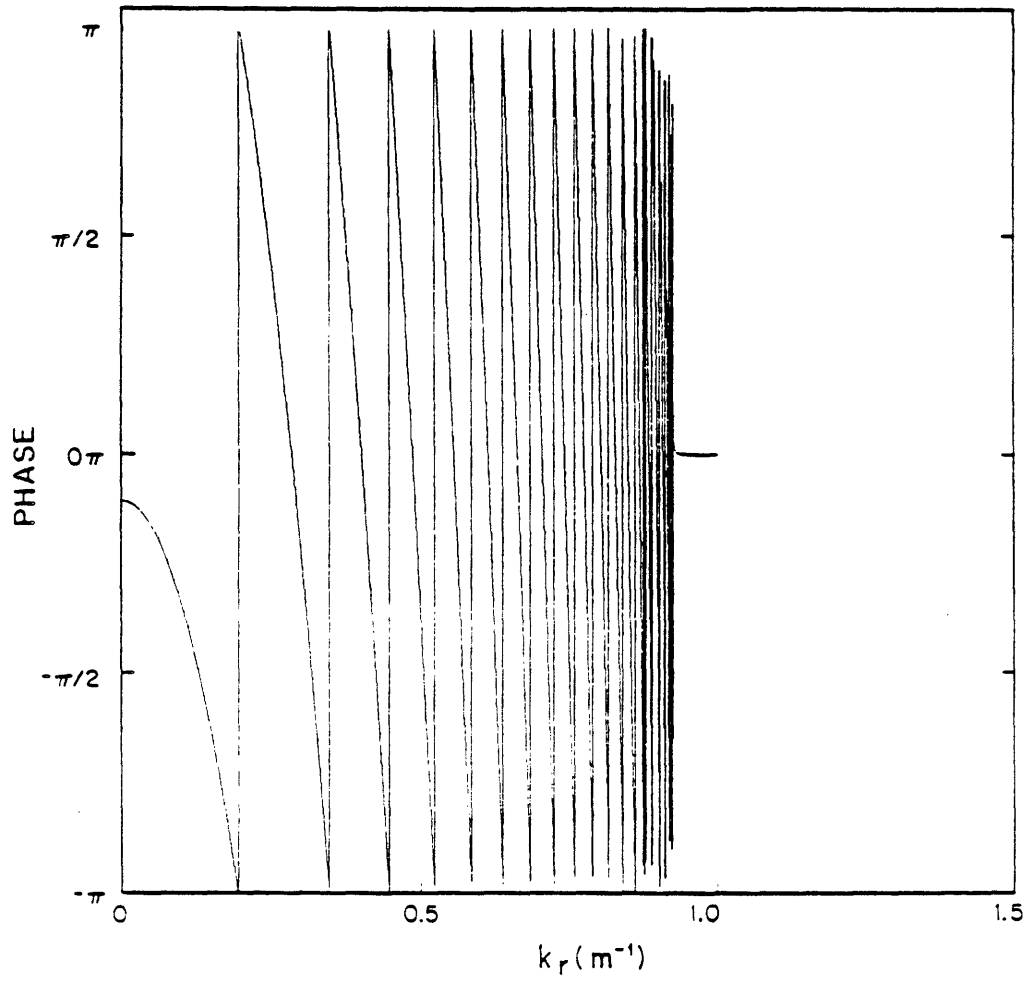


Figure VI.7b Phase of the true depth-dependent Green's function for the synthetic data

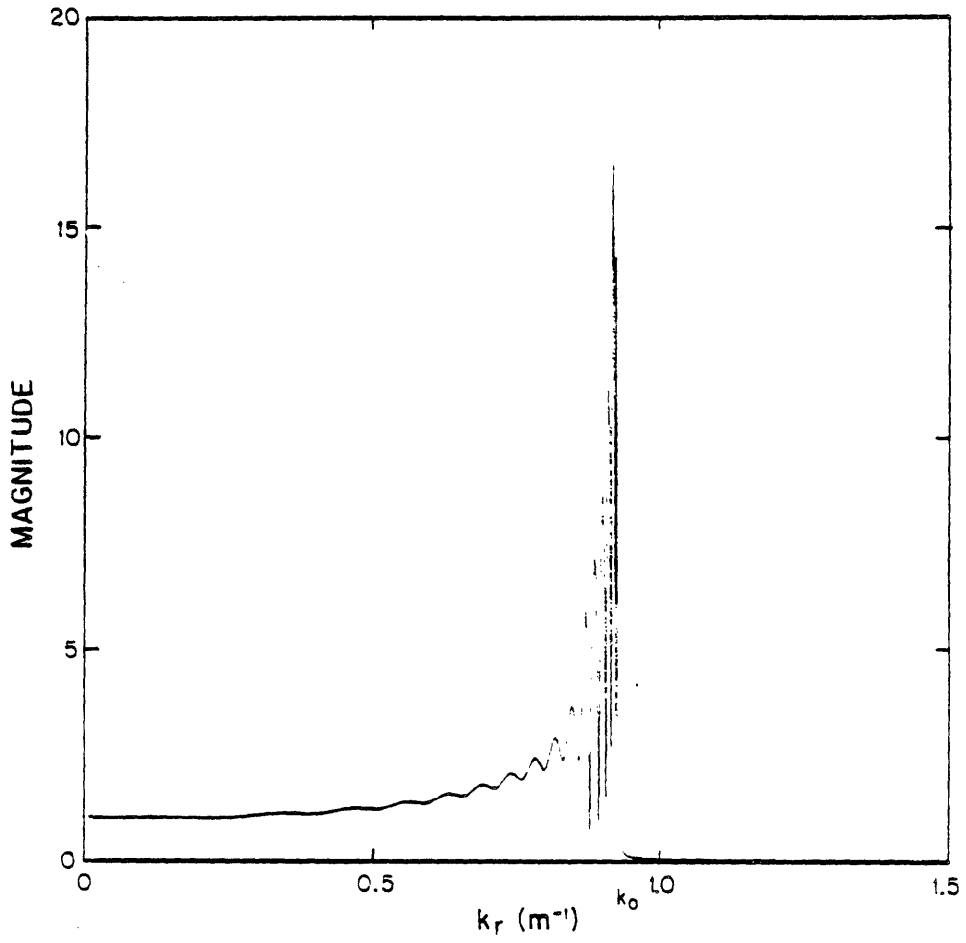


Figure VI.8a Magnitude of the depth-dependent Green's function estimated by taking the Hankel transform of the interpolated synthetic field

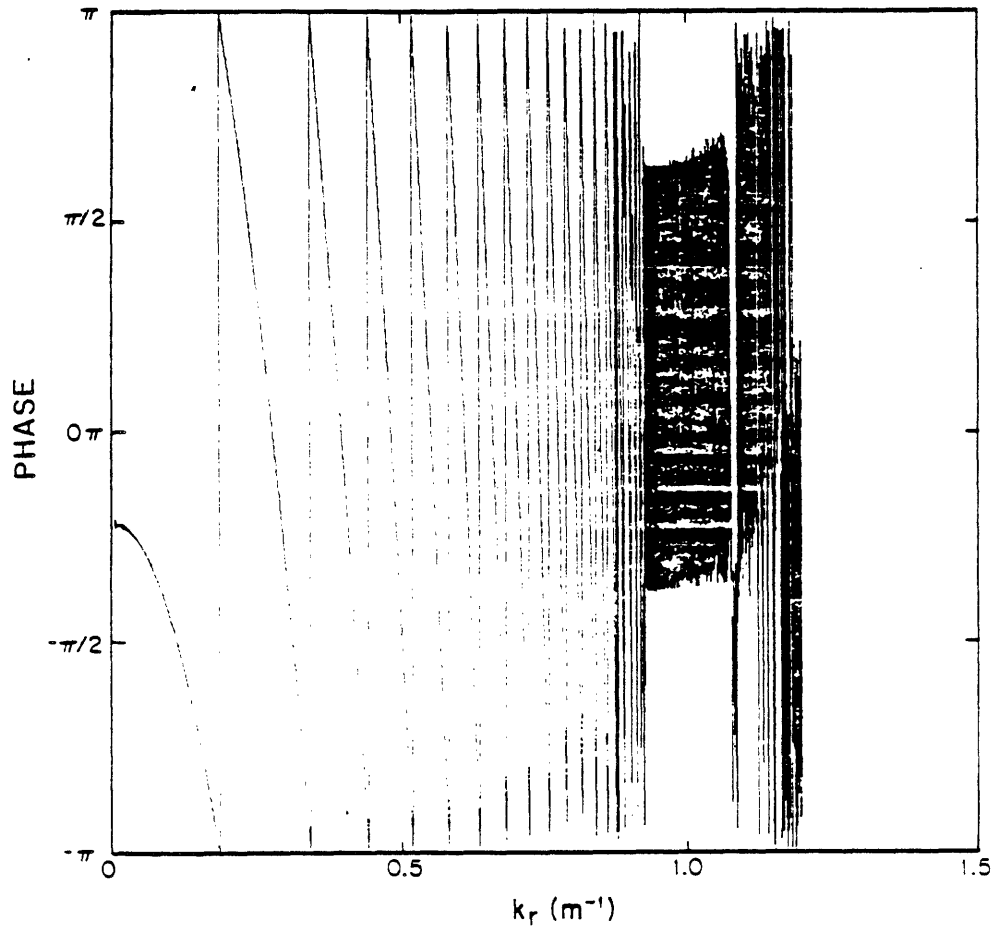


Figure VI.3b Phase of the depth-dependent Green's function estimated by taking the Hankel transform of the interpolated synthetic field

for the synthetic data shown in Figures (VI.7a) and (VI.7b) is excellent, particularly the agreement in the magnitudes. The phases differ slightly for low horizontal wave numbers. We believe that this is due to small errors in the synthetic field for low ranges. The phases differ dramatically in the evanescent region beyond the water wave number, where the magnitude of the Green's function is very small and consequently the phase is probably dominated by noise. The agreement in general between the true Green's function for the synthetic data and the Green's function estimated from the synthetic data is excellent, however, and confirms the results of Chapter V which indicated that for the sampling rate and range of values over which the data is known, it should be possible to determine the depth-dependent Green's function.

Figures (VI.9a) and (VI.9b) present the magnitude and phase of the Green's function calculated from the real data. Except for low wave numbers, the magnitude of this Green's function displays many of the features of the synthetic Green's function, including the same overall envelope due to the $\frac{1}{\sqrt{k_0^2 - k_r^2}}$ source spectrum term, and the interference pattern arising from the interaction of that portion of the Green's function associated with the source and that portion associated with the reflected field. The total Green's function also decays rapidly at the water wave number, as it should due to the $e^{i\sqrt{k_0^2 - k_r^2}|z+z_0|}$ migration terms. In the evanescent region, $k_r > k_0$, we see only noise, comparable to the noise we see superimposed upon the rest of the spectrum.

At low horizontal wave numbers the Green's function for the real data does not look like the Green's function for the synthetic data. Very near the origin we see a large peak not apparent in the total Green's function for the synthetic data. This peak is probably due to concentration of noise power there by the Hankel transform as discussed in Section (II.8). For slightly larger wave numbers the magnitude displays a jagged appearance not seen in the total Green's function for the synthetic data. In this region, the stationary phase approximation for the Sommerfeld integral is fairly good, allowing us to associate the behavior of the Green's function at low horizontal wave numbers with the behavior of the pressure field at low ranges. The

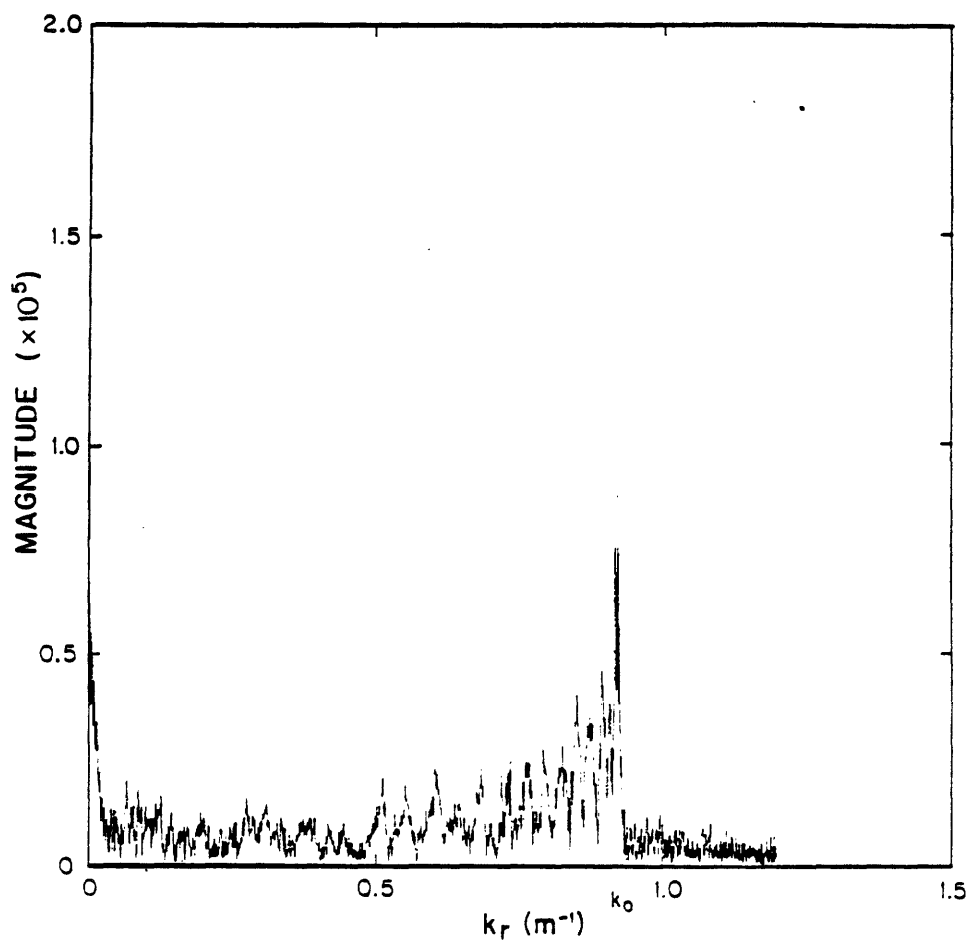


Figure VI.9a Magnitude of the depth-dependent Green's function estimated by taking the Hankel transform of the interpolated real data

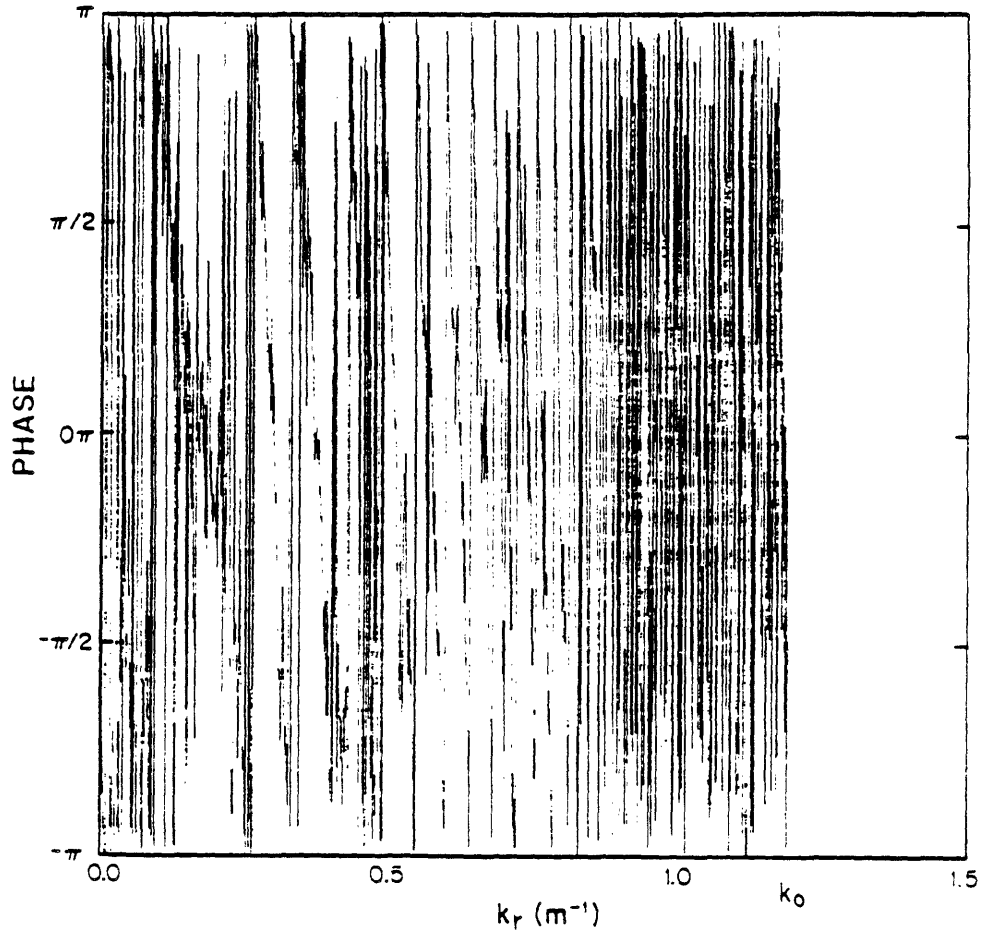


Figure VI.9a Phase of the depth-dependent Green's function estimated by taking the Hankel transform of the interpolated real data

uncharacteristic behavior of the Green's function at low horizontal wave numbers is consistent with the uncharacteristic behavior of the residual phase that we observed for low ranges and may be due to variations in the source-height. Some of this apparent jitter in the Green's function of the real data may be due in part to variation in the source-height. A rough sampling of the source-height over the course of the experiment was available from the experimental records. We interpolated between available samples using splines to obtain a rough estimate of the source-height variation present during the course of the experiment. The result is presented in Figure (VI.10). This curve is sufficiently similar to the sum of the two low frequency cosines discussed in Section (V.5b.iii) to qualitatively interpret the effect of source-height variation for this experiment in term of the results presented there. The analysis of Section (V.5) shows that sinusoidal variation in the source-height causes the estimated Green's function to be a reverberant version of the true Green's function, particularly for low k_r , corresponding to large k_z . Because the frequency of the variation is very small, the main effect is to smear the estimate of $\sqrt{k_r}G(k_r)$. As stated in that section, the phase of the estimated Green's function might be more seriously corrupted than its magnitude. The phase of the depth-dependent Green's function estimated from the real data and shown in Figure (VI.9b) does not strongly resemble the phase of the synthetic Green's function. The overall good appearance of the magnitude of the total Green's function and the poor appearance of its phase is consistent with the degradation that would be expected from source-height variation.

Figures (VI.11a) and (VI.11b) show the magnitude and phase of the plane wave reflection coefficient generated from the Green's function calculated from the synthetic data and shown in Figures (VI.8a) and (VI.8b). Figures (VI.12a) and (VI.12b) present the magnitude and phase of the plane wave reflection coefficient calculated from the Green's function for the real data. The estimate for the reflection coefficient for the real data does not appear to be a good one at this time.

Because the plane wave reflection coefficient is obtained from the total depth-dependent

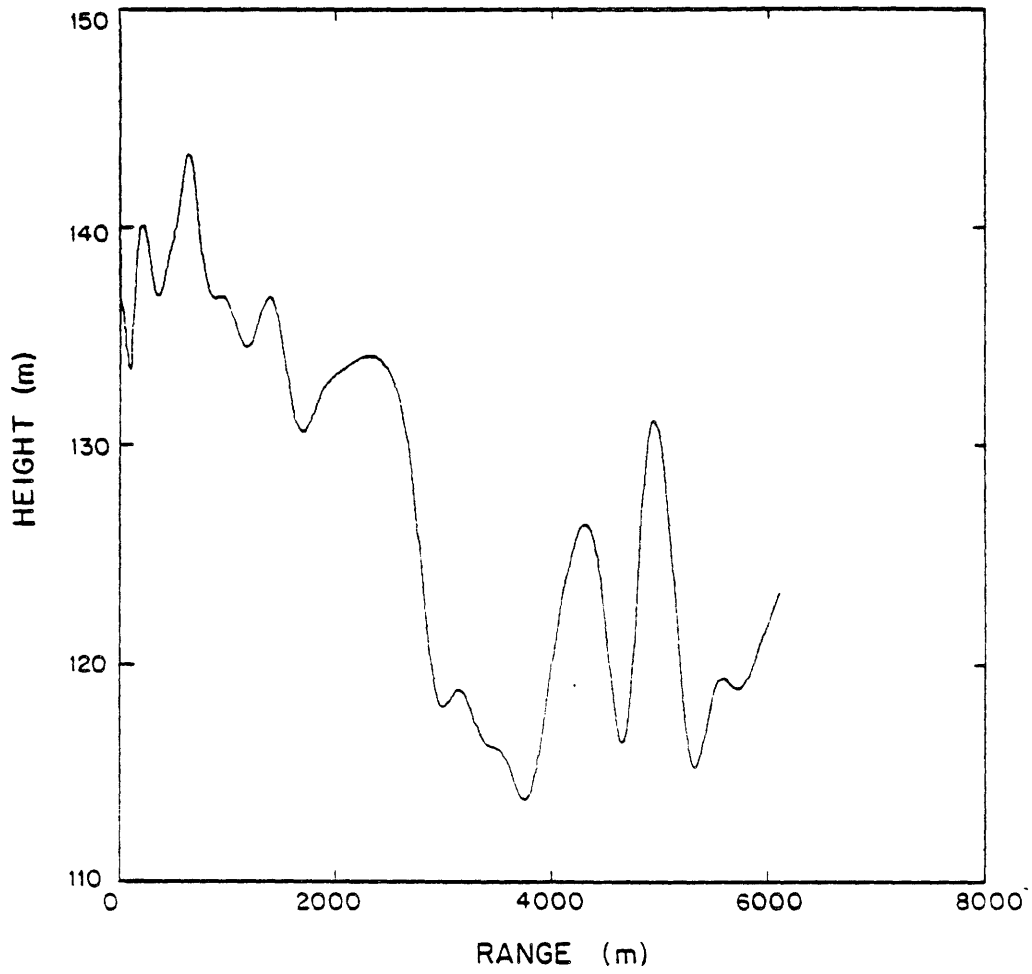


Figure VI.10 Interpolated measurements of the source-height variation measured during the acquisition of the experimental data

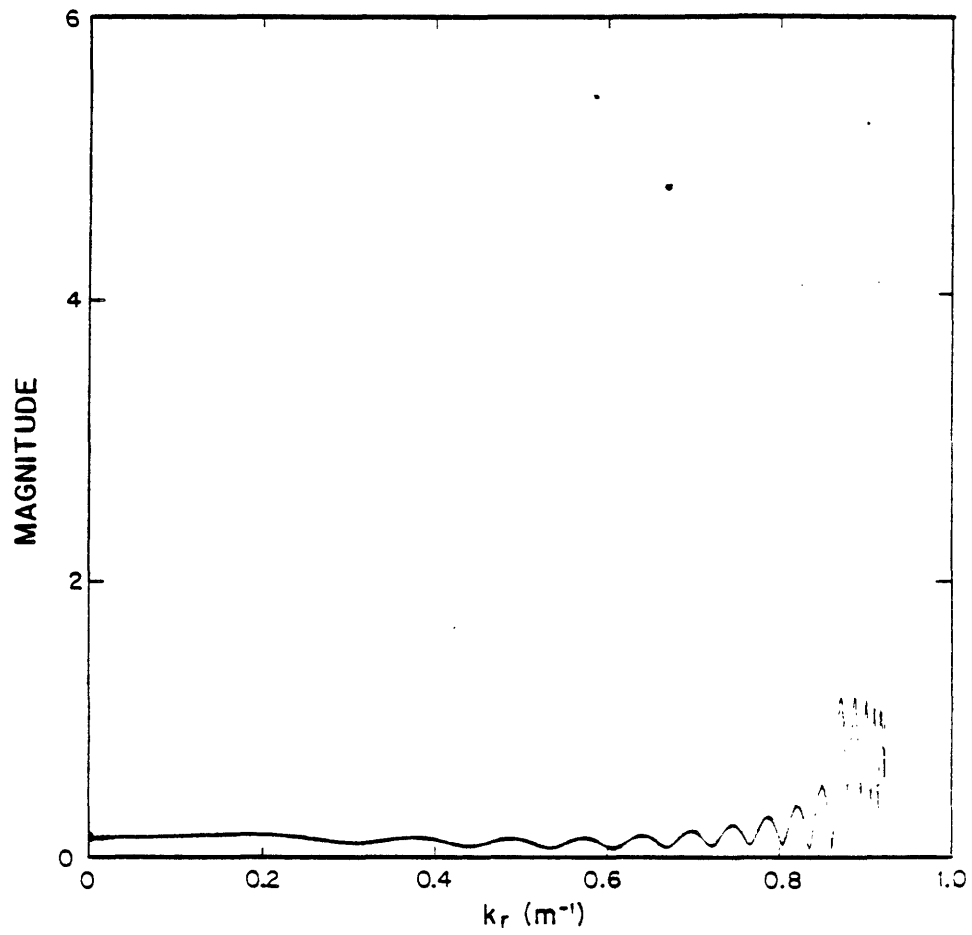


Figure VI.11a Magnitude of the plane wave reflection coefficient generated from the depth-dependent Green's function estimated from the synthetic data

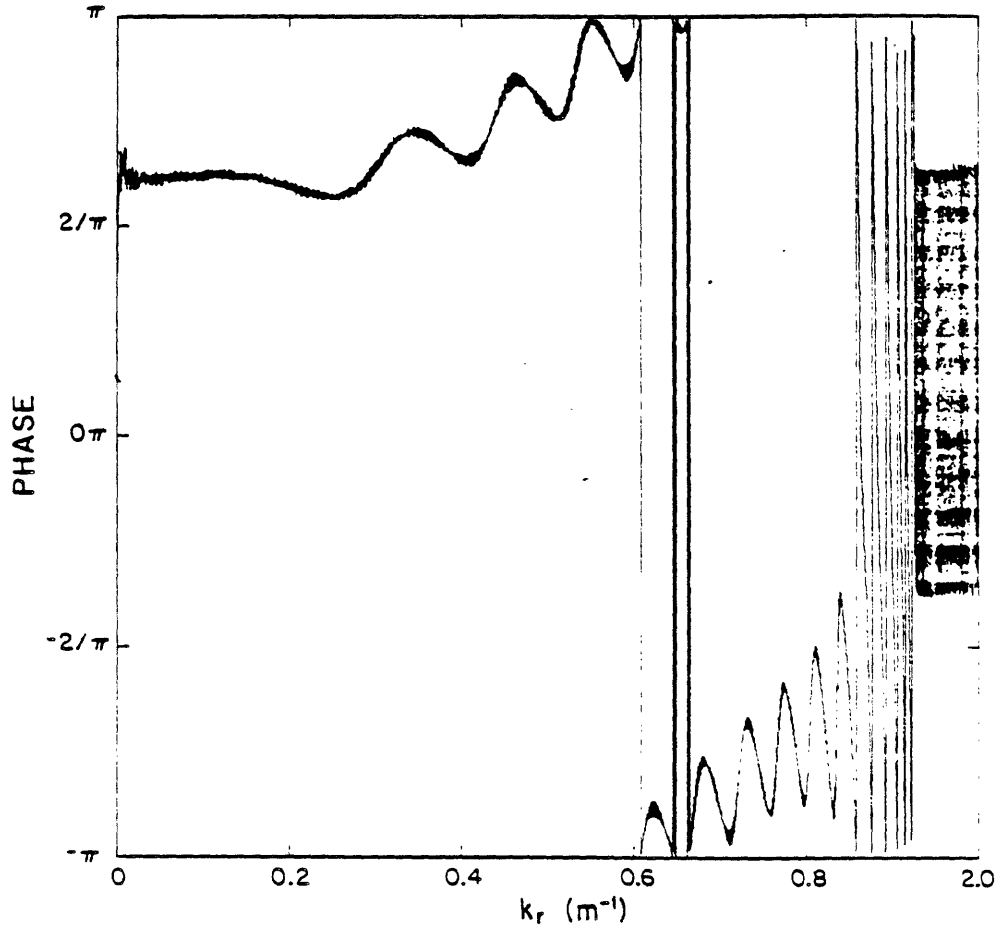


Figure VI.11b Phase of the plane wave reflection coefficient generated from the depth-dependent Green's function estimated from the synthetic data

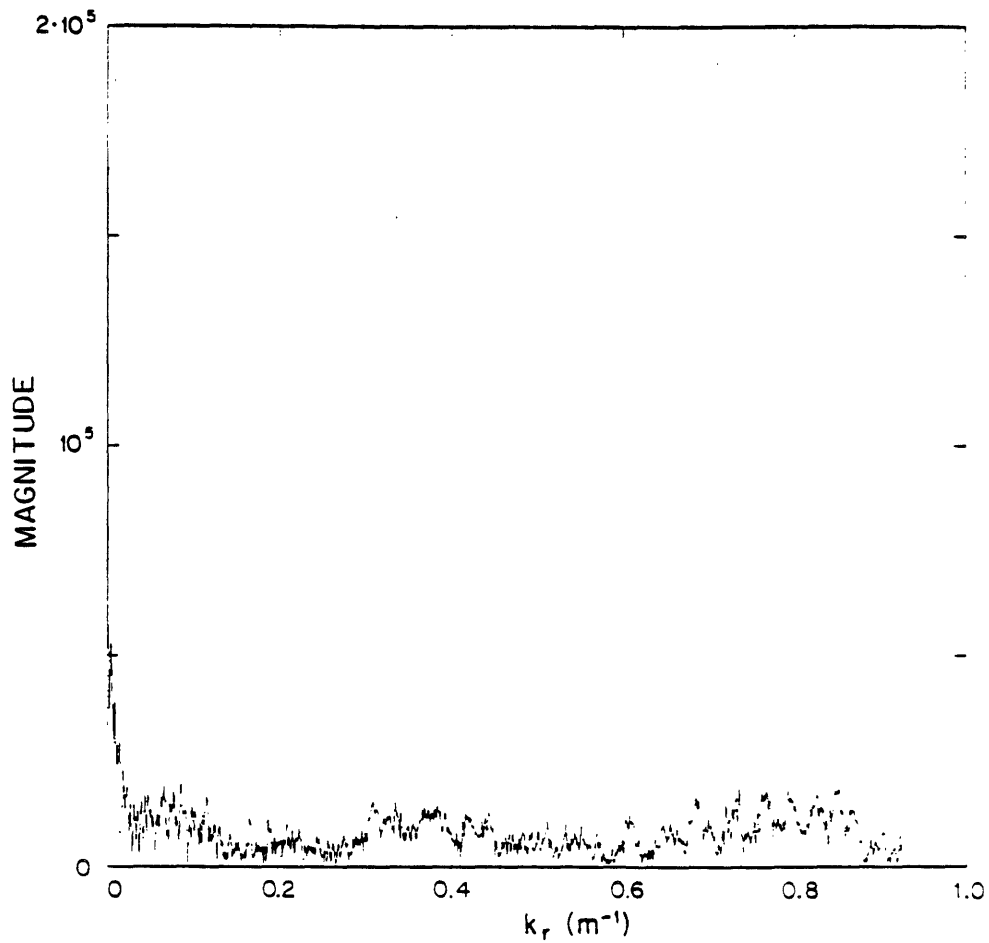


Figure VI.12a Magnitude of the plane wave reflection coefficient generated from the depth-dependent Green's function estimated from the real data

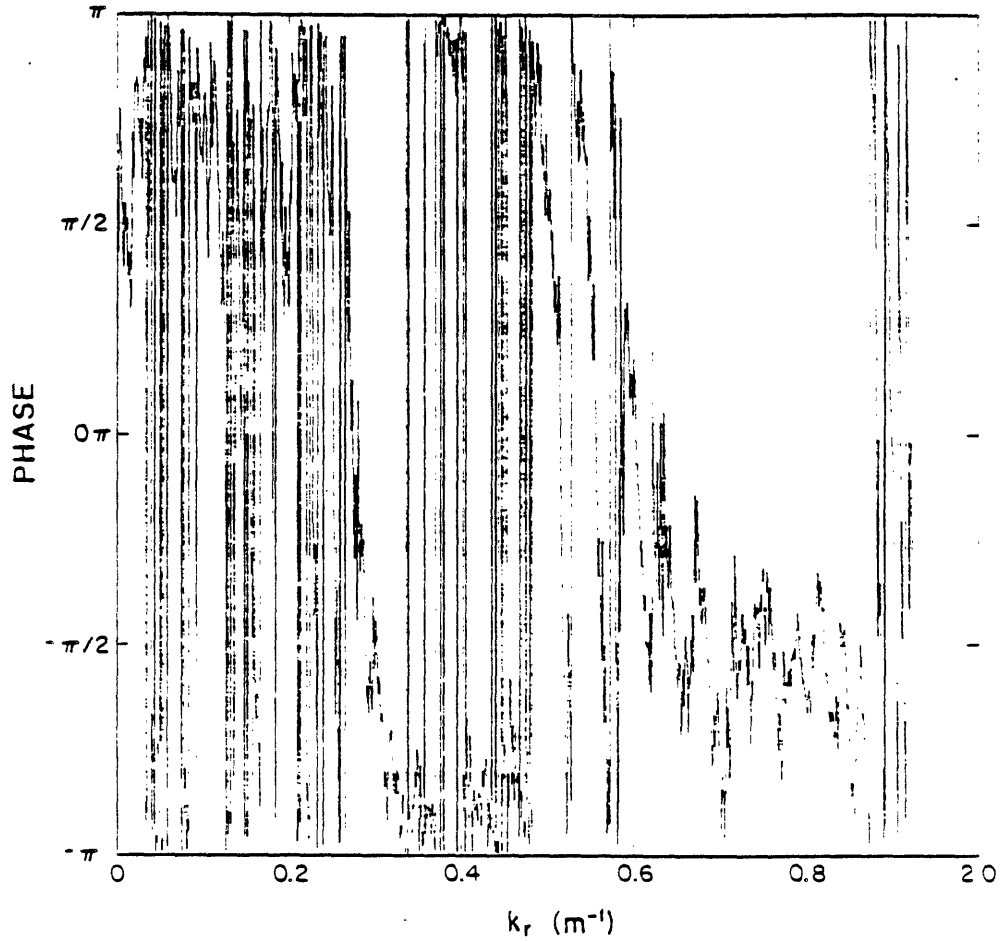


Figure VI.12b Phase of the plane wave reflection coefficient generated from the depth-dependent Green's function estimated from the synthetic data

Green's function by first coherently subtracting the source contribution and then multiplying by a term with a rapidly varying phase ($e^{-i\sqrt{k_0^2 - k^2}|z - z_0|}$) errors in the phase of the total Green's function would seriously degrade the estimate of plane wave reflection coefficient. The estimate for the reflection coefficient is probably much worse than the estimate for the Green's function because of the phase errors in the estimate for the total depth-dependent Green's function.

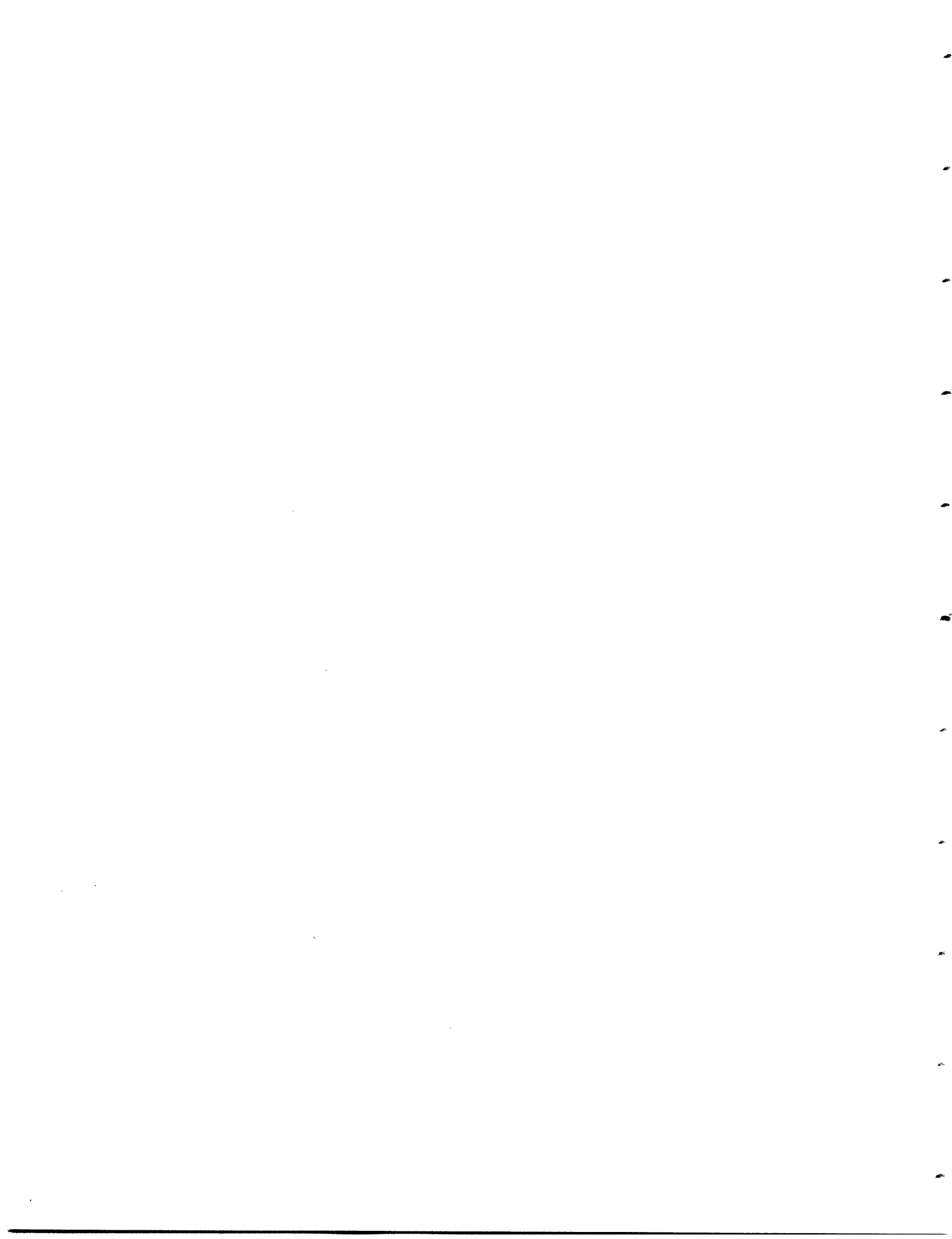
In conclusion, we believe most of the error apparent in the Green's function for the real data to be due to variation in the source-height near the origin. Direct evidence of this is the anomalous residual phase variation in the region $r < 300$ meters. The error in the estimated Green's function for very small horizontal wave numbers is probably due to additive noise. The errors in the estimated reflection coefficient are probably due to imperfect knowledge of the source-receiver geometry that affects the coherent additions. Overall, however, we are greatly encouraged by the good appearance of the magnitude of the total depth-dependent Green's function determined from the real data. The interference structure and the overall envelope suggest that we are very close to being able to estimate the plane wave reflection coefficient from real data. Work still needs to be done to compensate for the effect of source-height variation.

The potential returns from the successful inversion of pressure field data to obtain the plane wave reflection coefficient are enormous. Such a successful inversion is a vital step in the process of inferring the physical parameters of the bottom from acoustic measurements. [3, 4] The ability to make such inferences is of great interest to oceanographers and to exploration geophysicists. A successful inversion would also make it possible to predict the fields associated with an arbitrary source-receiver geometry from one set of measurements. This would greatly facilitate acoustic imaging in the ocean.

References

1. G.V. Frisk, D.R. Mook, J.A. Doutt, E.E. Hays, and A.V. Oppenheim, "The Application to Real Data of a Technique for Measuring the Plane-Wave Reflection Coefficient of the

- Ocean Bottom," *J. Acoustical Soc. Amer.* 72 (51) 597 (A) (1980).
2. D.R. Mook, "An Efficient Algorithm for the Numerical Evaluation of the Hankel and Abel Transforms," *IEEE ASSP*, to be published.
 3. H.E. Moses and C.M. deRidder, *Properties of Dielectrics from Reflection Coefficients in One Dimension*, Lincoln Laboratory Technical Report no. 322, Lincoln, Massachusetts (July 11 1963).
 4. D.C. Stickier and P.A. Deift, "Inverse Problem for a Stratified Ocean and Bottom," *J. Acoust. Soc. Am.* 70, pp.1723-1727 (1981).



CHAPTER VII: CONTRIBUTIONS AND FUTURE WORK

VII.1) *Contributions*

In this thesis we have studied both the numerical generation of synthetic pressure fields from the plane wave reflection coefficient and the inversion of measured pressure field data to estimate the plane wave reflection coefficient. We developed and implemented algorithms that efficiently generate high quality synthetic fields. We studied the major issues affecting the inversion of experimental data and were able to estimate the depth-dependent Green's function from measured data taken in the ocean with a high degree of success. We isolated source-height variation as a major factor preventing the successful estimation of the plane wave reflection coefficient at this time.

As a foundation for our studies we explored the Hankel transform in depth. In Chapter II we derived a number of important properties including the effects that windowing and sampling a function have on its Hankel transform. Our sampling results show that the associated degradation is often a more severe problem for the Hankel transform than for the Fourier transform. In particular it can seriously degrade synthetically generated pressure fields which decay as $\frac{1}{r}$ or even more slowly and its effect should always be carefully considered.

In Chapter II we also studied the noise properties of the Hankel transform. We showed that if a function is sampled on a square root grid in a noisy environment, its Hankel transform will have superior noise properties more characteristic of the underlying two dimension Fourier transform which the Hankel transform represents in the presence of cylindrical symmetry.

In Chapter III we considered a number of numerical techniques for performing the Hankel transform. We presented new results strengthening existing procedures such as the asymptotic and backsmear methods as well as an efficient, exact method developed as part of this thesis.

In our development of algorithms to generate high quality synthetic data we presented a

number of hybrid numerical-analytical techniques that greatly improve the quality of synthetic data. In the course of developing a technique that can adequately handle the effects of guided modes in slow speed layers under the ocean bottom, we derived an expression that may be of use for developing field expressions in modal expansions required to be accurate in both the near and far fields. We also presented a well behaved numerical procedure for implementing the Thomson-Haskell approach for generating the plane wave reflection coefficient.

In Chapter V we developed the major issues affecting the inversion of measured field to obtain the plane wave reflection coefficient. On the basis of this development we were able to identify the sources of error in an actual inversion. The phase unwrapping and interpolation results presented in this chapter also significantly improved the results of the processing of the experimental data in Chapter VI.

In Chapter VI we performed a preliminary inversion of real data to obtain estimates for the depth-dependent Green's function and the plane wave reflection coefficient. The results presented in this chapter represent a significant advance towards the complete inversion of measured pressure field data to obtain the plane wave reflection coefficient. We were able to generate a good estimate for the depth-dependent Green's function and were able to associate the effects of source-height variation with the degradation in the estimate for the plane wave reflection coefficient.

At this point work is continuing towards the complete estimation of the plane wave reflection coefficient from real data. The foundations laid by the work presented in this thesis provide a strong base for future work in this area. In addition they suggest research in a number of related areas. Some of these are presented in the next section.

VII.2) Future work

a) Cylindrical to Cartesian Coordinate Systems

In this thesis we have dealt with problems cast in a cylindrical coordinate system. In that coordinate system the familiar Fourier transform of cartesian systems became the less familiar Hankel transform. In that coordinate system the clean properties of additive white Gaussian noise through the Fourier transform were obscured until a square root grid was introduced. In that coordinate system windowing and aliasing approximately affected $\sqrt{r}\hat{f}(r)$ instead of $f(r)$. In that coordinate system the familiar impulse $\delta(x)$ became $\frac{\delta(x)}{x}$. In that coordinate system the $\frac{\partial^2}{\partial x^2}$ operator became $\nabla^2 \equiv \frac{\partial^2}{\partial r^2} + \frac{1}{r} \frac{\partial}{\partial r}$ so that the operator which nulls a pole in a cartesian coordinate system:

$$\left[\frac{\partial^2}{\partial x^2} + \rho_i^2 \right] f(x) = \left[\frac{\partial^2}{\partial x^2} + \rho_i^2 \right] \int_{-x}^{\infty} \frac{1}{\rho^2 - \rho_i^2} e^{i\rho x} d\rho = \int_{-x}^{\infty} \frac{-\rho^2 + \rho_i^2}{\rho^2 - \rho_i^2} e^{i\rho x} d\rho = -\delta(x) \quad (1)$$

became the less familiar:

$$\left[\nabla^2 + \rho_i^2 \right] f(r) = \left[\nabla^2 + \rho_i^2 \right] \int_0^{\infty} \frac{1}{\rho^2 - \rho_i^2} J_0(\rho r) \rho d\rho = \int_0^{\infty} \frac{-\rho^2 + \rho_i^2}{\rho^2 - \rho_i^2} J_0(\rho r) \rho d\rho = -\frac{\delta(r)}{r} \quad (2)$$

In short we frequently found that familiar problems in a cartesian system became more difficult when cast in a cylindrical coordinate system. The reverse is also true, however. In Section (III.7) we developed an efficient numerical algorithm for the Hankel transform by mapping it into a Fourier transform. The mapping was accomplished with the Abel transform:

$$HT \left\{ f(r) \right\} = FT \left\{ A \left\{ f(r) \right\} \right\} \quad (3)$$

The Abel transform also serves to map other linear operators in cylindrical form into linear operators in cartesian form (it must do so for any function that can be represented by a Hankel transform). It maps ∇^2 into $\frac{\partial^2}{\partial x^2}$ for example, in the sense that:

$$A \left\{ \nabla^2 f(r) \right\} = \frac{\partial^2}{\partial x^2} A \left\{ f(r) \right\} \quad (4)$$

In Section (III.7) we developed an efficient numerical algorithm for evaluating the Abel transform. One exciting area of future research is the extension of maximum entropy and other spectral estimation techniques into the cylindrical domain as we now describe.

An estimation scheme that might be of value for estimating the plane wave reflection coefficient is illustrated in Figure (VII.2a.1). Instead of estimating the plane wave reflection coefficient directly we estimate the position and residue of its poles (and possibly zeros) in the complex plane. We do this because the estimation of parameters instead of a function is a much better posed problem when the signal available for analysis has been corrupted. Because the plane wave reflection coefficient is related to the measured field by the (cylindrical) Hankel transform and not the Fourier transform, spectral estimation techniques available in the literature of digital signal processing do not apply. If we first process the pressure field data with an Abel transform, however, the resulting signal has the same poles and zeros but now in its Fourier transform. Modern spectral estimation techniques can therefore be used. We introduce the caution that the effect that branch cuts have on this procedure must be studied with care.

b) Analytical-Numerical Algorithms

The hybrid analytical-numerical technique used to implement the Abel transform in Section (III.6) is a very general procedure and springs from classical numerical methods of long standing. Traditionally, difficult integrals are evaluated numerically by removing their singular behavior as much as possible through coordinate changes and changes of variables and then numerically transforming the result. The success of the hybrid method points out that in fact it is often desirable to do just the opposite. The integral should be manipulated to produce as much singular behavior as possible. The singularities can be integrated analytically and will not suffer from numerical degradation. If the singularities are removed properly, the remaining numerical portion of the integral will be well behaved where it dominates and subordinate to the analytically determined portions of the integral where it does not. The art in this procedure is casting the

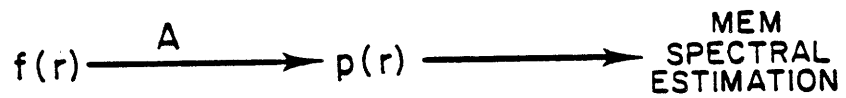


Figure VII.2a.1 The Proposed method allowing MEM to be used for problems cast in cylindrical coordinates

analytically determined portions of the integral carefully to insure that the numerical portion does not have infinities or undesirable asymptotics to cancel. Had the e^{-br} factor not been included in the procedure of Section (III.6), for example, the hybrid method for the Abel transform would not have worked.

Manipulating functions so that they can best be represented by parameterized functions and samples is part of the general issue of computer representation. As software systems become smarter this kind of approach will become increasingly more important.

c) Waveguides

In the course of generating synthetic data, we evaluated the integral:

$$I(r, z, \rho_i) \equiv \int_0^{\infty} \frac{i}{\sqrt{k^2 - \rho^2}} \frac{1}{\rho^2 - \rho_i^2} e^{i\sqrt{k^2 - \rho^2}|z|} J_0(\rho r) \rho d\rho \quad (1)$$

and showed that it satisfied

$$\left[\nabla_r^2 + \rho_i^2 \right] I(r, z, \rho_i) - \frac{e^{ik\sqrt{r^2 + z^2}}}{\sqrt{r^2 + z^2}} = 0 \quad (2)$$

We associated $I(r, z, \rho_i)$ with the contribution of the pole at ρ_i because our integrals always included the terms $\frac{i}{\sqrt{k^2 - \rho^2}} e^{i\sqrt{k^2 - \rho^2}|z|}$ as well. The advantage of this formulation was that $I(r, z, \rho_i)$ is everywhere finite, even at $r = 0$. The classical contribution associated with a pole is

$$-\frac{\pi i}{2} H_0^{(1)}(\rho_i r) \quad \text{when } \text{Im}(\rho_i) > 0 \quad (3)$$

The Hankel function above has a logarithmic singularity as the origin. Physically, poles in the depth-dependent Green's function make only finite contributions to the field. The migration term $e^{i\sqrt{k^2 - \rho^2}|z|}$ windows the pole in the Hankel domain so that its contribution to the pressure field is everywhere finite. For this reason we included the migration term into our pole expression. For convenience we also included the source term $\frac{i}{\sqrt{k^2 - \rho^2}}$.

Our formulation was carefully constructed to insure that the numerics were not required to generate infinities. It is potentially useful for many problems other than those considered directly in this thesis. One set of problems concerns the calculation of fields inside (possibly leaky) waveguides.

We develop an expression for the field inside a (dielectric) waveguide arising from a point source using the plane wave formulation of this thesis.¹ Figure (VII.2c.1) presents the geometry of the waveguide and the waves present.

The radial and time variation of all fields is given by:

$$J_0(k_r r) e^{-i\omega t} \quad (4)$$

and will be suppressed. We will use β for the vertical wave number. β and k_r are related through

$$k^2 = \beta^2 + k_r^2 \quad (5)$$

The source field is given by $P_I e^{i\beta|z-z_0|}$ and is the portion of the field that would be present even in the absence of impedance contrasts. We specify the boundary conditions at $z = h$ by giving the plane wave reflection coefficient there, $\Gamma_T(k_r)$, and at $z = 0$ by $\Gamma_B(k_r)$. These two interfaces together give rise to an up-going wave, $P_+ e^{i\beta z}$, and a down-going wave $P_- e^{-i\beta z}$, that would not be present without the impedance contrasts in the regions $z \geq h$ and $z \leq 0$. The total up-going and down-going fields for $z_0 < z \leq h$ is given by:

$$\begin{array}{ll} P_+ e^{i\beta z} + P_I e^{i\beta(z-z_0)} & \text{UP} \\ P_- e^{-i\beta z} & \text{DOWN} \end{array} \quad (6)$$

The plane wave reflection coefficient at $z = h$ provides the boundary condition:

$$\Gamma_T = \frac{P_- e^{-i\beta h}}{P_+ e^{i\beta h} + P_I e^{i\beta(h-z_0)}} \quad (7)$$

In the region $0 \leq z < z_0$ we have

$$\begin{array}{ll} P_- e^{-i\beta z} + P_I e^{i\beta(z_0-z)} & \text{DOWN} \\ P_+ e^{i\beta z} & \text{UP} \end{array} \quad (8)$$

¹A derivation for the field inside such a waveguide can also be found in [1]

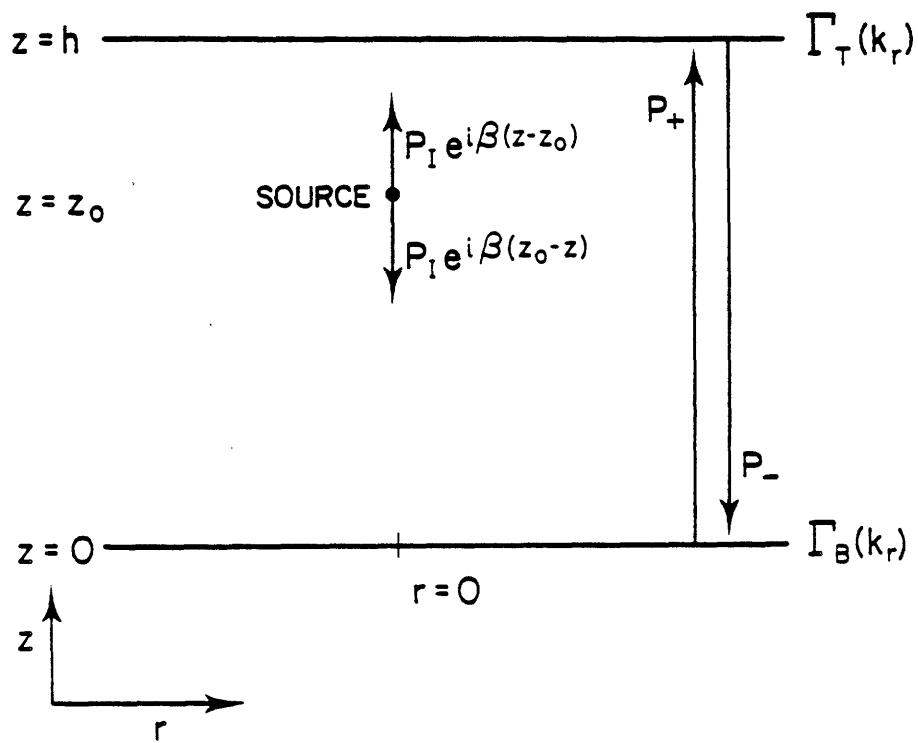


Figure VII.2c.1 The geometry and waves for extending the results of this thesis to waveguides

and

$$\Gamma_B = \frac{P_+ e^{i\beta 0}}{P_- e^{-i\beta 0} + P_I e^{i\beta z_0}} = \frac{P_+}{P_- + P_I e^{i\beta z_0}} \quad (9)$$

P_I is the known point source strength $\frac{i}{\sqrt{k^2 - k_r^2}} = \frac{i}{\beta}$. Γ_T and Γ_B are given as well.

The two boundary conditions are sufficient to determine P_+ and P_- from these quantities. We write:

$$\begin{aligned} \Gamma_T P_+ e^{i\beta h} + \Gamma_T P_I e^{i\beta h} e^{-i\beta z_0} &= P_- e^{-i\beta h} \\ \Gamma_B P_- + \Gamma_B P_I e^{i\beta z_0} &= P_+ \end{aligned} \quad (10)$$

Solving for P_+ and P_- we have

$$P_+ = \frac{\left[e^{-i\beta(h-z_0)} - \Gamma_T e^{i\beta(h-z_0)} \right] P_I}{\frac{1}{\Gamma_B} e^{-i\beta h} - \Gamma_T e^{i\beta h}} \equiv C_+ P_I \quad (11)$$

and

$$P_- = \frac{\left[\Gamma_B e^{i\beta(h+z_0)} - e^{i\beta(h-z_0)} \right] P_I}{\frac{1}{\Gamma_T} e^{-i\beta h} - \Gamma_B e^{i\beta h}} \equiv C_- P_I \quad (12)$$

The total field in the waveguide ($0 < z < h$) is given by

$$p(r, z) = \int_0^z \left[\frac{i}{\sqrt{k^2 - k_r^2}} \right] \left[e^{i\sqrt{k^2 - k_r^2}|z-z_0|} + C_+ e^{i\sqrt{k^2 - k_r^2}z} + C_- e^{-i\sqrt{k^2 - k_r^2}z} \right] J_0(k_r r) k_r dk_r \quad (13)$$

with

$$C_+ \equiv \frac{e^{-i\beta(h+z_0)} - \Gamma_T e^{i\beta(h-z_0)}}{\frac{1}{\Gamma_B} e^{-i\beta h} - \Gamma_T e^{i\beta h}} \quad (14)$$

and

$$C_- \equiv \frac{\Gamma_B e^{i\beta(h+z_0)} - e^{i\beta(h-z_0)}}{\frac{1}{\Gamma_T} e^{-i\beta h} - \Gamma_B e^{i\beta h}} \quad (15)$$

The zeros of $e^{-i\beta h} - \Gamma_B \Gamma_T e^{i\beta h} = 0$ contribute poles to the depth-dependent Green's function and give rise to the modes of the waveguide. Each of these poles in Equation (13)

makes a contribution to the field of the form

$$I(r, z, \rho_i) = \int_0^{\infty} \frac{i}{\sqrt{k^2 - \rho^2}} e^{i\sqrt{k^2 - \rho^2}|z|} \frac{1}{\rho^2 - \rho_i^2} J_0(\rho r) \rho d\rho \quad (16)$$

and the development we used for calculating fields in the presence of poles applies.

It should be noted that the inverse problem, that of resolving modes in a waveguide, can be cast into the classical signal processing form of finding poles in the Fourier transform by first generating the Abel transform of the pressure field! The effect of branch lines on this approach needs to be studied, however.

It is also possible to construct nulling operators to estimate the pole positions (as is done in Maximum Entropy spectral estimation techniques) by using Equation (2), which does include some branch line effects.

References

1. Brekhovskikh, *Waves in Layered Media*, Academic Press, New York (1960).

APPENDIX 1:

DETERMINING LIMITS FOR THE ALIASING RESULT OF SECTION (II.7)

In this appendix we determine the limits as $N \rightarrow \infty$ for the expressions:

$$\frac{\sin N \pi x}{\sin \frac{\pi x}{2}} \cos \frac{\pi x}{4} \quad (1)$$

and

$$\frac{\cos N \pi x}{\sin \frac{\pi x}{2}} \sin \frac{\pi x}{4} \quad (2)$$

To evaluate the limit in Equation (1) we use the known limit:

$$\lim_{N \rightarrow \infty} \frac{\sin 2\pi x (N - \frac{1}{2})}{\sin \pi x} = \lim_{N \rightarrow \infty} \frac{\sin 2\pi x N}{\sin \pi x} \cos \pi x = \sum_k \delta(x - k) \quad (3)$$

The limit in Equation (3) is zero except at the zeros of $\sin \pi x$, which occur at $x = k$ for $k = 0, \pm 1, \pm 2, \dots$. At these points $\cos \pi x = \cos \pi k = (-1)^k$. The effect of deleting the $\cos \pi x$ term is to generate alternating signs:

$$\lim_{N \rightarrow \infty} \frac{\sin 2\pi N x}{\sin \pi x} = \sum_k (-1)^k \delta(x - k) \quad (4)$$

A change of variables shows that

$$\lim_{N \rightarrow \infty} \frac{\sin \pi N x}{\sin \pi \frac{x}{2}} = \sum_k (-1)^k \delta(\frac{x}{2} - k) \quad (5)$$

We determine the limit of Equation (1) by multiplying by $\cos \frac{\pi x}{4}$ to find:

$$\lim_{N \rightarrow \infty} \frac{\sin \pi N x}{\sin \pi \frac{x}{2}} \cos \frac{\pi x}{4} = \cos \frac{\pi x}{4} \sum_k (-1)^k \delta(\frac{x}{2} - k) \quad (6)$$

We can simplify Equation (6) by using the fact that $f(x)\delta(x-x_0) = f(x_0)\delta(x-x_0)$ and that

$$\cos \frac{\pi k}{2} = \begin{cases} 1 & k=0,4,8, \dots \\ 0 & k=1,5,9, \dots \\ -1 & k=2,6,10, \dots \\ 0 & k=3,7,11, \dots \end{cases} \quad (7)$$

to find:

$$\lim_{N \rightarrow \infty} \frac{\sin \pi N x}{\sin \pi \frac{x}{2}} \cos \frac{\pi x}{4} = \sum_k (-1)^k \delta\left(\frac{x}{2} - 2k\right) \quad (8)$$

This is the result needed in the text.

To evaluate the limit of Equation (2):

$$\frac{\cos N \pi x}{\sin \frac{\pi x}{2}} \sin \frac{\pi x}{4} \quad (9)$$

we first consider the behavior of $\frac{\cos N \pi x}{\sin \frac{\pi x}{2}}$ near $x = 0$. The behavior at the other zeros of $\sin \frac{\pi x}{2}$

will be similar. We assume that x is sufficiently small so that $\sin \frac{\pi x}{2}$ can be replaced the first term of its Taylor series, $\frac{\pi x}{2}$. We consider:

$$\lim_{N \rightarrow \infty} \frac{\cos N \pi x}{\frac{\pi x}{2}} \quad (10)$$

Instead of evaluating the limit directly, we look at the Fourier transform of the limit. We evaluate this by taking the limit of the Fourier transforms of each term and write:¹

$$FT \left\{ \lim_{N \rightarrow \infty} \frac{\cos N \pi x}{\frac{\pi x}{2}} \right\} = \lim_{N \rightarrow \infty} FT \left\{ \frac{\cos N \pi x}{\frac{\pi x}{2}} \right\} \quad (11)$$

The Fourier transform of $\frac{\cos N \pi x}{\frac{\pi x}{2}}$ can be found by convolving the Fourier transform of

$\cos N \pi x$ with the Fourier transform of $\frac{2}{\pi x}$.

$$FT \left\{ \frac{\cos N \pi x}{\frac{\pi x}{2}} \right\} = FT \left\{ \cos N \pi x \right\} * FT \left\{ \frac{2}{\pi x} \right\} \quad (12)$$

so that:

¹These steps can be rigorously justified by using generalized functions. [1] They presume that two functions are said to be equal if the result of convolving their difference with any band-limited function is always zero. Alternately, two functions are said to be equal if the Fourier transform of their difference is zero for any finite band.

$$FT \left\{ \frac{\cos N \pi x}{\frac{\pi x}{2}} \right\} = \left[\delta \left(f - \frac{N}{2} \right) + \delta \left(f + \frac{N}{2} \right) \right] * \left[-2i \operatorname{sgn}(f) \right] \quad (13)$$

This function is plotted in Figure A1.1. It is given by

$$FT \left\{ \frac{\cos N \pi x}{\frac{\pi x}{2}} \right\} = \begin{cases} 4i & f < -\frac{N}{2} \\ 0 & -\frac{N}{2} < f < \frac{N}{2} \\ -4i & \frac{N}{2} < f \end{cases} \quad (14)$$

As $N \rightarrow \infty$ this Fourier transform becomes equal to zero over any finite interval. Consequently, as a generalized function

$$\lim_{N \rightarrow \infty} \frac{\cos N \pi x}{\frac{\pi x}{2}} = 0_g \quad (15)$$

where 0_g means 0 as a generalized function. Basically this means that as $N \rightarrow \infty$ $\frac{\cos N \pi x}{\frac{\pi x}{2}}$ oscillates

rapidly around zero in such a manner that when it is convolved with any bandlimited function, the result is zero. Since we will only use this functions inside integrals (strictly speaking impulses are only defined inside integrals) we will simply call it zero.

Given that this limit is zero, the limit of $\frac{\cos N \pi x}{\sin \frac{\pi x}{2}}$, which is simply a periodically repeated

version of $\frac{\cos N \pi x}{\frac{\pi x}{2}}$ near the zeros of $\sin \left(\frac{\pi x}{2} \right)$ (with sign changes), must also be zero. Since

$\sin \frac{\pi x}{2}$ is finite everywhere, we have the result needed in the text by multiplying:

$$\lim_{N \rightarrow \infty} \frac{\cos N \pi x}{\sin \frac{\pi x}{2}} \sin \frac{\pi x}{2} = 0 \quad (16)$$

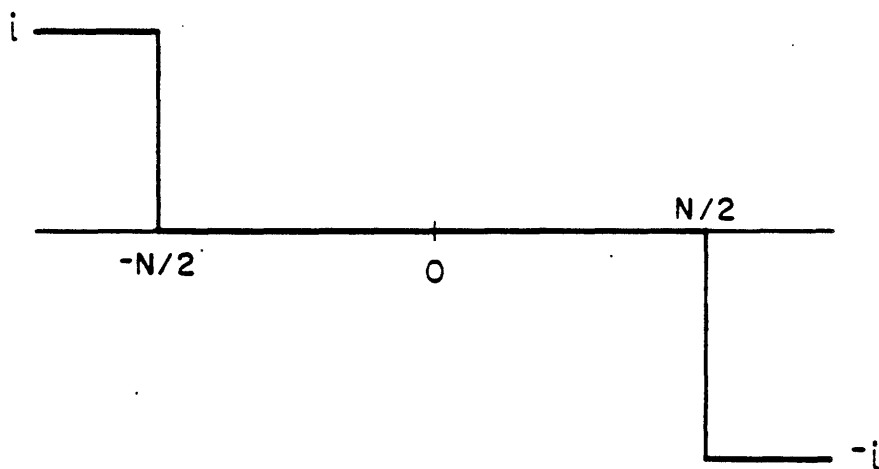
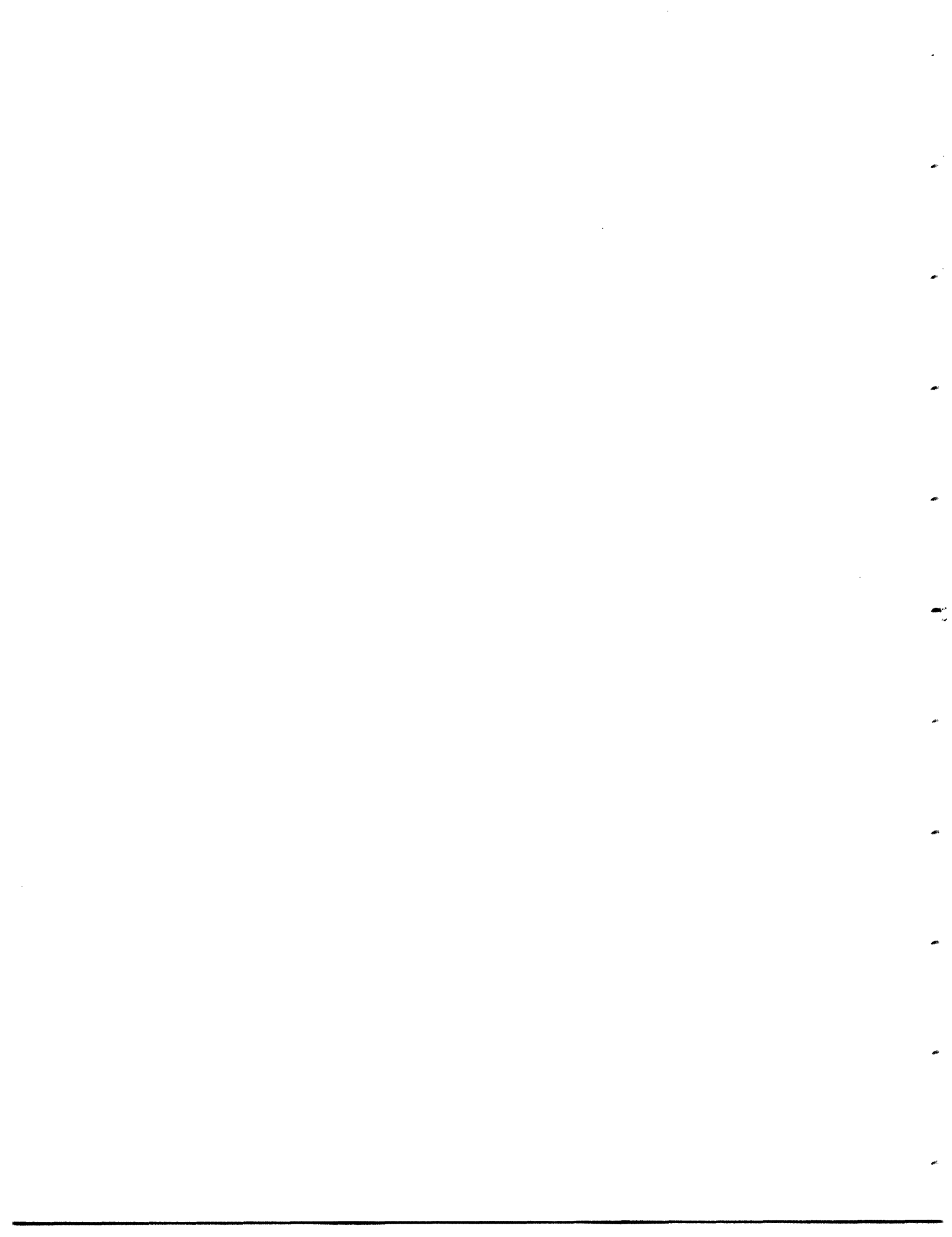


Figure A1.1 Fourier transform of $\frac{\cos N \pi x}{\frac{\pi x}{2}}$

References

1. M.J. Lighthill, *Introduction to Fourier Analysis and Generalized Functions*, Cambridge University Press, New York (1978).



APPENDIX II:
THE VALUE OF THE KERNEL
FOR THE NUMERICAL PORTION OF THE HYBRID ALGORITHM
AT THE WATER WAVE NUMBER

In this appendix we derive the value of $L(k_0)$ discussed in Section (IV.3a). $L(k_r)$ is defined by Equation (IV.3a.15) as:

$$L(k_r) = \frac{i [L(k_r) - L(k_0)]}{\sqrt{k_0^2 - k_r^2}} e^{i\sqrt{k_0^2 - k_r^2}|z|} \quad (1)$$

and we seek to evaluate the limit

$$\lim_{k_r \rightarrow k_0} L(k_r) \quad (2)$$

under the condition that the impedance of the bottom, $Z(k_r)$, is finite at $k_r = k_0$.

At $k_r = k_0$ Equation (1) takes the indeterminate form $\frac{0}{0}$. We evaluate the limit (2) by using L' Hospital's rule:

$$\lim_{k_r \rightarrow k_0} \frac{i \{ \Gamma(k_r) - \Gamma(k_0) \} e^{i\sqrt{k_0^2 - k_r^2}|z|}}{\sqrt{k_0^2 - k_r^2}} = \lim_{k_r \rightarrow k_0} \frac{\frac{\partial}{\partial k_r} i \{ \Gamma(k_r) - \Gamma(k_0) \} e^{i\sqrt{k_0^2 - k_r^2}|z|}}{\frac{\partial}{\partial k_r} \sqrt{k_0^2 - k_r^2}} \quad (3)$$

After separating out the terms that approach zero as $k_r \rightarrow k_0$ this expression becomes:

$$\lim_{k_r \rightarrow k_0} L(k_r) = \lim_{k_r \rightarrow k_0} \frac{-i \sqrt{k_0^2 - k_r^2}}{k_r} \dot{\Gamma}(k_r) e^{i\sqrt{k_0^2 - k_r^2}|z|} \quad (4)$$

We now express $\dot{\Gamma}(k_r)$ in terms of the characteristic impedance of the upper half space, Z_0 , and the impedance at the interface which we will denote at Z_1 . Both Z_0 and Z_1 are functions of k_r in general. In terms of these $\Gamma(k_r)$ is given by:

$$\Gamma(k_r) = \frac{Z_1 - Z_0}{Z_1 + Z_0} \quad (5)$$

Taking derivatives we find:

$$\dot{\Gamma}(k_r) = 2 \left[\frac{\dot{Z}_1 Z_0 - Z_1 \dot{Z}_0}{(Z_1 + Z_0)^2} \right] \quad (6)$$

We now use the characteristic impedance of the upper half space:

$$Z_0 = \frac{\rho_0 \omega}{\sqrt{k_0^2 - k_r^2}} \quad (7)$$

where ρ_0 is the density of the half space, ω is the temporal frequency, and $k_0 = \frac{\omega}{C_0}$ where C_0 is the speed of sound in the upper half space. Substituting Equation (7) into Equation (6) and evaluating \dot{Z}_0 we have:

$$\Gamma(k_r) = 2 \left[\frac{\dot{Z}_1 \frac{\rho_0 \omega}{\sqrt{k_0^2 - k_r^2}} - \frac{k_r \rho_0 \omega}{(k_0^2 - k_r^2)^{3/2}} Z_1}{Z_1^2 + 2 Z_1 \frac{\rho_0 \omega}{\sqrt{k_0^2 - k_r^2}} + \frac{\rho_0^2 \omega^2}{k_0^2 - k_r^2}} \right] = 2 \left[\frac{\dot{Z}_1 \rho_0 \omega - \frac{k_r \rho_0 \omega}{\sqrt{k_0^2 - k_r^2}} Z_1}{Z_1^2 (k_0^2 - k_r^2) + 2 Z_1 \rho_0 \omega \sqrt{k_0^2 - k_r^2} + \rho_0^2 \omega^2} \right] \quad (8)$$

Substituting (8) into (4) we find

$$\lim_{k_r \rightarrow k_0} L(k_r) = \lim_{k_r \rightarrow k_0} \frac{-i \sqrt{k_0^2 - k_r^2}}{k_r} \cdot 2 \cdot \left[\frac{\rho_0 \omega \dot{Z}_1 - \frac{k_r \rho_0 \omega}{\sqrt{k_0^2 - k_r^2}} Z_1}{Z_1^2 (k_0^2 - k_r^2) + 2 Z_1 \rho_0 \omega \sqrt{k_0^2 - k_r^2} + \rho_0^2 \omega^2} \right] \quad (9)$$

or

$$L(k_0) = \frac{-2i Z_1(k_0)}{\rho_0 \omega} \quad (10)$$

provided that $\lim_{k_r \rightarrow k_0} \sqrt{k_0^2 - k_r^2} \dot{Z}_1(k_r) = 0$

If the interface is between two isovelocity half spaces, the expression (10) for $L(k_0)$ can be written directly in terms of the material parameters. For this case $Z_1(k_r) = \frac{\rho_1 \omega}{\sqrt{k_1^2 - k_r^2}}$. $Z_1(k_0)$ is finite because $k_1 \neq k_0$ (if $k_1 = k_0$ there would be no interface). $L(k_0)$ is given by

$$L(k_0) = \frac{-2i \rho_1}{\rho_0 \sqrt{k_1^2 - k_0^2}} \quad (11)$$

APPENDIX III:

EVALUATION OF THE POLE CONTRIBUTION TO THE FIELD FOR SECTION (IV.3B)

Here we evaluate the pole contribution to Equation (1):

$$I(r, z; \rho_i) \equiv \int_0^{\infty} \frac{1}{\rho^2 - \rho_i^2} \frac{i}{\sqrt{k^2 - \rho^2}} e^{i\sqrt{k^2 - \rho^2}|z|} J_0(\rho r) \rho d\rho \quad (1)$$

We evaluate Equation (1) by determining a partial differential equation that it satisfies and solving that equation.

Taking the second partial derivative of Equation (1) with respect to z we have

$$\frac{\partial^2}{\partial z^2} I(r, z; \rho_i) = \int_0^{\infty} \frac{\rho^2 - k^2}{\rho^2 - \rho_i^2} \frac{i}{\sqrt{k^2 - \rho^2}} e^{i\sqrt{k^2 - \rho^2}|z|} J_0(\rho r) \rho d\rho + 2\delta(z) \int_0^{\infty} \frac{i\sqrt{k^2 - \rho^2}}{\rho^2 - \rho_i^2} \frac{i}{\sqrt{k^2 - \rho^2}} e^{i\sqrt{k^2 - \rho^2}|z|} J_0(\rho r) \rho d\rho \quad (2)$$

If we use

$$\delta(z) f(z) = \delta(z) f(0) \quad \text{for any } f(z) \quad (3)$$

then Equation (2) becomes

$$\frac{\partial^2}{\partial z^2} I(r, z; \rho_i) = \int_0^{\infty} \frac{\rho^2 - k^2}{\rho^2 - \rho_i^2} \frac{i}{\sqrt{k^2 - \rho^2}} e^{i\sqrt{k^2 - \rho^2}|z|} J_0(\rho r) \rho d\rho - 2\delta(z) \int_0^{\infty} \frac{1}{\rho^2 - \rho_i^2} J_0(\rho r) \rho d\rho \quad (4)$$

Putting it all together we have:

$$\left[\frac{\partial^2}{\partial z^2} - (\rho_i^2 - k^2) \right] I(r, z; \rho_i) = \int_0^{\infty} \frac{i}{\sqrt{k^2 - \rho^2}} e^{i\sqrt{k^2 - \rho^2}|z|} J_0(\rho r) \rho d\rho - 2\delta(z) \int_0^{\infty} \frac{1}{\rho^2 - \rho_i^2} J_0(\rho r) \rho d\rho \quad (5)$$

If we define $\beta^2 \equiv \rho_i^2 - k^2$, choosing real part of $\beta > 0$, and use

$$\int_0^{\infty} \frac{i}{\sqrt{k^2 - \rho^2}} e^{i\sqrt{k^2 - \rho^2}|z|} J_0(\rho r) \rho d\rho = \frac{e^{ik\sqrt{r^2 + z^2}}}{\sqrt{r^2 + z^2}} \quad (6)$$

together with

$$\int_0^{\infty} \frac{1}{\rho^2 - \rho_i^2} J_0(\rho r) \rho d\rho = K_0(-\text{sgn}[Im(\rho_i)] i \rho_i r) = \frac{-\pi i}{2} H_0^{(1)}(\rho_i r) \quad \text{when } Im(\rho_i) > 0 \quad (7)$$

then (A2.5) becomes

$$\left[\frac{\partial^2}{\partial z^2} - \beta^2 \right] I(r, z; \rho_i) = \frac{e^{ik\sqrt{r^2 + z^2}}}{r^2 + z^2} + i\pi\delta(z)H_0^{(1)}(\rho_i r) \quad (8)$$

when $Im(\rho_i) > 0$.

The Green's function for this differential equation is given by

$$G(r, z, \xi) = \frac{-1}{2\beta} e^{-|z-\xi|\beta} \quad (9)$$

Using this for the impulsive response and convolving with the continuous driving function to obtain the particular solution we obtain:

$$I(r, z; \rho_i) = \frac{-1}{2\beta} \int_{-\infty}^{\infty} \frac{e^{ik\sqrt{r^2+\xi^2}}}{\sqrt{r^2+\xi^2}} e^{-\beta|z-\xi|} d\xi - \frac{i\pi}{2\beta} H_0^{(1)}(\rho_i r) e^{-\beta|z|} \quad (10)$$

When $Im(\rho_i) > 0$.

The general form of this expression which is valid for all ρ_i is given by:

$$I(r, z; \rho_i) = \frac{-1}{2\beta} \int_{-\infty}^{\infty} \frac{e^{ik\sqrt{r^2+\xi^2}}}{\sqrt{r^2+\xi^2}} e^{-\beta|z-\xi|} d\xi + \frac{1}{\beta} K_0(-sgn[Im(\rho_i)]i\rho_i r) e^{-\beta|z|} \quad (11)$$

DISTRIBUTION LIST

	<u>DODAAD Code</u>	
Director Advanced Research Project Agency 1400 Wilson Boulevard Arlington, Virginia 22209 Attn: Program Management	HX1241	(1)
Group Leader Information Sciences Associate Director for Engineering Sciences Office of Naval Research 800 North Quincy Street Arlington, Virginia 22217	N00014	(1)
Administrative Contracting Officer E19-628 Massachusetts Institute of Technology Cambridge, Massachusetts 02139	N66017	(1)
Director Naval Research Laboratory Attn: Code 2627 Washington, D. C. 20375	N00173	(6)
Defense Technical Information Center Bldg. 5, Cameron Station Alexandria, Virginia 22314	S47031	(12)

